Innovative Photoelectrodes for Solar Water Splitting

Dissertation presented to the Faculty of Engineering of the University of Porto
for obtaining the degree of
Doctor in Chemical and Biological Engineering
by

Paula Manuela Monteiro Pereira Costa Dias

Adélio Miguel Magalhães Mendes, Full Professor – Supervisor
Luísa Manuela Madureira Andrade, Assistant Researcher – Co-Supervisor

Department of Chemical Engineering,
Faculty of Engineering, University of Porto, Portugal

2016

The present work was partially financially supported by: Project POCI-01-0145-FEDER-006939 (Laboratory for Process Engineering, Environment, Biotechnology and Energy – LEPABE) funded by FEDER funds through COMPETE2020 – Programa Operacional Competitividade e Internacionalização (POCI) – and by national funds through FCT – Fundação para a Ciência e a Tecnologia – within the Project H2Solar (PTDC/EQU-EQU/107990/2008) and for the PhD grant (SFRH/BD/81016/2011). This work was also supported by the European Commission through the Seventh Framework Programme, the Specific Programme "Ideas" of the European Research Council for research and technological development as part of an Advanced Grant under Grant Agreement No. 321315 (BI-DSC), by the NanoPEC Project (Contract No. 227179) and by the PECDEMO Project co-funded by the European Union's Seventh Framework Program (FP7/2007-2013) for the Fuel Cells and Hydrogen Joint Technology Initiative under grant agreement No. 621252.

Paula Manuela Monteiro Pereira Costa Dias
Laboratory for Process Engineering, Environment, Biotechnology and Energy
University of Porto – Faculty of Engineering
Rua Dr. Roberto Frias s/n, 4200-465 Porto
Portugal

ACKNOWLEDGMENTS

I am grateful to the Portuguese Foundation for Science and Technology (FCT) for my PhD grant (SFRH/BD/81016/2011) and to LEPABE, DEQ and FEUP for providing me all the facilities to develop my work.

There is a tremendous amount of people that participated to my growth, enlarge my horizons and inspired me that I would like to thank. First, I would like to express my gratitude to Prof. Adélio Mendes and Dr. Luísa Andrade, my supervisors, who have been great sources of my learning in the past years. Many thanks to Prof. Adélio for his wisdom, guidance and all the motivation during my PhD; the opportunity to develop my work in his group was an honor. Prof. Adélio has a huge heart, thanks for all teachings and friendship. I also have to make a heartfelt thanks to Dr. Luísa Andrade, for her guidance and all the transmitted knowledge, optimism and friendship. Luísa represents very well the woman power. Most of all, I am very thankful to both for believing in me and always pushing me to become better, as a scientist and a person. You are examples of inspiration.

A special thanks to my lab mates, especially to the members of Solar Group led by Prof. Adélio Mendes, whose work was mainly developed at UPTEC – Innovation Center. Whether science and, of course, life were smiling or not to me, I have always been motivated to go to work thanks to the cheerful and relaxed atmosphere created by my colleagues and friends. Thanks to my girls, Joana Ângelo, Isabel Mesquita, Suélen Amorim, Ana Pereira and Andreia Cruz. I am also very grateful to my solar water splitting mates, to Dr. Tânia Lopes for introducing me to this exciting field, for the fruitful discussions and extra supports, to António Vilanova for the great help, collaboration and friendship; it was a pleasure working with both. I also acknowledge Dr. Margarida Catarino, Dr. Cecília Mateus-Pedrero, Pedro Magalhães, João Azevedo, Dr. Verena Stockhausen and Dr. Arlete Apolinário for the usefull discussions and precious help.

I gratefully acknowledge Prof. Michael Grätzel and Prof. David Tilley, for accepting me in LPI group of research, as well as all the facilities and materials provided during four profitable months. Thanks to LPI members for welcoming me and promptly help me every time I needed, particularly, I thank everyone in the Hydrogen Group. During this period, I could take advantage of the unlimited knowledge of Prof. Michael Grätzel and the guidance and support of Prof. David Tilley were fundamental for the development of my work. Many thanks to Prof. David for the constant availability, for all the enlightening scientific discussions and the less serious ones. I also acknowledge Dr. Matthew Mayer for his precious help, transmitted knowdlege and the fruitful discussions; and Marcel Schreier for the help with the Faradaic measurements and all the funny time spent in the lab. A special thanks to Maurin Cornuz for doing everything to facilitate my integration in the group and for being an excellent friend, Ludmilla Steier for being like a sister to me; and Nicolas Tétreault for the good sense of humor and his way to enjoy life. I was lucky enough to become friend of some of you and I keep you and the amazing times that we spent together in my heart! A heartfelt thanks to Ms. Maria José for her hospitality, she was more than a friend, she was like a mother during this period.

I cannot forget thanking all my friends, for their support, affection and for always having been a source of happiness and encouragement. Thanks to my friends from Vizela, especially Ana Isabel, to my friends from Porto, Verinha, Silvi and Tobé, and to my friends from best group ever (in particular to Patrícia) for the good moments spent over the years, for making me smile and spending crazy antics. I am also very grateful to my pufetas' family for the true friendship: Marta Pimenta, Catarina Duarte, Isabel Gomes, Erica Doutel, Sara Paula, José Nogueira, João Mendes, Ricardo Teixeira, António Leal, André Santos and João Silva. To my sister from another mother, Anabela, thanks…just for being always there.

Pedro, I would like to express my love, thanks for your presence in my life! You are more than special!

Last but not least, I would like to express my warm gratitude to my family, in special to my grandparents, *Glorinha* and *Mindinho*, my great-aunt *Isabel*, and my lovely parents, *Nelinha* and *Chiquinho*, the most important people to me, to whom I owe much of who I am today. Thank you for making me feel special, thank you for all!

My sincere gratitude to all for being part of this story…and the story of my life!

To my eternal love,
my father Francisco Dias…

PREFACE

The present work was developed at the Laboratory for Process Engineering, Environment, Biotechnology and Energy (LEPABE) facilities, in the Chemical Engineering Department of the Faculty of Engineering - University of Porto (FEUP), between 2011 and 2016 and under the FCT (Foundation for Science and Technology) grant SFRH/BD/81016/2011. The work was supervised by Professor Adélio Mendes and co-supervised by Dr. Luísa Andrade from LEPABE-FEUP.

Part of this thesis was also performed at the Laboratory of Photonic and Interfaces (LPI) in École Polytechnique Fédérale de Lausanne (EPFL), in Switzerland, under the supervision of Professors Michael Grätzel and David Tilley.

This thesis presents seven chapters: one introduction chapter; five scientific papers, each paper represents one independent chapter; and a final chapter with the general conclusions and perspectives for future work.

CONTENTS

CHAPTER 1

INTRODUCTION

CHAPTER 2

TEMPERATURE EFFECT ON WATER SPLITTING USING A Si-DOPED HEMATITE PHOTOANODE

CHAPTER 3

PHOTOELECTROCHEMICAL WATER SPLITTING USING TUNGSTEN TRIOXIDE PHOTOANODES: THE SUBSTRATE AND TEMPERATURE ROLES

CHAPTER 4

EXTREMELY STABLE BARE HEMATITE PHOTOANODE FOR SOLAR WATER SPLITTING

CHAPTER 5

PHOTOELECTROCHEMICAL WATER OXIDATION USING HEMATITE PHOTOANODES COATED WITH RUTHENIUM DIOXIDE

CHAPTER 6

TRANSPARENT CUPROUS OXIDE PHOTOCATHODE ENABLING A STACKED TANDEM CELL FOR UNBIASED WATER SPLITTING

CHAPTER 7

ABSTRACT

Solar energy is one of the most important sources of renewable energy. The market of solar cells is growing quite fast but due to the intermittent nature of solar power, efficient storage is still needed to supply the current global energy demand and environmental sustainability. The production of solar fuels is a promising route and, in particular, hydrogen generated via photoelectrochemical (PEC) water splitting has been considered as a promising energy fuel in the near future. PEC cells integrate collection of sunlight and water electrolysis in a single device to further produce hydrogen and oxygen.

PEC research efforts rely on the design of earth-abundant semiconductor materials that are both highly efficient and chemically stable; the target of 10 % solar-to-hydrogen (STH) conversion efficiency is needed to enable commercialization. Materials commonly used in these devices are metal oxide semiconductors. This thesis concerns the study of three of these oxides, namely α-Fe_2O_3 (hematite), tungsten trioxide and cuprous oxide photoelectrodes.

For scaling-up PEC water splitting technology, it is not only necessary to find new semiconductors and to use a versatile PEC reactor, but also to understand the behavior of this reactor under real outdoor conditions Herein, the influence of temperature and photoelectrode substrates were evaluated as well as the stability of the photoelectrodes under operation. Emphasis was put on the optimization of hematite photoelectrode and a record full stability of 1000 h was achieved.

While much work is being devoted to identify the ideal semiconductor for solar-driven water splitting, nowadays the focus is shifting towards using two or more photoactive materials. Therefore, tandem PEC arrangements based on metal oxides, *e.g.* by coupling n- and p-type photoelectrodes or a photoelectrode with a photovoltaic (PV) cell, offer a potentially inexpensive route for solar hydrogen generation. This configuration allows simultaneously achieving high efficiencies and maximizing the fraction of solar energy collected. Hematite photoanode is of great interest thanks to its suitable bandgap (thermodynamic STH of *ca.* 16.8 %) and excellent stability, but the highly anodic potential required to initiate the oxygen evolution reaction is a major challenge. The photocurrent onset potential of hematite photoanodes was decreased

through a synergetic combination of surface modification by high temperature annealing at 800 ºC and by coating with RuO_2, a highly active water oxidation co-catalyst. Both treatments change the water oxidation kinetics at semiconductor/ electrolyte interface, resulting in a turn-on potential closer to hematite flatband potential (0.52 V_{RHE}) and a high photopotential of *ca.* 0.95 V. With the ongoing progress to reach maximum photocurrent at lower potentials (< 0.70 V_{RHE}), RuO_2-coated hematite photoanodes can be integrated in efficient and stable tandem devices. Cuprous oxide photocathode is also a promising material with the capability for low cost and large-scale solar energy conversion. Recent successes on improving the quality of protective overlayers and the use of RuO_2 as a co-catalyst greatly extended the stability of hydrogen evolving Cu_2O-based photocathodes. Towards the development of a tandem arrangement, a stable and efficient semi-transparent Cu_2O photocathode was optimized that enabled unassisted water splitting when coupled with the emerging and promising perovskite photovoltaic solar cells technology.

SUMÁRIO

A energia solar é uma das mais importantes fontes de energia renovável. O mercado de células solares tem crescido rapidamente, mas devido à natureza intermitente da energia solar, é necessário o seu armazenamento eficiente para colmatar a atual procura energética e a sustentabilidade ambiental. A produção fotoeletroquímica de combustíveis solares é uma via promissora e, em particular, o hidrogénio produzido através da fotohidrólise da água é considerado um combustível muito promissor para um futuro próximo. As células fotoeletroquímicas PEC (do inglês *photoelectrochemical*) acoplam a recolha da luz solar e a eletrólise da água num único dispositivo capaz de produzir hidrogénio e oxigénio.

Os esforços na área de investigação das células PEC têm vindo a focar-se no fabrico de materiais semicondutores abundantes, simultaneamente muito eficientes e quimicamente estáveis; atingir-se a meta de 10 % de eficiência de conversão da energia fotónica em hidrogénio é necessário para permitir a comercialização destas células. Os semicondutores de óxidos metálicos são os materiais mais comummente utilizados neste tipo de dispositivos. Nesta tese são estudados três destes óxidos: os fotoelétrodos de α-Fe_2O_3 (óxido de ferro (III) ou hematite), trióxido de tungstênio e óxido de cobre.

Para a comercialização com sucesso desta tecnologia é não só necessário encontrar novos semicondutores e usar um reator PEC versátil, mas também compreender o seu comportamento em condições reais de operação. Neste sentido, foi avaliada a influência da temperatura e dos substratos dos fotoelétrodos, bem como a estabilidade dos fotoelétrodos no funcionamento de uma célula fotoeletroquímica. Foi dado maior ênfase à otimização dos fotoelétrodos de hematite, permitindo alcançar um recorde de estabilidade de 1000 horas.

Mais recentemente os trabalhos de investigação nesta área têm-se dedicado, essencialmente, à identificação de um semicondutor ideal capaz de promover diretamente a autoclivagem da água através da radiação solar. Contudo, hoje em dia, os novos avanços prendem-se com a utilização de dois ou mais materiais fotoativos. Assim sendo, os dispositivos PEC tendo vindo a basear-se numa configuração conjunta de óxidos metálicos (do inglês configuração *PEC tandem*) permitem a geração de hidrogénio solar a baixos preços, por exemplo, através do acoplamento de

fotoelétrodos do tipo *n* e *p* ou de um fotoelétrodo e uma célula fotovoltaica. Esta configuração permite alcançar simultaneamente altas eficiências e maximizar a fração de energia solar absorvida. A hematite é um semicondutor de grande interesse para estas aplicações devido ao seu adequado hiato energético (eficiência termodinâmica de conversão da energia solar em hidrogénio de cerca de 16.8 %) e uma excelente estabilidade. No entanto, para a sua implementação o grande desafio passa por diminuir a elevada diferença de potencial que é necessário fornecer à célula para iniciar a reação de evolução de oxigénio. Este potencial nos fotoânodos de hematite foi reduzido através da combinação de dois tratamentos superficiais, nomeadamente o recozimento do filme de hematite a altas temperaturas (800 ºC) e a modificação da superfície com dióxido de ruténio, um co-catalisador altamente ativo para a oxidação da água. Ambos os tratamentos permitiram mudar a cinética da reação de oxidação da água na interface semicondutor/eletrólito, cujo resultado culminou com a diminuição deste potencial para um valor próximo do potencial de banda plana (do inglês *flatband*) da hematite (0.52 V_{RHE}) e um potencial elétrico gerado pela luz de cerca de 0.95 V. Por outro lado, com os atuais progressos para atingir a máxima fotocorrente a potenciais mais baixos (< 0.7 V_{RHE}), os fotoânodos de hematite com RuO_2 podem ser integrados em dispositivos *PEC tandem* eficientes e estáveis. O óxido de cobre é também conhecido como um material promissor com a capacidade de ser fabricado a baixo custo e em larga escala para a conversão da energia solar. Os sucessos recentes na melhoria da qualidade de camadas protetoras, bem como, a utilização de um co-catalisador de óxido de ruténio aumentou significativamente a estabilidade da evolução do hidrogénio nestes fotocátodos. Para o desenvolvimento de sistemas *PEC tandem*, os fotocátodos de óxido de cobre foram otimizados de modo a apresentarem semi-transparência, serem eficientes e estáveis. Estes resultados alcançados permitiram a fotohidrólise direta da água através do acoplamento dos fotocátodos de óxido de cobre com as emergentes e promissoras células solares sensibilizadas por perovskita.

FIGURE CAPTIONS

TABLE CAPTIONS

ABBREVIATIONS AND SYMBOLS

Variables	Definition	Units
A	active area	cm^2
abs	absorbance	%
a_i	activities of species	
b	cell thickness	m
C	capacitor	F
c_0	speed of light constant ($c_0 = 2.9979(25) \times 10^8$ $m \cdot s^{-1}$)	$m \cdot s^{-1}$
C_{Bulk}	bulk capacitance	F
C_H	Helmholtz capacitance	F
C_{RuO2}	RuO_2 capacitance	F
C_{SC}	space charge capacitance	F
C_{SS}	surface states capacitance	F
D_i	diffusion coefficient of the reactant species *i*	$cm^2 \cdot s^{-1}$
E	electrochemical potential	V
$E_{Ag/AgCl}$	potential of the Ag/AgCl reference electrode	V
E_{bias}	bias energy potential	V
E_{CB}	conduction band potential	V
${}_nE_d$	electron-induced decomposition potential	V
${}_pE_d$	hole-induced decomposition potential	V
E_F	Fermi level potential	V
$E_{F,\,n}$	potential of the quasi-Fermi levels for the electrons	V
$E_{F,\,p}$	potential of the quasi-Fermi levels for the holes	V
E_{fb}	flatband potential	V
E_g	bandgap potential	V
E_g (0)	bandgap potential at $T = 0$ K	V
E_{MPP}	potential at the maximum power point	V
E^o	standard reversible electrochemical potential	V
$E^o(H^+/H_2)$	water reduction potential in an acid electrolyte	V
$E^o(H_2O/O_2)$	water oxidation potential in an acid electrolyte	V
$E^o(H_2O/OH^-)$	water reduction potential in an alkaline electrolyte	V
$E^o(OH^-/O_2)$	water oxidation potential in an alkaline electrolyte	V

E_{onset}	onset potential	V
E_{photo}	photopotential	V
EQE	external quantum efficiency	%
E_{redox}	redox potential	V
E_{RHE}	potential of the reversible hydrogen electrode	V *vs.* RHE
E_{VAC}	vacuum potential	eV
E_{VB}	valence band potential	V
F	Faraday constant (F = 96 485,3(40) C·mol^{-1})	C·mol^{-1}
f_0	interception coefficient in the JMP software	
FF	fill factor	%
f_{i}	coefficients of dimensionless factors X_{i}	
f_{ii}	coefficients of quadratic effects	
f_{ij}	coefficients of cross interaction between factors X_{i} and X_{j}	
h	Planck constant ($h = 6.6260(69) \times 10^{-34}$ J·s)	J·s
hv	energy of the photons	eV
I	generated current	mA
$I(t)$	current response	mA
I_0	amplitude of the current signal	mA
IPCE	incident photon-to-current conversion efficiency	%
I_{sc}	short-circuit current	mA
$ISTC$	intrinsic solar to chemical conversion efficiency	%
j	imaginary number	
j_0	exchange photocurrent density at the counter-electrode	mA·cm^{-2}
J_{actual}	experimental photocurrent density in the JMP software	mA·cm^{-2}
j_{cell}	photocurrent density generated by the PEC cell	mA·cm^{-2}
J_{max}	maximum photocurrent in the optical limit	mA·cm^{-2}
J_{MPP}	photocurrent density at maximum power point	mA·cm^{-2}
J_{photo}	photocurrent density	mA·cm^{-2}
$J_{\mathrm{predicted}}$	predicted photocurrent density in the JMP software	mA·cm^{-2}
J_{sc}	short-circuit photocurrent density	mA·cm^{-2}
k_{B}	Boltzman constant ($k_{\mathrm{B}} = 1.3806(49) \times 10^{-23}$ J·K^{-1})	J·K^{-1}
k_{Bulk}	bulk electron trapping rate constant	s^{-1}
k_{CT}	charge transfer rate constant	s^{-1}
k_{r}	electron-hole recombination in the space charge	s^{-1}

k_{rec}	recombination rate constant	s^{-1}
L_D	short hole diffusion length	nm
n	number of electrons transferred in a reaction	
N_D	donor density	cm^{-3}
$N_{electrons}$	number of light-generated electrons	
n_i	density of the species i in the reaction	m^{-3}
n_{int}	intrinsic carrier population	m^{-3}
$N_{photons}$	number of incident photons at a given wavelength	
n^{ref}	reference particle density	m^{-3}
P	power conversion	$mW \cdot cm^{-2}$
$P_{electrical}$	electric power	$mW \cdot cm^{-2}$
P_{light}	power of incident light	$mW \cdot cm^{-2}$
q	elementary charge (q = 1.6021(76)×10^{-19} C)	C
R	ideal gas constant (R = 8.3144(72) $J \cdot K^{-1} \cdot mol^{-1}$)	$J \cdot K^{-1} \cdot mol^{-1}$
R_{Bulk}	bulk charge transport resistance	Ω
R_{CT}	charge transfer resistance	Ω
$R_{CT, RuO2}$	charge transfer resistance from the RuO_2 film	Ω
$R_{CT, SS}$	charge transfer resistance from the surface states	Ω
R_q	surface roughness	nm
R_{SC}	space charge resistance	Ω
R_{Series}	series resistance	Ω
T	temperature	K or ºC
t	time	s
U_{dark}	potential applied to reach the same current in dark	V
U_{light}	potential applied under illumination	V
v	sprayed volume of solution	mL
V	work potential	V
$V(t)$	voltage perturbation	V
V_0	amplitude of the voltage signal	V
V_{oc}	open-circuit potential	V
w	space charge width	nm
X_i	coded process factors in the JMP software	
x_i	actual process factors in the JMP software	
y	process response in the JMP software	

Z	impedance	Ω
Z'	real part of impedance	Ω
Z''	imaginary part of impedance	Ω

Greek symbols	Definition	Units
α	semiconductor absorbance coefficient	
α'	limit of the gap entropy when $T\rightarrow\infty$	$eV\cdot K^{-1}$
α_i	activities of the reactant and product species	
β	asymmetric parameter	
β'	limit of the gap entropy at the Debye temperature	K
ΔE^o	electric potential of the reaction	$V\cdot mol^{-1}$
ΔE_{photo}	internal photopotential	V
ΔG^o	Gibbs free energy for the overall cell reaction	$KJ\cdot mol^{-1}$
ΔS	standard entropy for the overall cell reaction	$J\cdot mol^{-1}\cdot K^{-1}$
ε_0	vacuum permittivity ($\varepsilon_0 = 8.8541(88)\times10^{-12}$ $C\cdot V^{-1}\cdot m^{-1}$)	$C\cdot V^{-1}\cdot m^{-1}$
ε_r	dielectric constant of the semiconductor	
η	efficiency	%
η_{cat}	catalytic charge transfer efficiency	%
η_{ct}	charge transport efficiency	%
η_{device}	overall PEC device efficiency	%
η_{el}	electrolysis efficiency	%
η_F	Faradaic efficiency	%
η_{hc}	hole collection efficiency	%
η_{light}	light absorption efficiency	%
η_{OER}	water oxidation quantum efficiency	%
η_{PA}	photoanode efficiency	%
η_{PC}	photocathode efficiency	%
$\eta_{photoelectrode}$	photoelectrode efficiency	%
η_{Pt}	overpotential at the platinum counter electrode	%
η_{STH}	solar-to-hydrogen efficiency	%
θ_D	Debye temperature	K
λ	wavelength	nm

μ_i	mobility of species i	$m^2 \cdot V^{-1} \cdot s^{-1}$
ν	frequency	Hz
υ_i	stoichiometric coefficients	
φ	phase angle	rad
ϕ_{H2}	rate of hydrogen production	mmol $H_2 \cdot s^{-1}$
ω	radial frequency	$rad \cdot s^{-1}$

Subscripts	**Definition**
d	decomposition
i	species in reaction
n	electrons
p	holes
0	ambient conditions

Superscripts	**Definition**
in	input
$^{\circ}$	standard conditions
out	output
z	number of electrons

Abbreviations	**Definition**
AES	atomic emission spectroscopy
AFM	atomic force microscopy
ALD	atomic layer deposition
AM	air mass
APCE	applied bias photon-to-current
APCVD	atmospheric pressure chemical vapor deposition
AZO	aluminium doped zinc oxide
CB	conduction band

CE	counter electrode
CIGS	copper indium gallium selenide
CPE	constant phase element
CST	concentrating solar thermal
CV	cyclic voltammetry
CVD	chemical vapor deposition
DOE	US Department of Energy
DSC	dye sensitized solar cell
e^-	electrons
ED	electrodeposition
EDS	energy dispersive X-Ray spectroscopy
EIS	electrochemical impedance spectroscopy
FTO	fluorine doped tin oxide
h^+	holes
HER	hydrogen evolution reaction
HiPIMS	high impulse power magnetron sputtering
ICDD	International Centre for Diffraction Data
ICP	inductively coupled plasma
IR	infrared
ITO	indium tin oxide
I-V	current-voltage characteristics
J	junction
JCPDS	Joint Committee on Powder Diffraction Standards
J-V	photocurrent density-voltage characteristics
LBG	large bandgap material
M	metal
MPP	maximum power point
MS	mass spectroscopy
MX	binary semiconductor
NHE	normal hydrogen electrode
OER	oxygen evolution reaction
PA	photoanode
PC	photocathode
PEC	photoelectrochemical cell

PLD	pulsed layer deposition
PSC	perovskite solar cell
PV	photovoltaic cell
PVD	physical vapor deposition
RE	reference electrode
RHE	reversible hydrogen electrode
SBG	small bandgap material
SCLJ	semiconductor liquid junction
SEM	scanning electron microscopy
SHE	standard hydrogen electrode
solv	solvation of the elements
SP	spray pyrolysis
SS	surface states
STC	solar thermochemical cycles
STH	solar-to-hydrogen
TCO	transparent conducting oxide
TEM	transmission electron microscopy
TEOS	tetraethyl orthosilicate
UHV	ultra-high vacuum
USP	ultrasonic spray pyrolysis
UV	ultraviolet
VB	valence band
WE	working electrode
WOC	water oxidation catalyst
WRC	water reduction catalyst
XPS	X-ray photoelectron spectroscopy
XRD	X-ray diffraction

CHAPTER 1

INTRODUCTION

1

INTRODUCTION

The future prospect of the so-called *Hydrogen Economy* is attracting much interest and several recent efforts are underway to develop renewable and cost-effective technologies for the production, storage, transport and use of hydrogen [1]. Photoelectrochemical (PEC) production of hydrogen from sunlight is one of the most promising technologies, owing the direct conversion of solar energy to chemical fuels, ideal for storage [2]. PEC systems use solar photons collected by photoelectrodes to decompose directly water into hydrogen and oxygen gases without the assistance of electrolyzers.

Numerous semiconductor materials, co-catalysts and cell configurations have been studied, as well as various research methodologies and characterization techniques have been applied to understand and optimize the behavior of these devices. Typical PEC devices use one photoactive semiconductor electrode coupled to a platinum counter electrode, both immersed in a water-based solution. However, in most cases, an external bias is necessary due to non-matching band edges or insufficient charge separation [3]. Nevertheless, the ideal PEC cell should work without any external bias; this can be accomplished by coupling n- and p-type photoelectrodes or a photoelectrode with a photovoltaic cell in a tandem system [4]. Though, the search for Earth-abundant and environmentally safe materials, able to fulfill the several requirements for solar water splitting applications, still a major challenge for solar hydrogen production.

The present chapter introduces and reviews the state-of-the-art materials and technologies of PEC cells for solar water splitting; the PEC cell operating mechanisms are discussed in detail. Finally, the main goals of the present thesis are addressed.

1.1 MOTIVATION

The most important challenge that humanity is nowadays facing is the development of a long-term and sustainable energy economy. Due to world population increasing and industrialization, the total energy consumption is expected to increase from the present 15 TW to 30 TW by 2050 [5, 6]. Presently, fossil fuels provide almost 80 % of our energy needs, which will be unable to keep up the global energy demand [7]. Additionally, in the last few years, the consumption of fossil fuels never stopped growing and this behavior is projected for the next decades [8]. As side effects, global warming consequences, natural resources depletion and global health deterioration are expected to be gradually intensified. Thus, the exploitation of new and promising technologies based on alternative, non-polluting and clean energy sources becomes imperative [9].

Solar energy is the largest and most widespread source of renewable energy. The sun irradiance reaching the Earth is enough to fulfill the humankind energy consumption more than 10 thousand times over (120 PW strikes the surface of the Earth, out of which 36 PW is on land) [10]. The solar cell market is one of the fastest growing in the last decade (*ca.* 40 % per year) [11]; however, the photovoltaic (PV) technology only works in a daily basis and it largely depends on the amount of solar irradiation available. Thus, the intermittent nature of sunlight requires the development of efficient approaches to energy storage [3, 9]. The direct production of chemical fuels from sunlight is a promising route [3]. Solar hydrogen is an attractive and flexible energy carrier due to its potential applications across all energy sectors: it is storable, transportable, it can be efficiently converted into electricity when used as a feedstock of fuel cells and it can be used for carbon dioxide recycling, *e.g.* via Fisher-Tropsch reaction and methanol synthesis [12, 13]. This offers the prospect of a future energy infrastructure based on sunlight, hydrogen and electricity - Figure 1.1 [6].

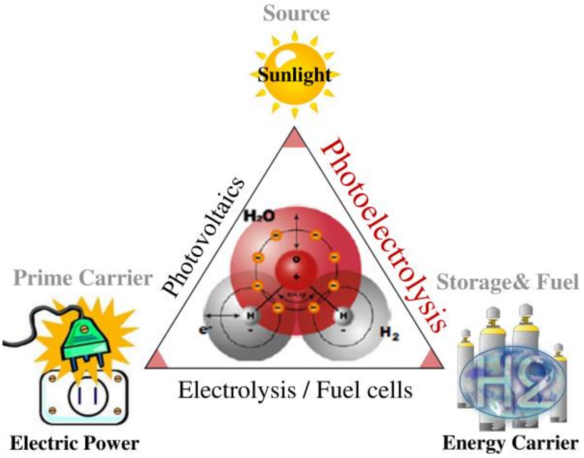

Figure 1.1: A possible future energy triangle based on solar energy (adapted from ref. [6]).

There are presently several approaches aiming solar-to-hydrogen (STH) conversion as illustrated in Figure 1.2 [14]. The two first processes are based on composed devices and consider solar-thermochemical cycles (STC). Process I comprehends two-step STH mechanisms, being the photon-to-thermal energy conversion followed by the thermal-to-chemical conversion. Process II involves the hydrogen generation through three steps, *i.e.* photon-to-heat, heat-to-electricity and electricity-to-chemical [15, 16]. Particularly, heat-to-electricity step uses concentrating solar thermal (CST) systems [14]. Process III considers the use of two devices, namely photovoltaic (PV) cells, responsible for the photon-to-electric conversion, associated with an electrolyzer or a PEC cell to convert electric energy into a chemical fuel [17]. Finally, process IV consists of a single PEC cell based on a semiconductor-liquid junction (SCLJ) that allows the direct photon-to-chemical energy conversion. The major advantage of PEC water splitting is that solar collection, conversion and storage are combined in a stand-alone system, promoting oxygen and hydrogen evolutions at separate electrodes [18, 19].

From the different approaches to generate renewable hydrogen, PEC devices are among the most promising, yet probably also the most challenging. Since the first report of PEC water splitting by Fujishima and Honda in 1972, using a TiO_2 photoanode illuminated with UV light [20], fundamental and engineering research has been devoted to develop semiconductor materials and reactor designs with high STH conversion efficiency and durability.

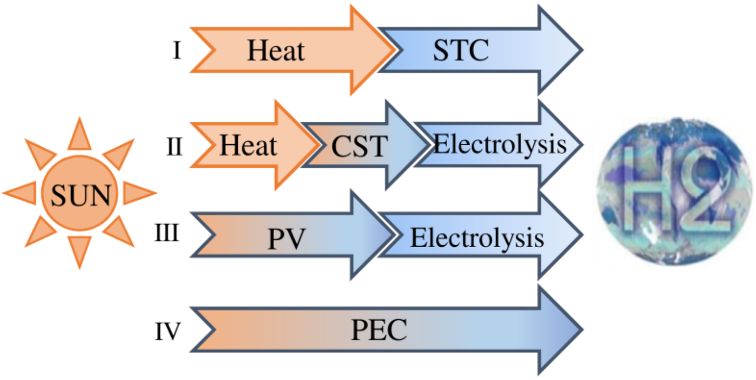

Figure 1.2: Solar-to-hydrogen (STH) conversion pathways (adapted from ref. [14]). STC is the solar-thermochemical cycles; CST is the concentrating solar thermal systems; PV is the photovoltaic solar cells; and PEC is the photoelectrochemical cell based on a semiconductor/ liquid junction (SCLJ).

1.2 PEC CELLS FOR WATER SPLITTING: WORKING PRINCIPLES

The working principles of a PEC system based on a single photoelectrode and a metal counter electrode are illustrated in the energy diagram of Figure 1.3. This is the simplest possible configuration consisting of two electrodes: a photoactive semiconductor electrode and a metal counter-electrode, both immersed in an electrolyte solution that allows the transport of the ionic species. The photoactive material can be either an n-type or p-type semiconductor. A semiconductor having large number of electrons in the conduction band is an n-type semiconductor, whereas in a p-type semiconductor the holes are the majority carriers. Therefore, a photoanode is an n-type semiconductor in PEC water splitting cells and the oxidation of water to oxygen occurs at the semiconductor/electrolyte interface and the photocathode is a p-type semiconductor evolving hydrogen.

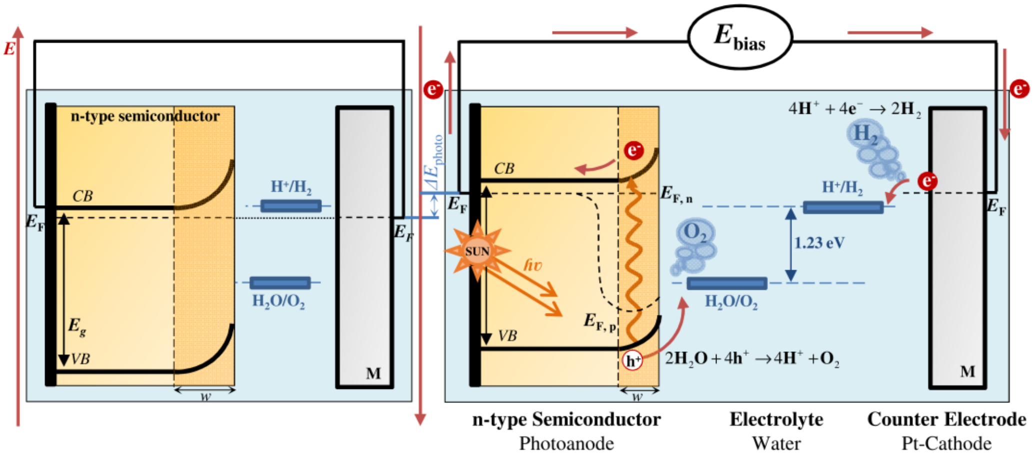

Figure 1.3: Energetic diagram of a PEC cell in the dark [left-side] and under illumination [right-side] based on a photoanode and a metal cathode.

When a semiconductor electrode is immersed in an electrolyte solution in dark, charge equilibration occurs at the interface forming a semiconductor/electrolyte junction (Figure 1.3 – left-side**)**. For establishing the thermodynamic equilibrium, the majority charge carriers (electrons in an n-type semiconductor and holes in a p-type semiconductor) are transferred to the second phase upon contact to equalize the Fermi levels. The excess of charges positioned on the semiconductor side is not located at its surface, as it would be in the case of a metallic electrode, but instead it extends into the electrode for a deeper distance, *i.e.* the space charge layer [21]. For an n-type semiconductor electrode, the Fermi level is normally higher than the redox potential of the electrolyte and then electrons are transferred from the electrode into the solution. Therefore, a positive space charge layer is formed, also called depletion layer since the region is depleted of majority charge carriers. On the other hand, a p-type semiconductor has an initial Fermi level below that of the electrolyte; a negative space charge layer is then formed as holes are transferred into the electrolyte. A charged layer of opposite sign is induced in the electrolyte adjacent to the interface with the solid electrode – Helmholtz layer. This layer consists of charged ions from the adsorbed electrolyte on the solid electrode surface. The Helmholtz layer width (few angstroms) is usually smaller than the space charge layer width [22].

Under illumination, a semiconductor absorbs photons with energies higher than its bandgap energy (E_g), injecting electrons from the valence band (VB) to the conduction band (CB) and, consequently, creating electron-hole pairs – Equation (1.1). For an n-type semiconductor photoanode, the case illustrated in Figure 1.3 (right-side), photogenerated electrons within the space charge region are driven by the electric field away from the semiconductor/electrolyte interface. Under illumination, the injected electrons raise the Fermi level decreasing the band bending and splitting into a quasi-Fermi level for electrons and for holes close to the interface. The excited electrons flow from the back contact of the semiconductor, via the external circuit, to the counter-electrode, where they reduce water to hydrogen – Equation (1.2) or Equation (1.4), depending of the electrolyte medium. Either water reacts with the semiconductor surface holes or OH^- ions diffuse back to react with holes at the surface of the photoelectrode, oxidizing holes to oxygen – respectively Equations (1.3) or (1.5).

A different design is also possible with a p-type semiconductor (photocathode) - Figure 1.4. In this case, the photocathode, converting incident photons to electron-hole pairs, reduces protons or water to hydrogen – Equations (1.2) or (1.4), depending on pH medium – at the interface, while oxygen is evolved at the metal anode.

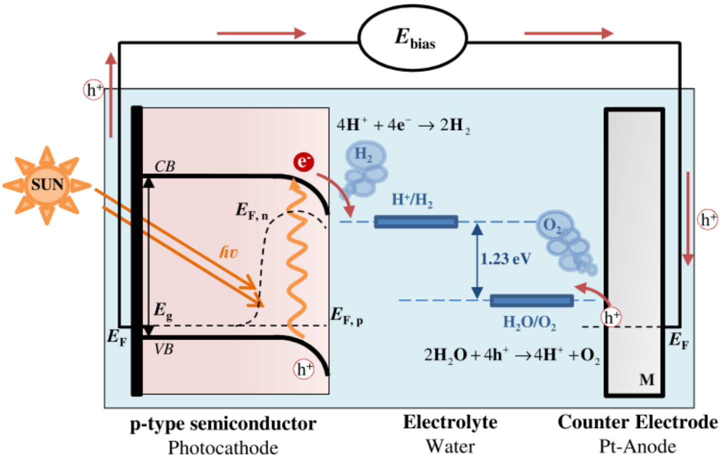

Figure 1.4: PEC cell under illumination based on a photocathode and a metal anode.

In a PEC cell with an acidic electrolyte the oxygen evolution reaction (OER) and hydrogen evolution reaction (HER) are as follows:

$$4h\nu \rightarrow 4e^- + 4h^+ \qquad (1.1)$$

$$4\mathrm{H}^{+} + 4e^{-} \rightarrow 2\,\mathrm{H}_2\,; \quad E^{\mathrm{o}}_{\mathrm{H}^{+}/\mathrm{H}_2} = +\,0.00\ \mathrm{V}_{\mathrm{NHE}} \tag{1.2}$$

$$2\mathrm{H}_2\mathrm{O} + 4\mathrm{h}^{+} \rightarrow 4\mathrm{H}^{+} + \mathrm{O}_2\,; \quad E^{\mathrm{o}}_{\mathrm{H_2O/O_2}} = -\,1.229\ \mathrm{V}_{\mathrm{NHE}} \tag{1.3}$$

For an alkaline medium, hydroxyl anions are formed from the dissociation reaction of water; the reduction and oxidation reactions can be written as [23]:

$$4\mathrm{H}_2\mathrm{O} + 4\mathrm{e}^{-} \rightarrow 2\mathrm{H}_2 + 4\mathrm{OH}^{-}\,; \quad E^{\mathrm{o}}_{\mathrm{H_2O/OH^{-}}} = -\,0.828\ \mathrm{V}_{\mathrm{NHE}} \tag{1.4}$$

$$4\mathrm{OH}^{-} + 4\mathrm{h}^{+} \rightarrow 2\mathrm{H}_2\mathrm{O} + \mathrm{O}_2; \quad E^{\mathrm{o}}_{\mathrm{O_2/OH^{-}}} = +\,0.401\ \mathrm{V}_{\mathrm{NHE}} \tag{1.5}$$

Therefore, the overall water splitting reaction is the following:

$$2\mathrm{H}_2\mathrm{O} + 4h\nu \rightarrow 2\mathrm{H}_2 + \mathrm{O}_2 \tag{1.6}$$

The number of absorbed photons is equal to the number of produced electron-hole pairs, which is twice that of produced H_2 molecules and four times the produced O_2 molecules.

The minimum thermodynamic potential needed for driving the water electrolysis is the electric reversible potential of ΔE^{o} = -1.23 V, based on a Gibbs free energy change of ΔG^{o} = 237 kJ·mol^{-1} (based on low heat of combustion, 298 K and 1 bar) [24].

1.3 PEC MATERIALS OVERVIEW

The key component of a PEC water splitting cell is the semiconductor photoelectrode, which has to meet several requirements for efficient solar water splitting [25, 26]:

i. Strong (visible) light absorption;
ii. Long-term stability in an aqueous solution;
iii. Suitable band edge positions to catalyze water reduction and oxidation;
iv. Low kinetic overpotentials for the reduction/oxidation reaction;
v. Efficient charge conduction;
vi. Earth-abundant and cost-effective.

The basic parameter that determines the spectral region in which the semiconductor absorbs light is its bandgap energy (E_g). Since only 1.23 V are needed for water splitting, a minimum bandgap of 1.23 eV could be sufficient. Based on the standard AM 1.5 G solar spectrum (*ca.* 100 mW·cm^{-2}), a semiconductor with such bandgap would give a maximum overall solar-to-hydrogen conversion efficiency of 47.4 %, assuming no losses [27]. However, there are significant back processes involved during the water photosplitting, such as the thermodynamic losses (0.3 - 0.4 eV) and overpotentials required for ensuring sufficiently fast reaction kinetics (0.4 - 0.6 eV) [6]. As a result, the semiconductor needs to have a minimum bandgap of *ca.* 1.9 eV, corresponding to an absorption onset at *ca.* 650 nm [25]. To achieve the US Department of Energy (DOE) target of 10 % STH efficiency, a minimum photocurrent density of *ca.* 8 $mA \cdot cm^{-2}$ is necessary, which means a maximum bandgap of *ca.* 2.3 - 2.4 eV. Therefore, the optimum value of the bandgap should be between 1.9 and 2.4 eV. This is consistent with the study by Murphy *et al.* [28] that indicates an ideal bandgap of *ca.* 2.03 eV. The semiconductor must have high chemical stability in the dark and under illumination. The stability against corrosion generally increases with semiconductor bandgap, but larger bandgaps limit the visible light absorption.

The third requirement above mentioned implies that the conduction band has to be above water reduction potential, $E^o(H^+/H_2)$, and the valence band has to be below the water oxidation potential, $E^o(H_2O/O_2)$. Moreover, the charge transport in the semiconductor must be efficient and with minimal recombination losses [25].

Only Earth-abundant materials and scalable thin film technology can meet the target cost of 5 $€ \cdot kg^{-1}$ H_2 set by the European Commission [29] and the target cost of \$2 to $\$4 \cdot kg^{-1}$ set by the DOE for future solar hydrogen production [30]. A recent techno-economic analysis showed that a PEC panel needs to cost less than \$160 per m^2 to become commercially competitive [31].

Due to the previously mentioned stringent requirements, it is very difficult to find an ideal semiconductor material for PEC water splitting. During the last decades, various metal oxides (TiO_2, ZnO, α-Fe_2O_3, WO_3, $BiVO_4$, Cu_2O, *etc.*) and non-oxides (silicon, GaAs, GaP, CdS, InP, TaON, Ta_3N_5, *etc.*) semiconductors have been extensively studied [32-34]. Metal oxides are often considered as the class of material suitable for water splitting, mainly due to their general stability in aqueous solution and relatively low-cost. However, they usually do not have very good semiconducting properties, such as carrier mobility, compared to III-V semiconductors or even Si. The challenge is then to overcome these limitations while taking advantage of the metal oxides properties. Figure 1.5 shows the relative band edge positions of several semiconductors.

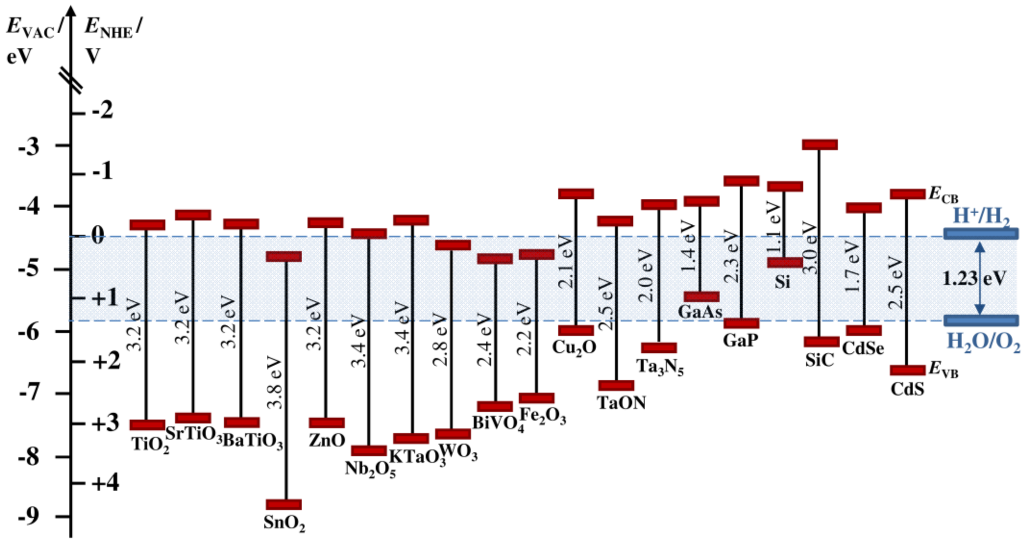

Figure 1.5: Energy band edge positions for semiconductors at pH 0 (adapted from ref. [35]).

1.3.1 PHOTOANODES FOR SOLAR WATER SPLITTING

A photoanode material for solar water splitting is responsible for the oxygen evolution, such that the electric field generated by band bending drives holes toward the surface and electrons to the current collector. Most of the photoanodes that have been studied are metal oxides, bare or doped but always nanostructured [3, 36].

Since the pioneering work by Fujishima and Honda [20], PEC cells with titanium dioxide (TiO_2) photoanodes of different types (single crystal, polycrystalline, thin films) have received special attention [37, 38]. TiO_2 material presents an adequate stability but the overall PEC performance is low due to its large bandgap (E_g = 3.2 eV), which only absorbs in UV range of the solar spectrum; the maximum thermodynamic STH efficiency is then limited to 2.2 % [28]. Also, the conduction band edge of this semiconductor is slightly positive to the HER. This limitation can be overcome using titanates, such as $SrTiO_3$ (E_g = 3.2 eV) and $BaTiO_3$ (E_g = 3.2 eV); the addition of Sr^{2+} and Ba^{2+} cations moves the potential of the conduction band edge to more negative values [3]. Although these materials can accomplish the direct water splitting the energy efficiency is very small, *e.g.* less than 1 % STH efficiency was obtained for $SrTiO_3$ [39]. Several other attempts have been made doping TiO_2 with ions such as Fe [40], Cr [41], Ni [42] and C [3, 43] without noticeable energy efficiency increase.

Small bandgap metal oxides, such as α-Fe_2O_3, WO_3 and $BiVO_4$, exhibit conduction band potentials more positive than water reduction and so an external bias potential should be provided to promote complete water splitting. Hematite (α-Fe_2O_3) is one of the most abundant and inexpensive oxide semiconductor with suitable energy bandgap (E_g = 2.0 – 2.2 eV) [44]. The thermodynamic maximum STH conversion efficiency is *ca.* 14 % - 17 %, which corresponds to a photocurrent density of 11 – 14 $mA \cdot cm^{-2}$ under AM 1.5 G illumination [28]. The first study on hematite ability for water photolysis was published in 1976 by Hardee and Bard [45]. These authors found hematite to be highly stable in neutral and alkaline electrolyte solutions that is of great importance for the commercial viability of the PEC systems [46]. As a drawback, in pure-phase α-Fe_2O_3 the photogenerated carriers show low mobility, which implies a short hole diffusion length (L_D = 2 – 4 nm) [47]. These intrinsic disadvantages combined with the sluggish water oxidation reaction are bound to give rise to the recombination of photogenerated electron-hole pairs, thereby leading lower PEC performances [26, 48]. Therefore, the main ongoing studies on hematite concern: i) improvement of photogenerated current density by morphology optimization (*e.g.* using different deposition methods [26]) and doping (Si [49], Ti [50], Sn [51], Pt [52] or other atoms); ii) improvement of generated photopotential minimizing the electron-hole recombination, especially at the photoelectrode surface [53]; and iii) reduction of the electrochemical activation overpotential using co-catalysts (*e.g.* IrO_2 [54], Co-Pi [52], $NiFeO_x$ [55]). Kim *et al.* [52] used a solution-based colloidal method to prepare a photoelectrode of hematite nanowires (*ca.* 500 nm thick) doped with Pt and activated with Co-Pi co-catalyst; the prepared photoelectrode showed *ca.* 4.32 $mA \cdot cm^{-2}$ at a bias potential of 1.23 V_{RHE} and remained stable over 180 minutes [52]. Recently, a new hematite record breaking of *ca.* 5.7 $mA \cdot cm^{-2}$ at 1.23 V_{RHE} was achieved by Guo *et al.* [56]. This highly photoactive material consists of a Ru-doped α-Fe_2O_3 nanorods film (Fe/Ru molar ratio of 100/5) prepared by deposition of the [Ru(acac)$_3$]-treated ultrathin α-FeOOH nanorods precursors onto FTO substrates via a doctor blading process, followed by a thermal annealing at 700 ºC in air. Nevertheless, its performance is still considerably lower than the thermodynamic value and recent efforts are now focused on the reduction of the onset potential for OER [57, 58]. Through the combination of high temperature annealing and surface modifications with catalysts it is observed a cathodic shift on the photocurrent onset potential (E_{onset}) [59]. The recent advances allowed to develop a PEC tandem device based on a hematite photoanode catalyzed with $NiFeO_x$ and an amorphous Si photocathode (with TiO_2/Pt overlayers) able to split water at an overall efficiency of *ca.* 0.91 % [60]. Very recently it was reported a bare hematite thin film (*ca.* 19 nm) photoelectrode that remained stable over 1000 h of PEC operation under 1-sun AM 1.5 G illumination, with no evidences of film degradation neither of photocurrent density losses [61].

Tungsten trioxide (WO_3) is also an interesting semiconductor material due to its high stability against photocorrosion in acidic aqueous solutions (pH < 4). Moreover, it has an indirect bandgap (E_g = 2.6 – 2.8 eV), which absorbs not only the near-UV but also the visible blue portion of the solar electromagnetic spectrum. Unfortunately, the thermodynamic STH efficiency is only around 4.8 % [62]. Usually, WO_3 crystalline and amorphous thin films can be used for water splitting, but a highly crystalline structure is desirable to reduce charge trapping and carrier recombination, therefore, improving its energy performance [63]. A photocurrent density of *ca.* 2.7 $mA\cdot cm^{-2}$ at 1.0 V_{RHE} was reported using a nanocrystalline WO_3 thin film synthesized by an aqueous sol–gel method on a conducting glass electrode; it remained stable over 144 h under 1-sun AM 1.5 G illumination [64]. A methane sulfonic acid solution was used to avoid the deactivation of the photoanode due to the formation and accumulation of peroxo species on its surface. The formation of secondary species becomes kinetically competitive with O_2 production; though, this aspect can be improved by placing a suitable O_2 evolution catalyst to enhance the photostability and efficiency towards water splitting reaction, *e.g.* a low-cost cobalt-phosphate (Co-Pi) co-catalyst [65].

Bismuth vanadate ($BiVO_4$) semiconductor is other candidate material for efficient PEC systems with a bandgap energy of 2.4 – 2.5 eV and a reasonable band edge alignment with respect to water redox potentials; a thermodynamic STH efficiency of *ca.* 11 % (7.5 $mA\cdot cm^{-2}$) can be obtained [66]. Moreover, it has also been reported that $BiVO_4$ shows both n- and p-type semiconducting properties and exhibit high photon-to-current conversion efficiencies under visible light radiation (> 40 % at 420 nm) [67-69]. Recently, a record photocurrent of 3.6 $mA\cdot cm^{-2}$ at 1.23 V_{RHE} was reported for a tungsten-gradient-doped $BiVO_4$ photoanode [70]. STH efficiency of 4.9 % was achieved for the device based on a double junction amorphous silicon solar cell [71].

More recently, tantalum (oxy)nitrides, such as TaON ($E_g = 2.5$ eV) and Ta_3N_5 ($E_g = 2.0$ eV), have experienced a rapid development as high-performance photoanodes [72]. Tantalum (oxy)nitrides show narrow bandgaps for visible light absorption ($\lambda < 600$ nm) and suitable band edges positions straddling over water redox potentials [13]. A photocurrent density of *ca.* 6.7 $mA \cdot cm^{-2}$ at 1.23 V_{RHE} was obtained for the Ba-doped Ta_3N_5 nanorod array modified with Co-Pi in an electrolyte solution of 0.5 M K_2HPO_4 (pH 13) [73]. This photoanode material showed a maximum STH conversion efficiency of 1.56 % at 0.87 V_{RHE} and remained stable over 100 min. Liu *et al.* [74] further modified Ta_3N_5 with the $Ni(OH)_x/MoO_3$ bilayer and improved its stability up to 24 h in 1 M LiOH aqueous solution (pH 12). Continuous efforts in this field, as well as the fundamental knowledge about the factors that most influence the PEC efficiency, is though still needed.

1.3.2 PHOTOCATHODES FOR SOLAR WATER SPLITTING

Photocathodes used for water splitting need to supply sufficient cathodic current for reduction of protons to H_2 and must be stable in aqueous environments. Single-crystal phosphides such as GaP ($E_g = 2.3$ eV) [75], InP ($E_g = 1.4$ eV) [76] and $GaInP_2$ ($E_g = 1.8$ eV) [77] have been studied as non-oxide photocathode semiconductors, but polycrystalline materials are desirable for large-scale applications of PEC systems due to their higher stability [4]. Polycrystalline-Si ($E_g = 1.1$ eV) decorated with a variety of catalysts can be used to reduce water [78]. The stability is higher in acids but it also suffers from limited durability due to surface oxidation. The formation of an oxide can be prevented by passivating the surface, *e.g.* with methyl groups [79]. Recently, an amorphous Si photocathode with TiO_2/Pt protective overlayers was reported exhibiting an impressive photocurrent of *ca.* 6.1 $mA \cdot cm^{-2}$ and reasonable stability at a large positive bias of 0.8 V_{RHE}; this is the highest photoelectrochemical performance of all reported Si photocathodes [80].

Cuprous oxide (Cu_2O) has been used as both photoanode and photocathode [3], but it appears as an attractive p-type oxide for solar hydrogen production with a direct bandgap energy of 2.0 – 2.1 eV suitable for visible light harvesting [81]. Thermodynamic calculations indicate that Cu_2O can produce up to 14.7 $mA \cdot cm^{-2}$, corresponding to a STH conversion efficiency of 18 % based on the AM 1.5 G spectrum [82]. It is abundant, cheap, environmentally friendly and has favorable energy band positions [83]. However, Cu_2O is easily reduced to Cu when exposed to aqueous electrolytes. This instability can be addressed by depositing protective layers on the electrode surface. Paracchino *et al.* [82] showed a highly active photocathode for solar hydrogen production, consisting of electrodeposited cuprous oxide protected with nanolayers of Al-doped zinc oxide and titanium oxide, and activated for HER with nanoparticulated Pt co-catalyst. This material showed photocurrents up to 7.6 $mA\cdot cm^{-2}$ at 0 V_{RHE} [82]. Furthermore, RuO_x top layer was investigated as a co-catalyst [84] and, together with a steam treatment of the multilayer structures, showed optimized electrodes with a stable photocurrent of *ca.* 5 $mA\cdot cm^{-2}$ during 50 h (photocurrent loss < 10 %) under 1-sun AM 1.5 G of light chopping (biased at 0 V_{RHE} in pH 5 electrolyte) [83]. However, the photopotential produced by this photocathode alone is insufficient to drive the water splitting reaction, so it should ideally be incorporated as the top, wide-bandgap component of a tandem arrangement. An innovative tandem device made of a transparent Cu_2O photocathode atop a perovskite photovoltaic cell demonstrated unassisted sunlight-driven water splitting up to 2.5 % STH efficiency [85].

1.3.3 CHALLENGES FOR IMPROVING PHOTOELECTRODES PERFORMANCE

Various strategies have been followed to improve the performances of the photoelectrodes for water splitting, including [86]:

i. Doping the bare semiconductor;
ii. Surface treatment of the semiconductor;
iii. Use of co-catalysts;
iv. Morphology control of the photoelectrode;
v. Other methods, *e.g.* band structure engineering using heterojunction structures, passivating the surface states or reduce back-reactions using oxide layers, change the distribution of electromagnetic energy using plasmonic metal nanoparticles on the semiconductors.

Doping a semiconductor material is used to simultaneously improve the visible light absorbance (decrease the bandgap) and the mobility of charge carriers. The band structural modification involves the introduction of foreign ions (cations or anions) into the semiconductor material to change its electronic and optical properties. Various dopants including metal ions (*e.g.* Ti, Sn, Fe) and non-metal elements (*e.g.* N, Si, C) have been used to improve the PEC efficiency. A review of the doping effect on a number of promised semiconductors is reported elsewhere [35].

The surface treatment is another method to improve the photoelectrode efficiency by protecting the surface against photocorrosion, surface states passivation, modifying the band edge positions or band bending and the selective extraction of carriers [87]. The photoelectrode stability can be enhanced by adding a protective overlayer, which should be sufficiently thick to act as a physical barrier between the semiconductor and the electrolyte but also semi-transparent and conductive to avoid the limiting of the light harvesting efficiency or charge transfer [82, 88]. The surface passivation can suppress the deleterious role of the surface states, which act as trapping sites and recombination centres of photoinduced carriers [86]. Therefore, the degree of band bending and band positions (surface energetics) may be changed by surface modifications for tuning of the driving force for the charge transfer processes [57].

The hydrogen and oxygen evolutions require an activation energy, overpotential, to run the electrolysis at the required rate. Co-catalysts can be divided into WOC (water oxidation catalyst) and WRC (water reduction catalyst), acting as activation sites for the evolution of O_2 (photoanode) or H_2 (photocathode), respectively. By improving the reaction kinetics, the potential bias is reduced and then the incident photon-to-current conversion efficiency (IPCE) is enhanced at lower bias. A good catalyst also increases plateau photocurrent and may contribute for the chemical and photochemical stability [89]. Among the WOCs employed so far, IrO_2 [54], RuO_2 [90], Co_3O_4 [91] and Co-Pi [92] are the most used for a photoanode; whereas MoS_2 [93] and Ni-Fe [94] or noble metals like Pt [82], Ru [84] and Pd are promising candidates for HER. The catalytic activity of the oxygen and hydrogen evolution reactions can be linked through volcano plots, as shown in Figure 1.6a and Figure 1.6b, respectively.

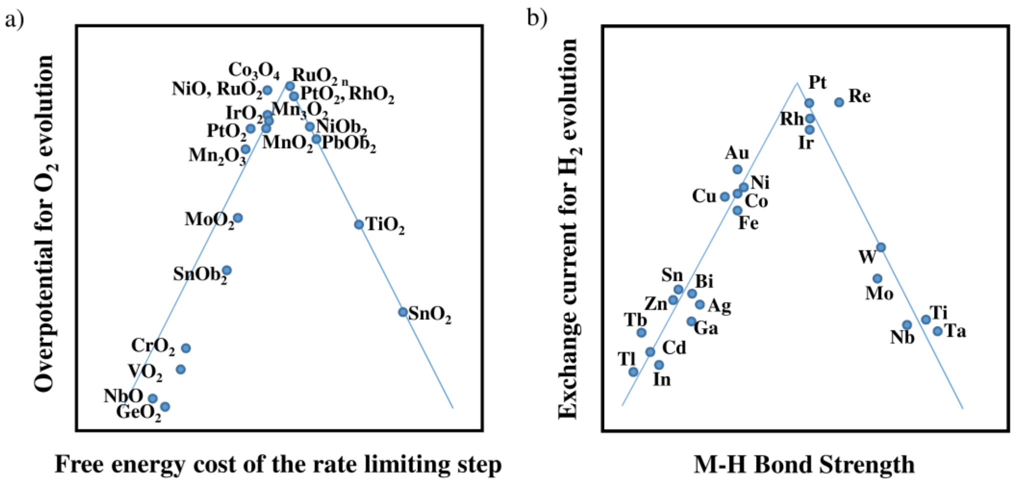

Figure 1.6: (a) Volcano plot of the overpotential of OER on various oxide surfaces *vs.* the free energy cost of the rate limiting step (adapted from ref. [95]); (b) Volcano plot of the exchange current density for the HER for several native metals as a function of the metal-hydrogen bond strength (adapted from ref. [96]).

For improving the energy efficiency the photoelectrode film must be thick enough to absorb more light and the deep photogenerated carriers within the photoelectrode must be able to reach the surface and then be collected [3]. Therefore, the morphology control of the photoelectrodes allows enhancing the light absorption and shortening the diffusion length of minority carriers. Nanostructuring the photoelectrode is usually used to increase the relative volume of the space charge layer with respect to that of the bulk, thereby reducing recombination rate and increasing the plateau current [54].

Although the impressive results achieved to date there is not a single semiconductor material able for direct PEC water splitting. Innovation and developments in new materials are needed, as well as innovative PEC cell designs are strongly required.

1.4 PEC DEVICES OVERVIEW

The PEC research over the past years allowed to develop innovative material systems, functionalized interfaces and devices aiming at stable 10 % solar-to-hydrogen efficiency, the target that will make this technology to move to the industrialization level [19]. Furthermore, it is also important to split water without any external bias supply.

Figure 1.7 summarizes the configurations of PEC devices for solar hydrogen production: i) two harvesting devices combining PV cells coupled to an electrolyzer system or to a PEC cell (Type I); ii) single harvesting PEC-based devices with at least one semiconductor-liquid junction (Type II); and iii) photocatalyst-based slurry devices (Type III). Type III consists of photoactive semiconductor particles (photocatalysts) free-floating as slurry in a solution bed [97]. This configuration still presents many drawbacks for solar water splitting and so it will not be considered in this chapter.

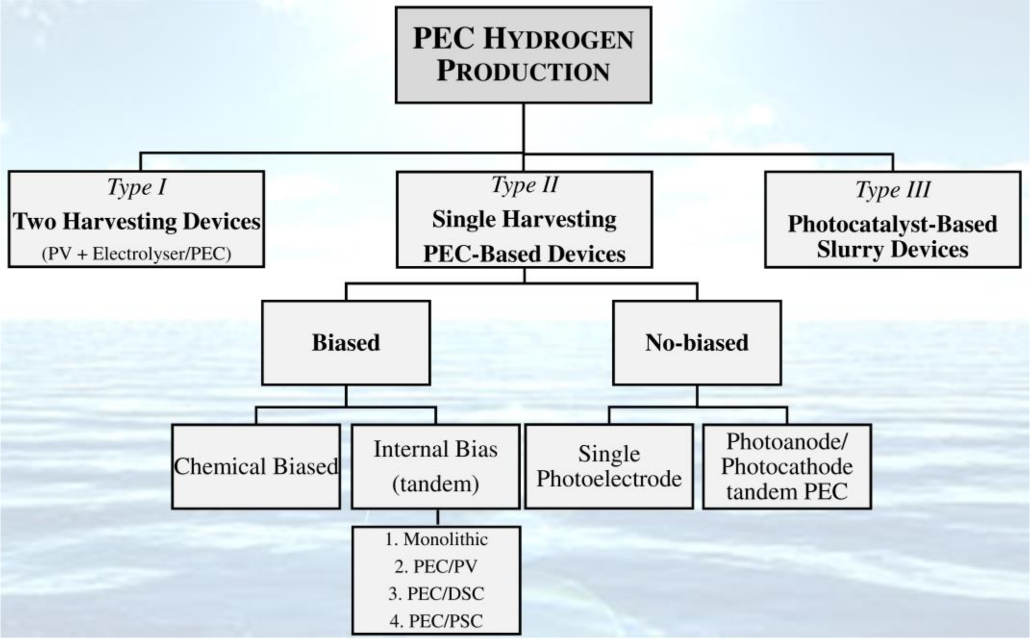

Figure 1.7: Photoelectrochemical device configurations for solar hydrogen production.

The success of PEC hydrogen production depends on the balance between device performance (STH efficiency and stability), complexity and cost; the simpler the device, the better. Single-junction photoelectrode systems offer the greatest simplicity but their energy efficiencies are generally low. On the other hand, tandem PEC devices are more complex but also more efficient, emerging as the best approach for solar water splitting [98]. Table 1.1 presents the advantages and disadvantages of these PEC configurations.

Table 1.1: **A**dvantages and disadvantages of the PEC configurations for H_2 production.

Device configurations	**Advantages**	**Disadvantages**
Type I Two Harvesting Devices	▪ Nontransparent substrates can be used; ▪ More efficient utilization of the solar spectrum; ▪ No stability issues (PV contact with electrolyte solution is avoided).	▪ Twice the collector area for the devices; ▪ Need to balance the current flow of both devices; ▪ Auxiliary system losses (*e.g.* collection of current from PV cell and transmission of electrons through external wiring); ▪ Add complexity and cost for large-scale deployment.
Type II Single Photoelectrode	▪ Only one substrate and one photoanode or photocathode is needed; ▪ Cheap nontransparent substrate can be used.	▪ Poor utilization of the solar spectrum since large bandgap ($E_g > 1.7$ eV) is needed.
Type II Tandem Photoelectrodes	▪ Needs only one substrate; ▪ More efficient utilization of the solar spectrum; ▪ Use of two smaller bandgap materials; ▪ Enhanced photopotentials (the photopotentials of each cell are additive).	▪ Need to identify suitable photoanode and photocathode or use a photoelectrode and PV solar cell; ▪ Need a transparent conducting substrate; ▪ Photocurrent limited by the component generating the smallest current value; ▪ Optical coupling effects between cells (minimize reflection at front surface); ▪ Adds complexity.

1.4.1 *TYPE I:* TWO HARVESTING DEVICES

Type I combines two physically separated devices to directly drive electrolysis; the most developed approach is based on a PV cell integrated with an electrolyzer system (PV + electrolyzer). The PV cells usually generate photopotentials over 2 V, converting sunlight to electricity, whereas the electrolysis unit converts electricity to hydrogen at efficiencies near 65 % [97]. The typical photovoltaic cell types are monocrystalline silicon (c-Si) and polycrystalline silicon (p-Si) and thin-film technologies, namely amorphous silicon (a-Si), cadmium telluride (CdTe), copper indium gallium diselenide (CIGS) [99], dye sensitized solar cells (DSC) [100] and perovskite solar cells (PSC) [101]. The viability of this type of approaches is limited by the cost of both devices; using commercially available PV and electrolyzer technologies, the hydrogen production cost would be greater than \$10·kg^{-1}, far exceeding the US DOE targets of \$2 - \$4·kg^{-1} [97]. Table 1.2 shows the STH efficiencies of relevant PV + electrolyzer approaches.

Table 1.2: Examples of two harvesting devices; photovoltaic efficiency (η_{PV}) and solar-to-hydrogen efficiency (η_{STH}), with an electrolyzer efficiency of 65 % (extracted from ref. [99]).

PV+ Electrolyzer	η_{PV} / %	η_{STH} / %
a-Si multijunction	12.1	7.8
III-V multijunction	32	20.8
c-Si modules	13.5	8.8
DSC	8.2	5.3

Alternatively, the PV cell can be connected in series with a PEC cell based on a SCLJ, instead of an electrolyzer, resulting in a cheaper but not necessarily more efficient arrangement [19]. Figure 1.8 shows a non-tandem configuration consisting of a photoanode PEC cell coupled to a PV cell; the majority carriers generated in the PV cell reduce water on the metal cathode and the minority holes generated in the photoanode oxidize water at its surface [19]. In the PV + PEC configuration the available solar exposure area must be substantially larger since both PV and PEC cells have to be directly illuminated [99]. To avoid these drawbacks, a more effective approach would incorporate PV cell and PEC photoelectrode into a single harvesting device, as described in the following section.

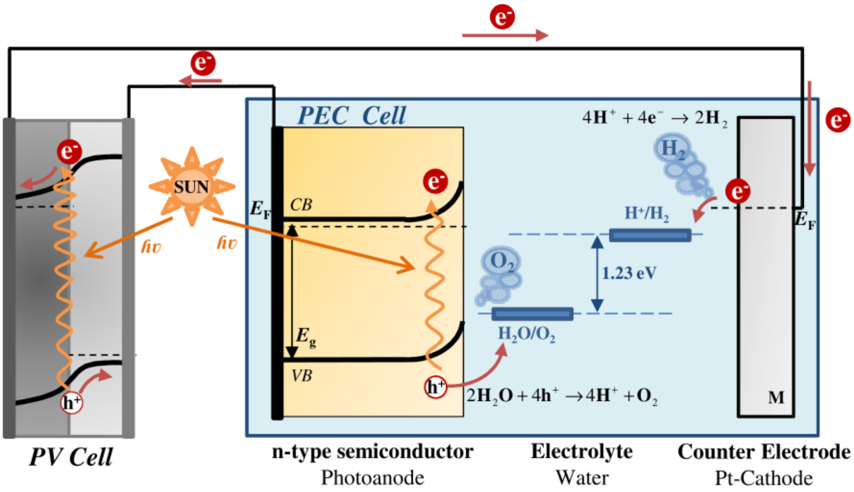

Figure 1.8: PV solar cell connected in series with a PEC device (non-tandem arrangement).

1.4.2 *Type II:* Single Harvesting PEC-Based Devices

Single harvesting PEC-based devices have been investigated as a promising alternative for large-scale solar hydrogen production. Type II devices are then divided into biased and non-biased systems - Figure 1.7. Concerning biased systems, the cells operate under illumination in combination with an appropriate bias source to directly promote hydrogen generation; there are chemically biased photo-assisted photoelectrolysis cells and internal biasing devices [17, 19]. Non-biased devices are based on single photoelectrodes or two photoelectrodes (photoanode and photocathode) in a tandem arrangement.

Biased Devices

1) Chemically Biased

A chemical bias is achieved using acidic and alkaline environments, placed in two half-cells separated by an ion exchange membrane - Figure 1.9. The electrolyte solutions are chosen to reduce the potential required to induce the chemical splitting. The photocurrent flowing between the electrodes lead to the consumption of ion species at the anodic and cathodic cell compartments, resulting in the electrolyte neutralization and the potential bias reduction. Therefore, this configuration is not self-sufficient, relying not only on sunlight but also on additional input of chemicals to maintain the pH gradient [19]. This approach is then unattractive for practical applications. Table 1.3 shows two examples of chemically biased PEC cells.

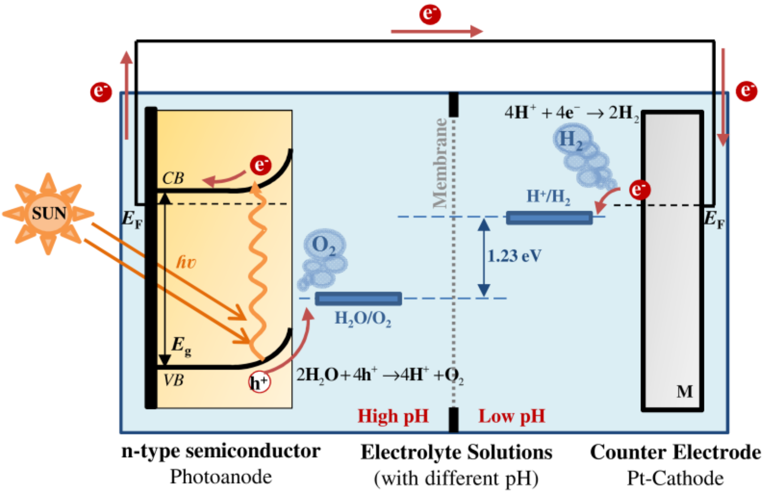

Figure 1.9: PEC cell with chemical biasing.

Table 1.3: Examples of chemically biased PEC cells, device conditions and correspondent performance: photocurrent-density (J_{photo}), STH conversion efficiency (η_{STH}) and stability.

Device configurations	**Electrolyte and Illumination Conditions**	**Performance**	**Stability**	**Ref./ Date**
TiO_2 photoanode Pt cathode	1 M HCl 1 M KOH	Chemical Bias = 0.84 V	not reported	[20]/ 1972
TiO_2 photoanode Cu-Ti-O photocathode	1 M KOH 0.1 M Na_2HPO_4 100 mW·cm^{-2}	Chemical Bias = 0.40 V J_{photo} = 0.25 mA·cm^{-2}; η_{STH} = 0.30 %	Photocathode corrosion after 4 h	[102]/ 2008

2) Internally Biased

An internal bias with an appropriate match of current and potential will directly increase the STH conversion efficiency, since the PEC system and the bias element with different absorption spectra can address a broader fraction of the solar spectrum [19]. In this configuration, at least one of the substructures must work as a bias source; the total bandgap should be large enough to split water. These systems, also called tandem devices, are normally characterized by layered stacked or hybrid structures involving several different semiconductor films placed on top of each other. Figure 1.10 shows a top PEC cell stacked to a PV cell in a two-junction (2J) tandem arrangement; the back contact of the PEC cell and the front contact of the PV cell are connected by a tunnel junction and the back contact of the PV cell is directly connected to the counter electrode. This approach eliminates the electron transmission through wires, reducing ohmic losses, but the process compatibility in fabricating the PEC cell directly onto the PV cell affects device quality and efficiency.

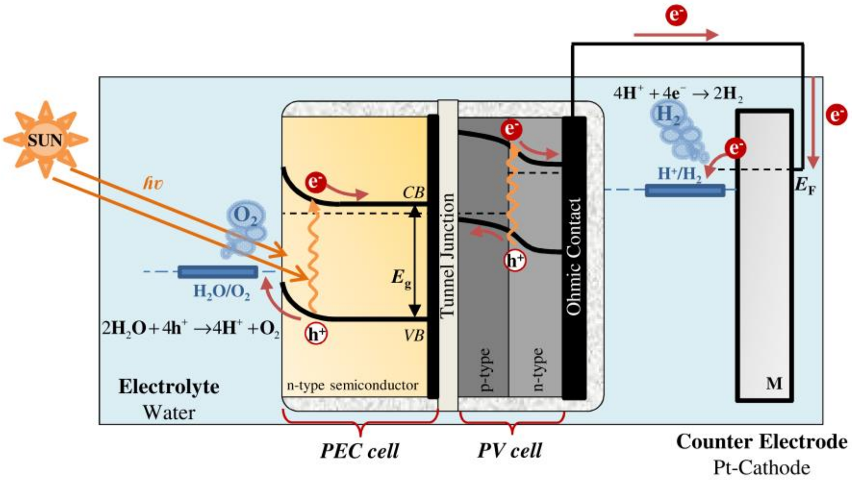

Figure 1.10: PEC/PV monolithic system using a two-junction hybrid tandem device.

The total photocurrent of a tandem arrangement is bound by the photocurrent limits of the highest bandgap material. Further optimization is achieved if a large bandgap material (LBG) is layered in front of a small bandgap material (SBG) [103]. Layering the photoabsorbers in this manner allows the short wavelength, greater energy photons, to be absorbed in the LBG and the long ones to be absorbed in the SBG. The top cell has to be semi-transparent to enable light transmission to the back photoelectrode, *i.e.* a transparent conducting oxide (TCO) substrate must be used. However, if the two junctions are stacked onto the same substrate as a single monolithic structure, no transparent substrate is needed [97].

The internally biased tandem structures can then be divided into: i) stacked monolithic devices (Figure 1.10); ii) PEC/PV tandem systems where the photoelectrode layer is semi-transparent, *e.g.* PEC/DSC (Figure 1.11) and PEC/PSC (Figure 1.12) devices; and iii) PEC/PV tandem systems where the PV layer is semi-transparent. A further extension of the PV/PEC device is based on the use of a triple-junction (3J) hybrid system (a PEC top cell and a double-junction PV cell) due to low photopotentials generated by the conventional PV materials (*e.g.* c-Si, p-Si, CIGS). This configuration develops higher photopotentials, but the photocurrent is limited by the component generating the smallest photocurrent value [97].

The best performing PEC/PV tandem system consists of a two-junction monolithic hybrid device: a p-type $GaInP_2$ (E_g = 1.8 eV) PEC electrode interconnected by a tunnel junction to a GaAs (E_g = 1.4 eV) PV cell grown on a GaAs wafer substrate [77]. Sunlight enters through the top $GaInP_2$ photocathode and is then filtered down to the GaAs PV solar cell. While this system performs a champion η_{STH} = 12.4 % under concentrated 11-sun illumination, and in 3 M H_2SO_4 electrolyte, the high cost III-V materials and the corrosion of the $GaInP_2$ limit its practical use. Therefore, finding semiconductor materials able to form stable junctions has been a major challenge in the field of PEC water splitting; stable metal oxides, *e.g.* WO_3, Fe_2O_3 and $BiVO_4$ are a promising option.

Grätzel and co-workers [2] proposed the use of a semi-transparent dye-sensitized solar cell (DSC), instead of the conventional PV solar cell, in a dual-absorber tandem configuration – see Figure 1.11. The DSC cell is made of a cheap semiconductor material of TiO_2, reducing the final costs [100]. In this system, the semi-transparent photoanode PEC cell (*e.g.* thin films of WO_3 [104] or Fe_2O_3 [105]) absorbs the blue part of the solar spectrum to generate O_2 from water, whereas the DSC cell captures the green and red lights to generate the external bias needed for H_2 production at the counter electrode. The successful demonstration of the PEC/DSC tandem device is, therefore, restricted to the use of two DSCs connected in series due to the additional energy required to overcome non-idealities of the photoanodes in the OER [100].

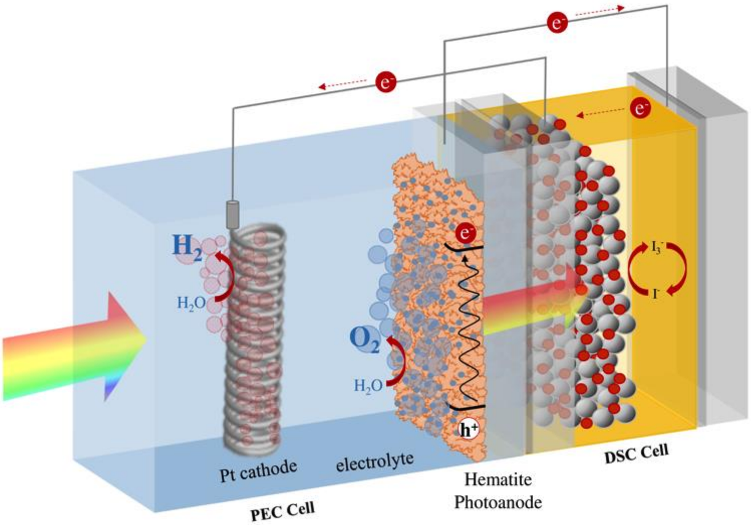

Figure 1.11: PEC/DSC tandem system using a semi-transparent hematite photoanode as PEC element and a DSC cell in series for overall water splitting.

Recently, promising hybrid organic–inorganic lead halide perovskites ($CH_3NH_3PbI_3$) have emerged as exceptional materials for the next-generation photovoltaic technologies [101, 106]. In a few short years of development, perovskite solar cell (PSC) efficiencies have already surpassed the mature DSC solar cells and organic photovoltaics [107, 108]. The lead iodide hybrid perovskites have a low bandgap and large absorption coefficient that facilitate light harvesting into the near-IR region of the solar spectrum. Moreover, PSCs exhibit extremely high photopotential in comparison to nearly all other single-junction PV technologies, fostering the exploration of this material in tandem water splitting architectures. Two series-connected PSC externally wired to NiFe electrocatalysts submerged in a NaOH electrolyte solution can provide sufficient potential to drive water photolysis with STH efficiency of *ca.* 12.3 % [109]. Therefore, the design of low-cost tandem assemblies employing single-junction hybrid perovskite materials establishes a potentially promising new frontier for solar water splitting research. Figure 1.12 shows a PEC/PSC tandem arrangement, where a semi-transparent CuO_2 photocathode is used as the PEC element.

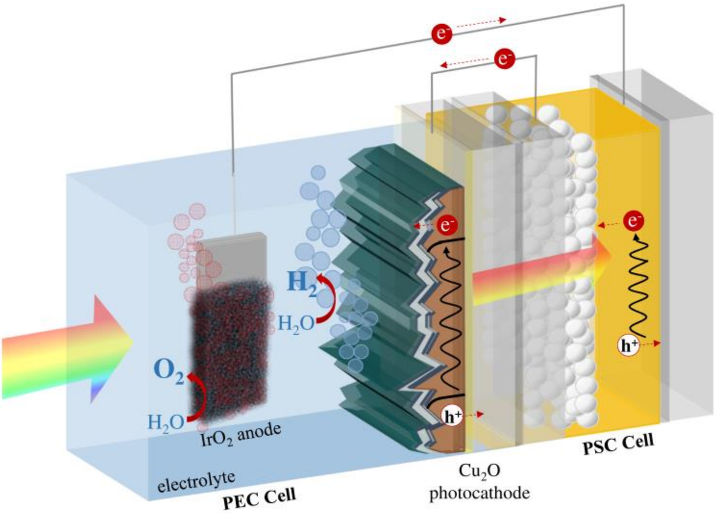

Figure 1.12: PEC/PSC tandem system using a semi-transparent Cu₂O photocathode as PEC element and PSC cells in series for overall water splitting (adapted from ref. [85]).

Table 1.5 summarizes relevant experimental reports of internally biased tandem devices for direct solar water slitting, including the performance and device configuration; Figure 1.13 depicts the configurations considered.

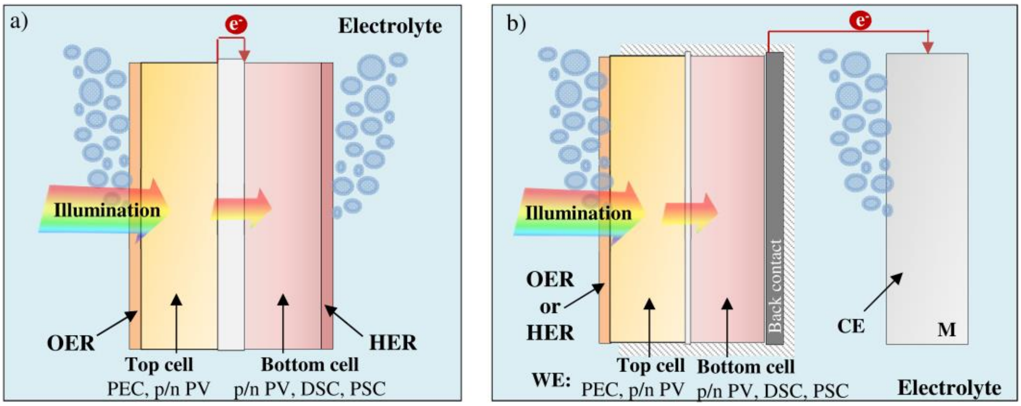

Figure 1.13: Configurations of internally biased tandem devices for overall water splitting: (a) the semiconductor elements are monolithically integrated (without wire connections); and (b) the light-absorbing elements are electrically wired, where the top element (PEC or PV) with the larger bandgap has to be semi-transparent to transmit the non-absorbed sunlight spectrum to the bottom element (normally the PV cell). The photoelectrodes can be coated with co-catalysts, *e.g.* n-type PEC coated with an OER co-catalyst and p-type PEC coated with a HER co-catalyst.

Table 1.4: Internally biased tandem devices for direct solar water splitting, including experimental conditions and corresponding performance (STH conversion efficiency - η_{STH} - and stability); grouped by type of arrangement and ordered by reverse chronological publication.

Device configurations	**Electrolyte and Illumination**	**η_{STH} / %**	**Stability, notes**	**Ref./ Date**
Monolithic PV (2J) Top PV: GaInP with AlInP/PO_x layers Bottom PV: GaInAs coated RuO_2 OER co-catalyst	1 M $HClO_4$ 100 mW·cm^{-2}	14 %	40 h > 50 % drop in current	[110]/ 2015
Monolithic PV (2J) Top PV: $GaInP_2$ Bottom PV: GaAs coated TiO_2 overlayer and Ni-based OER co-catalyst; wired Ni-Mo HER co-catalyst	1 M KOH 100 mW·cm^{-2}	10.5 %	80 h 15 % drop in current	[111]/ 2015
Monolithic PV (2J) Top PV: $GaInP_2$ Bottom PV: GaAs coated Pt OER co-catalyst; wired Pt HER co-catalyst	2 M KOH 100 mW·cm^{-2}	18.3 %	9 h stable current in outdoor test	[112]/ 2001
Monolithic PV (3J) PV: 3 × [$CuIn_xGa_{1-x}Se$ (CIGS)] wired side-by-side; wired Pt HER and OER co-catalysts	3 M H_2SO_4 100 mW·cm^{-2}	10 %	27 h stable H_2 production	[113]/ 2013
Monolithic PV (3J) PV: 3 × (a-Si) coated FTO OER co-catalyst; wired Pt or Ni HER co-catalyst	5 M KOH 100 mW·cm^{-2}	6.2 %	31 days stable current	[114]/ 2006

Monolithic PEC/PV (2J) Top PEC: Fe_2O_3 core-shell NW coated Au OER co-catalyst Bottom PV: c-Si; wired Pt HER co-catalyst	1 M Na_3PO_4 60 mW·cm^{-2}	6.0 %	40 min measurement of O_2	[115]/ 2014
Monolithic PEC/PV (2J) Top PEC: WO_3 core-shell NW Bottom PV: c-Si; wired Pt cathode	1 M H_2SO_4 1080 mW·cm^{-2} (*ca.* 11-sun)	< 0.01 %	10 min stable current	[116]/ 2014
Monolithic PEC/PV (2J) Top PEC: TiO_2 core-shell NW coated IrO_x OER co-catalyst Bottom PV: c-Si coated Pt HER co-catalyst	1 M H_2SO_4 1080 mW·cm^{-2} (*ca.* 11-sun)	0.12 %	4.5 h measurement of O_2 and H_2	[117]/ 2014
Monolithic PEC/PV (2J) Top PEC: TiO_2 Bottom PV: c-Si; wired Pt cathode	0.1 M NaOH sunlight	0.1 %	Not reported	[118]/ 2014
Monolithic PEC/PV (2J) Top PEC: $BiVO_4$ coated CoPi OER co-catalyst Bottom PV: a-Si:H; wired Pt HER co-catalyst	0.1 M K_3PO_4 (pH 7.3) 100 mW·cm^{-2} (1-sun)	3.6 %	1 h stable current	[70]/ 2013
Monolithic PEC/PV (2J) Top PEC: $GaInP_2$ Bottom PV: GaAs coated Pt HER co-catalyst; wired Pt OER co-catalyst	3 M H_2SO_4 11-sun	12.4 %	20 h 20 % drop in current	[77]/ 1998
Monolithic PEC/PV (2J) Top PEC: WO_3, with TiO_2 passivation layer Bottom PV: 2 × (c-Si) coated Pt HER co-catalyst	1 M $HClO_4$ Nafion membrane 200 mW·cm^{-2}	0.2 %	20 h stable H_2 generation (over 48 h)	[119]/ 2015

Monolithic PEC/PV (3J) Top PEC: $BiVO_4$ coated CoPi OER co-catalyst Medium PV: a-Si:H Bottom PV: nc-Si:H; wired Pt HER co-catalyst	0.1 M KPI (pH 7) 100 mW·cm^{-2}	5.2 %	1 h 5% drop in current	[71]/ 2014
Monolithic PEC/PV (3J) Top PEC: $BiVO_4$ coated CoPi OER co-catalyst Bottom PV: 2 × (a-Si:H); wired Pt HER co-catalyst	0.1 M K_3PO_4 (pH 7.3) 100 mW·cm^{-2}	4.9 %	1 h stable current	[70]/ 2013
Monolithic PEC/PV (3J) Top PEC: WO_3 Bottom PV: 2 × (a-Si); wired Pt HER co-catalyst	0.3 M H_3PO_4 100 mW·cm^{-2}	3 %	Not reported	[120]/ 2010
Monolithic PEC/PV (3J) Top PEC: WO_3 (PA) Bottom PV: 2 × (a-Si); wired Pt HER co-catalyst	1.0 M H_3PO_4 100 mW·cm^{-2}	0.7 %	10 h stable H_2 production	[121]/ 2010
PEC/DSC tandem (2J) Top PEC: embedded structure of $WO_3/BiVO_4$ coated FeOOH/NiOOH OER co-catalyst; wired Pt cathode	0.5 M Na_2SO_4 100 mW·cm^{-2}	5.7 %	120 min stable current	[122]/ 2015
PEC/DSC tandem (2J) 1) Top PEC: WO_3 2) Top PEC: Fe_2O_3 coated AlO_3 underlayer and Co OER co-catalyst; wired Pt HER catalyst	1) 1 M $HClO_4$ (pH 0) 2) 1 M NaOH (pH 13.6) 100 mW·cm^{-2}	1) 3.1 % 2) 1.2 %	8 h 30 % current drop	[123]/ 2012
PEC/DSC tandem (2J) Top PEC: WO_3; wired Pt HER co-catalyst	0.25 M Na_2SO_4 (pH 4) 200 mW·cm^{-2}	1.9 %	30 min measurement of H_2	[124]/ 2006

PEC/DSC tandem (3J) Top PEC: Fe_2O_3 with AlO_3 underlayer and coated Co OER co-catalyst Bottom: 2 × (DSC); wired Pt HER co-catalyst	1 M NaOH (pH 13.6) 100 mW·cm^{-2}	1.4 % 1.2 %	Not reported	[125]/ 2010
PEC/PSC tandem (2J) Top PEC: Cu_2O coated Al:ZnO/TiO_2 overlayer and coated RuO_x HER co-catalyst; wired IrO_2 OER catalyst	0.5 M Na_2SO_4 100 mW·cm^{-2}	2.5 %	2 h 30 % current drop	[85]/ 2015
PEC/PSC tandem (2J) Top PEC: embedded structure of TiO_2/$BiVO_4$ core-shell, coated CoPi OER co-catalyst; wired Pt HER catalyst	0.1 M phosphate buffered saline (pH 7) 100 mW·cm^{-2}	1.2 %	6 h measurement of H_2	[126]/ 2015
PEC/PSC tandem (2J) Top PEC: $BiVO_4$ coated CoPi OER co-catalyst; wired Pt HER co-catalyst	0.5 M Na_2SO_4 + 0.5 M Na_2SO_3 (pH 9.3) 100 mW·cm^{-2}	2.5 %	1 h stable current	[127]/ 2014
PEC/PSC tandem (2J) Top PEC: Mn-doped Fe_2O_3 core-shell NW coated CoPi OER co-catalyst wired Pt HER co-catalyst	1 M NaOH 100 mW·cm^{-2}	2.4 %	8 h measurement of H_2 with 25 % loss	[128] / 2014

NON-BIASED DEVICES

Photoelectrochemical devices with no additional bias represent a prospective pathway to overcome the complexity of biased systems. Non-biased devices comprise two types of PEC systems: i) single photoelectrode system, which can be divided into a typical PEC cell (equipped with a large bandgap photoelectrode and a counter-electrode); and ii) a photoanode/photocathode PEC tandem cell.

1) Single Photoelectrode System

The ideal PEC system for solar hydrogen production should aim at the use of a single-junction photoelectrode without any bias, as shown in Figure 1.3 and Figure 1.4 respectively for n-type and p-type semiconductor materials. Up to now, only materials with a very large bandgap, such as $SrTiO_3$ [39] and $KTaO_4$ [129], have demonstrated direct water splitting; however, they exhibit STH efficiencies below 1 % [14]. Therefore, improvements on semiconductor fundamental electronic structure and stability are needed for the viability of this approach.

2) Photoanode/Photocathode PEC System

The most direct and simple way to construct a dual photo-system for water splitting is using an n-type semiconductor (photoanode) connected in series with an appropriate p-type semiconductor (photocathode) - Figure 1.14.

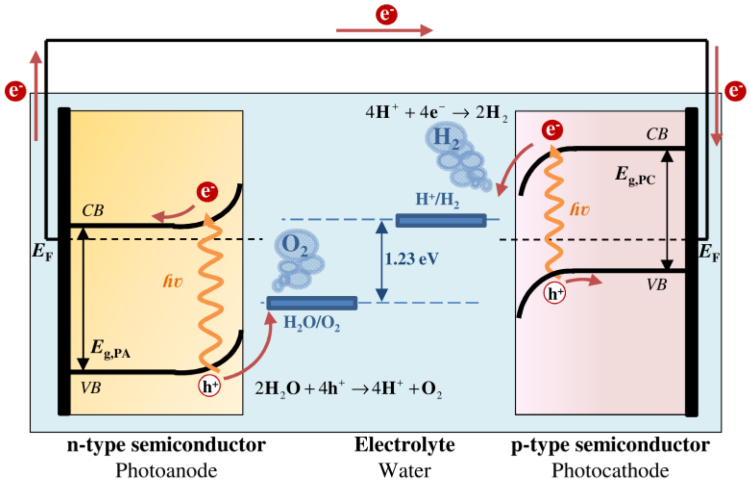

Figure 1.14: PEC cell based on a photoanode and a photocathode in tandem.

For this arrangement, the materials should be carefully selected since the following requirements have to be fulfilled: the energy level of the photocathode conduction band ($E_{CB,\ PC}$) has to be above the water reduction energy – $E^o(H^+/H_2)$ – and the photoanode valence band energy ($E_{VB,\ PA}$) has to be below the water oxidation energy – $E^o(H_2O/O_2)$. Moreover, the photocathode valence band energy level ($E_{VB,\ PC}$) should be higher than $E^o(H_2O/O_2)$, whereas the photoanode conduction band energy level

($E_{CB,\ PA}$) should be lower than $E^{o}(H^{+}/H_2)$. Briefly, $E_{CB,\ PC} > E^{o}(H^{+}/H_2) > E_{CB,\ PA} > E_{VB,\ PC} > E^{o}(H_2O/O_2) > E_{VB,\ PA}$. Only few works have considered this approach due to the lack of suitable photocathode materials for HER; the performance and the stability in aqueous solutions of these p-type materials (*e.g.* $GaInP_2$, Si, SiC, WS_2, Cu(In,Ga)Se_2, Cu_2O, $CuYO_2$, $CaFeO_4$ and p-type Mg doped Fe_2O_3) are actually a limiting factor [17]. Relevant works on photoanode (PA)/photocathode (PC) PEC tandem devices are presented in Table 1.5.

Table 1.5: Photoanode/Photocathode PEC tandem devices for direct solar water splitting, including experimental conditions and corresponding performance (STH conversion efficiency - η_{STH} - and stability); ordered by reverse chronological publication.

Device configurations	**Electrolyte and Illumination**	**η_{STH} / %**	**Stability, notes**	**Ref./ Date**
PA/PC PEC (2J tandem) Top PEC: Fe_2O_3 coated $NiFe_x$ OER co-catalyst Bottom PEC: a-Si with TiO_2/Pt overlayers HER	phosphate buffered (pH 11.8) 100 mW·cm^{-2}	0.91 %	10 h stable current	[60]/ 2015
PA/PC PEC (2J tandem) Top PEC: Fe_2O_3 coated IrO_x OER co-catalyst Bottom PC: a-Si (PV) with TiO_2/Pt overlayers HER	0.1 M KNO_3 (pH 1.01) 100 mW·cm^{-2}	0.44 %	5 h 5 % drop in current	[130]/ 2015
PA/PC PEC (2J tandem) Top PEC: $BiVO_4$ coated CoPi OER co-catalyst Bottom PEC: Cu_2O coated RuO_x HER co-catalyst	$K_{3-X}H_xPO_4$ buffer (pH 6) 100 mW·cm^{-2}	0.5 %	2 min 20 % drop in current	[131]/ 2014
PA/PC PEC (2J tandem) Top PEC: WO_3 coated NiO_x OER co-catalyst Bottom PEC: Cu_2O	0.1 M Na_2SO_4 (pH 6) 100 mW·cm^{-2}	0.04 %	Not reported	[132]/ 2012

PA/PC PEC (2J tandem) Top PEC: TiO_2 Bottom PEC: $CaFe_2O_4$	0.1 M NaOH 100 mW·cm^{-2}	< 0.01 %	Not reported	[133]/ 2011
PA/PC PEC (2J tandem) Top PEC: Fe_2O_3 Bottom PEC: Zn-doped Fe_2O_3	0.1 M H_2SO_4 100 mW·cm^{-2}	0.11 %	Not reported	[134]/ 2006
PA/PC PEC (2J tandem) Top PEC: GaAs coated MnO OER co-catalyst Bottom PEC: InP coated Pt HER co-catalyst	6 M KOH	8.2 %	10 h 10 % drop in current	[135]/ 1987
PA/PC PEC (2J tandem) Top PEC: Si-doped Fe_2O_3 Bottom PEC: SiC	0.01 M NaOH 100 mW·cm^{-2}	5×10^{-4} %	320 h stable current	[136]/ 1984
PA/PC PEC (2J tandem) Top PEC: Fe_2O_3 coated RuO_2 OER co-catalyst Bottom PEC: GaP coated Pt HER co-catalyst	1 M Na_2SO_4 fritted compartments sunlight	0.02 – 0.1 %	Not reported	[137]/ 1981
PA/PC PEC (2J tandem) Top PEC: $SrTiO_3$ Bottom PEC: GaP	1 M NaOH 100 mW·cm^{-2}	10.7 %	6 h measurement of H_2	[138]/ 1977
PA/PC PEC (2J tandem) Top PEC: TiO_2 Bottom PEC: GaP	0.2 M H_2SO_4 85 mW·cm^{-2}	0.3 %	Not reported GaP photocorrosion	[139]/ 1976

1.5 EFFICIENCY OF SOLAR WATER SPLITTING IN A PEC CELL

The energy conversion efficiency is one of the key performance indicators of the PEC cell. The four fundamental processes involved in solar water splitting are: light harvesting (ratio of the electron-hole pairs created to the amount of incident photons), separation of the photogenerated electrons and holes, transport of photoinjected electric charges and transfer of charge carrier at the electrolyte interface. These photogenerated electrons and holes are then separated by two possible transport mechanisms such as drift and diffusion. Drift is the motion of these charged-particles in response to the electric field inside the semiconductor, while diffusion is associated with a gradient in the local concentration of the charged particles. Therefore, the external quantum efficiency of the PEC water splitting reaction, EQE (also called solar-to-hydrogen efficiency, η_{STH}), can be defined as [140]:

$$\mathrm{EQE}(\lambda) = \eta_{\mathrm{light}}(\lambda) \times \eta_{\mathrm{ct}}(\lambda) \times \eta_{\mathrm{cat}} \tag{1.7}$$

where λ is the wavelength, η_{light} is the light absorption efficiency (ratio of the electron-hole pairs created to the amount of incident photons), η_{ct} is the charge separation/ transport efficiency (ratio between the amount of electrons and holes reaching the interfaces to the photogenerated electron-hole pairs), η_{cat} is the quantum efficiency of the catalytic charge transfer to the redox species in the electrolyte.

An alternative definition for the STH efficiency is based on the ratio of the chemical energy produced by the solar energy input, as described in Equation (1.8) [10]. The chemical energy produced is the rate of hydrogen production ($\phi_{\mathrm{H_2}}$, in mmol $H_2 \cdot s^{-1}$) multiplied by the change in Gibbs free energy per mol of H_2 (ΔG^{o} = 237 kJ·mol^{-1}).

$$\eta_{\mathrm{STH}} = \frac{\phi_{\mathrm{H_2}} \times \Delta G^{\circ}}{P_{\mathrm{light}} \times A} \tag{1.8}$$

The solar energy input is the incident illumination power density, P_{light}, and A is the illuminated area. This equation involves the measurement of the H_2 production rate, which may be difficult when very small devices are used. However, assuming a faradaic efficiency of 100 %, the STH efficiency can be determined simply from Equation (1.9):

$$\eta_{\mathrm{STH}} = \left.\frac{E_{\mathrm{redox}} \times J_{\mathrm{photo}}}{P_{\mathrm{light}}}\right|_{\mathrm{AM\ 1.5\ G}} \tag{1.9}$$

where J_{photo} is the photocurrent density responsible for H_2 generation ($\mathrm{mA \cdot cm^{-2}}$) obtained from the photocurrent-voltage (J-V) characteristics; E_{redox} is the potential corresponding to the Gibbs energy and corresponds to the thermodynamic potential needed to drive the water electrolysis, $\Delta E^{o} = \Delta G^{o}/nF = -1.23$ V (n is the number of moles of electrons used to produce one mole of H_2 – in this case $n = 2$). Assuming 1-sun AM 1.5 G incident sunlight ($P_{\mathrm{light}} = 100\ \mathrm{mW \cdot cm^{-2}}$) under zero bias conditions, which means that no external potential is applied between the working and the counter electrodes, Equation (1.9) can be related directly to the photocurrent density of a PEC cell [14]:

$$\eta_{\mathrm{STH}}\big|_{\mathrm{AM\ 1.5\ G}}(\%) = 1.23 \times J_{\mathrm{photo}} \tag{1.10}$$

It is then clear that the PEC photocurrent density is the main determining factor for STH efficiency. When an external potential bias is applied to the PEC system, a new efficiency is defined, named as “applied bias photon-to-current efficiency” - APCE [141]:

$$\eta_{\mathrm{APCE}} = \frac{P_{\mathrm{electrical}}^{\mathrm{out}} - P_{\mathrm{electrical}}^{\mathrm{in}}}{P_{\mathrm{light}}} = \frac{\left(E_{\mathrm{redox}} - E_{\mathrm{bias}}\right) \times J_{\mathrm{photo}}}{P_{\mathrm{light}}} \tag{1.11}$$

where $P_{\mathrm{electrical}}^{\mathrm{out}}$ is the electric power output, $P_{\mathrm{electrical}}^{\mathrm{in}}$ is the electric power input, E_{bias} is the potential applied to the system to obtain the J_{photo}. To separately assess the properties of individual photoelectrodes, a three-electrode configuration should be employed. This configuration is advantageous because when a reference electrode is present, the potential of the working photoelectrode can be accurately determined, which provides an estimate of how much electrical energy is put into the electrode. This allows obtaining power conversion efficiency of photoelectrodes based on the half reaction of water splitting. The efficiency of a photoanode (η_{PA}) should translate its ability to convert photonic energy into chemical energy used for oxidizing water [142]:

$$\eta_{\mathrm{PA}} = \frac{\left(E^{o}_{\mathrm{O_2/H_2O}} - E_{\mathrm{bias}}\right) \times J_{\mathrm{photo}}\big|_{\mathrm{MPP}}}{P_{\mathrm{light}}} \tag{1.12}$$

For a photocathode, the efficiency becomes as follows:

$$\eta_{\mathrm{PC}} = \frac{\left(E_{\mathrm{bias}} - E^{\mathrm{o}}_{\mathrm{H^+/H_2}}\right) \times J_{\mathrm{photo}}\Big|_{\mathrm{MPP}}}{P_{\mathrm{light}}} \tag{1.13}$$

where the J_{photo} is the photocurrent-density obtained at the maximum power point (MPP) and the $E^{\mathrm{o}}(O_2/H_2O)$ and $E^{\mathrm{o}}(H^+/H_2O)$ are the thermodynamic potential of water splitting half reactions [142]. These two equations are meaningful when no additional energy is supplied to the counter electrode for the other half reaction; therefore, they should be used mainly for comparing the performance of various photoelectrodes.

The parameter that determines the light harvesting ability of the photoelectrode is its bandgap E_g. Radiation of energy lower than E_g is not absorbed, while energy higher than the bandgap, $E \geq E_g$, is partly lost as heat by intraband thermalization processes [14]. Additional losses may occur as: i) thermodynamic losses related to the water splitting process and ii) bulk and interfacial transport losses related to recombination, interfacial kinetics (overpotentials) and band bending in the semiconducting electrodes. Then, it is difficult to achieve high STH conversion efficiencies in a single-junction PEC photoelectrode system. Large bandgap semiconductors with adequate band edge positions would be needed to generate sufficient usable photopotential to drive the redox reactions for water splitting; this limits photon absorption and, therefore, reduces the photocurrent. Thus, the bandgap tradeoff between photopotential and photocurrent is detrimental for single junctions. Taking this into account, for semiconductor materials exhibiting bandgaps greater than 3.2 eV, the photocurrent is limited to less than 1 mA·cm^{-2}, which corresponds to a maximum STH efficiency of < 1.23 %, according to Equation (1.10). Under ideal conditions, *i.e.* including thermalization losses but with no overpotential losses, a bandgap of $E_g = 1.6$ eV should be sufficient and the thermodynamic maximum efficiency of a device involving a single semiconductor photoelectrode is 30.7 % – Equation (1.10) [143]. Figure 1.15 plots the maximum attainable photocurrent densities and STH efficiencies as a function of the bandgap energy for standard AM 1.5 G illumination.

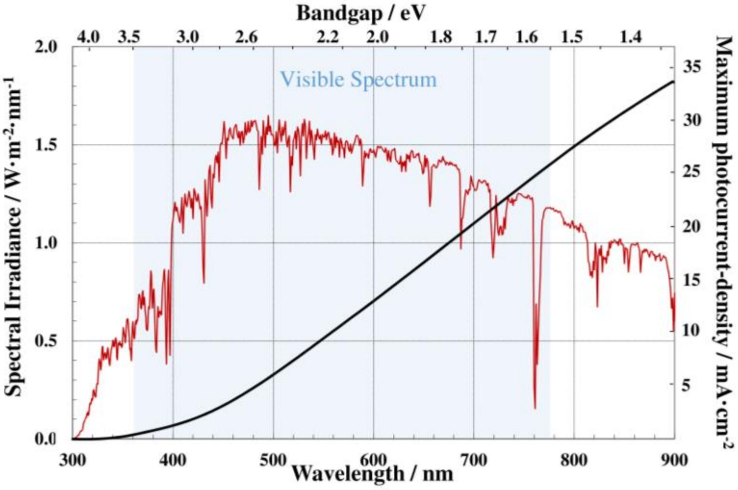

Figure 1.15: Spectral irradiance at AM 1.5 G and maximum thermodynamic photocurrent densities for a single system (adapted from ref. [14]).

While a multijunction device (tandem arrangement) is more complicated, some recent calculations have shown that this approach has the potential to yield photocatalytic water splitting efficiencies up to 29 % [103]. The tandem strategy allows the use of two smaller bandgap materials, which in turn absorb a much larger fraction of the solar spectrum. Many researchers have investigated the optimal bandgaps for two-junction systems taking energy losses into account; the general conclusion is that the LBG should have a bandgap of 1.7 eV while the SBG's bandgap should be 1.0 eV [103].

In the case of PEC tandem devices for unassisted water splitting, the maximum thermodynamic photocurrent density and corresponding η_{STH} are predicted from the interception point of the *J*-*V* characteristic curves of the photoanode and photocathode (when each photoelectrode is operating in a single PEC configuration), as shown in Figure 1.16. It is, therefore, important to shift the two curves so that the operation point is close to the MPP of each individual *J*-*V* curve. This means that the combined onset potential (E_{onset}) values, *i.e.* the potential at which a photocurrent is first measured, or the sum of the photopotentials (E_{photo}), should be greater than 1.23 V. For a photoanode E_{photo} = 1.23 V - E_{onset}; whereas $E_{\mathrm{photo}} = E_{\mathrm{onset}}$ for the photocathode [142]. Currently, the practical STH efficiencies are much lower than the thermodynamic values, due to the mismatch of their *J*-*V* curves.

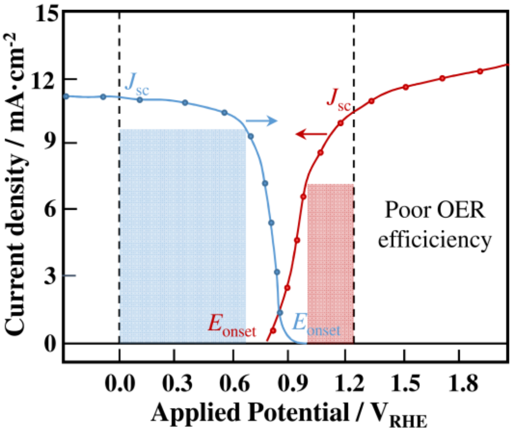

Figure 1.16: Photocurrent density-voltage curves for a photoanode and photocathode with external bias potential *vs.* reversible hydrogen electrode (RHE). The blue shadow is the maximum power conversion efficiency of a photoanode, while the red shadow is for the photocathode (adapted from ref. [142]).

According to Figure 1.17, a photoanode/photocathode system composed by a photoanode with a bandgap of $E_{g,\,PA}$ = 2.0 eV and a photocathode with a bandgap of $E_{g,\,PC}$ = 1.0 eV, has a thermodynamic STH efficiency of *ca.* 19 %; this corresponds to a modest increase over the approximately 16 % predicted with a single semiconductor configuration with E_g = 2.0 eV.

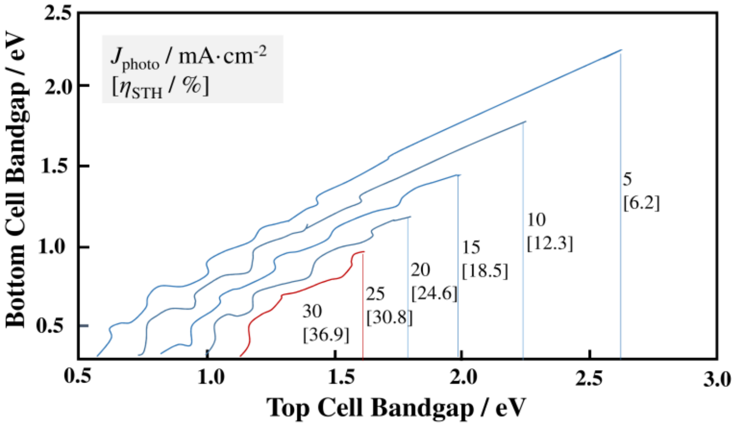

Figure 1.17: Maximum attainable AM 1.5 G photocurrent densities for dual bandgap devices, as a function of top cell and bottom cell bandgaps, corresponding to the higher and lower bandgap materials, respectively. Included in brackets are the corresponding PEC STH efficiencies in tandem devices determined by Equation (1.10) (adapted from ref. [14]).

1.6 STABILITY – PHOTOCORROSION

In solar water splitting, the stability/long-term performance of the photoelectrodes is one of the present critical research topics [25]. The electrolytic photoreduction of a semiconductor is often associated with the electrons in the valence band, while the electrolytic photooxidation reaction is related to holes in the conduction band as electronic reactants [144]. The Pourbaix diagram is used to analyze the thermodynamic potential for corrosion of the photoelectrodes, since it maps the possible stable phases in an aqueous electrochemical system. Photochemical corrosion can be described by the Gerischer and Bard model [145, 146]. The photochemical corrosion of a binary semiconductor MX and the solvation (complexing) of the elements (labeled hereafter as “solv”), which leads to the anodic and cathodic decomposition, may be represented by the following reaction, respectively [147]:

$$\mathrm{MX} + ze^- + \mathrm{solv} \rightarrow \mathrm{M} + \mathrm{X}^{z^-}_{\mathrm{solv}} \tag{1.14}$$

$$\mathrm{MX} + zh^+ + \mathrm{solv} \rightarrow \mathrm{M}^{z^+}_{\mathrm{solv}} + \mathrm{X} \tag{1.15}$$

where z is the number of holes or electrons. Using H^+/H_2 standard potentials as reference, the corresponding reaction for hydrogen may be written as [8]:

$$1/2\, z\mathrm{H}_2 + \mathrm{solv} \rightarrow z\mathrm{H}^+_{\mathrm{solv}} + ze^- \tag{1.16}$$

The addition of Equation (1.16) to Equation (1.14) or to Equation (1.15) yields the corresponding equations for the free energy values, ${}_{\mathrm{n}}\Delta G_{\mathrm{sH}}$ and ${}_{\mathrm{p}}\Delta G_{\mathrm{sH}}$, respectively. The equations for determining the decomposition potentials for the oxidation and reduction of the semiconductor are, respectively:

$${}_{\mathrm{p}}E_{\mathrm{d}} = {}_{\mathrm{p}}\Delta G_{\mathrm{sH/z}} \tag{1.17}$$

$${}_{\mathrm{n}}E_{\mathrm{d}} = -{}_{\mathrm{n}}\Delta G_{\mathrm{sH/z}} \tag{1.18}$$

The energy positions of the electron-induced potential ${}_{\mathrm{n}}E_{\mathrm{d}}$ and the hole-induced corrosion value ${}_{\mathrm{p}}E_{\mathrm{d}}$ can be plotted with respect to the band edges E_{CB} and E_{VB} – Figure 1.18. In fact, the criterion for thermodynamic stability of the semiconductor is:

$${}_{\mathrm{p}}E_{\mathrm{d}} > E_{\mathrm{redox}} > {}_{\mathrm{n}}E_{\mathrm{d}} \tag{1.19}$$

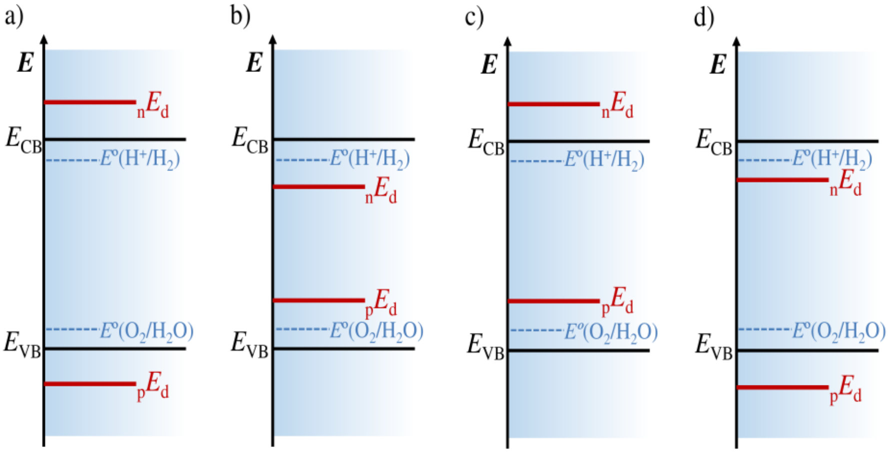

Figure 1.18: Relative positions of decomposition Fermi Levels of a semiconductor with respect to its band edges: (a) stable; (b) unstable; (c) cathodically stable but anodically unstable; and (d) anodically stable but cathodically unstable (adapted from ref. [8]).

Figure 1.19 shows the decomposition potentials for different oxide and non-oxide semiconductors. Actually, none of the semiconductors presented in Figure 1.19 show their Fermi levels edges positioned as in Figure 1.18a, meaning that they are cathodically and/or anodically unstable. Therefore, the stability of a semiconductor in contact with an electrolyte solution strongly depends on the competition between anodic dissolution and redox reaction, which are controlled by thermodynamic and kinetic parameters, respectively [147]. Thus, even if the semiconductor oxides are not thermodynamically stable, following the calculations of Gerischer [148], they can be kinetically stabilized in the presence of a suitable redox system. For instance, even if the metal oxide semiconductors are thermodynamically stable towards cathodic photocorrosion, most of them are unstable towards anodic photocorrosion. Accelerating the kinetics of water oxidation prevents the oxidation of the photoelectrode, *e.g.* the slow kinetics of water oxidation at hematite photoelectrode often leads to hole accumulation [86]. The instability can also be prevented by passivating the surface via applying an optically transparent metal and/or metal-oxide coatings by atomic layer deposition (ALD) or physical vapor deposition (PVD) or by adding a suitable co-catalyst to favor the water splitting reaction. However, the corrosion of the electrocatalysts should also be considered. For example, RuO_2 and

IrO_2 are more stable in acidic media, while anodic dissolution occurs in alkaline conditions, Co_3O_4 and Co-Pi are more stable in alkaline than in acidic media.

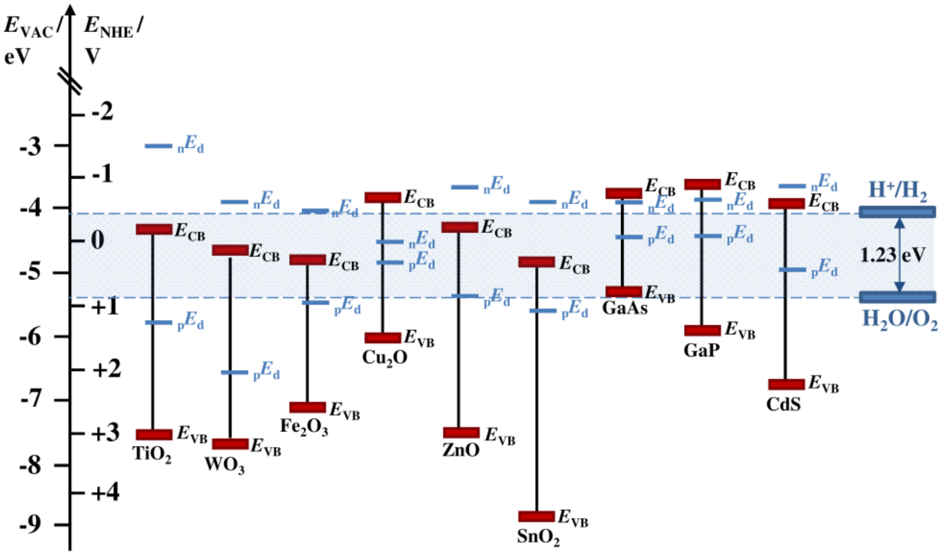

Figure 1.19: Positions of band edges and decomposition Fermi levels for different oxide and non-oxide semiconductors at pH 7 (adapted from ref. [147]).

Extensive overview of existing PEC systems and their performance (photocurrent-density and stability) can be found in the literature [24]. However, hard technological and economic targets have to be met for bringing solar water splitting commercial. As outlined in the European topic SP1-JTI-FCH.2013.2.5 "Validation of photoelectrochemical hydrogen production processes" through H2020, lifetimes of more than 1000 h have to be demonstrated up to 2017 [29]. Most reports assess lifetime of semiconductors during less than 24 h. Only few semiconductor-liquid junction (SCLJ) devices demonstrated to display stabilities of more than 1 day [24]. Recently, a record-breaking was obtained for bare hematite photoanode: 1000 h of PEC operation under AM 1.5 G illumination. These results opened one more door in the endeavor to make PEC cells into a competitive technology for solar hydrogen production [61].

1.7 PEC REACTORS

One of the key components of a photoelectrochemical setup is the PEC cell in which the photoelectrode is assembled [149]. A PEC cell consists basically of a reservoir that contains the electrolyte, where the two electrodes are immersed: the photoactive material (working electrode – WE) and the counter electrode (CE); however, both electrodes can be photoactive. When a three-electrode configuration is used, mainly in a laboratory setup, there is also the reference electrode (RE) – Figure 1.20.

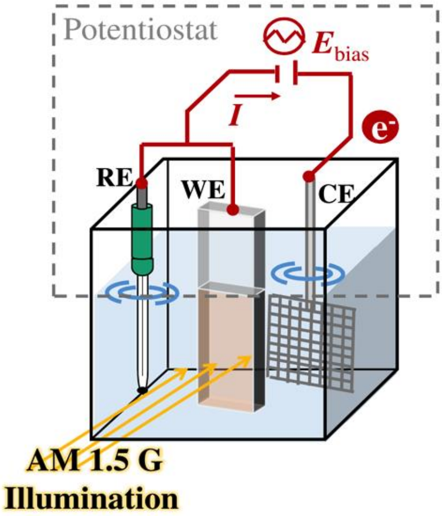

Figure 1.20: Scheme of a PEC cell for water splitting in a three-electrode configuration: WE – working electrode; CE – counter electrode; and RE – reference electrode.

The main aspect that distinguishes the PEC cell design from a standard electrochemical cell is the presence of an optically transparent window through which the sample is illuminated. For instance, a normal soda lime glass cut-off the transmission for wavelengths lower than 350 nm, while a quartz window have normally a transmittance higher than 90 % from 250 nm [150]. Nevertheless, a cheaper material should be used and fused silica (amorphous silica) also allows transmission values higher than 90 % and shows an excellent stability in both alkaline and acid solutions (except for fluoridric acid) [149]. Presently there are some PEC cell devices available commercially; the best performing PEC cell should be PortoCell –Figure 1.21 [151]. PortoCell complies with several requirements for lab applications [152]:

i. Maximizes the light penetration through the cell to reach the photoelectrodes;
ii. The illuminated photoelectrode area is completely immersed in the electrolyte;
iii. Allows different photoelectrodes configurations;
iv. The cell is resistant to corrosive electrolytes;
v. Provides a continuously electrolyte feeding;
vi. Allows the use of a membrane to maintain the evolved gases separated;
vii. Has facilities to electrically connect the electrodes to the external bias source.

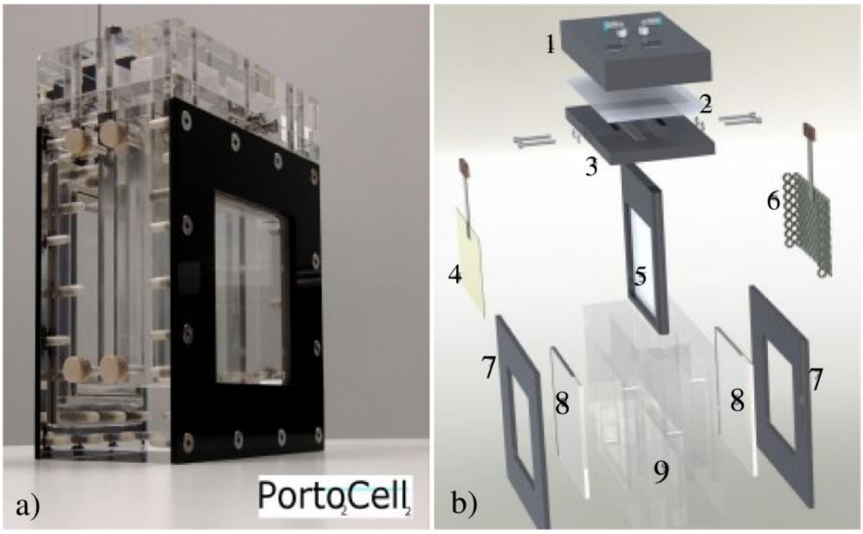

Figure 1.21: PortoCell assembled (a) and disassembled (b): 1 - acrylic cap (gas collection chamber); 2 - teflon membrane; 3 - acrylic cap (electrode contacts); 4 - photoelectrodes; 5 - diaphragm to separate both electrodes; 6 - Pt-counter-electrode; 7 - black acrylic for light blocking; 8 - transparent window; 9 - transparent PEC cell body (adapted from [152]).

1.7.1 THE WORKING ELECTRODE

In PEC devices the photoelectrode materials (WE) are mostly deposited onto glasses previously covered with a transparent conductive oxide (TCO) thin layer to ensure a transparent photoelectrode. The substrate should then form an ohmic contact with the photoactive material to ensure current flow. For n-type photoanodes, this requires conducting materials with a work function that is lower than that of the photoanode itself; while for p-type photocathodes, high-work function back-contacts such as gold and platinum should be used [149]. Fluorine doped tin oxide (FTO) is currently the conducting substrate of choice due to its commercial availability, high carrier concentration and mobility, acceptable electric conductivities at higher temperatures and an optical transparency higher than 80 % [149]. The development of a transparent semiconductor will allow to transmit the fraction of solar radiation not absorbed by the material and to convert it by other photosystems, improving their overall energy performance. On the other hand, when the transparency is not important, a metal substrate can be a potential alternative.

1.7.2 THE ELECTROLYTE

The electrolyte in an electrochemical cell consists of a polar solvent with active species to be reduced or oxidized, depending on if it is an alkaline medium or an acidic medium; the electrolyte should not conduct electrons. Photoactive semiconductor materials immersed in a redox electrolyte are greatly affected by the electrolyte solution properties; therefore, the choice of a suitable solution is very important, mainly in what concerns the redox couple selection and the pH compatibility with the photoelectrode [150]. It should contribute to improve charge-transfer kinetics, stability, as well as assist in preventing undesirable phenomena, such as surface recombination and trapping. Also, the electrolyte concentration should be sufficiently high to minimize the ohmic potential losses (concentrations of at least 0.5 M are recommended) and should display a high conductivity [149].

1.7.3 THE COUNTER ELECTRODE

The reaction at the counter electrode (CE) should be as fast as possible and have high catalytic activity. In a single photon-system PEC cell, platinum is usually used as counter electrode for hydrogen evolution; this material presents good stability over a wide range of electrolytes and pH, as well as it shows low overpotentials for hydrogen evolution (*ca.* 0.1 V) [149]. In a PEC/PV tandem configuration, the surface area of a CE should be several times larger than the illuminated photoelectrode area as a tactic toward reducing the overpotential required for supporting tandem photocurrent in a tandem device [85]. In PEC devices a compromise must be maintained between the WE, the CE and the electrolyte solution in order to ensure low overpotentials, fast charge transport and efficient light absorption.

1.7.4 THE REFERENCE ELECTRODE

Two-electrode and three-electrode systems are used to measure the efficiency of a whole PEC cell and the performance of a working electrode as a half cell, respectively. In a two-electrode configuration, the dark- and photocurrents are recorded as a function of potential against a counter electrode. The three-electrode configuration allows measuring the applied potential with respect to a fixed reference electrode, which allows to turn visible the independent response of the working electrode to any change in the applied potential. In water splitting studies the applied potential is normally reported against RHE (Reversible Hydrogen Electrode), thus the potential measured with the Ag/AgCl electrode must be converted into RHE scale as follows [149]:

$$E_{\mathrm{RHE}} = E_{\mathrm{Ag/AgCl}} + 0.059\ \mathrm{pH} + E^{\mathrm{o}}_{\mathrm{Ag/AgCl}\,vs.\,\mathrm{SHE}} \quad \left(E^{\mathrm{o}}_{\mathrm{Ag/AgCl}\,vs.\,\mathrm{SHE}} = 0.1976\ \mathrm{V\ at\ 25\ ^{o}C}\right) \qquad (1.20)$$

where E^{o}(Ag/AgCl *vs.* SHE) is the potential of the Ag/AgCl reference electrode with respect to the SHE (Standard Hydrogen Electrode). All the reference electrodes are very sensitive and so their maintenance is crucial.

1.8 ELECTROCHEMICAL CHARACTERIZATION

Characterization and modeling are essential to the development of PEC cell technology. The characterization techniques used are the flowing: UV-vis spectroscopy, electrochemical methods (*I-V*, CV and EIS), incident monochromatic photon-to-current conversion efficiency (IPCE) and faradaic efficiency determination.

The UV-vis spectroscopic measurement is used to assess the optical bandgap properties of the bulk semiconductor, *e.g.* the absorption data allows to estimate the film thickness, assuming a Lambertian absorption behavior [22]:

$$\ln\left(1 - abs\right) = -\alpha \cdot \ell \qquad (1.21)$$

where *abs* is the absorbance, α is the semiconductor absorbance coefficient at a specific wavelength and ℓ is the thickness of the film.

Current-voltage (*I-V*) measurement is the most important technique to evaluate the performance of a photoelectrode for water splitting; it consists of applying an external potential bias to the cell and measuring the generated photocurrent. These measurements are recorded using a potentiostat, which has at least two leads: one connects to the CE, while the other connects to the WE. Often a standard three-electrode configuration is used, a third lead is provided for the RE and, then, the current is passed between the WE and CE – Figure 1.22.

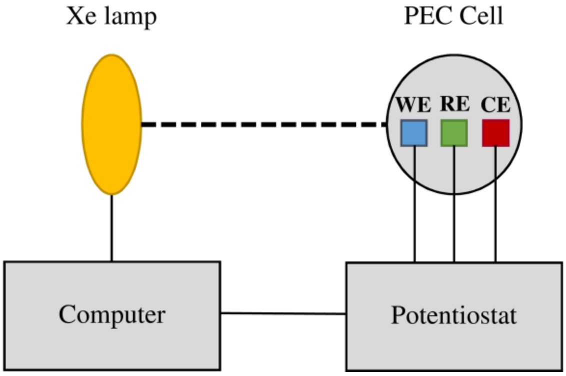

Figure 1.22: Experimental arrangement for a potentiostatic measuring system: WE – working electrode; RE – reference electrode; and CE – counter electrode.

This steady-state technique allows obtaining the current-voltage response in dark and under different light conditions, the photocurrent onset potential and, therefore, understanding the electron *vs.* hole transport limitations and transient effects that indicate recombination [149]. The photocurrent density tends to saturate at a certain applied bias, establishing the upper limit for the rate of PEC hydrogen production on a semiconductor and then the STH conversion efficiency - Equations (1.8) to (1.13). Figure 1.23 shows the ideal behavior of the *I-V* curves for an n-type semiconductor in the dark and under illumination conditions (conventionally, 1-sun AM 1.5 G illumination [153]).

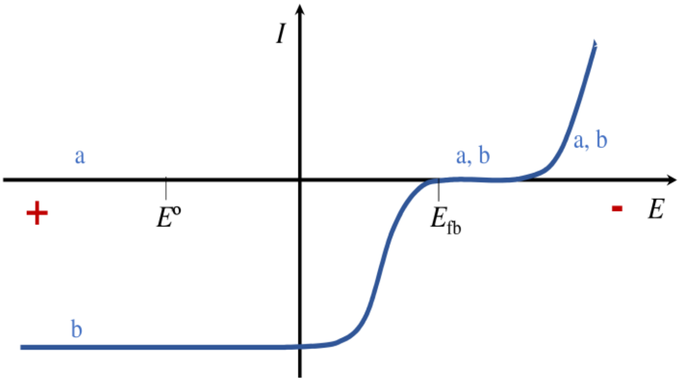

Figure 1.23: Ideal behavior for an n-type semiconductor: (a) in the dark and (b) under illumination conditions (adapted from [154]).

In cyclic voltammetry (CV) test the potential of a system is swept between two voltage limits while the current response is measured. The CV curves are used for acquiring information about electrochemical reactions, similar to *J-V* characteristics, and mainly for analyzing photocorrosion activity in a PEC cell [10].

Once it is considered that the photoelectrode is a promising material for solar water splitting, its durability is clearly desired. Stability tests consist in applying a constant potential on a PEC cell system over several hours and measure the resulting time-dependent photocurrent response, under 1-sun AM 1.5 G illumination. The overall stability is controlled by physical and chemical factors; physical stability is related to electrolyte evaporation, which heats up under the solar simulator illumination; the chemical stability is associated to irreversible electrochemical and thermal degradation of the semiconductor and electrolyte [155].

The electrochemical impedance spectroscopy (EIS) is a powerful characterization technique used to distinguish the different pathway losses (ohmic, activation and concentration) that limit the efficiency of the photoelectrochemical cells [156]. EIS analysis allows to perform a complete diagnostic of the PEC [157]:

i. external and shunt resistances;
ii. electron injection and its lifetime;
iii. recombination of the electron-hole pairs;
iv. charge transport resistance in the electrolyte;
v. reduction reaction at the counter electrode (Pt wire);

vi. diffusivity of the ionic species in the electrolyte.

Despite being a relatively easy method to apply, the correct interpretation of the results requires the use of suitable theoretical methods. Equivalent electric analogues are used to fit the experimental EIS data; their construction are therefore an important tool to identify and interpret the charge transfer phenomena occurring in the PEC cell under operating conditions. A small sinusoidal voltage perturbation $V(t)$ is applied to the system and the amplitude and phase shift of the resulting current response $I(t)$ are monitored, at the corresponding frequency – Figure 1.24. The response in current has the same period as the voltage perturbation but is phase-shifted by φ [156].

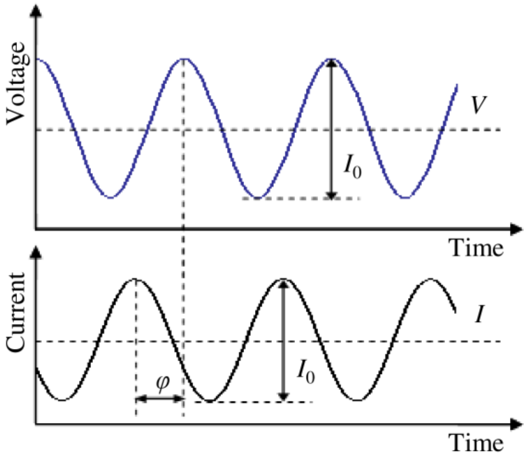

Figure 1.24: Sinusoidal voltage perturbation and resulting sinusoidal current response, phase-shifted by an amount φ. V_0 - amplitude of the voltage signal; I_0 - amplitude of the current signal; V – work voltage; I – generated current (adapted from [158]).

The impedance technique is a measure of the ability of a system to impede the flow of electrical current and is given by the ratio of a time-dependent voltage and a time-dependent current as defined by [156]:

$$Z = \frac{V(t)}{I(t)} = \frac{V_0 \cos(\omega t)}{I_0 \cos(\omega t - \varphi)} = Z_0 \frac{\cos(\omega t)}{\cos(\omega t - \varphi)} \tag{1.22}$$

where V_0 and I_0 are the amplitudes of voltage and current signals, respectively, and $\omega = 2\pi v$ is the angular frequency in radians per second. Alternatively, the impedance response can be expressed in terms of a magnitude, Z_0, and a phase shift, φ, or in terms of real and imaginary components, as follows [159]:

$$Z = Z_0 \frac{\exp(j\omega t)}{\exp(j\omega t - j\varphi)} = Z_0 \left(\cos\varphi + j\sin\varphi\right) \tag{1.23}$$

where j is the imaginary number ($j = \sqrt{-1}$). After knowing the impedance values of real ($Z' = Z_0 \cos\phi$) and imaginary ($Z'' = Z_0 j \sin\varphi$) parts and the phase angle φ, the Nyquist and Bode diagrams can be plotted. The former is the representation of $-Z''$ *vs.* Z', while the Bode diagram is the representation in a semi-logarithmic plot of the symmetric of the phase angle φ *vs.* the frequency [158].

EIS technique is also used to determine the flatband potential (E_{fb}) and the donor density of the semiconductor (N_{D}) applying the well-known Mott-Schottky relation [22]. Moreover, a deeper understanding of the complex impedance spectra allows a detailed characterization of electronic features, *e.g.* the determination of resistances and capacitances related to charge transport in the semiconductor layer, charge diffusion in the space charge region, surface trap charging by electrons and holes and phenomena occurring in the semiconductor-electrolyte interface [160].

The incident monochromatic photon-to-current conversion efficiency (IPCE) is also an advantageous parameter to evaluate the PEC performance, since it quantifies the effectiveness in converting photons from monochromatic light incident to photocurrent flowing between the working and counter electrodes. Thus, the IPCE is defined as the ratio of the number of electrons generated by light that follows in the external circuit ($N_{\mathrm{electrons}}$) to the number of incident photons as a function of wavelength (N_{photons}) [41]:

$$\mathrm{IPCE}(\lambda) = \frac{N_{\mathrm{electrons}}}{N_{\mathrm{photons}}} \tag{1.24}$$

Substituting the current definition ($I_{sc} = qN_{\mathrm{electrons}}/t$) in the previous equation, the IPCE is therefore defined as:

$$\mathrm{IPCE}(\lambda) = \frac{N_{\mathrm{electrons}}}{N_{\mathrm{photons}}} = \frac{qN_{\mathrm{electrons}}/t}{qN_{\mathrm{photons}}/t} = \frac{I_{\mathrm{sc}}}{qN_{\mathrm{photons}}/t} \tag{1.25}$$

where q is the elementary charge and t is the time [158]. The number of incident photons with a given wavelength relates to the power of the incident light (P_{light}) by:

$$P_{\mathrm{light}} = \frac{N_{\mathrm{photons}}}{t} h\upsilon = \frac{N_{\mathrm{photons}}}{t} h \frac{c_0}{\lambda} \tag{1.26}$$

where h is the Planck constant, v is the frequency, c_0 is the speed of light and λ is the wavelength. Manipulating Equation (1.26) in order to obtain N_{photons} and after introducing it into Equation (1.25), the IPCE value can be rewritten as [158]:

$$\mathrm{IPCE}(\lambda)=\frac{I_{\text{sc}}}{q\lambda P_{\text{light}}/hc_0}=\frac{I_{\text{sc}}hc_0}{P_{\text{light}}q\lambda}=\frac{I_{\text{sc}}}{P_{\text{light}}}\frac{1240}{\lambda}\times 100\,\% \qquad (1.27)$$

Finally, the IPCE is calculated measuring the current in a cell when a particular wavelength range with known irradiance P_{light} focus on the photoelectrode. The IPCE is normally determined at the bias potentials corresponding to the maximum power point. Efficient cells display very high IPCE values over a broad range of visible spectrum. Nevertheless, efficiencies lower than 100 % are expected due namely to reflection losses of incident photons and recombination of charge carriers [17].

Figure 1.25 shows the usual setup of an IPCE apparatus. A high-pressure xenon lamp with an AM 1.5 G filter deliveries the standard solar spectrum [153]. The incident wavelength is selected by a grating monochromator, and appropriate filters are used. The incident light intensity is generally low, so that photodecomposition reactions and thermal effects are minimized. The mechanical chopper interrupts the light periodically in order to allow a lock-in amplifier to be used to distinguish small photocurrents from dark currents [154].

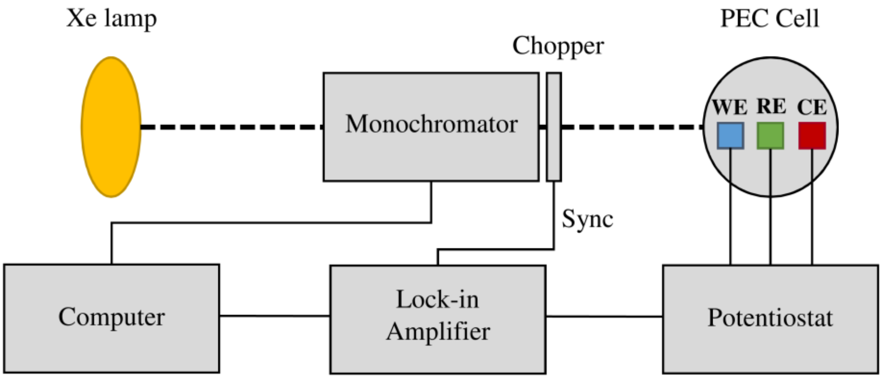

Figure 1.25: Experimental arrangement for an IPCE measuring system: WE – working electrode; RE – reference electrode; and CE – counter electrode (adapted from [154]).

Although initial measurements are often made assuming a faradaic efficiency for water splitting of 100 %, this assumption is not always valid, *i.e.* when there are parasite reactions [10]. The direct detection of evolved H_2 and O_2 gases, typically by mass spectroscopy or gas chromatography, is used to obtain the faradaic and then the STH efficiencies [10]. The quantitative detection of H_2 and O_2 evolved flowrates require perfect sealing of the PEC cell reactor.

1.9 STRUCTURAL AND MORPHOLOGICAL CHARACTERIZATION

The electrochemical methods previously mentioned can provide great information on the photoelectrode, the electrode/electrolyte interface and the corresponding processes, as an effort to identify which elements significantly influence the PEC cell performance. However, these methods are typically macroscopic; they are based on measurements over large areas compared to the pore structure and electrode/electrolyte chemistry. *Ex situ* characterization techniques allow to evaluate in detail the physical or chemical structures and properties of the individual components comprising the PEC cell [156, 161]. This way, to provide structural and morphological information about the photoelectrode, surface microscopic methods are needed, such as: Scanning Electron Microscopy (SEM) and Atomic Force Microscopy (AFM); X-ray diffraction (XRD); and X-ray photoelectron spectroscopy (XPS).

SEM analyses allow to obtain information about the morphology and chemical composition of the semiconductor film, by offering elemental identification when coupled to an auxiliary Energy Dispersive X-Ray Spectroscopy (EDS) detector [162, 163]. Moreover, this technique is also crucial to identify the modifications on the photoelectrodes surfaces induced by the stability tests. The surface topography can be assessed by AFM technique, which provides three-dimensional images and powerful information about surface measurements, *e.g.* surface roughness. XPS technique also allows surface analysis, providing information about both chemical composition and structure of the semiconductor materials [164]. In XPS measurements the atomic layers under study are located at the surface (1 nm depth) and near surface region (up to 10 nm depth); on these regions some important electrochemical phenomena can occur, such as water oxidation or reduction reactions, photocorrosion or passivation effects [165]. XRD technique can provide structural information about preferential crystal orientations, average grain size, film crystallinity and crystal defects [156]. Better photoelectrode performances are expected for improved crystallinity materials, ascribed to the decreased number of recombination sites [166].

On the other hand, the analyses of the electrolyte composition are performed using the inductively coupled plasma (ICP) technique. The main goals are the identification and quantification of all elements (with the exception of argon) available in solutions by plasma mass spectroscopy (ICP-MS) and atomic emission spectroscopy (ICP-AES), respectively [167]. These techniques are also relevant to identify the modifications on the elemental composition of the electrolytes after performing the stability tests related to the degradation of the photoelectrodes surfaces.

1.10 OBJECTIVES AND OUTLINE OF THIS WORK

In the last few years, research on PEC technology has been growing quite fast and remarkable developments on various aspects have been achieved, mainly in finding new semiconductors materials capable of better stabilities, photocurrents and photopotentials. Nevertheless, the primary goal of PEC research is to develop a system that balances complexity, cost and performance in a stand-alone device. Hard technological and economic targets have to be met for bringing solar water splitting commercial: a minimum STH efficiency of *ca.* 10 % and 5-year lifetime [168].

This thesis aims to contribute to the insightful study and characterization of PEC cells for solar hydrogen generation.

Chapter 1 introduces the different routes for solar hydrogen generation giving emphasis to photoelectrochemical water splitting. It discusses important aspects of the working principles of PECs and provides an overview of the most promising materials and systems used up to date. The device efficiency and stability are considered the two major challenges for future development. An overview of the applied characterization techniques is also given.

Chapter 2 focuses on the temperature effect on Si-doped hematite photoanodes for water splitting. Temperature influences the photoelectrochemical kinetics, charge transfer, electrode stability, ionic conductivity of the electrolyte, and therefore the device efficiency. An experimental test bench was built and a PEC cell setup was designed with a temperature controlling system. This work provides crucial insights on the photoelectrochemical systems operating under real outdoor conditions, strongly contributing for the development of commercial devices.

Chapter 3 studies the role of photoelectrode substrate on PEC performance using WO_3 photoanodes as a function of temperature. Two types of samples were studied: WO_3 deposited on a FTO glass and WO_3 anodized on a tungsten foil. The optimal operating temperatures were assessed; for temperatures higher than 45 ºC, the bulk electron-hole recombination phenomenon greatly affects the overall performance of WO_3 photoanodes. These findings showed that substrate and application method have a significant role on the photoelectrode energy performance and stability.

Chapter 4 concerns the development and optimization of a very stable bare hematite photoanode prepared by spray pyrolysis, following a design of experiments approach. A record-breaking stable result of 1000 h was obtained with no evidences of hematite film degradation neither of current density loss. These results open the door to turn PEC cells into a competitive technology in the solar fuel economy.

The most pronounced disadvantage of using hematite photoanodes is their low photopotential, characterized by the late onset potentials in its photoelectrochemical behaviors (typically 0.8 – 1.0 V_{RHE}). The structural disorders on or near the surfaces are the main causes. **Chapter 5** optimizes the energy performance of a hematite photoanode by surface modification combining two strategies: annealing at 800 ºC and coating with RuO_2 co-catalyst. The annealing treatment allowed the Sn doping from the FTO layer and the RuO_2 coating improved the water oxidation kinetics. A turn-on potential of 0.52 V_{RHE} and a high photopotential of *ca.* 0.95 V were achieved, which is the highest reported for hematite-based photoanodes.

In **Chapter 6** a new high-performance transparent photocathode based on electrodeposited cuprous oxide is developed, which drives efficiently the hydrogen evolution. A tandem arrangement with a hybrid perovskite photovoltaic cell (PEC/ PSC device) is capable of performing complete sunlight-driven water splitting with a solar to hydrogen efficiency of 2.5 %.

Finally, in **Chapter 7** the main conclusions and future work suggestions are presented.

REFERENCES

1. Dobran, F. *Energy supply options for climate change mitigation and sustainable development*. in *XXI World Energy Congress*. 2010. Montreal.
2. Grätzel, M., *Photoelectrochemical cells.* Nature, **2001**. 414(6861): p. 338-344.
3. Walter, M.G., Warren, E.L., McKone, J.R., Boettcher, S.W., Mi, Q., Santori, E.A. and Lewis, N.S., *Solar Water Splitting Cells.* Chemical Reviews, **2010**. 110(11): p. 6446-6473.
4. Abe, R., *Recent progress on photocatalytic and photoelectrochemical water splitting under visible light irradiation.* Journal of Photochemistry and Photobiology C: Photochemistry Reviews, **2010**. 11(4): p. 179-209.
5. EIA. *Annual Energy Outlook 2015*. **2015** [accessed 2015 September]; Available from: www.eia.doe.gov.
6. van de Krol, R. and Grätzel, M., *Introduction*, in *Photoelectrochemical Hydrogen Production*, R. van de Krol, Grätzel, Michael, Editor. **2012**, Springer Science Business Media: New York, USA. p. 3-11.
7. REN21. *Renewables 2015 Global Status Report*. **2015** [accessed 2015 October]; Available from: www.ren21.net.
8. Lopes, T., Andrade, L. and Mendes, A., *Photoelectrochemical Cells for Hydrogen Production from Solar Energy*, in *Solar Energy Sciences and Engineering Applications*, N.E.A. Akbarzadeh, Editor. **2013**, CRC Press. p. 293–341.
9. Pinaud, B.A., Benck, J.D., Seitz, L.C., Forman, A.J., Chen, Z., Deutsch, T.G., James, B.D., Baum, K.N., Baum, G.N., Ardo, S., Wang, H., Miller, E. and Jaramillo, T.F., *Technical and economic feasibility of centralized facilities for solar hydrogen production via photocatalysis and photoelectrochemistry.* Energy & Environmental Science, **2013**. 6(7): p. 1983-2002.
10. Chen, Z., Jaramillo, T.F., Deutsch, T.G., Kleiman-Shwarsctein, A., Forman, A.J., Gaillard, N., Garland, R., Takanabe, K., Heske, C., Sunkara, M., McFarland, E.W., Domen, K., Miller, E.L., Turner, J.A. and Dinh, H.N., *Accelerating materials development for photoelectrochemical hydrogen production: Standards for methods, definitions, and reporting protocols.* J. Mater. Res., **2010**. 25(01): p. 3-16.

11. SPE. *Global Market Outlook for Solar Power 2015–2019*. [accessed 2015 May]; Available from: www.solarpowereurope.org.
12. Nowotny, J., Sorrell, C.C., Sheppard, L.R. and Bak, T., *Solar-hydrogen: Environmentally safe fuel for the future*. International Journal of Hydrogen Energy, **2005**. 30(5): p. 521-544.
13. Hisatomi, T., Kubota, J. and Domen, K., *Recent advances in semiconductors for photocatalytic and photoelectrochemical water splitting*. Chemical Society Reviews, **2014**. 43(22): p. 7520-7535.
14. Miller, E.L., *Solar Hydrogen Production by Photoelectrochemical Water Splitting: The Promise and Challenge*, in *On Solar Hydrogen & Nanotechnology*, L. Vayssieres, Editor. **2010**, John Wiley & Sons: Asia. p. 3-32.
15. Coelho, B., Oliveira, A.C. and Mendes, A., *Concentrated solar power for renewable electricity and hydrogen production from water—a review*. Energy & Environmental Science, **2010**. 3(10): p. 1398-1405.
16. Grimes, C.A., Varghese, O.K. and Ranjan, S., *Hydrogen Generation by Water Splitting*, in *Light, Water, Hydrogen*. **2008**, Springer. p. 35-114.
17. Grimes, C.A., Varghese, O.K. and Ranjan, S., *Photoelectrolysis*, in *Light, Water, Hydrogen*. **2008**, Springer. p. 115-190.
18. Aruchamy, A., Aravamudan, G. and Subba Rao, G., *Semiconductor based Photoelectrochemical Cells for Solar Energy Conversion - An overview*. Bulletin of Materials Science, **1982**. 4(5): p. 483-526.
19. Minggu, L.J., Wan Daud, W.R. and Kassim, M.B., *An overview of photocells and photoreactors for photoelectrochemical water splitting*. International Journal of Hydrogen Energy, **2010**. 35(11): p. 5233-5244.
20. Fujishima, A. and Honda, K., *Electrochemical Photolysis of Water at a Semiconductor Electrode*. Nature, **1972**. 238(5358): p. 37-38.
21. Nozik, A.J., *Photoelectrochemistry: Applications to Solar Energy Conversion*. Annual Review of Physical Chemistry, **1978**. 29(1): p. 189-222.
22. Lopes, T., Andrade, L., Le Formal, F., Gratzel, M., Sivula, K. and Mendes, A., *Hematite photoelectrodes for water splitting: evaluation of the role of film thickness by impedance spectroscopy*. Physical Chemistry Chemical Physics, **2014**. 16(31): p. 16515-16523.

23. Lopes, T., Dias, P., Andrade, L. and Mendes, A., *E-MRS/MRS Bilateral Energy Conference Innovative Technological Configurations of Photoelectrochemical Cells*. Energy Procedia, **2012**. 22: p. 35-40.
24. Ager Iii, J.W., Shaner, M., Walczak, K., Sharp, I.D. and Ardo, S., *Experimental Demonstrations of Spontaneous, Solar-Driven Photoelectrochemical Water Splitting*. Energy & Environmental Science, **2015**. 8(10): p. 2811-2824.
25. Krol, R., Liang, Y. and Schoonman, J., *Solar Hydrogen Production with Nanostructured Metal Oxides*. Journal of Materials Chemistry, **2008**. 18(20): p. 2311-2320.
26. Sivula, K., Le Formal, F. and Grätzel, M., *Solar Water Splitting: Progress Using Hematite (α-*Fe_2O_3*) Photoelectrodes*. ChemSusChem, **2011**. 4(4): p. 432-449.
27. Weber, M.F. and Dignam, M.J., *Efficiency of splitting water with semiconducting photoelectrodes*. J. Electrochem. Soc., **1984**. 131(6): p. 1258-1265.
28. Murphy, A.B., Barnes, P.R.F., Randeniya, L.K., Plumb, I.C., Grey, I.E., Horne, M.D. and Glasscock, J.A., *Efficiency of solar water splitting using semiconductor electrodes*. International Journal of Hydrogen Energy, **2006**. 31(14): p. 1999-2017.
29. CORDIS, E.C.-. *SP1-JTI-FCH.2013.2.5 - Validation of photoelectrochemical hydrogen production processes*. **September 2015**; Available from: http://ec.europa.eu/index_en.htm.
30. James, B.D., Baum, G.N., Perez, J. and Baum, K.N., *Technoeconomic Analysis of Photoelectrochemical (PEC) Hydrogen Production*, U.D. Report, Editor. **2009**, Directed Technologies Inc.: Virginia.
31. Keable, J. and Holcroft, B., *Economic and Business Perspectives*, in *Photoelectrochemical Hydrogen Production*, R. van de Krol and M. Grätzel, Editors. **2012**, Springer US. p. 277-292.
32. Grimes, C.A., Varghese, O.K. and Ranjan, S., *Oxide Semiconducting Materials as Photoanodes*, in *Light, Water, Hydrogen* **2008**, Springer. p. 191-255.
33. Grimes, C.A., Varghese, O.K. and Ranjan, S., *Non-Oxide Semiconductor Nanostructures*, in *Light, Water, Hydrogen*. **2008**, Springer. p. 427-483.
34. Osterloh, F.E., *Inorganic Materials as Catalysts for Photochemical Splitting of Water*. Chem. Mater., **2008**. 20(1): p. 35-54.

35. Wang, G., Ling, Y., Wang, H., Xihong, L. and Li, Y., *Chemically modified nanostructures for photoelectrochemical water splitting.* Journal of Photochemistry and Photobiology C: Photochemistry Reviews, **2014**. 19: p. 35-51.
36. Warren, S.C., Voïtchovsky, K., Dotan, H., Leroy, C.M., Cornuz, M., Stellacci, F., Hébert, C., Rothschild, A. and Grätzel, M., *Identifying champion nanostructures for solar water-splitting.* Nat Mater, **2013**. 12(9): p. 842-849.
37. Nowotny, J., Bak, T., Nowotny, M.K. and Sheppard, L.R., *Titanium dioxide for solar-hydrogen I. Functional properties.* International Journal of Hydrogen Energy, **2007**. 32(14): p. 2609-2629.
38. Grimes, C.A., Varghese, O.K. and Ranjan, S., *Oxide Semiconductors: Nano-Crystalline, Tubular and Porous Systems*, in *Light, Water, Hydrogen*. **2008**: Springer. p. 257-369.
39. Mavroides, J.G., Kafalas, J.A. and Kolesar, D.F., *Photoelectrolysis of water in cells with* $SrTiO_3$ *anodes.* Applied Physics Letters, **1976**. 28(5): p. 241-243.
40. Wang, C., Chen, Z., Jin, H., Cao, C., Li, J. and Mi, Z., *Enhancing visible-light photoelectrochemical water splitting through transition-metal doped* TiO_2 *nanorod arrays.* Journal of Materials Chemistry A, **2014**. 2(42): p. 17820-17827.
41. Bak, T., Nowotny, J., Rekas, M. and Sorrell, C.C., *Photo-electrochemical hydrogen generation from water using solar energy. Materials-related aspects.* International Journal of Hydrogen Energy, **2002**. 27(10): p. 991-1022.
42. Liu, Q., Ding, D., Ning, C. and Wang, X., *Black Ni-doped* TiO_2 *photoanodes for high-efficiency photoelectrochemical water-splitting.* International Journal of Hydrogen Energy, **2015**. 40(5): p. 2107-2114.
43. Khan, S.U.M., Al-Shahry, M. and Ingler, W.B., Jr., *Efficient Photochemical Water Splitting by a Chemically Modified n-*TiO_2. Science, **2002**. 297(5590): p. 2243-2245.
44. Satsangi, V.R., Dass, S. and Shrivastav, R., *Nanostructured* α-Fe_2O_3 *in PEC Generation of Hydrogen*, in *On Solar Hydrogen & Nanotechnology*. **2010**, John Wiley & Sons, Ltd. p. 349-397.
45. Hardee, K.L. and Bard, A.J., *Semiconductor Electrodes: V. The Application of Chemically Vapor Deposited Iron Oxide Films to Photosensitized Electrolysis.* Journal of The Electrochemical Society, **1976**. 123(7): p. 1024-1026.

46. Kim, J.Y., Jang, J.-W., Youn, D.H., Magesh, G. and Lee, J.S., *A Stable and Efficient Hematite Photoanode in a Neutral Electrolyte for Solar Water Splitting: Towards Stability Engineering.* Advanced Energy Materials, **2014**. 4(13): p. 1614-6840.
47. Satsangi, V.R., Kumari, S., Singh, A.P., Shrivastav, R. and Dass, S., *Nanostructured hematite for photoelectrochemical generation of hydrogen.* International Journal of Hydrogen Energy, **2008**. 33(1): p. 312-318.
48. Mayer, M.T., Lin, Y., Yuan, G. and Wang, D., *Forming Heterojunctions at the Nanoscale for Improved Photoelectrochemical Water Splitting by Semiconductor Materials: Case Studies on Hematite.* Accounts of Chemical Research, **2013**. 46(7): p. 1558-1566.
49. Cesar, I., Sivula, K., Kay, A., Zboril, R. and Grätzel, M., *Influence of Feature Size, Film Thickness, and Silicon Doping on the Performance of Nanostructured Hematite Photoanodes for Solar Water Splitting.* The Journal of Physical Chemistry C, **2008**. 113(2): p. 772-782.
50. Hu, Y.-S., Kleiman-Shwarsctein, A., Stucky, G.D. and McFarland, E.W., *Improved photoelectrochemical performance of Ti-doped* α-Fe_2O_3 *thin films by surface modification with fluoride.* Chemical Communications, **2009**(19): p. 2652-2654.
51. Ling, Y., Wang, G., Wheeler, D.A., Zhang, J.Z. and Li, Y., *Sn-Doped Hematite Nanostructures for Photoelectrochemical Water Splitting.* Nano Letters, **2011**. 11(5): p. 2119-2125.
52. Kim, J.Y., Magesh, G., Youn, D.H., Jang, J.-W., Kubota, J., Domen, K. and Lee, J.S., *Single-crystalline, wormlike hematite photoanodes for efficient solar water splitting.* Sci. Rep., **2013**. 3: p. 2681.
53. Le Formal, F., Pendlebury, S.R., Cornuz, M., Tilley, S.D., Grätzel, M. and Durrant, J.R., *Back Electron–Hole Recombination in Hematite Photoanodes for Water Splitting.* Journal of the American Chemical Society, **2014**. 136(6): p. 2564-2574.
54. Tilley, S.D., Cornuz, M., Sivula, K. and Grätzel, M., *Light-Induced Water Splitting with Hematite: Improved Nanostructure and Iridium Oxide Catalysis.* Angew. Chem., Int. Ed., **2010**. 49(36): p. 1521-3773.

55. Morales-Guio, C.G., Mayer, M.T., Yella, A., Tilley, S.D., Grätzel, M. and Hu, X., *An Optically Transparent Iron Nickel Oxide Catalyst for Solar Water Splitting.* Journal of the American Chemical Society, **2015**. 137(31): p. 9927-9936.
56. Guo, X., Wang, L. and Tan, Y., *Hematite nanorods Co-doped with Ru cations with different valence states as high performance photoanodes for water splitting.* Nano Energy, **2015**. 16: p. 320-328.
57. Thorne, J.E., Li, S., Du, C., Qin, G. and Wang, D., *Energetics at the Surface of Photoelectrodes and Its Influence on the Photoelectrochemical Properties.* The Journal of Physical Chemistry Letters, **2015**. 6(20): p. 4083-4088.
58. Iandolo, B., Wickman, B., Zoric, I. and Hellman, A., *The rise of hematite: origin and strategies to reduce the high onset potential for the oxygen evolution reaction.* Journal of Materials Chemistry A, **2015**. 3(33): p. 16896-16912.
59. Zandi, O. and Hamann, T.W., *The potential versus current state of water splitting with hematite.* Physical Chemistry Chemical Physics, **2015**. 17(35): p. 22485-22503.
60. Jang, J.-W., Du, C., Ye, Y., Lin, Y., Yao, X., Thorne, J., Liu, E., McMahon, G., Zhu, J., Javey, A., Guo, J. and Wang, D., *Enabling unassisted solar water splitting by iron oxide and silicon.* Nat Commun, **2015**. 6: p. 7447.
61. Dias, P., Vilanova, A., Lopes, T., Andrade, L. and Mendes, A., *Extremely stable bare hematite photoanode for solar water splitting.* Nano Energy, **2016**. 23: p. 70-79.
62. Liu, X., Wang, F. and Wang, Q., *Nanostructure-based WO_3 photoanodes for photoelectrochemical water splitting.* Physical Chemistry Chemical Physics, **2012**. 14(22): p. 7894-7911.
63. Zhu, T., Chong, M.N. and Chan, E.S., *Nanostructured Tungsten Trioxide Thin Films Synthesized for Photoelectrocatalytic Water Oxidation: A review.* ChemSusChem, **2014**. 7(11): p. 2974-2997.
64. Solarska, R., Jurczakowski, R. and Augustynski, J., *A highly stable, efficient visible-light driven water photoelectrolysis system using a nanocrystalline WO_3 photoanode and a methane sulfonic acid electrolyte.* Nanoscale, **2012**. 4(5): p. 1553-1556.

65. Seabold, J.A. and Choi, K.-S., *Effect of a Cobalt-Based Oxygen Evolution Catalyst on the Stability and the Selectivity of Photo-Oxidation Reactions of a* WO_3 *Photoanode.* Chemistry of Materials, **2011**. 23(5): p. 1105-1112.
66. Abdi, F.F., Firet, N. and van de Krol, R., *Efficient BiVO4 Thin Film Photoanodes Modified with Cobalt Phosphate Catalyst and W-doping.* ChemCatChem, **2013**. 5(2): p. 490-496.
67. Sayama, K., Nomura, A., Arai, T., Sugita, T., Abe, R., Yanagida, M., Oi, T., Iwasaki, Y., Abe, Y. and Sugihara, H., *Photoelectrochemical Decomposition of Water into* H_2 *and* O_2 *on Porous* $BiVO_4$ *Thin-Film Electrodes under Visible Light and Significant Effect of Ag Ion Treatment.* The Journal of Physical Chemistry B, **2006**. 110(23): p. 11352-11360.
68. Walsh, A., Yan, Y., Huda, M.N., Al-Jassim, M.M. and Wei, S.-H., *Band Edge Electronic Structure of* $BiVO_4$*: Elucidating the Role of the Bi s and V d Orbitals.* Chemistry of Materials, **2009**. 21(3): p. 547-551.
69. Wang, Z., Luo, W., Yan, S., Feng, J., Zhao, Z., Zhu, Y., Li, Z. and Zou, Z., $BiVO_4$ *nano-leaves: Mild synthesis and improved photocatalytic activity for* O_2 *production under visible light irradiation.* CrystEngComm, **2011**. 13(7): p. 2500-2504.
70. Abdi, F.F., Han, L., Smets, A.H.M., Zeman, M., Dam, B. and van de Krol, R., *Efficient solar water splitting by enhanced charge separation in a bismuth vanadate-silicon tandem photoelectrode.* Nat Commun, **2013**. 4: p. 2195.
71. Han, L., Abdi, F.F., van de Krol, R., Liu, R., Huang, Z., Lewerenz, H.-J., Dam, B., Zeman, M. and Smets, A.H.M., *Efficient Water-Splitting Device Based on a Bismuth Vanadate Photoanode and Thin-Film Silicon Solar Cells.* ChemSusChem, **2014**. 7(10): p. 2832-2838.
72. Zhen, C., Chen, R., Wang, L., Liu, G. and Cheng, H.-M., *Tantalum (oxy)nitride based photoanodes for solar-driven water oxidation.* Journal of Materials Chemistry A, **2016**. 4(8): p. 2783-2800.
73. Li, Y., Zhang, L., Torres-Pardo, A., González-Calbet, J.M., Ma, Y., Oleynikov, P., Terasaki, O., Asahina, S., Shima, M., Cha, D., Zhao, L., Takanabe, K., Kubota, J. and Domen, K., *Cobalt phosphate-modified barium-doped tantalum nitride*

nanorod photoanode with 1.5% solar energy conversion efficiency. Nat Commun, **2013**. 4: p. 2566.

74. Liu, G., Fu, P., Zhou, L., Yan, P., Ding, C., Shi, J. and Li, C., *Efficient Hole Extraction from a Hole-Storage-Layer-Stabilized Tantalum Nitride Photoanode for Solar Water Splitting.* Chemistry – A European Journal, **2015**. 21(27): p. 9624-9628.
75. Memming, R. and Schwandt, G., *Electrochemical properties of gallium phosphide in aqueous solutions.* Electrochim. Acta, **1968**. 13(6): p. 1299-1310.
76. Heller, A., *Conversion of sunlight into electrical power and photoassisted electrolysis of water in photoelectrochemical cells.* Acc. Chem. Res., **1981**. 14(5): p. 154-162.
77. Khaselev, O. and Turner, J.A., *A Monolithic Photovoltaic-Photoelectrochemical Device for Hydrogen Production via Water Splitting.* Science, **1998**. 280(5362): p. 425-427.
78. Nakato, Y., Yano, H., Nishiura, S., Ueda, T. and Tsubomura, H., *Hydrogen photoevolution at p-type silicon electrodes coated with discontinuous metal layers.* J. Electroanal. Chem., **1987**. 228(1-2): p. 97-108.
79. Hamann, T.W. and Lewis, N.S., *Control of the Stability, Electron-Transfer Kinetics, and pH-Dependent Energetics of Si/*H_2O *Interfaces through Methyl Termination of Si(111) Surfaces.* The Journal of Physical Chemistry B, **2006**. 110(45): p. 22291-22294.
80. Lin, Y., Battaglia, C., Boccard, M., Hettick, M., Yu, Z., Ballif, C., Ager, J.W. and Javey, A., *Amorphous Si Thin Film Based Photocathodes with High Photovoltage for Efficient Hydrogen Production.* Nano Letters, **2013**. 13(11): p. 5615-5618.
81. Meyer, B.K., Polity, A., Reppin, D., Becker, M., Hering, P., Klar, P.J., Sander, T., Reindl, C., Benz, J., Eickhoff, M., Heiliger, C., Heinemann, M., Bläsing, J., Krost, A., Shokovets, S., Müller, C. and Ronning, C., *Binary copper oxide semiconductors: From materials towards devices.* physica status solidi (b), **2012**. 249(8): p. 1487-1509.
82. Paracchino, A., Laporte, V., Sivula, K., Grätzel, M. and Thimsen, E., *Highly active oxide photocathode for photoelectrochemical water reduction.* Nat Mater, **2011**. 10(6): p. 456-461.

83. Azevedo, J., Steier, L., Dias, P., Stefik, M., Sousa, C.T., Araujo, J.P., Mendes, A., Graetzel, M. and Tilley, S.D., *On the stability enhancement of cuprous oxide water splitting photocathodes by low temperature steam annealing.* Energy & Environmental Science, **2014**. 7(12): p. 4044-4052.
84. Tilley, S.D., Schreier, M., Azevedo, J., Stefik, M. and Graetzel, M., *Ruthenium Oxide Hydrogen Evolution Catalysis on Composite Cuprous Oxide Water-Splitting Photocathodes.* Advanced Functional Materials, **2013**. 24(3): p. 1616-3028.
85. Dias, P., Schreier, M., Tilley, S.D., Luo, J., Azevedo, J., Andrade, L., Bi, D., Hagfeldt, A., Mendes, A., Grätzel, M. and Mayer, M.T., *Transparent Cuprous Oxide Photocathode Enabling a Stacked Tandem Cell for Unbiased Water Splitting.* Advanced Energy Materials, **2015**. 5(24): p. 1614-6840.
86. Li, Z., Luo, W., Zhang, M., Feng, J. and Zou, Z., *Photoelectrochemical cells for solar hydrogen production: current state of promising photoelectrodes, methods to improve their properties, and outlook.* Energy & Environmental Science, **2013**. 6(2): p. 347-370.
87. Guijarro, N., Prevot, M.S. and Sivula, K., *Surface modification of semiconductor photoelectrodes.* Physical Chemistry Chemical Physics, **2015**. 17(24): p. 15655-15674.
88. Hisatomi, T., Le Formal, F., Cornuz, M., Brillet, J., Tetreault, N., Sivula, K. and Gratzel, M., *Cathodic shift in onset potential of solar oxygen evolution on hematite by 13-group oxide overlayers.* Energy & Environmental Science, **2011**. 4(7): p. 2512-2515.
89. Fabbri, E., Habereder, A., Waltar, K., Kotz, R. and Schmidt, T.J., *Developments and perspectives of oxide-based catalysts for the oxygen evolution reaction.* Catalysis Science & Technology, **2014**. 4(11): p. 3800-3821.
90. Zeradjanin, A.R., Topalov, A.A., Van Overmeere, Q., Cherevko, S., Chen, X., Ventosa, E., Schuhmann, W. and Mayrhofer, K.J.J., *Rational design of the electrode morphology for oxygen evolution - enhancing the performance for catalytic water oxidation.* RSC Advances, **2014**. 4(19): p. 9579-9587.
91. Liao, M., Feng, J., Luo, W., Wang, Z., Zhang, J., Li, Z., Yu, T. and Zou, Z., *Co_3O_4 Nanoparticles as Robust Water Oxidation Catalysts Towards Remarkably*

Enhanced Photostability of a Ta_3N_5 Photoanode. Advanced Functional Materials, **2012**. 22(14): p. 3066-3074.

92. Gamelin, D.R., *Water splitting: Catalyst or spectator?* Nat Chem, **2012**. 4(12): p. 965-967.
93. Morales-Guio, C.G., Tilley, S.D., Vrubel, H., Gratzel, M. and Hu, X., *Hydrogen evolution from a copper(I) oxide photocathode coated with an amorphous molybdenum sulphide catalyst.* Nat Commun, **2014**. 5: p. 3059.
94. Zhang, D., Meng, L., Shi, J., Wang, N., Liu, S. and Li, C., *One-step preparation of optically transparent Ni-Fe oxide film electrocatalyst for oxygen evolution reaction.* Electrochimica Acta, **2015**. 169: p. 402-408.
95. Li, J. and Wu, N., *Semiconductor-based photocatalysts and photoelectrochemical cells for solar fuel generation: a review.* Catal. Sci. Technol., **2015**. 5(3): p. 1360-1384.
96. Kang, D., Kim, T.W., Kubota, S.R., Cardiel, A.C., Cha, H.G. and Choi, K.-S., *Electrochemical Synthesis of Photoelectrodes and Catalysts for Use in Solar Water Splitting.* Chemical Reviews, **2015**. 115(23): p. 12839-12887.
97. Miller, E., DeAngelis, A. and Mallory, S., *Multijunction Approaches to Photoelectrochemical Water Splitting*, in *Photoelectrochemical Hydrogen Production*, R. van de Krol and M. Grätzel, Editors. **2012**, Springer US. p. 205-273.
98. Prévot, M.S. and Sivula, K., *Photoelectrochemical Tandem Cells for Solar Water Splitting.* The Journal of Physical Chemistry C, **2013**. 117(35): p. 17879-17893.
99. Conibeer, G.J. and Richards, B.S., *A comparison of PV/electrolyser and photoelectrolytic technologies for use in solar to hydrogen energy storage systems.* International Journal of Hydrogen Energy, **2007**. 32(14): p. 2703-2711.
100. Grätzel, M., *Solar Energy Conversion by Dye-Sensitized Photovoltaic Cells.* Inorg. Chem., **2005**. 44(20): p. 6841-6851.
101. Snaith, H.J., *Perovskites: The Emergence of a New Era for Low-Cost, High-Efficiency Solar Cells.* The Journal of Physical Chemistry Letters, **2013**. 4(21): p. 3623-3630.
102. Mor, G.K., Varghese, O.K., Wilke, R.H.T., Sharma, S., Shankar, K., Latempa, T.J., Choi, K.S. and Grimes, C.A., *p-Type Cu−Ti−O Nanotube Arrays and Their*

Use in Self-Biased Heterojunction Photoelectrochemical Diodes for Hydrogen Generation. Nano Letters, **2008**. 8(10): p. 3555-3555.

103. Seger, B., Castelli, I.E., Vesborg, P.C.K., Jacobsen, K.W., Hansen, O. and Chorkendorff, I., *2-Photon tandem device for water splitting: comparing photocathode first versus photoanode first designs.* Energy & Environmental Science, **2014**. 7(8): p. 2397-2413.
104. Grätzel, M. and Augustynski, J., *Tandem cell for water cleavage by visible light* **2001**, EPFL.
105. Duret, A. and Gratzel, M., *Visible Light-Induced Water Oxidation on Mesoscopic* α*-*Fe_2O_3 *Films Made by Ultrasonic Spray Pyrolysis.* The Journal of Physical Chemistry B, **2005**. 109(36): p. 17184-17191.
106. Park, N.-G., *Organometal Perovskite Light Absorbers Toward a 20% Efficiency Low-Cost Solid-State Mesoscopic Solar Cell.* The Journal of Physical Chemistry Letters, **2013**. 4(15): p. 2423-2429.
107. Manser, J.S. and Kamat, P.V., *Band filling with free charge carriers in organometal halide perovskites.* Nat Photon, **2014**. 8(9): p. 737-743.
108. Hodes, G., *Perovskite-Based Solar Cells.* Science, **2013**. 342(6156): p. 317-318.
109. Luo, J., Im, J.-H., Mayer, M.T., Schreier, M., Nazeeruddin, M.K., Park, N.-G., Tilley, S.D., Fan, H.J. and Grätzel, M., *Water photolysis at 12.3% efficiency via perovskite photovoltaics and Earth-abundant catalysts.* Science, **2014**. 345(6204): p. 1593-1596.
110. May, M.M., Lewerenz, H.-J., Lackner, D., Dimroth, F. and Hannappel, T., *Efficient direct solar-to-hydrogen conversion by in situ interface transformation of a tandem structure.* Nat Commun, **2015**. 6: p. 8286.
111. Verlage, E., Hu, S., Liu, R., Jones, R.J.R., Sun, K., Xiang, C., Lewis, N.S. and Atwater, H.A., *A monolithically integrated, intrinsically safe, 10% efficient, solar-driven water-splitting system based on active, stable earth-abundant electrocatalysts in conjunction with tandem III-V light absorbers protected by amorphous* TiO_2 *films.* Energy & Environmental Science, **2015**. 8(11): p. 3166-3172.

112. Khaselev, O., Bansal, A. and Turner, J.A., *High-efficiency integrated multijunction photovoltaic/electrolysis systems for hydrogen production.* International Journal of Hydrogen Energy, **2001**. 26(2): p. 127-132.
113. Jacobsson, T.J., Fjallstrom, V., Sahlberg, M., Edoff, M. and Edvinsson, T., *A monolithic device for solar water splitting based on series interconnected thin film absorbers reaching over 10% solar-to-hydrogen efficiency.* Energy & Environmental Science, **2013**. 6(12): p. 3676-3683.
114. Kelly, N.A. and Gibson, T.L., *Design and characterization of a robust photoelectrochemical device to generate hydrogen using solar water splitting.* International Journal of Hydrogen Energy, **2006**. 31(12): p. 1658-1673.
115. Wang, X., Peng, K.-Q., Hu, Y., Zhang, F.-Q., Hu, B., Li, L., Wang, M., Meng, X.-M. and Lee, S.-T., *Silicon/Hematite Core/Shell Nanowire Array Decorated with Gold Nanoparticles for Unbiased Solar Water Oxidation.* Nano Letters, **2013**. 14(1): p. 18-23.
116. Shaner, M.R., Fountaine, K.T., Ardo, S., Coridan, R.H., Atwater, H.A. and Lewis, N.S., *Photoelectrochemistry of core-shell tandem junction* $n\text{-}p^{+}\text{-}Si/n\text{-}WO_3$ *microwire array photoelectrodes.* Energy & Environmental Science, **2014**. 7(2): p. 779-790.
117. Liu, C., Tang, J., Chen, H.M., Liu, B. and Yang, P., *A Fully Integrated Nanosystem of Semiconductor Nanowires for Direct Solar Water Splitting.* Nano Letters, **2013**. 13(6): p. 2989-2992.
118. Morisaki, H., Watanabe, T., Iwase, M. and Yazawa, K., *Photoelectrolysis of water with titanium dioxide-covered solar-cell electrodes.* Appl. Phys. Lett., **1976**. 29: p. 338-340.
119. Walczak, K., Chen, Y., Karp, C., Beeman, J.W., Shaner, M., Spurgeon, J., Sharp, I.D., Amashukeli, X., West, W., Jin, J., Lewis, N.S. and Xiang, C., *Modeling, Simulation, and Fabrication of a Fully Integrated, Acid-stable, Scalable Solar-Driven Water-Splitting System.* ChemSusChem, **2015**. 8(3): p. 544-551.
120. Gaillard, N., Chang, Y., Kaneshiro, J., Deangelis, A. and Miller, E.L. *Status of research on tungsten oxide-based photoelectrochemical devices at the University of Hawai'i*. 2010.
121. Miller, E.L., Paluselli, D., Marsen, B. and Rocheleau, R.E., *Development of reactively sputtered metal oxide films for hydrogen-producing hybrid*

multijunction photoelectrodes. Solar Energy Materials and Solar Cells, **2005**. 88(2): p. 131-144.

122. Shi, X., Zhang, K., Shin, K., Ma, M., Kwon, J., Choi, I.T., Kim, J.K., Kim, H.K., Wang, D.H. and Park, J.H., *Unassisted photoelectrochemical water splitting beyond 5.7% solar-to-hydrogen conversion efficiency by a wireless monolithic photoanode/dye-sensitised solar cell tandem device.* Nano Energy, **2015**. 13: p. 182-191.
123. Brillet, J., Yum, J.-H., Cornuz, M., Hisatomi, T., Solarska, R., Augustynski, J., Graetzel, M. and Sivula, K., *Highly efficient water splitting by a dual-absorber tandem cell.* Nat Photon, **2012**. 6(12): p. 824-828.
124. Park, J.H. and Bard, A.J., *Photoelectrochemical Tandem Cell with Bipolar Dye-Sensitized Electrodes for Vectorial Electron Transfer for Water Splitting.* Electrochem. Solid-State Lett., **2005**. 8(2): p. E5-E8.
125. Brillet, J., Cornuz, M., Le Formal, F., Yum, J.-H., Grätzel, M. and Sivula, K., *Examining architectures of photoanode-photovoltaic tandem cells for solar water splitting.* Journal of Materials Research, **2010**. 25(1): p. 17-24.
126. Zhang, X., Zhang, B., Cao, K., Brillet, J., Chen, J., Wang, M. and Shen, Y., *A perovskite solar cell-*TiO_2*@*$BiVO_4$ *photoelectrochemical system for direct solar water splitting.* Journal of Materials Chemistry A, **2015**. 3(43): p. 21630-21636.
127. Chen, Y.-S., Manser, J.S. and Kamat, P.V., *All Solution-Processed Lead Halide Perovskite-*$BiVO_4$ *Tandem Assembly for Photolytic Solar Fuels Production.* Journal of the American Chemical Society, **2014**. 137(2): p. 974-981.
128. Gurudayal, Sabba, D., Mulmudi, H.K., Wong, L.H., Barber, J., Grätzel, M. and Mathews, N., *Perovskite- Hematite Tandem Cells for Efficient Overall Solar Driven Water Splitting.* Nano Letters, **2015**. 15(6): p. 3833-3839.
129. Ellis, A.B., Kaiser, S.W. and Wrighton, M.S., *Semiconducting potassium tantalate electrodes. Photoassistance agents for the efficient electrolysis of water.* The Journal of Physical Chemistry, **1976**. 80(12): p. 1325-1328.
130. Li, W., Sheehan, S.W., He, D., He, Y., Yao, X., Grimm, R.L., Brudvig, G.W. and Wang, D., *Hematite-Based Solar Water Splitting in Acidic Solutions: Functionalization by Mono- and Multilayers of Iridium Oxygen-Evolution*

Catalysts. Angewandte Chemie International Edition, **2015**. 54(39): p. 11428-11432.

131. Bornoz, P., Abdi, F.F., Tilley, S.D., Dam, B., van de Krol, R., Graetzel, M. and Sivula, K., *A Bismuth Vanadate–Cuprous Oxide Tandem Cell for Overall Solar Water Splitting.* The Journal of Physical Chemistry C, **2014**. 118(30): p. 16959-16966.
132. Lin, C.-Y., Lai, Y.-H., Mersch, D. and Reisner, E., *$Cu_2O|NiO_x$ nanocomposite as an inexpensive photocathode in photoelectrochemical water splitting.* Chemical Science, **2012**. 3(12): p. 3482-3487.
133. Snaith, H.J., Stavrinadis, A., Docampo, P. and Watt, A.A.R., *Lead-sulphide quantum-dot sensitization of tin oxide based hybrid solar cells.* Solar Energy, **2011**. 85(6): p. 1283-1290.
134. Ingler, W.B. and Khan, S.U.M., *A self-driven p/n-Fe_2O_3 tandem photoelectrochemical cell for water splitting*. Vol. 9. **2006**, Pennington, NJ, ETATS-UNIS: Institute of Electrical and Electronics Engineers.
135. Kainthla, R.C., Zelenay, B. and Bockris, J.O., *Significant Efficiency Increase in Self-Driven Photoelectrochemical Cell for Water Photoelectrolysis.* J. Electrochem. Soc., **1987**. 134(4): p. 841-845.
136. Turner, J.E., Hendewerk, M. and Somorjai, G.A., *The photodissociation of water by doped iron oxides: The unbiased p/n assembly*. Chemical Physics Letters, **1984**. 105(6): p. 581-585.
137. Mettee, H., Otvos, J.W. and Calvin, M., *Solar induced water splitting with p/n heterotype photochemical diodes: n-Fe_2O_3/p-GaP.* Sol. Energy Mater., **1981**. 4(4): p. 443-453.
138. Ohashi, K., McCann, J. and Bockris, J.O.M., *Stable photoelectrochemical cells for the splitting of water.* Nature, **1977**. 266(5603): p. 610-611.
139. Nozik, A.J., *P-n photoelectrolysis cells.* Applied Physics Letters, **1976**. 29(3): p. 150-153.
140. Jacobsson, T.J., Fjällström, V., Edoff, M. and Edvinsson, T., *A theoretical analysis of optical absorption limits and performance of tandem devices and series interconnected architectures for solar hydrogen production.* Solar Energy Materials and Solar Cells, **2015**. 138: p. 86-95.

141. Dias, P., Lopes, T., Andrade, L. and Mendes, A., *Temperature effect on water splitting using a Si-doped hematite photoanode.* Journal of Power Sources, **2014**. 272: p. 567-580.
142. Yang, X., Liu, R., He, Y., Thorne, J., Zheng, Z. and Wang, D., *Enabling practical electrocatalyst-assisted photoelectron-chemical water splitting with earth abundant materials.* Nano Research, **2015**. 8(1): p. 56-81.
143. Bolton, J.R., Strickler, S.J. and Connolly, J.S., *Limiting and realizable efficiencies of solar photolysis of water.* Nature, **1985**. 316(6028): p. 495-500.
144. Gadgil, P.N., *Preparation of Iron Pyrite Films for Solar Cells by Metalorganic Chemical Vapor Deposition*. **1990**, Simon Fraser University. p. 241.
145. Gerischer, H., *On the stability of semiconductor electrodes against photodecomposition.* Journal of Electroanalytical Chemistry, **1977**. 82(1-2): p. 133-143.
146. Bard, A.J. and Wrighton, M.S., *Thermodynamic Potential for the Anodic Dissolution of n-Type Semiconductors.* J. Electrochem. Soc., **1977**. 124(11): p. 1706-1710.
147. Memming, R., *Semiconductor Electrochemistry*. 1st ed. **2001**: Wiley-VCH.
148. Sinn, C., Meissner, D. and Memming, R., *Charge Transfer Processes at WSe_2 Electrodes with pH-Controlled Stability.* Journal of The Electrochemical Society, **1990**. 137(1): p. 168-172.
149. van de Krol, R., *Photoelectrochemical Measurements,* in *Photoelectrochemical Hydrogen Production*, R. van de Krol and M. Grätzel, Editors. **2012**, Springer Science Business Media: New York, USA. p. 13-67.
150. Lopes, T., *Characterization and Phenomenoligal Modeling of Photoelectrochemical Cells for Hydrogen Production from Solar Energy*, in *Chemical Engineering Departement*. **2014**, University of Porto - FEUP: Porto.
151. Fre3energy. *Photoelectrochemical - Laboratory test cell: PORTOCell*. **November 2015**; Available from: http://www.redox-flow.com/.
152. Lopes, T., Dias, P., Andrade, L. and Mendes, A., *An innovative photoelectrochemical lab device for solar water splitting.* Solar Energy Materials and Solar Cells, **2014**. 128: p. 399-410.

153. Ding, I.K., Tétreault, N., Brillet, J., Hardin, B.E., Smith, E.H., Rosenthal, S.J., Sauvage, F., Grätzel, M. and McGehee, M.D., *Pore-Filling of Spiro-OMeTAD in Solid-State Dye Sensitized Solar Cells: Quantification, Mechanism, and Consequences for Device Performance.* Adv. Funct. Mater., **2009**. 19(19): p. 2431-2436.
154. Archer, M.D. and Nozik, A.J., *Nanostructured and photoelectrochemical systems for solar photon conversion*. Series on photoconversion of solar energy, v. 3. **2008**, London; Singapore; Hackensack, NJ: Imperial College Press ; World Scientific Pub. Co.
155. Hinsch, A., Kroon, J.M., Kern, R., Uhlendorf, I., Holzbock, J., Meyer, A. and Ferber, J., *Long-term stability of dye-sensitised solar cells.* Progress in Photovoltaics: Research and Applications, **2001**. 9(6): p. 425-438.
156. O'Hayre, R., Cha, S.-W., Colella, W. and Prinz, F.B., *Fuel cell fundamentals*. **2006**, New York: John Wiley & Sons. XXII, 409.
157. Barsoukov, E. and Macdonald, J.R., *Impedance spectroscopy : theory, experiment, and applications*. 2nd ed. **2005**, Hoboken, N.J.: Wiley-Interscience. 595
158. Andrade, L., *Study and characterization of Grätzel solar cells*, in *Chemical Engineering Departement*. **2010**, University of Porto - FEUP: Porto.
159. Barsoukov, E. and Macdonald, J.R., *Impedance Spectroscopy: Theory, Experiment and Applications*. Second ed. **2005**, New Jersey: John Wiley & Sons.
160. Andrade, L., Zakeeruddin, S.M., Nazeeruddin, M.K., Ribeiro, H.A., Mendes, A. and Grätzel, M., *Influence of Sodium Cations of* N_3 *Dye on the Photovoltaic Performance and Stability of Dye-Sensitized Solar Cells.* ChemPhysChem, **2009**. 10(7): p. 1117-1124.
161. Archer, M.D. and Nozik, A.J., *Nanostructured and Photoelectrochemical Systems for Solar Photon Conversion*. Series on Photoconversion of Solar Energy. **2008**, London: Imperial College Press.
162. Goldstein, J., *Scanning electron microscopy and x-ray microanalysis*. **2002**, New York: Kluwer Academic/Plenum Publishers.
163. Reimer, L., *Scanning electron microscopy: physics of image formation and microanalysis*. Springer series in optical sciences, 45. **1998**, Berlin [u.a.]: Springer.

164. Lucas, C.A., *8. Surface Structure Determination by Interference Techniques*, in *Surface Analysis: The Principal Techniques*, J.C. Vickerman and I. Gilmore, Editors. **2011**, Wiley. p. 686.
165. Watts, J.F. and Wolstenholme, J., *Electron Spectroscopy: Some Basic Concepts*, in *An Introduction to Surface Analysis by XPS and AES*. **2005**, John Wiley & Sons, Ltd. p. 1-15.
166. Ng, C., Ng, Y.H., Iwase, A. and Amal, R., *Influence of Annealing Temperature of* WO_3 *in Photoelectrochemical Conversion and Energy Storage for Water Splitting.* ACS Applied Materials & Interfaces, **2013**. 5(11): p. 5269-5275.
167. Hill, S.J., *Inductively coupled plasma spectrometry and its applications*. **2006**, Ames, Iowa: Blackwell Pub.
168. Miller, E.L., DeAngelis, A. and Mallory, S., *Multijunction Approaches to Photoelectrochemical Water Splitting*, in *Photoelectrochemical Hydrogen Production*, R.v.d. Krol and M. Graetzel, Editors. **2012**, Springer US. p. 205-273.

CHAPTER 2

TEMPERATURE EFFECT ON WATER SPLITTING USING A SI-DOPED HEMATITE PHOTOANODE

2

TEMPERATURE EFFECT ON WATER SPLITTING USING A SI-DOPED HEMATITE PHOTOANODE

Paula Dias, Tânia Lopes, Luísa Andrade and Adélio Mendes

Adapted from Journal of Power Sources, 2014, 272

ABSTRACT

The influence of temperature on the performance of a photoelectrochemical (PEC) cell using a Si-doped hematite photoanode was studied for water splitting. The cell performance was characterized by photocurrent-voltage (*J*-*V*) characteristic curves and electrochemical impedance spectroscopy at different cell operating temperatures, from 25 ºC to 65 ºC. A standard three-electrode configuration comprehending the photoelectrode of hematite, the counter electrode of pure platinum wire (99.9 %) and the reference electrode of Ag/AgCl/Sat. KCl was used. The identification of possible degradation pathways was addressed. It was observed that the generated photocurrent density increases with temperature. However, the photoelectrode became unstable above 50 ºC. The experiments performed concerning the study of the temperature effect and the aging showed that the optimal operation temperature of the PEC cell is *ca.* 45 ºC; this temperature ensures simultaneously the highest photocurrent density and stability. This study is particularly important for understanding the behavior of hematite photoelectrodes operating under real outdoor conditions.

Keywords: Photoelectrochemical Cell; Solar Water Splitting; Hematite Photoanodes; Temperature Effect; Aging Effect.

2.1 INTRODUCTION

Photoelectrochemical (PEC) cells for water splitting, as all other solar devices, are very sensitive to temperature. Two important works reporting the effect of temperature on photovoltaic parameters of solar cells were developed by Gupta *et al.* [1] and Sarswat *et al.* [2]. On Si-based solar cells, the temperature variations were intensively studied [3-6] and it was observed a decrease in the efficiency of the cell with temperature, mainly due to the decrease of the open-circuit voltage. According to the experimental investigations on several silicon cells, the output power decreases *ca.* 0.65 % per 1 K of temperature increase and the conversion efficiency decreases *ca.* 0.08 $\%\cdot K^{-1}$ [7]. For the organic solar cells, containing organic semiconductors such as polymer-fullerene [8], polyphenylene vinylene and copper phthalocyanine, the increase of temperature causes a monotonic increase of the short-circuit current (I_{sc}) and fill-factor (FF) and a linear decrease of the open-circuit voltage (V_{oc}) [9]. The overall result is an increase of the energy conversion efficiency at higher temperatures, reaching a maximum efficiency in the range of 47 ºC – 60 ºC [10]. Similar studies were developed for dye-sensitized solar cells (DSC) [11-13]. Up to normal operation temperatures (45 ºC – 50 ºC) it is observed a slight gain in I_{sc} due to more efficient electron diffusion on the TiO_2 film; on the other hand, at higher temperatures, the I_{sc} decreases due to an increased recombination rate [14]. The V_{oc} linearly decreases with temperature and, therefore, the energy efficiency dependence of the temperature is basically dominated by the I_{sc} and a maximum efficiency is reached for the normal operation temperatures [15-17].

In what concerns the study of the temperature effect on PEC cells for water splitting, there are only few works. Recently, Andrade *et al.* [18] simulated the effect of outdoor conditions (temperature and solar radiation variations) on the energy performance of the PEC cells. A linear increase of the current-density with temperature was observed for undoped hematite photoanodes. Lopes *et al.* [19] studied the energy performance at 25 ºC and 35 ºC of a PEC cell using a Si-doped hematite photoanode and an 8 % increase on the photocurrent density at 1.45 V_{RHE} was observed.

Knowing the output performance of PEC cells as a function of temperature is especially important since electrode kinetics, catalytic activity, charge transfer, photoelectrode quantum efficiency, electrode stability, ionic mobility, diffusion and conductivity in the electrolyte significantly vary with temperature [20]. Understanding the behavior of these parameters gain special interest for outdoor applications since the cells are subjected to severe changes in temperature. The aging tests can also give essential information concerning the stability over time of the overall PEC system and, in particular, the durability of the photoelectrodes. In PEC cells, stability issues is one of the major problem to be solved [21]. The stability of a semiconductor in contact with an electrolyte solution strongly depends on the competition between anodic dissolution and redox reaction, which are controlled by thermodynamic and kinetic parameters, respectively [22]. Indeed, predicting the PEC cells performance as a function of the temperature and corresponding photoelectrode stability are crucial for the development of commercial devices.

Among the stable and low-cost PEC systems under investigation, hematite (α-Fe_2O_3) photoanodes have been shown great potential for practical applications due to its good light absorption, abundance and photochemical stability. Hematite photoanodes were then selected to evaluate the influence of temperature on the performance of PEC cells. In the present work, the PEC cell was operated from 25 ºC to 65 ºC with steps of *ca.* 10 ºC. *J-V* characteristics were obtained in the dark and under 1-sun AM 1.5 G illumination conditions and electrochemical impedance spectroscopy tests were performed in the dark. Aging tests were also conducted at three different temperatures, 25 ºC, 45 ºC and 60 ºC, during 72 hours to analyze the stability of the PEC cell.

2.2 THEORY

Two temperature effects on photoelectrochemical cells can be anticipated: thermal bandgap narrowing of the photoanode and decrease of potential required for electrolysis of water. Semiconductors are materials in which the range of excitation energies is interrupted by an energy bandgap of width E_g. In the case of n-type semiconductors (photoanodes), the valence band (VB) is nearly completely occupied with electrons and the conduction band (CB) is nearly empty. In order to excite an electron from the VB to the CB by the absorption of a photon, it must equal at least the energy of the bandgap. As temperature increases the energy bandgap of a semiconductor reduces and the generated photocurrent tends to slightly increase since lower energy photons are absorbed [23]. The dependence of the bandgap energy with temperature (T) is given by the Varshni model [1]:

$$E_{\mathrm{g}}(T)=E_{\mathrm{g}}(0)-\frac{\alpha' T^2}{T+\beta'} \tag{2.1}$$

where E_{g} (0) is the bandgap of the semiconductor at 0 K, α’ is the limit of the gap entropy when $T\to\infty$ and β’ is expected to be comparable with the Debye temperature θ_{D} for a given material. A combination of a quadratic behavior, dominant in the low temperature range, with a linear behavior, dominant in the high temperature region, is expected [1].

A semiconductor operating at lower temperatures will have fewer available free electrons and holes for charge transport. At the same time, heating exponentially increases the intrinsic carrier population, n_{int}, given by [18]:

$$n_{\mathrm{int}}^2 \approx \exp\left(-\frac{E_{\mathrm{g}}}{k_{\mathrm{B}}T}\right) \tag{2.2}$$

where k_{B} is the Boltzman constant. This effect is enhanced by the decrease of the bandgap at higher temperatures – Equation (2.1). Mass transport is also favored by an increased temperature as stated by the Einstein relation [18]:

$$D_{\mathrm{i}}=\frac{k_{\mathrm{B}}T}{q}\mu_{\mathrm{i}} \tag{2.3}$$

where q is the elementary charge and μ_{i} is the mobility of species i.

However, increasing the temperature will also increase the current density produced by the PEC cell, as described by the Butler-Volmer equation [18]:

$$j_{\mathrm{cell}}=j_0\left[\frac{n_{\mathrm{H_2O}}(b)}{n_{\mathrm{H_2O}}^{\mathrm{ref}}(b)}\exp\left(\frac{\beta nq\eta_{\mathrm{Pt}}}{k_{\mathrm{B}}T}\right)-\frac{n_{\mathrm{H_2}}(b)n_{\mathrm{OH^-}}^2(b)}{n_{\mathrm{H_2}}^{\mathrm{ref}}(b)\left(n_{\mathrm{OH^-}}^{\mathrm{ref}}\right)^2(b)}\exp\left(\frac{-(1-\beta)nq\eta_{\mathrm{Pt}}}{k_{\mathrm{B}}T}\right)\right] \tag{2.4}$$

where j_0 is the exchange current density at the Pt counter electrode, n_{i} is the density of the species i in the reaction, n^{ref} is the reference particle density, n is the number of electrons transferred in the reaction, q is the elementary charge and η_{Pt} is the overpotential at the platinum counter electrode. The Butler-Volmer kinetics defines an exponential relation between the electric current crossing the electrolyte/platinum interface and the activation overpotential at the platinum cathode, where water is reduced to H_2 gas with the consumption of two electrons, n = 2 in Equation (2.4).

The temperature also influences the thermodynamics of a photoelectrochemical cell. The Nernst equation outlines how reversible electrochemical cell potential, E, varies as a function of species concentration and gas pressure [24]:

$$E = E^{o} - \frac{RT}{nF} \ln\left(\frac{\Pi a_{\text{products}}^{\nu_i}}{\Pi a_{\text{reactants}}^{\nu_i}} \right) \tag{2.5}$$

where E^{o} is the standard reversible potential, R is the ideal gas constant, F is the Faraday constant, a_i are the activities (concentrations or gas pressures) of the reactant and product species and ν_i are the stoichiometric coefficients. For accounting the temperature dependence, the Nernst equation should be modified [24]:

$$E = E^{o} + \frac{\Delta S}{nF}\left(T - T_0\right) - \frac{RT}{nF} \ln\left(\frac{\Pi a_{\text{products}}^{\nu_i}}{\Pi a_{\text{reactants}}^{\nu_i}} \right) \tag{2.6}$$

where ΔS is the standard entropy of the reaction (assumed to be temperature independent), T is the actual temperature of the system and T_0 is the ambient temperature. For the water splitting Equation (2.6) becomes:

$$E = E^{o} + \frac{\Delta S}{nF}\left(T - T_0\right) - \frac{RT}{nF} \ln\left(\frac{a_{H_2} a_{O_2}^{1/2}}{a_{H_2O}} \right) \tag{2.7}$$

Since the entropy variation is negative, the electrolysis potential decreases with temperature.

The overall solar-to-hydrogen (STH) conversion efficiency, η_{STH}, is a critical property of a PEC cell. However, there is no agreement on the equation that should be used to obtain the PEC cell efficiency. According to the US Department of Energy (DOE), the photoelectrochemical efficiency, η_{STH}, is defined as [25]:

$$\eta_{\text{STH}} = \frac{J_{\text{photo}} \times E_{\text{redox}} \times \eta_{\text{F}}}{P_{\text{light}}} \tag{2.8}$$

where J_{photo} is the generated photocurrent, E_{redox} is usually taken to be 1.23 V, based on a Gibbs free energy change for water splitting of 237 $\text{kJ}\cdot\text{mol}^{-1}$, η_{F} is the faradaic efficiency for hydrogen evolution and P_{light} is the incident sunlight illumination (usually 100 $\text{mW}\cdot\text{cm}^{-2}$ with 1-sun AM 1.5 G). The faradaic efficiency for the hydrogen evolution and oxygen evolution reactions is normally assumed to be unit, since the measured photocurrent corresponds to the molar generation of H_2, *i.e.* there are no parasite reactions [25]. Equation (2.8) describes the overall efficiency under zero bias conditions, which means that no external potential is applied between the working electrode (WE) and counter electrode (CE). When a bias is applied between the photo- and counter electrodes, a new efficiency definition is needed, named applied bias photon-to-current efficiency (ABPE) [25]:

$$\eta_{\mathrm{ABPE}} = \frac{J_{\mathrm{photo}} \times \left(E_{\mathrm{redox}} - \left| E_{\mathrm{bias}} \right| \right)}{P_{\mathrm{light}}} \tag{2.9}$$

where E_{bias} is the potential applied to obtain the J_{photo} [26]. This definition, however, is meaningless since it does not tell the efficiency that should be assigned to the photonic conversion nor to the electrical conversion; aberrations such as obtaining null efficiency for a bias of 1.23 V, where the photoelectrochemical contribution is to overcome the overpotentials, are then possible. To overcome this limitation, the authors propose a set of new definitions for the efficiency to be used in PEC devices. The first definition concerns the overall PEC device efficiency (η_{device}), given by the ratio between the energy of the produced hydrogen and the total energy spent to accomplish the water splitting reaction, namely solar energy and external bias:

$$\eta_{\mathrm{device}} = \frac{J_{\mathrm{photo}} \times E_{\mathrm{redox}}}{P_{\mathrm{light}} + \left(J_{\mathrm{photo}} \times E_{\mathrm{bias}} \right)} \tag{2.10}$$

Equation (2.10) says nothing concerning the efficiency of the photoelectrodes. The efficiency of a photoanode should translate its ability to convert photonic energy into chemical energy used for oxidizing water. The energy needed to promote electrons coming from the anode to actually reduce water at the counter electrode - the external bias - must not enter into this definition. The proposed definition for the photoactive electrode efficiency is then:

$$\eta_{\mathrm{photoelectrode}} = \frac{J_{\mathrm{photo}} \times \left(E_{\mathrm{redox}} - \left| E_{\mathrm{fb}} \right| \right)}{P_{\mathrm{light}}} \tag{2.11}$$

where E_{fb} is the flatband potential (note that this equation is valid either for photoanodes or photocathodes). The photoelectrode efficiency is then the energy of the produced hydrogen divided by the photonic energy supplied, assuming an external bias to provide the energy needed to bring the electron from the conduction band to the potential observed at the counter electrode.

2.3 EXPERIMENTAL

In the present work, temperature influence on solar-to-hydrogen efficiency and stability of the PEC cells for water splitting was analyzed. Five temperatures were studied (25 ºC, 35 ºC, 45 ºC, 55 ºC and 65 ºC); a reference experiment at 25 ºC was performed between experiments in order to check the Si-doped hematite photoanode stability. The preparation of photoanode materials, the experimental test bench and the PEC cell setup used to control the temperature, as well as the electrochemical measurements and the structural and morphological characterization of the PEC cells, are described in the following sections.

2.3.1 PREPARATION OF Si-DOPED α-Fe_2O_3 PHOTOANODES

The mesoporous films of silicon-doped hematite were deposited on conducting fluorine-doped tin oxide ($F:SnO_2$) glass substrates by ultrasonic spray pyrolysis (USP) as described elsewhere [27, 28]. The substrates were first pretreated with a diluted TEOS, tetraethyl orthosilicate, solution (10 % volume in ethanol) at *ca.* 400 ºC by hand-spraying *ca.* 3 mL per substrate of the diluted TEOS solution with a glass atomizer. These samples were cooled down to the room temperature before being heated up again at 400 ºC to deposit the hematite film. To prepare the hematite films, a solution containing 20 mM iron(III) acetylacetonate ($Fe(acac)_3$) in EtOH with 1 wt% TEOS as dopant was sprayed onto a temperature controlled substrate surface heated at 400 ºC with an ultrasonic spray nozzle from a distance of *ca.* 30 cm. A total of 60 sprays (one every 30 s) at a flowrate of 12 $mL\cdot min^{-1}$ (spray length of 5 s) were performed, corresponding to a final film thickness of *ca.* 50 nm. A carrier gas flow (compressed air flow set to 15 $L\cdot min^{-1}$) directed the spray towards the substrates. After the spray, the samples were annealed for 30 min at *ca.* 500 ºC before cooling to room temperature [27].

2.3.2 PREPARATION OF ELECTRIC CONTACT ON PHOTOANODES

To prevent the contact of the electrolyte solution with the electric current collector of the photoanode and thus inducing corrosion, the current collector at the glass substrate of the photoanode was protected with an epoxy resin resistant to high temperatures. A conductive insulated wire was glued to the current collector using the epoxy resin.

2.3.3 EXPERIMENTAL TEST BENCH

When a photoelectrochemical cell is exposed to real atmospheric conditions, solar radiation and temperature are the two main factors that affect its performance. Thus, it is of great importance to know how a PEC cell behaves at different temperatures. An experimental test bench with a temperature controlling system was designed and built – Figure 2.1.

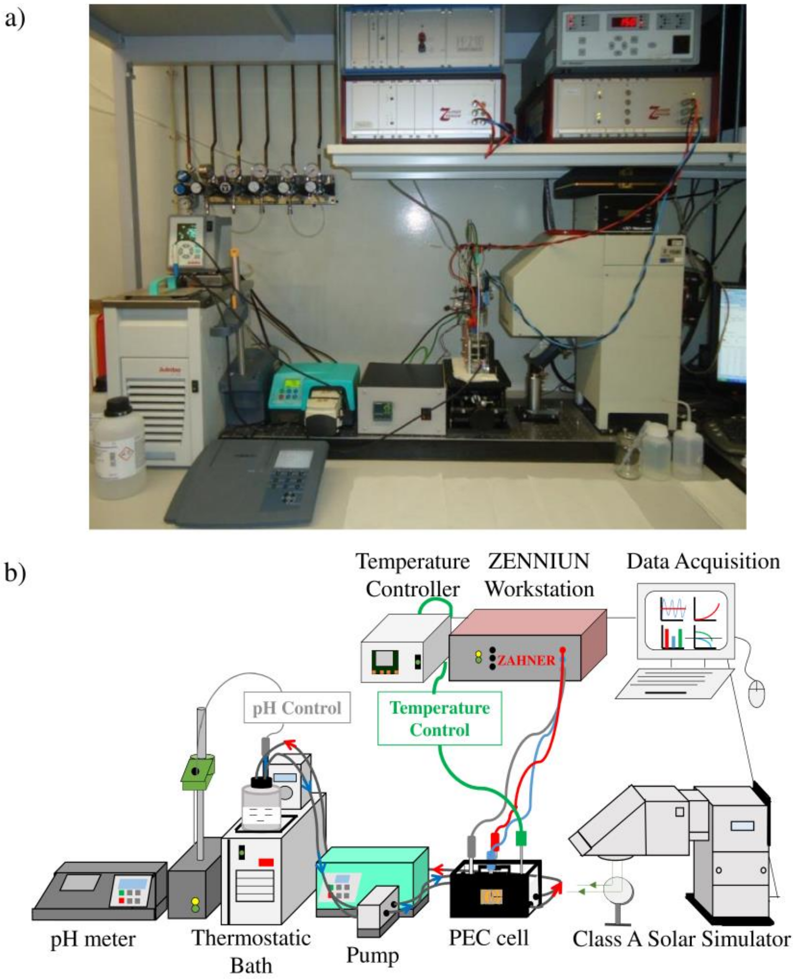

Figure 2.1: Test bench for PEC cell characterization at different temperatures: (a) photo of the actual setup; and (b) the corresponding scheme.

The electrolyte temperature was controlled using a water bath (Julabo, Germany) and the electrolyte was continuously pumped in and out of the PEC cell by a recirculation system, as sketched in Figure 2.1. The pH of the electrolyte was controlled using a compact pH meter (WTW, Deutschland). For a more precise temperature control, a rubber heater (Omega Engineering Inc., US & Canada) was stuck to a stainless steel window, which was fixed against a window made of Teflon. These three new parts were screwed to a transparent acrylic part and screwed to the cell – Figure 2.2. A Teflon coated thermocouple was placed inside the PEC cell contacting the electrolyte for reading the actual temperature; this temperature was used to control the rubber heater. The PEC cell configuration used is described elsewhere [29, 30].

A standard three-electrode configuration was used with the Si-doped α-Fe_2O_3 as photoanode, a 99.9 % pure platinum wire (Alfa Aesar, Germany) as counter electrode and an Ag/AgCl/Sat. KCl (Metrohm, Switzerland) as a reference electrode. Thus, two sample holders are used: one keeps the semiconductor vertically aligned and facing perpendicularly the light beam and the second one keeps the platinum wire aligned at the back of the sample. The distance between the holders is *ca.* 1 cm. The cell was filled with an electrolyte aqueous solution of 1 M NaOH (25 ºC, pH 14), being its maximum volume of *ca.* 125 mL. The total immersed photoanode area was 4 cm^2.

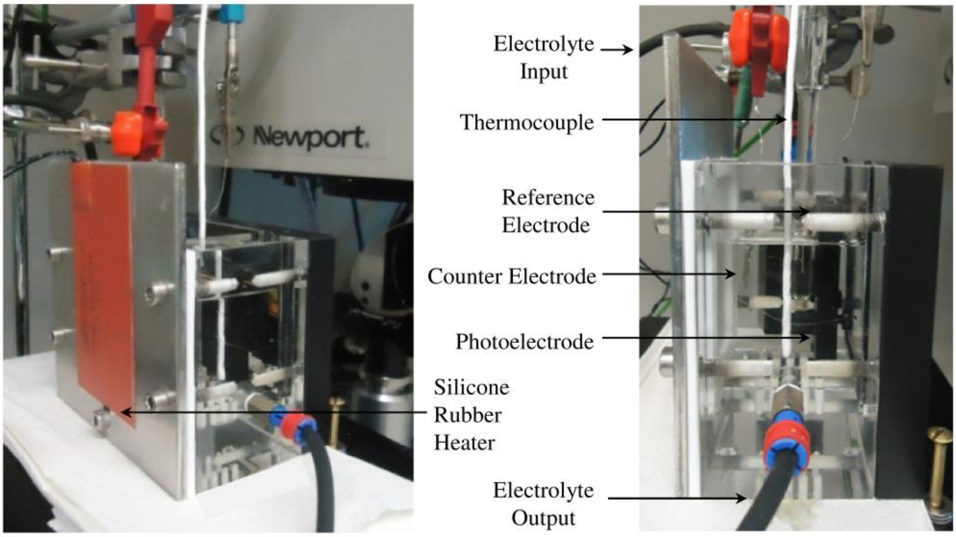

Figure 2.2: Detail of the PEC cell equipped with a rubber heater for temperature controlled measurements.

2.3.4 ELECTROCHEMICAL CHARACTERIZATION

J-V MEASUREMENTS

The photocurrent-voltage (*J-V*) characteristic curves were recorded applying an external potential bias to the cell and measuring the generated photocurrent using a ZENNIUM (Zahner Elektrik, Germany) workstation controlled by the Thales software package (Thales Z 1.0). The measurements were performed in the dark and under simulated sunlight (Oriel class B solar simulator equipped with a 150 W Xe lamp, Newport, USA), using an AM 1.5 G filter (Newport, USA), at a scan rate of 10 $mV·s^{-1}$ for the potential range between 0.6 V_{RHE} and 1.8 V_{RHE}. The light beam was calibrated with a c-Si photodiode. The potential was reported against the reversible hydrogen electrode (RHE).

EIS MEASUREMENTS

Electrochemical impedance spectroscopy (EIS) is a dynamic technique where a small potential sinusoidal perturbation is applied to the system and the amplitude and phase shift of the resulting current response are recorded. EIS spectra were obtained also with the ZENNIUM workstation in dark conditions. The frequency range used was 0.1 Hz – 100 kHz and the magnitude of the modulation signal was 10 mV [31]. The measurements were performed at 0.8 V_{RHE}, 1.0 V_{RHE}, 1.2 V_{RHE} and 1.4 V_{RHE}. A ZView software (Scribner Associates Inc., USA) was used to fit an appropriate electrical analog to the EIS spectra.

AGING TESTS

Aging tests consisted in applying a constant potential to the PEC cell over several hours and measure the resulting time-dependent photocurrent response. The photocurrent history of the selected semiconductors provides important information about the stability/corrosion of the semiconductor. The measurements were performed at a constant applied potential of *ca.* 1.23 V_{RHE} during several hours and under constant irradiation conditions (1-sun AM 1.5 G, *ca.* 100 $mW·cm^{-2}$).

2.3.5 SEM CHARACTERIZATION

Scanning electron microscope (SEM) was used to obtain information about morphology and surface topography of the photoelectrode materials. The morphology of the Si-doped hematite films was characterized using a high-resolution (50000× and 200000×) scanning electron microscope (Quanta 400 FEG, FEI Company, USA). The acceleration voltage was 15 keV while an in-lens detector was employed with a working distance of about 10 mm. The surface of the samples was investigated before and after performing the photoelectrochemical measurements and after performing the aging tests to assess modifications in the surface morphology. These analyses were made at CEMUP (Centro de Materiais da Universidade do Porto).

2.3.6 ICP ANALYSIS

The inductively coupled plasma (ICP) technique is based on atomic spectrometry and offers extremely high accuracy and precision. In the present work, ICP-MS (Mass Spectroscopy) was used to quantify all elements with masses between 5 and 250 au present in the electrolyte solutions. ICP-AES (Atomic Emission Spectroscopy) was also used to determine more accurately the concentration of iron in the 1 M NaOH electrolyte solutions. The electrolyte volume tested was *ca.* 50 cm^3.

2.4 RESULTS AND DISCUSSION

2.4.1 *J-V* MEASUREMENTS

Figure 2.3 shows the photocurrent density-voltage characteristic curves (*J-V*) of α-Fe_2O_3 photoanode doped with 5 % of silicon at five different temperatures, in the dark and under 1-sun AM 1.5 G illumination conditions. Before performing each *J-V* curve, the cell was left to stabilize for *ca.* 5 min. The performance of the cell increases with temperature – Figure 2.3.

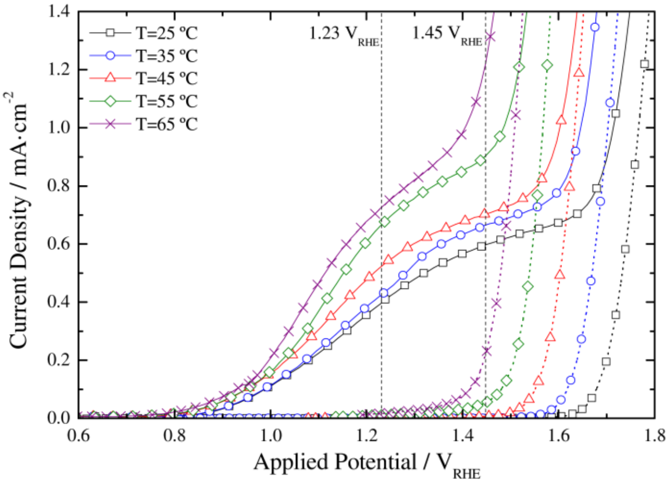

Figure 2.3: Photocurrent density-voltage (*J*-*V*) characteristics of Si-doped α-Fe_2O_3 photoanode at different temperatures, in the dark (dashed lines) and under 1-sun AM 1.5 G illumination (solid lines). (□) *T* = 25 ºC, (○) *T* = 35 ºC, (△) *T* = 45 ºC, (◊) *T* = 55 ºC, (×) *T* = 65 ºC.

At 25 ºC and under dark conditions, the current density rises steeply for a potential higher than 1.60 V_{RHE} – the so-called dark current corresponding to the electrocatalytic water oxidation onset potential. Under sunlight conditions at 25 ºC, the photocurrent density is 0.40 $mA\cdot cm^{-2}$ at the potential of reversible oxygen electrode (1.23 V_{RHE}), but it reaches a plateau only at *ca.* 1.45 V_{RHE} with a current of *ca.* 0.60 $mA\cdot cm^{-2}$. When the temperature of the electrolyte is increased to 35 ºC the dark current starts at *ca.* 1.55 V_{RHE}; the dark current starts earlier than for the experiment performed at 25 ºC. Under sunlight conditions the photocurrent density reaches 0.43 $mA\cdot cm^{-2}$ at 1.23 V_{RHE}, corresponding to an increase of almost 8 %. Following the same analysis, a temperature increase of 40 ºC (sample characterized at 65 ºC) originates an 83 % enhancement of the photocurrent density at 1.23 V_{RHE}, but the dark current onset happens at *ca.* 1.17 V_{RHE}.

Indeed, the photocurrent density of the PEC cell increases with temperature because the photoelectrode energy bandgap decreases and the charge transfer rate increases, *cf.* Equations (2.1) - (2.5). Moreover, the onset potential is shifted to lower potentials as the cell temperature increases, reducing the applied potential needed to initiate the water splitting reaction (bias). The influence of temperature on the energy conversion efficiency of the PEC cells is presented in Figure 2.4.

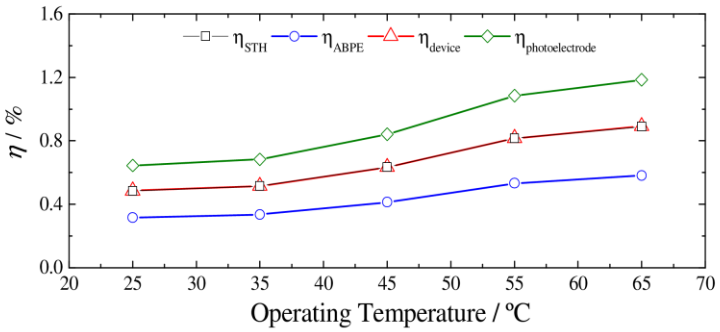

Figure 2.4: Efficiency results obtained for Si-doped α-Fe_2O_3 photoanode as a function of the operating temperature: (□) solar-to-hydrogen, η_{STH}, (○) applied bias photon-to-current", η_{ABPE}, (△) PEC device, η_{device}, (◊) photoanode, $\eta_{\mathrm{photoelectrode}}$.

The efficiencies η_{STH}, η_{ABPE}, η_{device} and $\eta_{\mathrm{photoelectrode}}$ were calculated using Equations (2.8), (2.9), (2.10) and (2.11), respectively. The faradaic efficiency in Equation (2.8) was assumed to be unit, since the measured photocurrent corresponds to the molar generation of H_2 without parasite reactions. For Equations (2.9), (2.10) and (2.11), the efficiencies were calculated for an external bias of 1.23 V_{RHE}. The incoming light considered was *ca.* 100 mW·cm^{-2} and the flatband potential for the Si-doped α-Fe_2O_3 photoelectrode was 0.40 V_{RHE}. The efficiency of the cell increases with temperature – *cf.* Figure 2.4. However, the maximum current density is limited also by the onset potential of the dark current, which decreases with temperature. This effect should be also taken into account, since it has a strong contribution on the generated photopotential. Considering that the photopotential is given by the potential shift between the light current and the dark current, when the internal resistance of the photoanode is small, the photopotential decreases with temperature and the highest decrease was observed for temperatures above 45 ºC. Moreover, reference tests at 25 ºC performed between runs revealed possible degradation of the photoanode after running the PEC cell at 55 ºC and 65 ºC, since it resulted in changes in the *J*-*V* curves at 25 ºC - see Figure 2.5. Therefore, the best operating temperature of the PEC cell should be *ca.* 45 ºC, where the performance is the highest, acceptable photopotential and dark current onset potential and no degradation were observed.

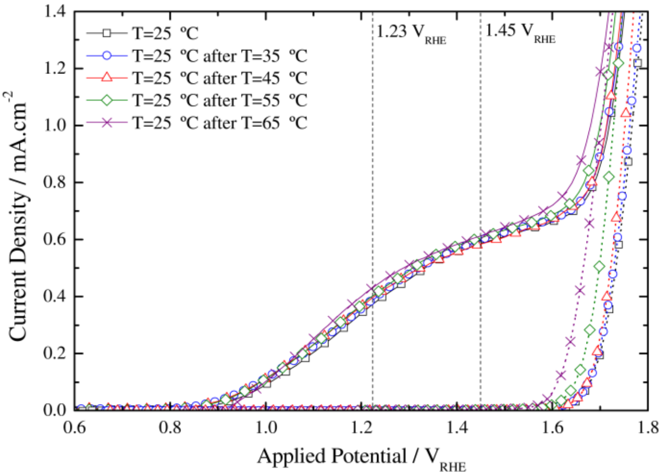

Figure 2.5: Reference tests performed at 25 °C between experiments and before increasing the temperature of the cell in the dark (dashed lines) and under 1-sun AM 1.5 G illumination (solid lines). (□) T = 25 °C, (○) T = 25 °C after T = 35 °C, (Δ) T = 25 °C after T = 45 °C, (◊) T = 25 °C after T = 55 °C, (×) T = 25 °C after T = 65 °C.

Figure 2.6 shows SEM images of the Si-doped α-Fe_2O_3 photoanode film, before and after performing the high-temperature tests. The sample area analyzed by SEM was made to coincide with the illuminated area during the different experiments. Actually, it was not noticed significant differences before and after running tests at 65 °C. Thus, the shift on the dark current onset was not due to modifications on the hematite structure. The electrolyte solution used in these experiments was analyzed by ICP-AES and only trace amounts of Fe were found: 0.113 mg·L^{-1}, 0.130 mg·L^{-1}, 0.202 mg·L^{-1} and 0.323 mg·L^{-1} for fresh solution and for tests performed at 25 °C, 45 °C and 65 °C, respectively. The iron concentration slightly increased, but the hematite sample did not suffer noticeable corrosion with the temperature tests as observed in Figure 2.6, which may induce that this modification cannot be responsible for such significant cathodic shift of the dark current onset potential with temperature. In order to pursue the comprehension of the such strong effect of temperature in the onset potential of the dark current, J-V curves of a bare transparent conductive oxide (TCO) glass substrate up to 65 °C were obtained – Figure 2.7.

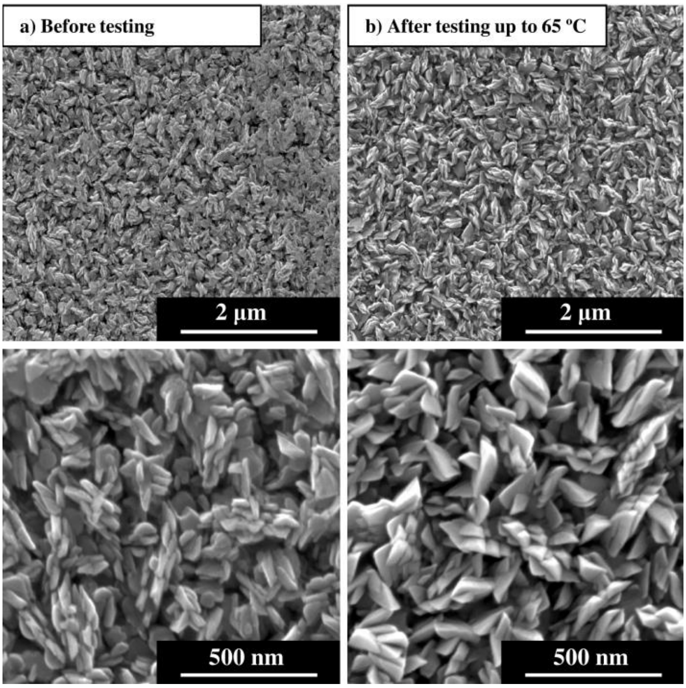

Figure 2.6: SEM images of Si-doped α-Fe_2O_3 film: (a) before and (b) after performing the temperature tests until *ca*. 65 ºC with different resolution (top: 50000×; bottom: 200000×).

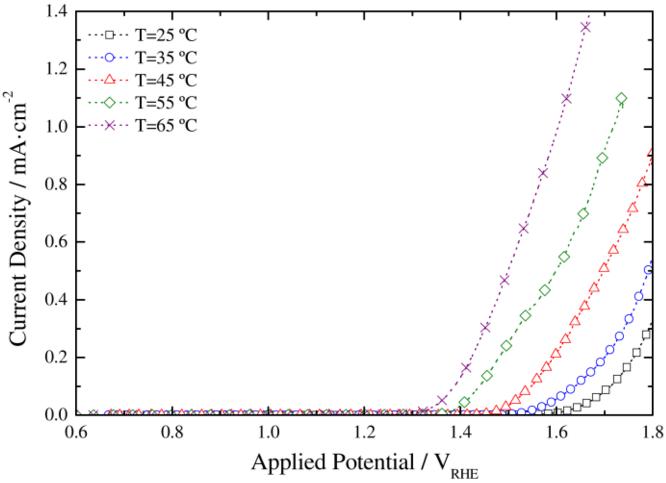

Figure 2.7: Temperature effect in the photocurrent density-voltage (*J*-*V*) characteristics of bare TCO substrate at a range of temperatures from 25 ºC to 65 ºC under dark conditions. (□) *T* = 25 ºC, (○) *T* = 35 ºC, (∆) *T* = 45 ºC, (◊) *T* = 55 ºC, (×) *T* = 65 ºC.

The dark current of the bare TCO substrate starts at lower onset potentials values as temperature increases, behavior similar to the one obtained for the hematite photoanodes (Figure 2.3). The reference *J-V* curves at 25 ºC performed after each run shows that the TCO substrate is being progressively damaged, which is more noticeable after tests at 55 ºC and at 65 ºC (Figure 2.8). This effect was also observed with the hematite photoanodes. So, the shift on the dark current onset should be assigned to the temperature effect on the TCO-glass substrate and not due to changes in the photoanode material [32].

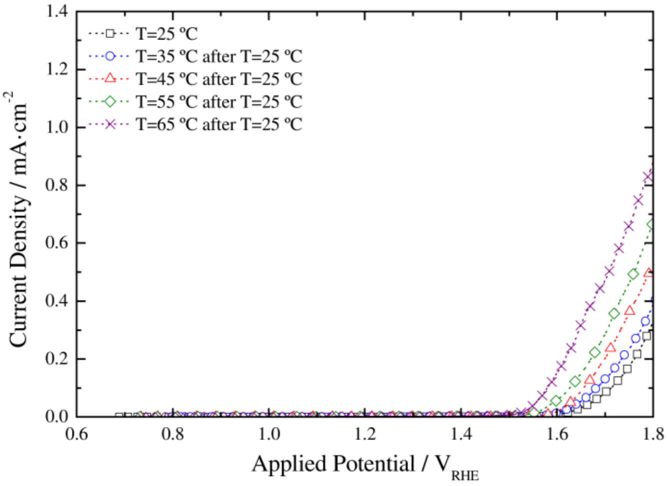

Figure 2.8: Reference tests performed at 25 ºC with the bare TCO substrate between experiments and before increasing the temperature of the cell under dark conditions. (□) *T* = 25 ºC, (○) *T* = 25 ºC after *T* = 35 ºC, (Δ) *T* = 25 ºC after *T* = 45 ºC, (◊) *T* = 25 ºC after *T* = 55 ºC, (×) *T* = 25 ºC after *T* = 65 ºC.

The morphology of the TCO substrates was studied using SEM – Figure 2.9. The surface of TCO exhibits sharp, well-defined blocky crystal grains of F:SnO_2 30-300 nm in size; however, after being tested at high temperatures (65 ºC), the surface crystal edges appear softer, *i.e.* without the same sharpness. Again the concentration of metals in the NaOH electrolyte solution that contacted with the bare TCO substrates was analyzed by ICP-MS. The concentration of fluorine in the electrolyte used at 65 ºC doubled, showing the possible degradation of the bare TCO made of fluorine doped tin oxide (FTO).

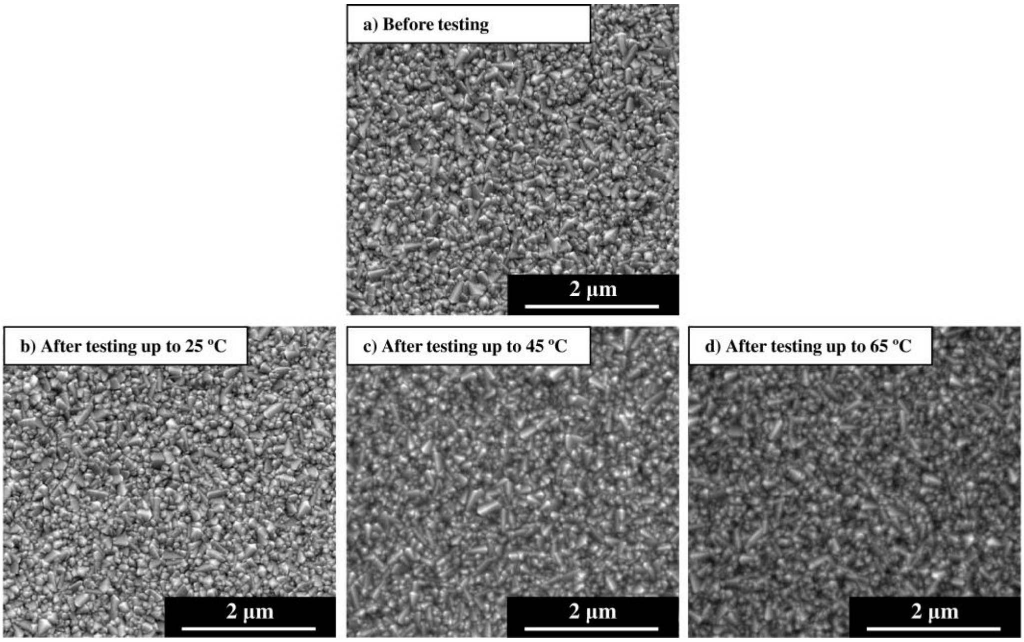

Figure 2.9: SEM images of TCO films before (a) and after performing the temperature tests at 25 ºC (b), 45 ºC (c) and 65 ºC (d).

Table 2.1 presents the concentrations of all elements detected in the solutions (25 ºC, 45 ºC and 65 ºC); these values are lower than 100 mg·L^{-1}, with the exception of sodium that exhibits values around 200 mg·L^{-1}.

Table 2.1: Metals concentration present in the electrolyte solution (1 M NaOH – pH 14) used for characterizing the TCO glass substrates at 25 ºC, 45 ºC and 65 ºC.

	Concentration of metals, mg·L^{-1}						
Tests	F	Sn	Al	Si	Na	Zn	Cu
TCO sample at 25 ºC	0.20	0.01	0.10	0.03	210	0.07	0.02
TCO sample at 45 ºC	0.20	0.01	0.10	0.04	210	0.08	0.03
TCO sample at 65 ºC	0.40	0.06	0.20	0.04	212	0.10	0.04

2.4.2 AGING TESTS

The stability of a PEC cell for water splitting is controlled by two factors: physical and chemical factors. Physical stability is related to electrolyte evaporation, which heats up under illumination. The chemical stability is associated to irreversible electrochemical and thermal degradation of the semiconductor and electrolyte [33]. The corrosion phenomena were investigated analyzing the content of iron in the electrolyte by ICP and the surface morphology of the photoelectrode by SEM. The measurements were performed at different temperatures (25 ºC, 45 ºC and 60 ºC) under constant 1-sun AM 1.5 G illumination, using an electrolyte solution of 1 M NaOH and applying a constant bias potential of 1.23 V_{RHE}. The photocurrent-density history was performed only up to 60 ºC, since a significant negative shift on dark current onset was observed at 55 ºC and higher temperatures; this shift compromises the maximum current density. Moreover, for higher temperatures the samples have no practical application for water splitting. Fresh photoelectrodes of Si-doped hematite with similar performances were used for each run, in a standard three-electrode configuration. The setup used is presented in Figure 2.1.

STABILITY AT 25 ºC

First, the stability performance was studied at 25 ºC during two periods of 72 h. Between the two testing periods, the photoelectrode was submitted to a heating treatment in an oven (1.5 $ºC\cdot min^{-1}$ to 400 ºC) [34] and the cell was filled with fresh electrolyte solution. Moreover, the hematite photoanode was analyzed in terms of photoelectrochemical performance by sweeping *J-V* scans in the dark and under simulated solar illumination. The corresponding *J-V* curves before and after running the two periods of stability tests are shown in Figure 2.10 (left-side).

The dark current density of the fresh hematite sample rises steeply for a potential higher than 1.55 V_{RHE}. Under simulated light conditions, the current density reaches a photocurrent value of *ca.* 0.22 $mA\cdot cm^{-2}$ at 1.23 V_{RHE}. Photocurrent density-time dependent experiments are plotted in Figure 2.10 (right-side) showing that the photocurrent density is acceptably stable over the time, with a performance decrease of *ca.* 9 % after 72 h and *ca.* 22 % after 144 h. This may indicate that some irreversible degradation occurs; however, the photoanode did not exhibit signs of visual degradation. SEM characterization revealed that the grain size of the hematite film becomes smaller due to chemical etching during the two periods of stability tests, Figure 2.11b *vs.* Figure 2.11a. Moreover, the iron concentration in the electrolyte solution was determined by ICP and it increased from 0.113 mg·L^{-1} to 0.416 mg·L^{-1}. Photocurrent values of 0.21 mA·cm^{-2} and 0.19 mA·cm^{-2} are obtained for aged cell after 72 h and 144 h under irradiated sunlight, respectively – Figure 2.10. Moreover, the dark current rose for negative potentials, from 1.55 V$_{RHE}$ to 1.45 V$_{RHE}$ for the aged sample.

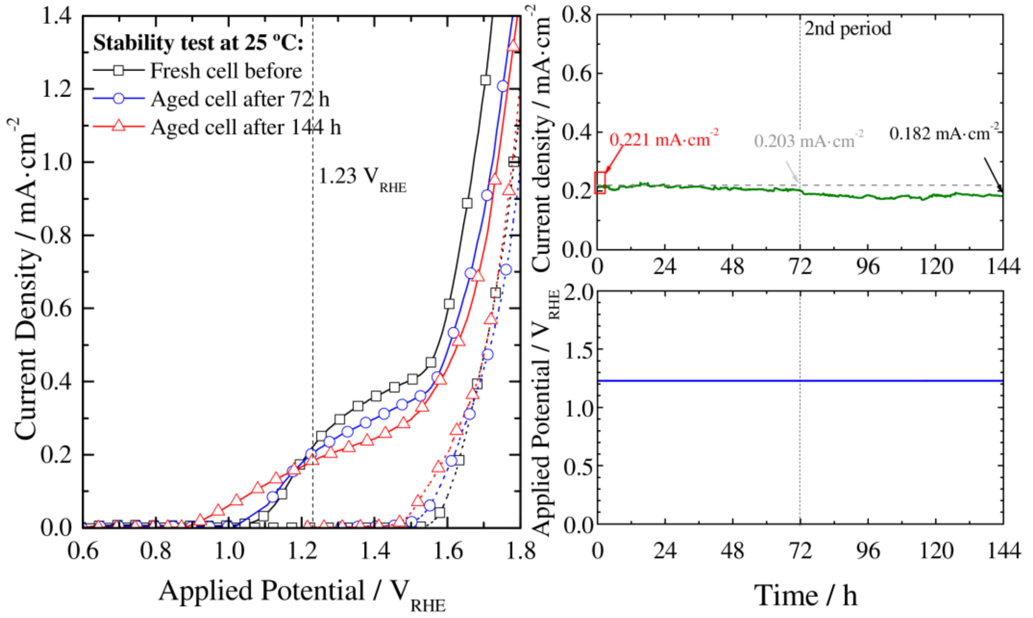

Figure 2.10: Left-side: Photocurrent density-voltage (*J*-*V*) characteristic curves of the Si-doped α-Fe_2O_3 photoanode tested in the dark (dashed lines) and under 1-sun simulated light at 25 ºC (solid lines) before and after the stability test. (□) fresh cell before stability, (○) aged cell after 1st period of stability, (Δ) aged cell after 2nd period of stability. Right-side: Correspondent photocurrent history at a constant potential of *ca.* 1.23 V$_{RHE}$ and continuous 1-sun AM 1.5 G illumination at 25 ºC.

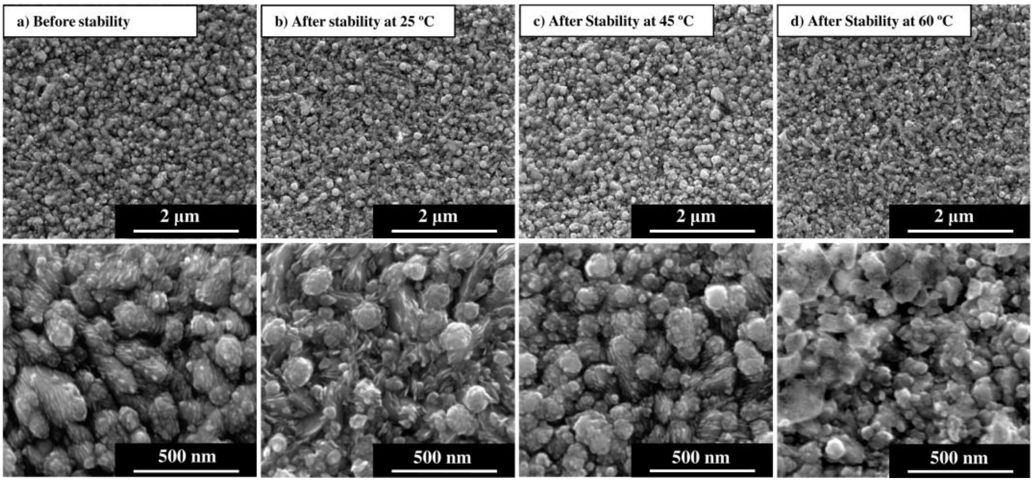

Figure 2.11: SEM images of Si-doped α-Fe_2O_3 film before (a) and after performing the stability tests with a constant potential of 1.23 V_{RHE} and continuous 1-sun AM 1.5 G illumination at three different temperatures: 25 ºC (b), 45 ºC (c) and 60 ºC (d). (Top: 50000×; bottom: 200000×).

STABILITY AT 45 ºC

Figure 2.12 (left-side) shows the *J-V* characteristics obtained before and after performing 72 h single period stability test at 45 ºC. The photocurrent density for the fresh sample increases from of 0.20 mA·cm^{-2} to 0.27 mA·cm^{-2} at 1.23 V_{RHE}, respectively from 25 ºC to 45 ºC. After, the photocurrent density history was obtained for the temperature of 45 ºC – Figure 2.12 (right-side). The photocurrent density is mostly stable over the first 60 hours with an average photocurrent value of 0.26 mA cm^{-2}. However, after 72 h of stability test, a decay of *ca.* 9 % in photocurrent was observed. No significant changes in the surface morphology of the sample were observed by SEM – Figure 2.11c. The iron concentration in the electrolyte increased from *ca.* 0.113 mg·L^{-1} to 0.150 mg·L^{-1} after the stability test.

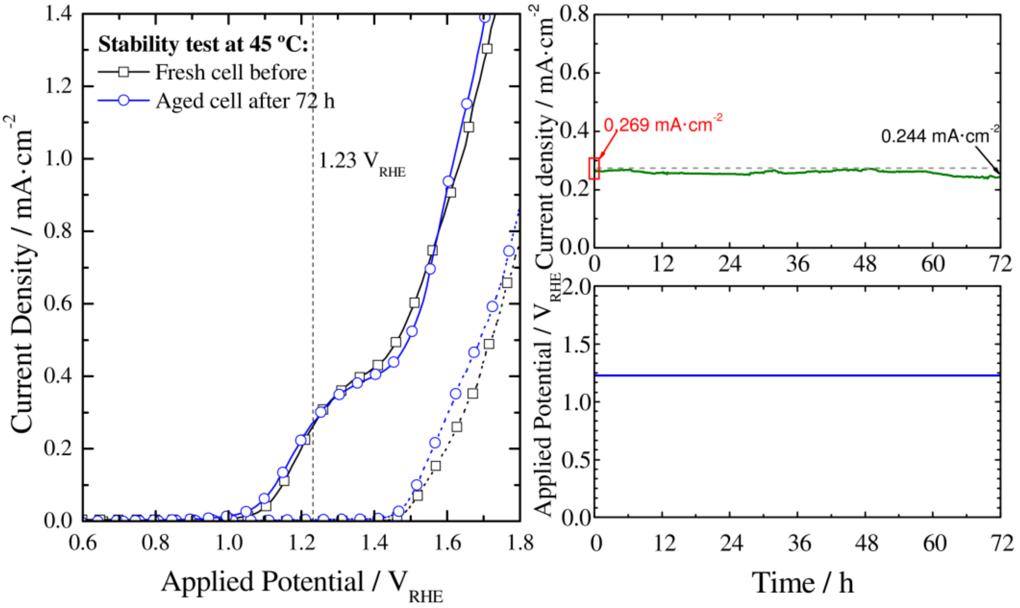

Figure 2.12: Left-side: Photocurrent density-voltage (*J*-*V*) characteristic curves of the Si-doped α-Fe_2O_3 photoanode tested in the dark (dashed lines) and under 1-sun simulated light at 45 ºC (solid lines) before and after stability. (□) fresh cell, (○) aged cell after 72 h of stability. Right-side: Correspondent photocurrent history at a constant potential of *ca.* 1.23 V_{RHE} and continuous 1-sun AM 1.5 G illumination at 45 ºC.

STABILITY AT 60 ºC

Figure 2.13 (left-side) shows the *J-V* curves at 25 ºC and 60 ºC, in the dark and under simulated solar illumination, before and after performing the 72 h stability test at 60 ºC. The fresh sample exhibited a photocurrent density of 0.18 mA·cm^{-2} at 25 ºC and increased to 0.35 mA·cm^{-2} at 60 ºC, for an external bias of 1.23 V_{RHE}. The photocurrent density of the photoelectrode at 60 ºC was mostly stable up to 30 h, decreasing afterwards to 0.19 mA·cm^{-2} – Figure 2.13 (right-side).

After the aging tests, the photoanode sample exhibited some visual signs of degradation in the illuminated area, suggesting that corrosion phenomena took place. SEM images of the fresh and aged hematite sample are shown in Figure 2.10d. The aged sample exhibits a corroded surface with not well-defined grains and an overlapping structure of particles with smaller sizes. The electrolyte solution contained

1.130 mg·L^{-1} of iron (electrolyte initial iron concentration was 0.113 mg·L^{-1}), the highest value obtained for the studied electrodes.

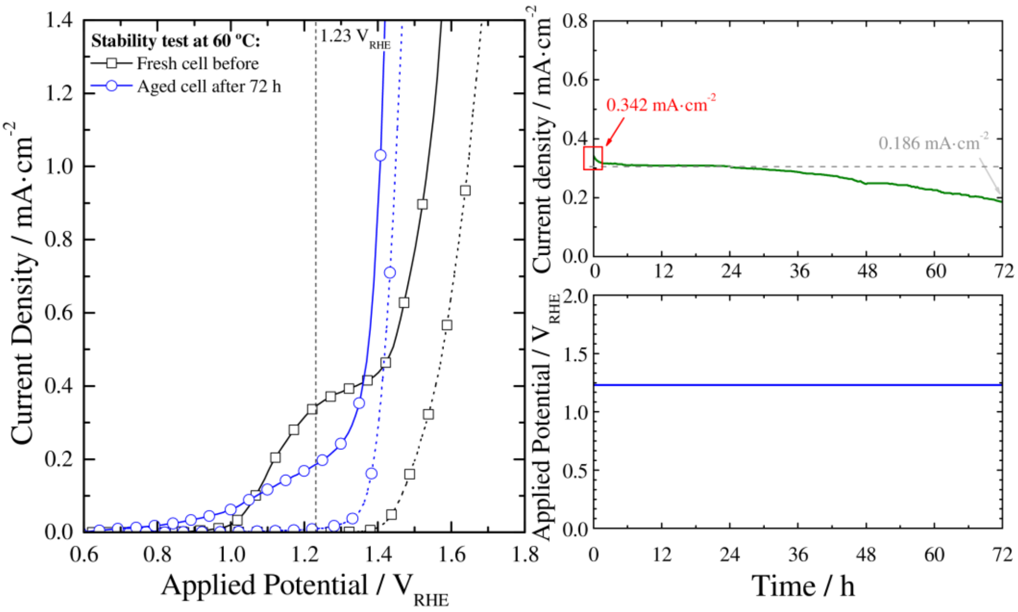

Figure 2.13: Left-side: Photocurrent density-voltage (*J*-*V*) characteristic curves of the Si-doped α-Fe_2O_3 photoanode tested in the dark (dashed lines) and under 1-sun simulated light at 60 ºC (solid lines) before and after stability. (□) fresh cell, (○) aged cell after 72 h of stability. Right-side: Correspondent photocurrent history at a constant potential of *ca.* 1.23 V_{RHE} and continuous 1-sun AM 1.5 G illumination at 60 ºC.

2.4.3 *EIS* MEASUREMENTS

A three-electrode configuration was used to obtain information about the charge transfer kinetics at the semiconductor/electrolyte interface since the potential was measured with respect to a fixed reference potential, short-circuited with the counter electrode [29]. The impedance spectra were obtained after performing the *J*-*V* characteristics of the hematite photoelectrode at the selected temperatures, *i.e.* from 25 ºC to 65 ºC with steps of 10 ºC. For each operating temperature, the charge transport resistances and the charge transfer at the interface of the photoelectrode/electrolyte of the PEC cell were obtained by fitting the EIS data to an electrical analogue – Figure 2.14.

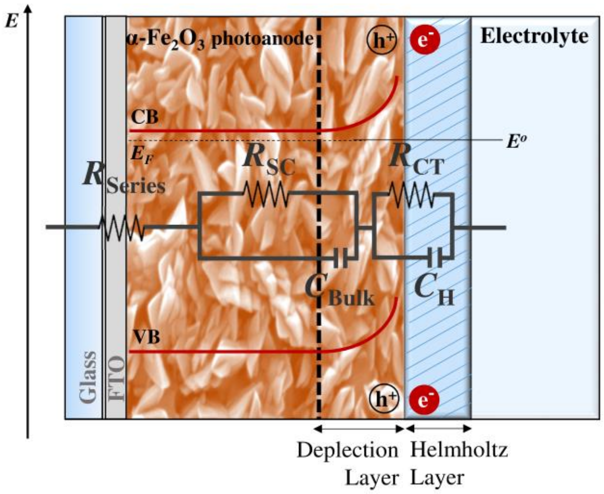

Figure 2.14: Electrical circuit analogue used to fit the experimental impedance data.

Under dark conditions, the proposed electrical analogue considers a series resistance element, R_{Series}, and two RC elements in series: the first RC element models the electron transport in the semiconductor bulk, where R_{SC} is the semiconductor charge resistance and C_{SC} is the capacitance at the space charge layer on the semiconductor side; the second RC element represents the charge transfer resistance at semiconductor/electrolyte interface, where R_{CT} is the charge transfer resistance and C_H is the capacitance at the Helmholtz layer on the electrolyte side. The low-frequency response was assigned to the phenomena occurring in the semiconductor/electrolyte interface, whereas the high-frequency range was assigned to the faster electronic processes occurring in the semiconductor bulk. Moreover, in photoelectrodes formed by nanostructured semiconductors, the capacitance element is not ideal, showing a constant phase element (CPE) behavior [35]. Figure 2.15 shows the Nyquist plots obtained at an applied potential of 0.8, 1.0, 1.2 and 1.4 V_{RHE} under dark conditions.

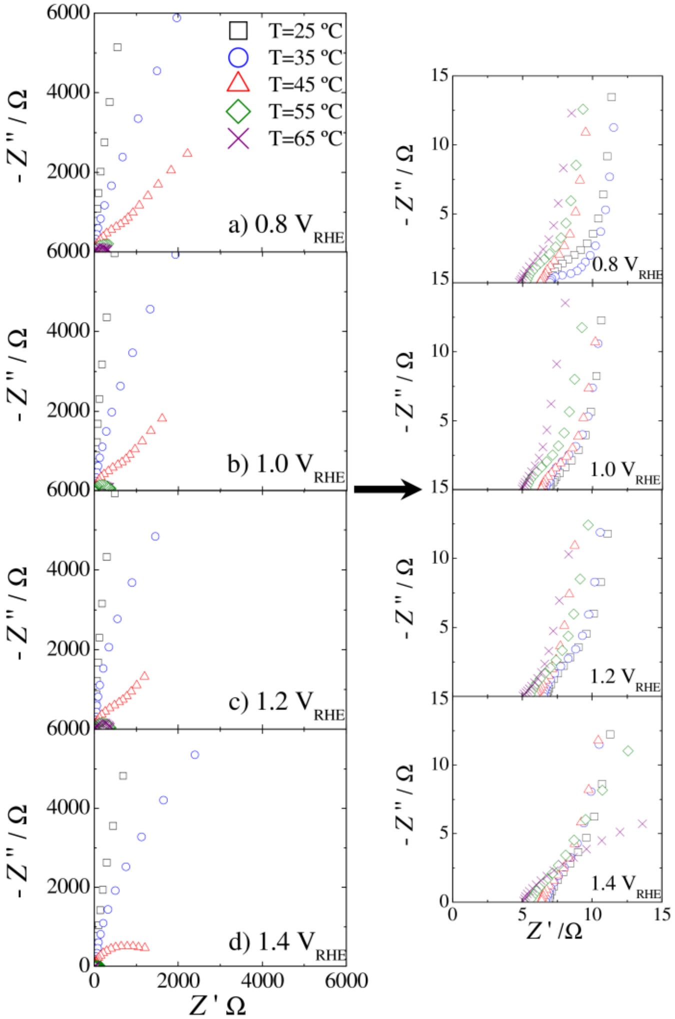

Figure 2.15: Nyquist diagrams for a Si-doped α-Fe_2O_3 photoanode obtained in the dark at different temperatures and forward biases: (a) 0.8 V_{RHE}; (b) 1.0 V_{RHE}; (c) 1.2 V_{RHE}; and (d) 1.4 V_{RHE}. Z': real impedance, Z'': imaginary impedance; (□) T = 25 ºC, (○) T = 35 ºC, (△) T = 45 ºC, (◊) T = 55 ºC, (×) T = 65 ºC. On the right-side is a zoom-out of the left-side plots.

The overall charge transfer resistance of the PEC system ($R_{Series} + R_{SC} + R_{CT}$) decreases with temperature for all applied potentials, explaining the overall increase of the photocurrent density with temperature. Two semicircles can be clearly distinguished (see inset of Figure 2.15): one responding in the high frequencies range and the larger one responding in the low frequencies range. In fact, the low frequencies range semicircle decreases considerably with the temperature, being this decrease more obvious at higher temperatures (55 ºC and 65 ºC). Thus, the temperature increase strongly influences the phenomena occurring at the semiconductor/electrolyte interface.

Figure 2.16 shows the impedance parameters for an applied potential of 1.2 V_{RHE} as a function of the operating temperature. The potential of 1.2 V_{RHE} was selected since it is the closest potential to the reversible oxygen electrode potential (1.23 V_{RHE}).

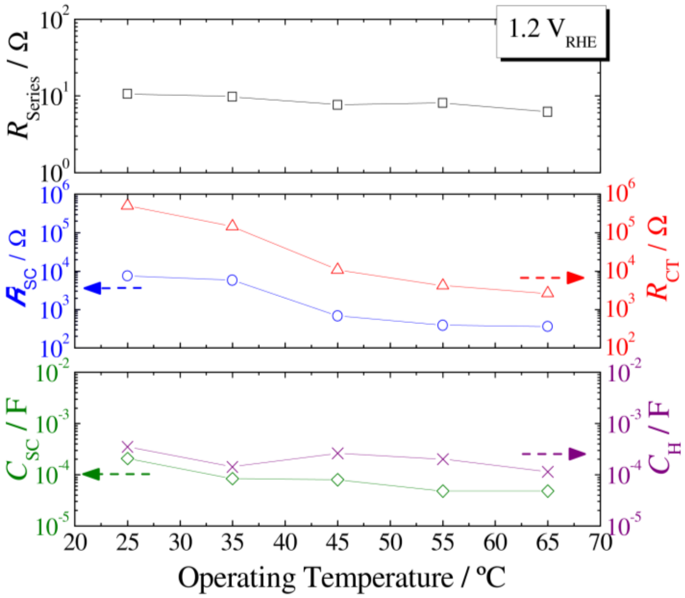

Figure 2.16: Impedance results obtained by fitting the experimental data shown in Figure 2.15 for an applied potential of 1.2 V_{RHE} as a function of the operating temperature. (□) Series Resistance – R_{Series}, (○) Bulk Semiconductor Resistance – R_{SC}, (Δ) Charge Transfer Resistance – R_{CT}, (◊) Space Charge Capacitance – C_{SC}, (×) Helmholtz Capacitance – C_H.

From Figure 2.16 the series resistance, R_{Series}, decreases from 10.7 Ω to 6.2 Ω when temperature increases from 25 ºC to 65 ºC; this decrease is more pronounced at 55 ºC and at 65 ºC. R_{Series} comprises the TCO layer resistance and the external contacts resistance (*e.g.* wire connections); since the environment temperature around the external contacts did not change, the main contributor to R_{Series} is the TCO resistance.

The electrical resistance of the bulk semiconductor, R_{SC}, should decrease with temperature since faster electron transport is noticed [36, 37]; however, the highest decrease was observed at 45 ºC with R_{SC} presenting 7.0 × 10^2 Ω - see Figure 2.16. In fact, at *ca.* 60 ºC the photoelectrode degrades with time, as observed from stability tests at 60 ºC – Figure 2.13. Thus, for temperatures above or equal to 55 ºC the semiconductor matrix starts degrading, which should lead to stabilize the bulk resistance. Indeed, the behavior of the charge transport resistance in the bulk semiconductor with the temperature is the result of a balance between the photocurrent and the stability. Concerning the charge transfer resistance, R_{CT}, it decreases from 5.1×10^5 Ω to 2.7×10^3 Ω for the temperature range, also leveling out above 45 ºC. The level out of the charge transfer resistance should be related to the degradation of the semiconductor that may be losing electrocatalytic activity. Indeed, it was found fluorine and tin in the electrolyte, probably resulting from the degradation of the TCO made of fluorine doped tin oxide (FTO).

The capacitances values were also plotted as a function of the operating temperatures in Figure 2.16. The Helmholtz capacitance (C_H) remains almost temperature independent (values in the order of magnitude of 10^{-4} F) and the space charge capacitance (C_{SC}) decreases with temperature. Though, a slightly increase for both capacitances is observed at 45 ºC with 8.0×10^{-5} F and 2.6×10^{-4} F for C_{SC} and C_H, respectively. As R_{SC} decreases, the charge flow increases and, therefore, the thickness of the space charge layer decreases thereby justifying the C_{SC} increase at around 45 ºC, since the capacitance is inversely proportional to the thickness of the layer. The C_H values are higher than the C_{SC} values, since the Helmholtz double layer width is generally smaller than the width of the depletion layer [38, 39]. This is the typical behavior of these capacitances for photo-assisted water splitting systems. Moreover, since the hematite semiconductor is doped with silicon, Si^{4+} acts as an electron donor improving its electrical conductivity and, at the same time, reducing the width of the space charge layer that contributes to an increase of the C_{SC} [40]. In the case of heavily doped semiconductors, C_{SC} will be of the same order as C_H [41].

Figure 2.17 shows the Nyquist diagrams of three hematite photoanodes aged at different temperatures: 25 ºC (a), 45 ºC (b) and 60 ºC (c) and for an applied potential of 1.2 V_{RHE}.

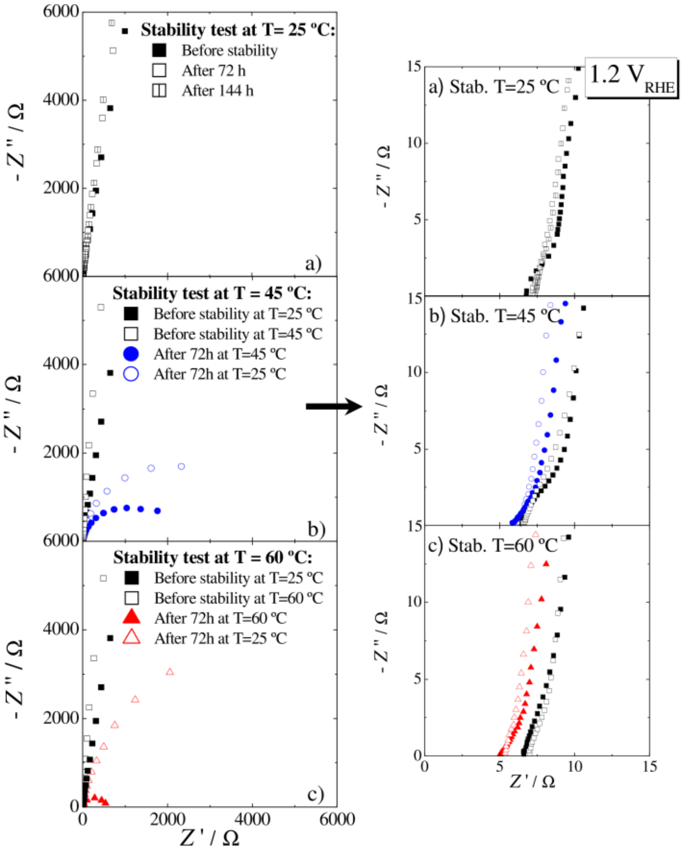

Figure 2.17: Nyquist diagrams for a Si-doped α-Fe_2O_3 photoanode obtained in the dark with an applied potential of 1.2 V_{RHE} at aged temperatures of 25 ºC (a), 45 ºC (b) and 60 ºC (c). $Z\,'$: real impedance; $Z\,''$: imaginary impedance.

The first semicircle in the high frequency range, which is ascribed to the electron transfer process in the bulk semiconductor, is not clearly visible in the inset of Figure 2.17. Though, the overall resistances tend to be smaller with time, being this behavior more evident as the temperature of stability test increases. After performing the stability test at 25 ºC, the sample did not reveal significant differences for the frequency range studied, even after 144 h of testing - Figure 2.17a. For the sample tested at 45 ºC during 72 h, the low-frequencies arc, assigned to the charge transfer in the semiconductor/electrolyte interface, becomes larger with the aging time, as shown in Figure 2.17b. From Figure 2.17c is visible different behaviors at the two frequency regions, which proves that a higher temperature (60 ºC) influences the stability of the electrode. Then, the electrical analog presented in Figure 2.14 was used to fit the impedance data and the corresponding resistance and capacitance parameters were determined – Figure 2.18.

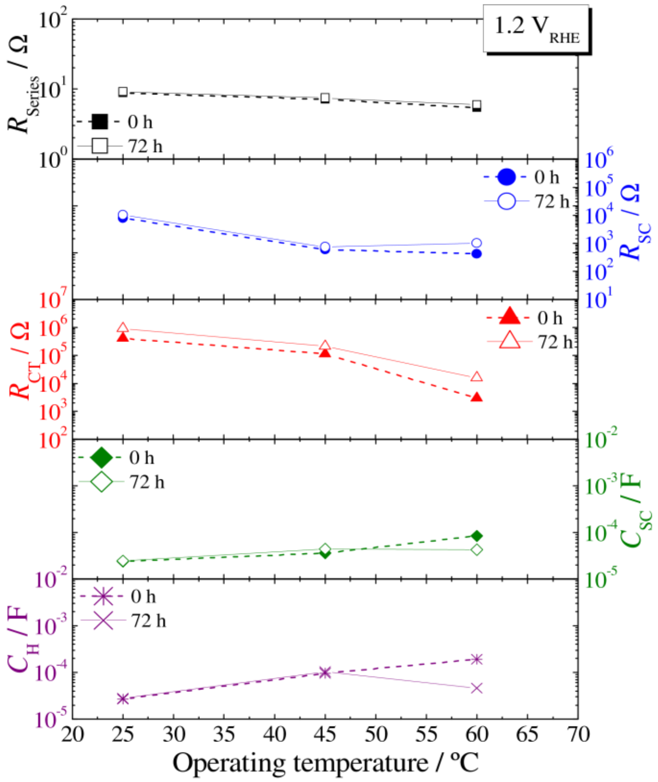

Figure 2.18: Impedance results obtained by fitting the experimental data shown in Figure 2.17 for an applied potential of 1.2 V$_{RHE}$ before (filled symbols) and after (open symbols) performing the stability tests during 72 h at three different temperatures: 25 ºC, 45 ºC and 65 ºC. (□) Series Resistance – R_{Series}, (○) Bulk Semiconductor Resistance – R_{SC}, (Δ) Charge Transfer Resistance – R_{CT}, (◊) Space Charge Capacitance – C_{SC}, (×) Helmholtz Capacitance – C_H.

Figure 2.18 shows the resistances and capacitances obtained for fresh and aged hematite photoanodes. The series resistance slightly increases from 5.4 Ω to 6.0 Ω after 72 h of stability test, being the highest increase observed at 60 ºC. This series resistance change was assigned to the decrease of the TCO conductivity. Concerning the bulk semiconductor resistance, a significant variation from 4.2×10^2 Ω to 1.0×10^3 Ω was verified for the experiment performed at 60 ºC. This behavior is due to degradation of hematite photoanode with time – *cf.* Figure 2.13. Similarly, the charge transfer resistance at the semiconductor/electrolyte interface increased with time and the major change was observed again at 60 ºC, since the deterioration of the semiconductor limits the charge transfer at the semiconductor/electrolyte interface. R_{CT} increased from *ca.* $3.0 \times 10^3\ \Omega$ to $1.6 \times 10^4\ \Omega$ after running 72 h of stability test at 60 ºC.

Finally, both C_{SC} and C_H are mostly constant during the stability tests at 25 ºC and 45 ºC. At 60 ºC the capacitances tend to decrease with aging time: C_{SC} decreased from $8.4 \times 10^{-5}\ \Omega$ to $4.3 \times 10^{-5}\ \Omega$ and C_H decreased from $1.9 \times 10^{-5}\ \Omega$ to $4.7 \times 10^{-5}\ \Omega$, respectively. The hematite photoelectrode at 60 ºC showed surface corrosion, which should be related to the decrease of generated charges and further decrease of accumulated charges. These results confirm that 45 ºC is the highest temperature before the hematite photoelectrode start to corrode, simultaneously producing the highest photocurrent density.

2.5 CONCLUSIONS

A study of the temperature effect on the performance of a photoelectrochemical cell for water splitting with hematite photoelectrodes was reported. *J-V* characteristic curves and EIS measurements were used to investigate the temperature- and time-induced changes in the PEC cells behavior. Understanding this behavior is especially important for the development of commercial devices, since the cells are subjected to severe changes in temperature under outdoor applications. The PEC device composed by Si-doped α-Fe_2O_3 photoanodes in a standard three-electrode configuration was tested from 25 ºC to 65 ºC with steps of 10 ºC. The results showed that the global performance of the PEC cell increases with temperature. A 33 % increase on the photocurrent density at 1.23 V_{RHE} was observed when the temperature was increased from 25 ºC to 45 ºC. On the other hand, an 83 % increase was obtained for the test temperature of 65 ºC, but here the dark current onset starts at *ca.* 1.17 V_{RHE}, before the potential of reversible oxygen electrode (1.23 V_{RHE}).

The effect of temperature on the dark current can be explained by the effect of temperature on TCO substrate, *i.e.* as temperature increases the onset potential tends to occur at negative potentials. Indeed, the very thin hematite layer employed allows the electrolyte to access to the TCO layer and this phenomenon increases with the operating temperature. The photocurrent density history (stability tests) at different temperatures (25 ºC, 45 ºC and 60 ºC) was obtained for fresh photoelectrodes during 72 h. Photoelectrode corrosion was observed at 60 ºC and, as a consequence, the current density decreased *ca.* 46 % after the aging period. The best operation conditions were obtained for 45 ºC with improved energy performance and sufficient stability. The impedance analysis also indicates that increasing the temperature makes the overall charge transfer resistance in the semiconductor/electrolyte interface of the cell to decrease. Additionally, the EIS spectra at 60 ºC for fresh and 72 h aged sample evidenced significant loss of activity.

ACKNOWLEDGMENTS

P. Dias and T. Lopes are grateful to the Portuguese Foundation for Science and Technology (FCT) for their PhD fellows (references: SFRH/BD/81016/2011 and SFRH/BD/62201/2009, respectively). L. Andrade acknowledges European Research Council for funding within project BI-DSC – Building Integrated Dye sensitized Solar Cells (Contract number: 321315). The authors acknowledge also the European Commission for funding (Project NanoPEC - Nanostructured Photoelectrodes for Energy Conversion; contract number 227179) and the Portuguese Foundation for Science and Technology (FCT) through the project H2Solar (PTDC/EQU-EQU/104217/2008). The authors are also very thankful to Professor Michael Grätzel and his group from LPI-EPFL for providing the Si-doped α-Fe_2O_3 photoelectrodes.

REFERENCES

1. Gupta, L., Rath, S., Abbi, S.C. and Jain, F.C., *Temperature dependence of the fundamental band gap parameters in cadmium-rich* $Zn_xCd_{1-x}Se$ *using photoluminescence spectroscopy.* Pramana, **2003**. 61(4): p. 729-737.
2. Sarswat, P.K. and Free, M.L., *A study of energy band gap versus temperature for* Cu_2ZnSnS_4 *thin films.* Physica B: Condensed Matter, **2012**. 407(1): p. 108-111.
3. Radziemska, E. and Klugmann, E., *Thermally affected parameters of the current–voltage characteristics of silicon photocell.* Energy Conversion and Management, **2002**. 43(14): p. 1889-1900.
4. Radziemska, E., *Effect of temperature on dark current characteristics of silicon solar cells and diodes.* International Journal of Energy Research, **2006**. 30(2): p. 127-134.
5. Singh, P., Singh, S.N., Lal, M. and Husain, M., *Temperature dependence of I–V characteristics and performance parameters of silicon solar cell.* Solar Energy Materials and Solar Cells, **2008**. 92(12): p. 1611-1616.
6. Wen, C., Fu, C., Tang, J., Liu, D., Hu, S. and Xing, Z., *The influence of environment temperatures on single crystalline and polycrystalline silicon solar cell performance.* SCIENCE CHINA Physics, Mechanics & Astronomy, **2012**. 55(2): p. 235-241.
7. Radziemska, E., *The effect of temperature on the power drop in crystalline silicon solar cells.* Renewable Energy, **2003**. 28(1): p. 1-12.
8. Thompson, B.C. and Fréchet, J.M.J., *Polymer–Fullerene Composite Solar Cells.* Angewandte Chemie International Edition, **2008**. 47(1): p. 58-77.
9. Hoppe, H. and Sariciftci, N.S., *Organic solar cells: An overview.* Journal of Materials Research, **2004**. 19(07): p. 1924-1945.
10. Paulauskas, I.E., Jellison, G.E. and Boatner, L.A., *Photoelectrochemical properties of n-type* $KTaO_3$ *single crystals in alkaline electrolytes.* Journal of Materials Research, **2010**. 25(01): p. 52-62.
11. Sebastian, P.J., Olea, A., Campos, J., Toledo, J.A. and Gamboa, S.A., *Temperature dependence and the oscillatory behavior of the opto-electronic properties of a dye-sensitized nanocrystalline* TiO_2 *solar cell.* Solar Energy Materials and Solar Cells, **2004**. 81(3): p. 349-361.

12. Berginc, M., Opara Krasovec, U., Jankovec, M. and Topic, M., *The effect of temperature on the performance of dye-sensitized solar cells based on a propyl-methyl-imidazolium iodide electrolyte.* Solar Energy Materials and Solar Cells, **2007**. 91(9): p. 821-828.
13. Snaith, H.J., Schmidt-Mende, L., Grätzel, M. and Chiesa, M., *Light intensity, temperature, and thickness dependence of the open-circuit voltage in solid-state dye-sensitized solar cells.* Physical Review B, **2006**. 74(4): p. 045306.
14. Liu, Z., Shen, S. and Guo, L., *Study on photocatalytic performance for hydrogen evolution over CdS/M-MCM-41 (M = Zr, Ti) composite photocatalysts under visible light illumination.* International Journal of Hydrogen Energy, **2012**. 37(1): p. 816-821.
15. Berginc, M., Opara Krašovec, U., Hočevar, M. and Topič, M., *Performance of dye-sensitized solar cells based on Ionic liquids: Effect of temperature and iodine concentration.* Thin Solid Films, **2008**. 516(20): p. 7155-7159.
16. Toivola, M., Peltokorpi, L., Halme, J. and Lund, P., *Regenerative effects by temperature variations in dye-sensitized solar cells.* Solar Energy Materials and Solar Cells, **2007**. 91(18): p. 1733-1742.
17. Raga, S.R. and Fabregat-Santiago, F., *Temperature effects in dye-sensitized solar cells.* Physical Chemistry Chemical Physics, **2013**. 15(7): p. 2328-2336.
18. Andrade, L., Lopes, T. and Mendes, A., *Dynamic Phenomenological Modeling of Pec Cells for Water Splitting Under Outdoor Conditions.* Energy Procedia, **2012**. 22: p. 23-34.
19. Lopes, T., Dias, P., Andrade, L. and Mendes, A., *E-MRS/MRS Bilateral Energy Conference Innovative Technological Configurations of Photoelectrochemical Cells.* Energy Procedia, **2012**. 22: p. 35-40.
20. Esposito, D.V., Goue, O.Y., Dobson, K.D., McCandless, B.E., Chen, J.G.G. and Birkmire, R.W., *A new photoelectrochemical test cell and its use for a combined two-electrode and three-electrode approach to cell testing.* Review of Scientific Instruments, **2009**. 80(12): p. 125107.
21. Krol, R., Liang, Y. and Schoonman, J., *Solar Hydrogen Production with Nanostructured Metal Oxides.* Journal of Materials Chemistry, **2008**. 18(20): p. 2311-2320.
22. Memming, R., *Semiconductor Electrochemistry*. 1st ed. **2001**: Wiley-VCH.

23. Nelson, J., *Analysis of the p-n Junction*, in *The Physics of Solar Cells*. **2003**, Imperial College Press. p. 145-176.
24. O'Hayre, R., Cha, S.-W., Colella, W. and Prinz, F.B., *Fuel cell fundamentals*. **2006**, New York: John Wiley & Sons. XXII, 409.
25. Chen, Z., Jaramillo, T.F., Deutsch, T.G., Kleiman-Shwarsctein, A., Forman, A.J., Gaillard, N., Garland, R., Takanabe, K., Heske, C., Sunkara, M., McFarland, E.W., Domen, K., Miller, E.L., Turner, J.A. and Dinh, H.N., *Accelerating materials development for photoelectrochemical hydrogen production: Standards for methods, definitions, and reporting protocols.* J. Mater. Res., **2010**. 25(01): p. 3-16.
26. Krol, R., *Introduction*, R. van de Krol and M. Grätzel, Editors. **2012**, Springer US. p. 3-12.
27. Formal, F.L., Grätzel, M. and Sivula, K., *Controlling Photoactivity in Ultrathin Hematite Films for Solar Water-Splitting.* Advanced Functional Materials, **2010**. 20(7): p. 1099-1107.
28. Duret, A. and Gratzel, M., *Visible Light-Induced Water Oxidation on Mesoscopic* α*-*Fe_2O_3 *Films Made by Ultrasonic Spray Pyrolysis.* The Journal of Physical Chemistry B, **2005**. 109(36): p. 17184-17191.
29. T. Lopes, L.A., A. Mendes, *Photoelectrochemical Cells for Hydrogen Production from Solar Energy*, in *Solar Energy Sciences and Engineering Applications*, N.E.A. Akbarzadeh, Editor. **2013**, CRC Press. p. 293–341.
30. Lopes, T., Dias, P., Andrade, L. and Mendes, A., *An innovative photoelectrochemical lab device for solar water splitting.* Solar Energy Materials and Solar Cells, **2014**. 128: p. 399-410.
31. Dotan, H., Sivula, K., Gratzel, M., Rothschild, A. and Warren, S.C., *Probing the photoelectrochemical properties of hematite (*α*-*Fe_2O_3*) electrodes using hydrogen peroxide as a hole scavenger.* Energy & Environmental Science, **2011**. 4(3): p. 958-964.
32. Dias, P., Lopes, T., Meda, L., Andrade, L. and Mendes, A., *Photoelectrochemical water splitting using* WO_3 *photoanodes: the substrate and temperature roles.* Physical Chemistry Chemical Physics, **2016**. 18(7): p. 5232-5243.

33. Hinsch, A., Kroon, J.M., Kern, R., Uhlendorf, I., Holzbock, J., Meyer, A. and Ferber, J., *Long-term stability of dye-sensitised solar cells.* Progress in Photovoltaics: Research and Applications, **2001**. 9(6): p. 425-438.
34. Sivula, K., Zboril, R., Le Formal, F., Robert, R., Weidenkaff, A., Tucek, J., Frydrych, J. and Grätzel, M., *Photoelectrochemical Water Splitting with Mesoporous Hematite Prepared by a Solution-Based Colloidal Approach.* Journal of the American Chemical Society, **2010**. 132(21): p. 7436-7444.
35. Lopes, T., Andrade, L., Le Formal, F., Gratzel, M., Sivula, K. and Mendes, A., *Hematite photoelectrodes for water splitting: evaluation of the role of film thickness by impedance spectroscopy.* Physical Chemistry Chemical Physics, **2014**. 16(31): p. 16515-16523.
36. Wang, Q., Ito, S., Grätzel, M., Fabregat-Santiago, F., Mora-Seró, I., Bisquert, J., Bessho, T. and Imai, H., *Characteristics of High Efficiency Dye-Sensitized Solar Cells†.* The Journal of Physical Chemistry B, **2006**. 110(50): p. 25210-25221.
37. Lu, N., Ji, A. and Cao, Z., *Nearly Constant Electrical Resistance over Large Temperature Range in Cu3NMx (M = Cu, Ag, Au) Compounds.* Sci. Rep., **2013**. 3: p. 3090.
38. Nozik, A.J., *Photoelectrochemistry: Applications to Solar Energy Conversion.* Annual Review of Physical Chemistry, **1978**. 29(1): p. 189-222.
39. Aruchamy, A., Aravamudan, G. and Subba Rao, G., *Semiconductor based Photoelectrochemical Cells for Solar Energy Conversion - An overview.* Bulletin of Materials Science, **1982**. 4(5): p. 483-526.
40. Cesar, I., Kay, A., Gonzalez Martinez, J.A. and Gratzel, M., *Translucent Thin Film* Fe_2O_3 *Photoanodes for Efficient Water Splitting by Sunlight: Nanostructure-Directing Effect of Si-Doping.* Journal of the American Chemical Society, **2006**. 128(14): p. 4582-4583.
41. Le Formal, F., Tetreault, N., Cornuz, M., Moehl, T., Gratzel, M. and Sivula, K., *Passivating surface states on water splitting hematite photoanodes with alumina overlayers.* Chemical Science, **2011**. 2(4): p. 737-743.

CHAPTER 3

PHOTOELECTROCHEMICAL WATER SPLITTING USING TUNGSTEN TRIOXIDE PHOTOANODES: THE SUBSTRATE AND TEMPERATURE ROLES

3

PHOTOELECTROCHEMICAL WATER SPLITTING USING TUNGSTEN TRIOXIDE PHOTOANODES: THE SUBSTRATE AND TEMPERATURE ROLES

Paula Dias, Tânia Lopes, Laura Meda, Luísa Andrade and Adélio Mendes

Adapted from Physical Chemistry Chemical Physics, 2016, 18(7)

ABSTRACT

The influence of the substrate on the performance of WO_3 photoanodes is assessed as a function of the temperature. Two samples were studied: WO_3 deposited on a FTO glass and anodized on a tungsten foil. Photocurrent-voltage curves and electrochemical impedance spectroscopy measurements were used to characterize these samples between 25 ºC and 65 ºC. The photocurrent density increased with temperature for both samples and the onset potential shifted to lower potentials. However, for WO_3/FTO, a negative shift of the dark current onset was also observed. The intrinsic resistivity of this substrate limits the photocurrent plateau potential range. On the other hand, this behavior was not observed for WO_3/metal. Therefore, the earlier dark current onset observed for WO_3/FTO was assigned to the FTO layer. The optimal operating temperatures observed were 45 ºC and 55 ºC for WO_3/FTO and WO_3/metal, respectively. For higher temperatures, the bulk electron-hole recombination phenomenon greatly affects the overall performance of WO_3 photoanodes. The stability behavior was then studied at these temperatures over 72 h. For WO_3/FTO, a crystalline-to-amorphous phase transformation occurred during the stability test, which may justify the current decrease observed after the aging period. The WO_3/metal remained stable, maintaining its morphology and good crystallinity. Interestingly, the preferential orientation of the aged crystals was shifted to the (-222) and (222) planes, suggesting that this was responsible for its better and more stable performance. These findings provide crucial information for allowing further developments on the preparation of WO_3 photoanodes, envisaging their commercial application in PEC water splitting cells.

Keywords: Photoelectrochemical Cells; Water Splitting; Temperature Effect; Aging Tests; Tungsten Trioxide Photoanodes; FTO Layer; Tungsten Foil.

3.1 INTRODUCTION

For scaling up the photoelectrochemical (PEC) hydrogen generation technology it is not only necessary to find efficient and stable semiconductor materials and to use a versatile PEC cell reactor, but also to understand the behavior of the cell under real outdoor conditions [1, 2]. The performance of the PEC cells for water splitting should vary essentially as a function of solar irradiance and temperature. Depending on the operating environment (indoor/outdoor applications, geographical location and specific time of the year), temperatures ranging between subzero to near 70 ºC can be expected [3]. Despite, only few works have reported the temperature dependence on the PEC cells performance. Mendes *et al.* [4] simulated the effect of outdoor conditions (temperature and solar radiation variations) on the energy performance of PEC cells. A linear increase of the photocurrent density with the temperature was observed and the maximum production of hydrogen occurred between 11:00 AM and 1:00 PM (solar time) for undoped hematite photoanodes. Recently, the same group studied the combined effect of temperature variations (from 25 ºC to 65 ºC) and the aging behavior of a PEC system using Si-doped hematite photoanodes. The results showed a photocurrent density increase with temperature; however, taking into account performance and stability the optimal operation temperature of the PEC cell was *ca.* 45 ºC. This study also evidenced that the temperature influences the behavior of the bare transparent conducting oxide (TCO) layer, which exhibits an earlier dark current onset potential for higher temperatures [5].

TCO films have been extensively used as a transparent electrode for optoelectronic device applications, *e.g.* for solar cells [6, 7]. Besides the conductivity and transparency, the main requirements of TCO coatings are the electronic compatibility with adjacent layers in the electrodes and the stability under operating conditions. From the common TCO materials, fluorine doped tin oxide (FTO), indium tin oxide (ITO) and aluminum doped zinc oxide (AZO), only FTO is stable in acidic/alkaline environments [8]. In PEC devices, the photoelectrode materials are mostly deposited onto glasses previously covered with a TCO thin layer to assure a transparent photoelectrode. The development of a transparent semiconductor will allow to transmit the fraction of solar radiation not absorbed by the material and to convert it by other photosystems, improving their overall energy performance. On the other hand, when the transparency is not important, the metal substrate can be a potential alternative for TCO glass substrates. Metal has the advantages of cost-effectiveness, excellent mechanical flexibility and thermal stability in the industrial fabrication processes. Furthermore, metal has high conductivity and good dimensional stability during the processing at elevated temperature [9].

The present study aims to evaluate the effect of temperature on the performance of PEC water splitting cells equipped with tungsten trioxide (WO_3) n-type semiconductors. In particular, the main goal of this work is to understand if the photoelectrode substrate plays a critical role on the PEC devices behavior with temperature. Nanostructured WO_3 semiconductor was selected due to its close to optimal bandgap (E_g = 2.5 - 2.7 eV) able to capture *ca.* 12 % of the solar spectrum, moderate hole diffusion length (*ca.* 150 nm) and good chemical stability in acidic aqueous solutions under solar illumination, as well as easy and cheap preparation procedures [10, 11]. The morphology (*e.g.* shape, size and porosity) and crystallinity of WO_3 nanoparticles depend critically on preparation parameters and annealing temperatures, being also limiting factors for PEC cell performance [12-14]. Herein, the WO_3 photoanodes were prepared using two types of substrates: glass covered with a FTO layer and tungsten metal substrate, *i.e.* WO_3 were deposited by doctor blade on the FTO glass substrate and anodized on a tungsten metal foil.

An experimental setup was developed to control the temperature inside the PEC device, allowing its characterization as a function of the temperature. Five temperatures were considered, equally spaced from 25 ºC to 65 ºC, and the correspondent current-voltage (*J*-*V*) characteristic curves were obtained in dark and under 1-sun AM 1.5 G illumination ($100\,mW\cdot cm^{-2}$) conditions. Electrochemical impedance spectroscopy (EIS) measurements were also performed in dark to extract detailed information concerning the charge transfer and accumulation processes occurring in the PEC cell and how they are related to its performance at different temperatures. Aging tests were then conducted for both samples at their best operating temperature during several hours for assessing their stability. Scanning electron microscopy (SEM) and X-ray diffraction (XRD) analysis were carried out to compare the morphology and crystallinity of the WO_3 films under study with the performance of the PEC cell.

3.2 EXPERIMENTAL

The temperature effect on the performance of water splitting cells using tungsten trioxide photoanodes was studied. The PEC cell was operated from 25 ºC to 65 ºC with steps of 10 ºC. A reference test at 25 ºC was always performed between experiments in order to check the photoanode behavior under reference operating conditions. The WO_3 photoanodes were prepared using two types of substrates, FTO glass and tungsten foil; their deposition techniques are described in detail hereafter. The experimental test bench with the PEC cell setup used to control the temperature and the photoelectrochemical measurements are described. Moreover, the stability of these photoanodes was assessed at their best operating temperature (45 ºC for WO_3/FTO and 55 ºC for WO_3/metal) and their structural and morphological characterization before and after aging tests were also studied.

3.2.1 PHOTOANODE MATERIALS PREPARATION

WO_3 PHOTOELECTRODE ON FTO GLASS SUBSTRATE (coded hereafter as WO_3/FTO)

The WO_3 photoelectrodes were deposited onto FTO (TEC 8, 8 $\Omega\cdot\text{square}^{-1}$) glass substrate by the blade-spreading method at Institute ENI Donegani (Novara, Italy), following the procedure named Synt-1, as described elsewhere [15]. Briefly, tungstic acid was obtained by passing 5 mL of an aqueous Na_2WO_4 solution (10 wt%, Carlo–Erba) through a proton exchange resin (Amberlite IR120H) and the eluted solution was collected in 5 mL of ethanol to slow down the tungstic acid condensation. To the resulting colloidal dispersion, 0.5 g of organic dispersing agent was added and stirred until complete dissolution. WO_3 photoanodes were prepared by blade-spreading the resulting H_2WO_4 colloidal precursor on FTO glass substrates. The resulting films were annealed at 550 ºC in air for 2 h [15].

WO_3 PHOTOELECTRODE ON W METAL SUBSTRATE (coded hereafter as WO_3/METAL)

The WO_3 photoelectrode on a tungsten foil substrate was prepared by the anodization method at Institute ENI Donegani (Novara, Italy), as described elsewhere [16]. The tungsten foil, prior to anodization, was carefully cleaned with acetone and ethanol and sonicated in an Alconox/water solution to remove surface contaminants and oily or greasy impurities. Then, the WO_3 photoanodes were prepared by applying a potential difference of 40 V (Aim-TTi EX752M DC power supply) across the two tungsten foils, which were kept at a distance of about 3 mm. To avoid electrode corrosion, care was taken to reach the final 40 V in about 1 min. This way, a passivation compact oxide was formed during the initial stages of anodization. The total duration of anodization was 5 h in a thermostatic bath at 40 ºC [17]. At the end it was made a sintering at 500 ºC in air for 1 h to ensure the formation of a nanocrystalline layer (monoclinic phase).

3.2.2 EXPERIMENTAL SETUP

To study the temperature effect on the PEC cell performance, an experimental test bench with a temperature controlling system was designed and built, as previously reported by the same group [5]. Briefly, the electrolyte temperature was controlled using a thermostatic water bath (Julabo model ME, Germany) and the electrolyte pH was monitored using a pH meter (Inolab pH/Cond 740, WTW GmbH, Germany). The PEC cell used has a continuous electrolyte feeding system, described in detail elsewhere [2]. Moreover, a thermocouple was placed inside the cell and a rubber heater was stuck to its back to ensure the desired temperature. Figure 3.1 shows the experimental setup used to analyze the behavior of the PEC cell at different temperatures.

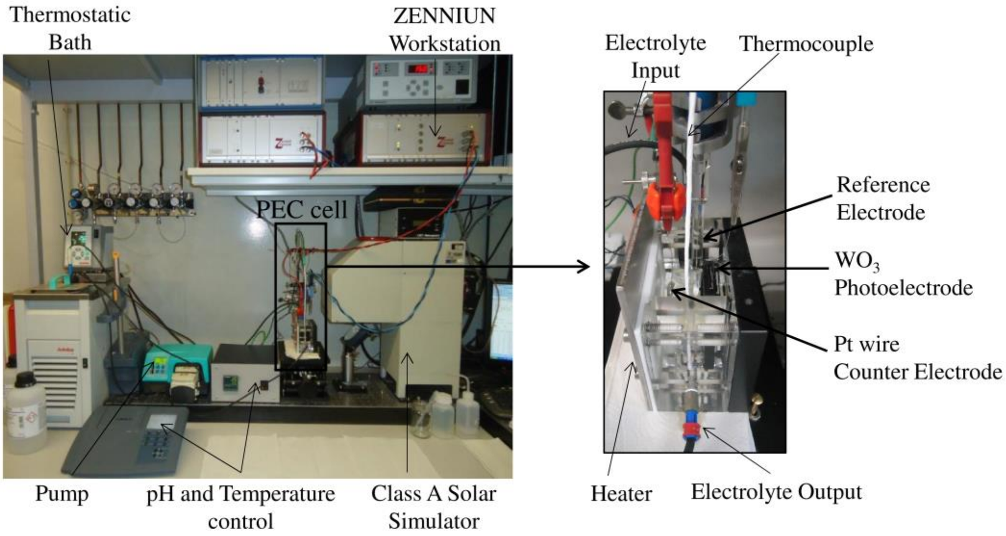

Figure 3.1: Test bench setup used to characterize the PEC cell at different temperatures.

A standard three-electrode configuration was used with the tungsten trioxide as photoanode, a 99.9 % pure platinum wire (Alfa Aesar, Germany) as counter electrode and an Ag/AgCl/Sat. KCl (Metrohm, Switzerland) as reference electrode. The cell was filled with an electrolyte aqueous solution of 3 M methanesulfonic acid (25 ºC, pH 0.42) in which the photoanode was immersed. The total immersed area of the photoanode was 4 cm^2.

3.2.3 PHOTOELECTROCHEMICAL CHARACTERIZATION

J-V MEASUREMENTS

The photocurrent density-voltage (*J-V*) characteristic curves were recorded applying an external potential bias to the cell and measuring the generated photocurrent using a ZENNIUM (Zahner Elektrik, Germany) workstation controlled by the Thales software package (Thales Z 1.0) - Figure 3.1. The potential was reported against the reversible hydrogen electrode (RHE). The measurements were performed in the dark and under simulated sunlight (Oriel class B solar simulator equipped with a 150 W Xe lamp, Newport, USA), using an AM 1.5 G filter (Newport, USA), at a scan rate of 10 $mV \cdot s^{-1}$ for the potential range between 0.3 V_{RHE} and 2.5 V_{RHE}. The light beam was calibrated with a single crystal Si photodiode (Newport, USA), resulting in a lamp spectrum that is adjusted to best match the 1-sun spectrum (*ca.* 100 $mW \cdot cm^{-2}$).

EIS MEASUREMENTS

Electrochemical impedance spectroscopy (EIS) was performed applying a small potential sinusoidal perturbation to the system and recording the amplitude and the phase shift of the resulting current response using also the ZENNIUM workstation - Figure 3.1. The frequency range used was 0.1 Hz – 100 kHz and the magnitude of the modulation signal was 10 mV. The measurements were carried out in dark conditions and at 0.7 V_{RHE}, 1.0 V_{RHE}, 1.3 V_{RHE} and 1.6 V_{RHE}. An appropriate electrical analog was then fitted to the obtained EIS spectra using the ZView software (Scribner Associates Inc., USA).

AGING TESTS

A constant potential was applied to the PEC cell over several hours and the resulting time-dependent photocurrent response was then measured in order to obtain crucial information about the stability/corrosion of the semiconductor. In this work, the WO_3 photoanodes were continuously exposed to 1-sun AM 1.5 G illumination (100 $mW \cdot cm^{-2}$) over 72 h and at a constant bias potential of 1.23 V_{RHE}. The stability was evaluated at their best operating temperature, *i.e.* WO_3/FTO was tested at 45 ºC and WO_3/metal was tested at 55 ºC.

3.2.4 STRUCTURAL CHARACTERIZATION

SEM ANALYSIS

Scanning electron microscopy (SEM) was performed to obtain information about morphology, surface topography and thickness of the WO_3 films in the WO_3/FTO and WO_3/metal samples. The SEM and EDS analyses were made at CEMUP (Centro de Materiais da Universidade do Porto) using a high-resolution scanning electron microscope (Quanta 400 FEG, FEI Company, USA). The acceleration voltage used was 15 keV while an in-lens detector was employed with a working distance of *ca.* 10 mm. The high resolution images were collected from 2500× up to 200000×. The surface of the samples was investigated for fresh and aged samples to assess modifications in their morphology.

XRD ANALYSIS

X-ray diffraction (XRD) analysis was carried out in a PANalytical X'Pert MPD (Spectris plc, England) equipped with an X'Celerator detector and secondary monochromator (Cu $K\alpha$ $\lambda = 0.154$ nm, 40 kV and 30 mA). The spectra were collected in the range 15º - 95º (2 theta) with step size 0.017º and the time acquisition was set to 100 $s \cdot step^{-1}$. Rietveld refinement with Powder-Cell software was used to identify the crystallographic phases from the XRD diffraction patterns.

3.3 RESULTS AND DISCUSSION

3.3.1 TEMPERATURE EFFECT IN PEC CELL PERFORMANCE

J-*V* and EIS measurements were conducted for the two types of WO_3 photoanodes under study, *i.e.* for WO_3 photoanode deposited on FTO glass substrate (WO_3/FTO) and for WO_3 photoanode anodized on a tungsten foil substrate (WO_3/metal). Five different temperatures (25 ºC, 35 ºC, 45 ºC, 55 ºC and 65 ºC) were considered in dark and under 1-sun AM 1.5 G illumination conditions. Before performing the analysis at each temperature, the cell was left to stabilize for *ca.* 5 minutes. Figure 3.2 a) and b) show the *J*-*V* responses for WO_3/FTO and WO_3/metal samples, respectively.

From Figure 3.2 is clear that the generated photocurrent density of the PEC cell using WO_3 photoanodes increases with temperature; a similar behavior was also observed with Si-doped hematite photoanodes [5]. Moreover, the photocurrent density values obtained for WO_3/metal sample is significantly higher than the values obtained for WO_3/FTO sample, being these differences not only due to the preparation methods, but also due to the higher charge transport resistance of the FTO layer in the glass substrate [2]. Actually, the photocurrent values obtained are in straight agreement with the ones reported in literature [11, 17].

For WO_3/FTO sample, at 25 ºC and under dark conditions, the current onset is observed for a potential higher than 2.1 V_{RHE} (the electrolysis threshold for water oxidation with WO_3/FTO photoanodes) – *cf.* Figure 3.2a [15]. Under sunlight conditions, the photocurrent onset potential begins for 0.5 V_{RHE} and rises steeply up to 1.2 V_{RHE}, reaching a plateau for 1.2 – 2.0 V_{RHE} potential range; a photocurrent density of *ca.* 0.38 $mA \cdot cm^{-2}$ was observed at 1.7 V_{RHE}. After increasing the temperature of the system to 35 ºC, a photocurrent density increase of 5 % was achieved at 1.7 V_{RHE} and no significant differences exist between the dark current onset potential at 25 ºC and 35 ºC. Experiments at higher temperatures were then performed (45 ºC, 55 ºC and 65 ºC) and the same behavior was observed: an improvement of the photocurrent with temperature. In particular, the experiment at 65 ºC originated a 64 % photocurrent enhancement at 1.7 V_{RHE} (J_{photo} = 0.60 $mA \cdot cm^{-2}$) compared with the experiment performed at 25 ºC. However, at this high temperature the dark current onset started at an earlier potential (*ca.* 1.8 V_{RHE}).

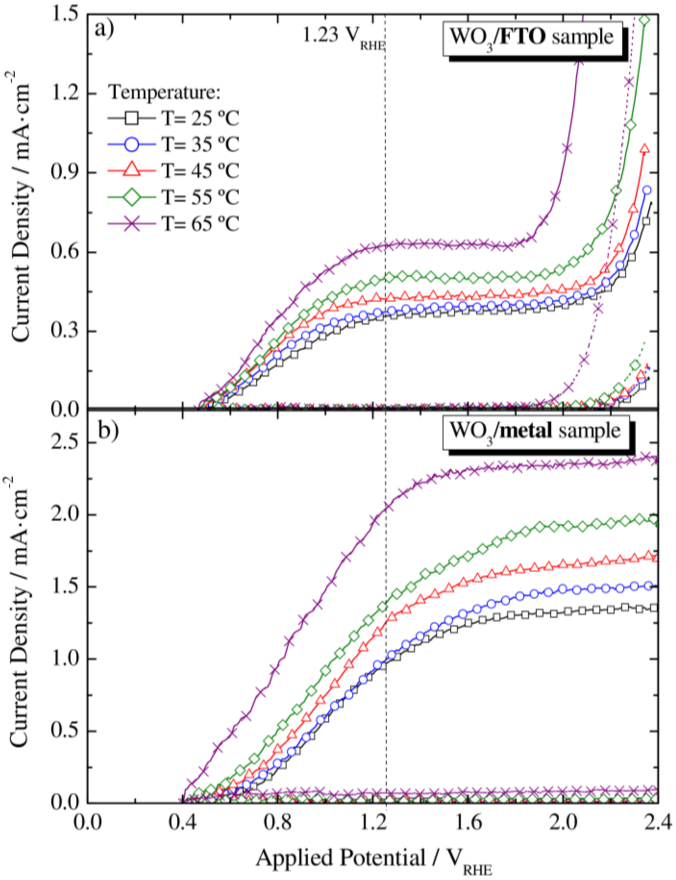

Figure 3.2: Temperature effect in the photocurrent density-voltage (*J*-*V*) characteristics of the WO_3 photoanodes: (a) WO_3/FTO and (b) WO_3/metal; for a range of temperatures from 25 ºC to 65 ºC, in the dark (dashed lines) and under 1-sun AM 1.5 G illumination (solid lines) conditions. (□) *T* = 25 ºC, (○) *T* = 35 ºC, (△) *T* = 45 ºC, (◇) *T* = 55 ºC, (×) *T* = 65 ºC.

Reference tests at 25 ºC performed among runs showed only changes in the *J*-*V* curves after running the PEC cell at 55 ºC and 65 ºC; the dark current onset potential was at lower potentials, *i.e.* at 1.9 V_{RHE} and 1.8 V_{RHE}, respectively - see Figure 3.3a. Regarding the WO_3/metal sample, the highest photocurrent density was also achieved at 65 ºC, reaching *ca.* 2.01 $mA\cdot cm^{-2}$ at 1.23 V_{RHE} and 2.31 $mA\cdot cm^{-2}$ at 1.7 V_{RHE}, as shown in Figure 3.2b. Considering 25 ºC as the reference temperature, improvements of *ca.* 114 % and 81 %, respectively at 1.23 V_{RHE} and at 1.7 V_{RHE}, were observed. As temperature increases, the onset potential is also shifted to lower potentials, *i.e.* it passed from 0.52 V_{RHE} to 0.40 V_{RHE}, respectively at 25 ºC and 65 ºC. However, at

65 ºC a small current under dark conditions is observed, a behavior that was not observed for temperatures up to 55 ºC. Herein, reference tests performed at 25 ºC between experiments were also performed and no major changes were observed - Figure 3.3b.

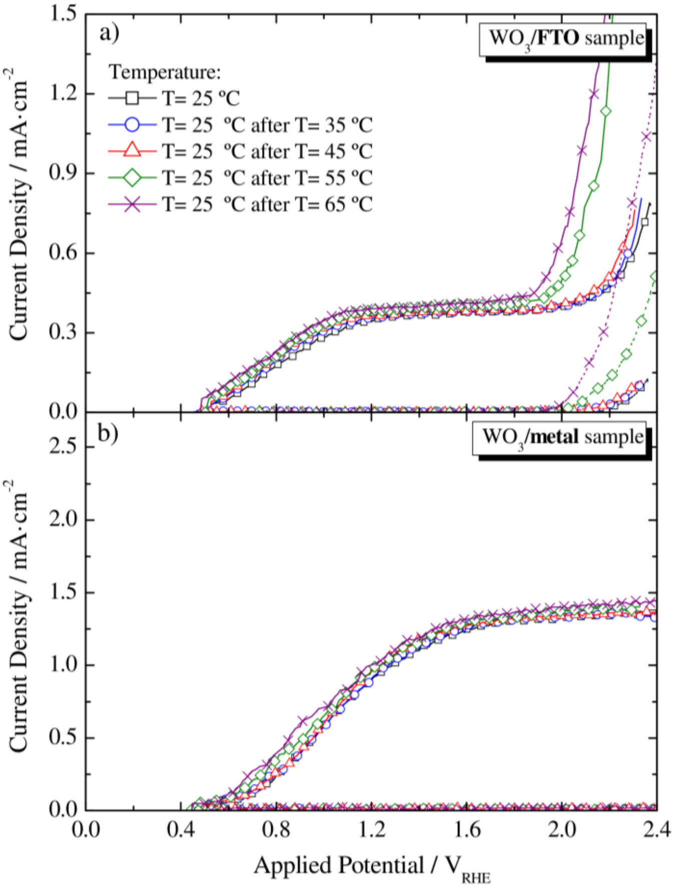

Figure 3.3: Photocurrent density-voltage (*J*-*V*) characteristics of the WO_3 photoanodes: (a) WO_3/FTO and (b) WO_3/metal for reference tests performed at 25 ºC between experiments and before increasing the temperature of the cell; obtained in the dark (dashed lines) and under 1-sun AM 1.5 G illumination (solid lines) conditions. (□) $T = 25$ ºC, (○) $T = 35$ ºC, (△) $T = 45$ ºC, (◇) $T = 55$ ºC, (×) $T = 65$ ºC.

Analyzing the results presented in Figure 3.2, it can be concluded that the photocurrent density increases with temperature and the onset potential shifts to lower potentials, allowing to improve the efficiency of the cell and to reduce the external potential needed to promote the water splitting reaction (bias). Thus, improvements in the PEC cell performance are observed at higher temperatures since temperature contributes to thermal bandgap narrowing of the photoanode (broadening the spectrum range absorption) and also decrease the potential required for the water electrolysis (described by the Nernst equation). Then, a semiconductor operating at higher temperatures will have more available free electrons and holes for charge transport, an increased intrinsic carrier population and electrolyte conductivity. Finally, mass transport and electroreaction kinetics are also favored by temperature increase, as stated by the Einstein relation and by the Butler-Volmer equation, respectively, outlining a photocurrent improvement with temperature [4, 5].

To assess the substrate contribution for the dark current onset potential, *J*-*V* characteristic curves for the water hydrolysis were obtained for naked substrates of FTO glass and tungsten foil, as shown in Figure 3.4. The hydrogen evolution reaction (HER) is made at a platinum wire cathode and the oxygen evolution reaction (OER) takes place at a FTO glass electrode and at a tungsten foil electrode. For the bare FTO substrate, the dark current onset begins at lower potential values as temperature increases, *e.g.* it begins at 1.9 V_{RHE} and 1.4 V_{RHE} for temperatures of 25 ºC and 65 ºC, respectively. This behavior is similar to the one obtained for the WO_3/FTO photoanode (Figure 3.2).

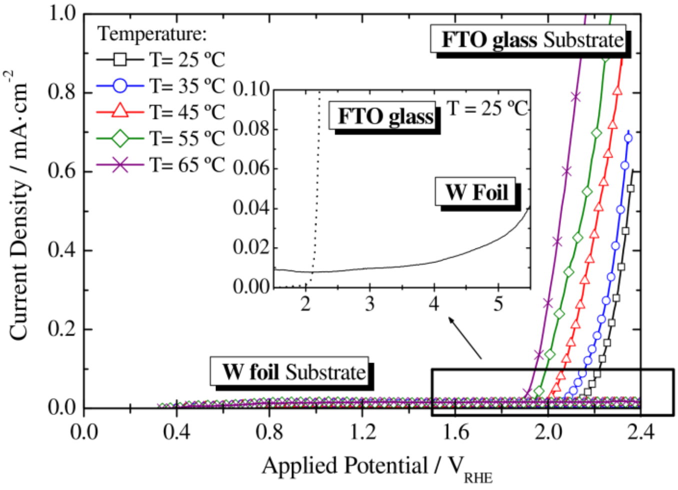

Figure 3.4: Temperature effect in the photocurrent density-voltage (*J*-*V*) characteristics of a bare FTO-glass substrate and a tungsten foil substrate for a range of temperatures from 25 ºC to 65 ºC in the dark conditions. (□) *T* = 25 ºC, (○) *T* = 35 ºC, (△) *T* = 45 ºC, (◇) *T* = 55 ºC, (×) *T* = 65 ºC.

In typical photoelectrochemical systems the dark current appears at the potential bias when the oxidation/reduction of water occurs. When in contact with an electrolyte in the dark, charge equilibration occurs at the interface, favoring electron-hole recombination. Increasing the temperature, the kinetics is favored due to an increased concentration of free holes in the valence band and so the oxidation of water starts at lower potentials (as outlined by the Nernst equation). For the tungsten foil (metal) substrate this phenomenon is not observed and only a very small anodic dark current density (< 0.02 mA·cm^{-2}) was observed as a response to the applied potential bias – Figure 3.4 [5].

The inset plot of Figure 3.4 shows a detail of the *J-V* curves for the water hydrolysis at 25 ºC. It is clearly apparent the difference in the electrochemical activity of both electrodes, being tungsten electrode much less active for OER. For FTO glass substrate the electrocatalytic oxygen evolution starts at *ca.* 1.9 V_{RHE}, when the dark current sharply increased; for the tungsten substrate a small anodic current density of *ca.* 0.01 mA·cm^{-2} is measured up to *ca.* 4.0 V_{RHE}, when the dark current started to slowly increase. So, the negative shift on the dark current onset as a function of the temperature should be related to the FTO layer and not to the photoanode material.

EIS technique was used to extract detailed information about the group of resistances and capacitances that describe the behavior of the electrochemical reaction kinetics, ohmic conduction processes and mass transport limitations on the PEC cell performance. After obtaining the *J-V* characteristic curves at the selected temperatures (25 ºC, 35 ºC, 45 ºC, 55 ºC and 65 ºC), EIS measurements were conducted under dark conditions in a three-electrode configuration. This configuration allows understanding the phenomena occurring at the semiconductor/electrolyte interface, since the potential is measured with respect to a fixed reference potential, short-circuited with the counter electrode [18]. For each operating temperature, a suitable electrical analogue was fitted to the EIS data, as described elsewhere [5]. The proposed electrical analogue comprises a series resistance (R_{Series}) and two RC elements in series representing the semiconductor bulk (R_{SC} and C_{SC}) and the semiconductor/electrolyte interface (R_{CT} and C_{H}) – Figure 3.5. The double layer capacitor does not behave ideally, since the semiconductors are nanostructured and so a constant phase element (CPE) was used instead [18]. The impedance tests of the two samples were carried out in the potential range of 0.7 V_{RHE} to 1.6 V_{RHE}, with steps of 0.3 V_{RHE} and the correspondent Nyquist plots are shown Figure 3.6 [left plots] and [right plots] for WO_3/FTO and WO_3/metal samples, respectively.

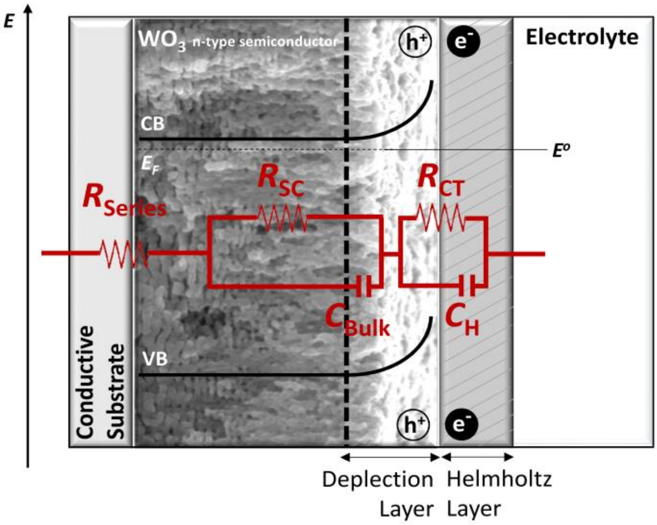

Figure 3.5: Electrical circuit analog used to fit the EIS data for the WO_3 photoanodes.

The overall resistance (R_{Series} + R_{SC} + R_{CT}) decreases with temperature for both WO_3 samples, in line with the photocurrent density increase; however, the overall PEC cell resistance is higher for the WO_3/FTO sample. Zooming the Nyquist diagram at the high frequency range, it is observed that a temperature independent small semicircle appears for the WO_3/FTO sample [inset plots in Figure 3.6 (left-side)], which is imperceptible in the WO_3/metal sample [inset plots in Figure 3.6 (right-side)]. The latter is assigned to FTO exposure to the electrolyte; this new interface (FTO/electrolyte interface) imposes an extra resistance to the system (not considered in the proposed model).

The EIS spectra obtained at the high frequency range, assigned to the faster electronic processes occurring in the semiconductor bulk, was fitted to the RC element composed of R_{SC} and C_{SC}, whereas the low frequency range spectra, assigned to the phenomena occurring at the semiconductor/electrolyte interface, was fitted to R_{CT} and C_H. In fact, the temperature increase strongly affects the phenomena occurring at the semiconductor/electrolyte interface, since the low frequencies range semicircle decreases considerably with temperature, being this decrease even more obvious at higher temperatures (65 ºC).

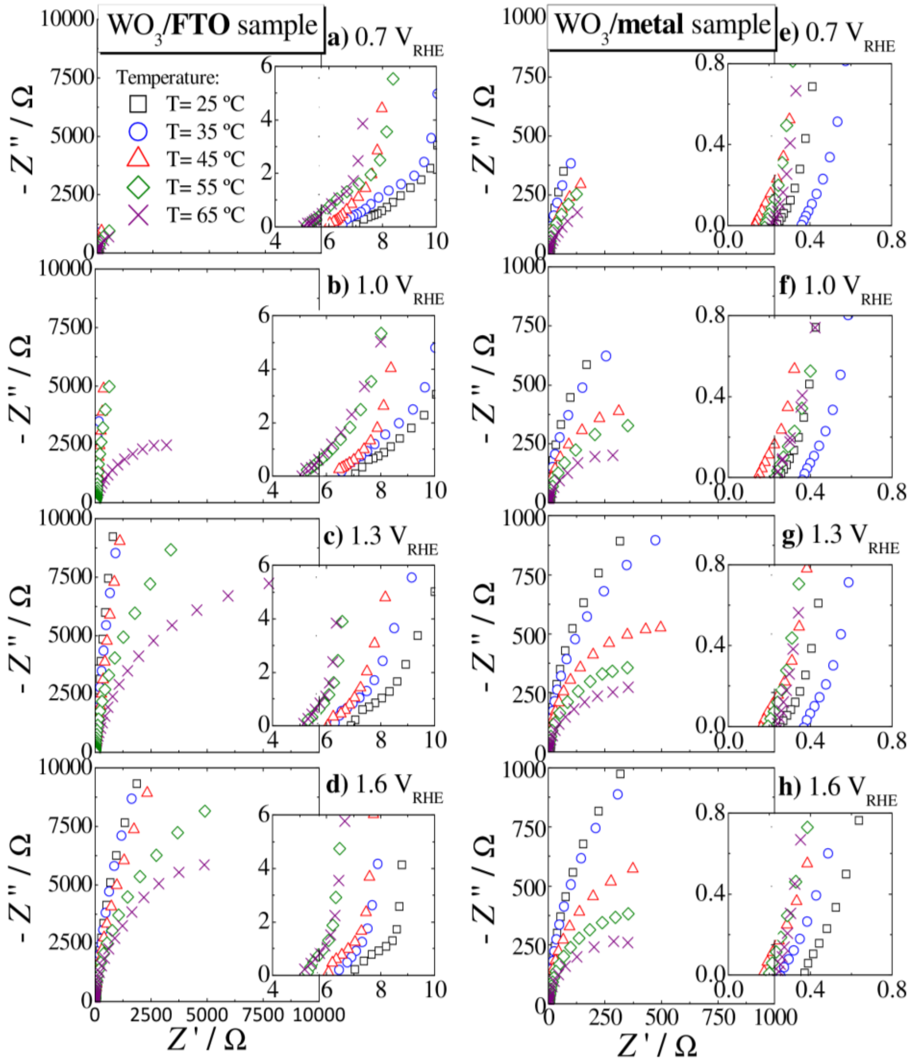

Figure 3.6: Temperature effect in the Nyquist diagrams of the WO$_3$/FTO sample [left-side plots] and WO$_3$/metal sample [right-side plots] obtained for a range of temperatures from 25 ºC to 65 ºC, in dark and forward biases: (a) and (e) 0.7 V$_{RHE}$; (b) and (f) 1.0 V$_{RHE}$; (c) and (g) 1.3 V$_{RHE}$; (d) and (h) 1.6 V$_{RHE}$. *Z* ': real impedance, *Z* '': imaginary impedance; (□) *T* = 25 ºC, (○) *T* = 35 ºC, (△) *T* = 45 ºC, (◇) *T* = 55 ºC, (×) *T* = 65 ºC. On the right-side of each plot is a zoom-out of the left-side plots.

Fitting the electrical circuit analogue shown in Figure 3.5 to experimental EIS data, the impedance parameters such as R_{Series}, R_{SC}, C_{SC}, R_{CT}, C_{H} and k_r were then obtained. The obtained values are plotted in Figure 3.7 as a function of the operating temperature for the applied potential of 1.6 V_{RHE}; both WO_3 samples exhibit a current plateau at this potential.

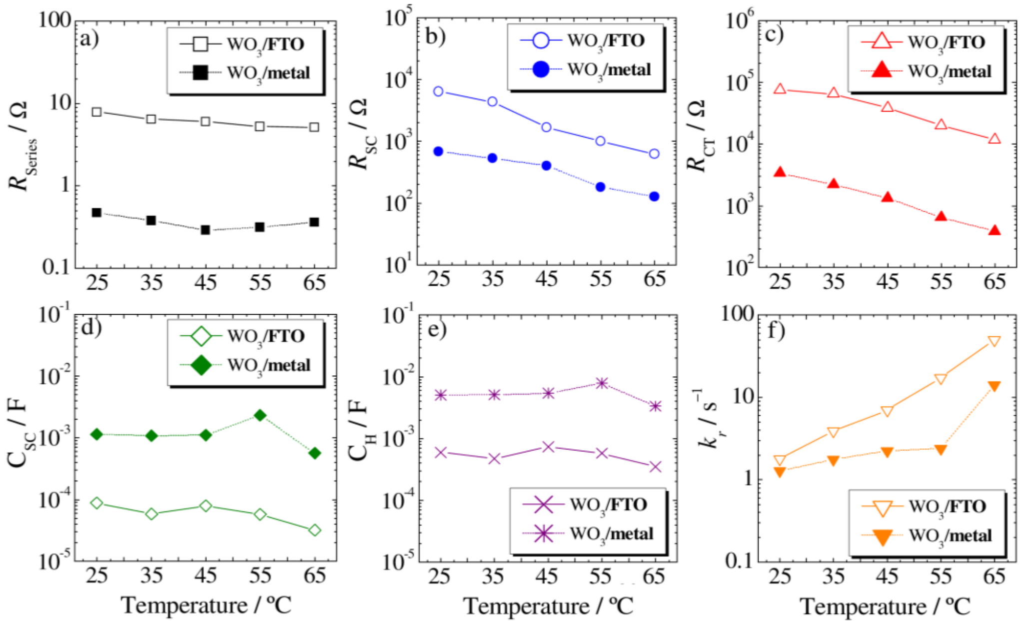

Figure 3.7: Temperature effect in the impedance parameters of the WO_3/FTO sample (empty symbols) and WO_3/metal sample (filled symbols) obtained at 1.6 V_{RHE}: (a) series resistance – R_{Series} (□); (b) bulk semiconductor resistance – R_{SC} (○); (c) charge transfer resistance – R_{CT} (△); (d) space charge capacitance – C_{SC} (◇); (e) Helmholtz capacitance – C_{H} (×); (f) rate constant of the electron-hole recombination – k_r (▽).

Figure 3.7 shows the differences between the impedance parameter values for the two photoanodes under study. The series resistances, R_{Series}, for the WO_3/FTO sample are considerable higher than the ones obtained for the WO_3/metal sample, as shown in Figure 3.7a. Additionally, R_{Series} for WO_3/FTO sample decreases from 8.0 Ω to 5.1 Ω when the temperature increases from 25 ºC to 65 ºC. This behavior is not observed for the WO_3/metal sample, remaining the R_{Series} values almost constant (*ca.* 0.4 Ω) for the studied temperatures. The series resistance comprehends the substrate resistance, the resistance related to the electrolyte ion conductivity and the resistance of the external contacts (*e.g.* wire connections) [19]. It can then be concluded that the main contribution to the R_{Series} is the substrate resistance to the transport of charges, since the other series resistances are equal for both electrodes. FTO layer imposes a higher resistance and, consequently, decreases the charge collection efficiency in the external circuit.

The electrical resistance related to the bulk semiconductor, R_{SC}, should decrease with temperature, associated to a faster electron transport through the WO_3 photoactive material [5]. For the WO_3/metal sample, R_{SC} decreases from $6.9 \times 10^2\ \Omega$ to $1.3 \times 10^2\ \Omega$ when temperature increases from 25 ºC to 65 ºC and a more pronounced decrease is observed at 55 ºC (Figure 3.7c) shows the behavior of the charge transfer resistance, R_{CT}, and a decrease with temperature is observed for both samples; so no differences related to the temperature effect in the resistance contribution on the substrate material are noticed. The major differences are related to the electrocatalytic activity of the WO_3 semiconductor material [20]; in the temperature range studied, R_{CT} decreased from $3.4 \times 10^3\ \Omega$ to $3.9 \times 10^2\ \Omega$ and $7.5 \times 10^4\ \Omega$ to $1.2 \times 10^4\ \Omega$ for the WO_3/metal and WO_3/FTO samples, respectively. Moreover, the R_{CT} decrease with temperature is responsible by an enhanced charge transfer phenomena. If the overall resistance in the system favors the photocurrent increase with temperature, this means that the R_{CT} decrease has a more pronounced effect than the R_{SC} decrease.

On the other hand, the space charge capacitance (C_{SC}) and the Helmholtz capacitance (C_{H}) are almost temperature independent – *cf.* Figure 3.7d and Figure 3.7e, respectively. The C_{H} values are higher than the C_{SC} values, since the Helmholtz double layer width is generally smaller than the width of the depletion layer in photo-assisted water splitting systems [5].

Figure 3.7f shows the evolution of the rate constant (k_{r}) of the bulk electrons recombination with holes in the space charge layer as a function of the operating temperature. It corresponds to the inverse of the time constant of the bulk semiconductor RC element (obtained by multiplying the semiconductor resistance, R_{SC}, with the correspondent capacitance, C_{SC}). The recombination rate constant is in the range of $100 – 1\ \mathrm{s}^{-1}$ and a faster electron-hole recombination (higher k_{r}) is observed with temperature for both samples. This process is ascribed to an increased back electron reaction promoted by accumulated charges on the surface of the photoanode, resulting in higher electron-hole recombination. The recombination loss pathway has to be taken into account for the performance of PEC cells, since it is potentially in direct kinetic competition with water oxidation by accumulated holes. In particular, the recombination rate constant strongly increases at 55 ºC and 65 ºC for WO_3/FTO sample and at 65 ºC for WO_3/metal sample.

The intrinsic power characteristics of the WO_3 photoelectrodes were obtained from the *J-V* curves (Figure 3.2) as a function of the temperature: power conversion (*P*) efficiency, fill factor (*FF*), intrinsic solar to chemical (*ISTC*) conversion efficiency of the photoanode, photocurrent density (J_{photo}) and correspondent photopotential (E_{photo}). These parameters were determined following the work reported by Dotan *et al.* [21]. The intrinsic photovoltaic power of the photoanodes is the product of photocurrent by photopotential; by plotting it *vs.* photopotential, the maximum power point (MMP) can be obtained and the respective potential (E_{MPP}) and current (J_{MPP}). The *ISTC* efficiency was determined from the following equation:

$$ISTC = \eta_{\mathrm{el}} \left. \frac{J_{\mathrm{photo}} \times E_{\mathrm{photo}}}{P_{\mathrm{light}}} \right|_{\mathrm{AM1.5\ G}} \cong \frac{1.23\left(\mathrm{V_{RHE}}\right)}{U_{\mathrm{dark}}\left(\mathrm{V_{RHE}}\right)} \left[\frac{J_{\mathrm{photo}}\left(\mathrm{mA \cdot cm^2}\right) \times E_{\mathrm{photo}}(\mathrm{V})}{100(\mathrm{mW \cdot cm^2})} \right] \quad (3.1)$$

where η_{el} is the electrolysis efficiency and U_{dark} is the potential that must be applied to the photoanode in order to reach the correspondent current in the dark. The temperature effect in the intrinsic power characteristics of the WO_3/FTO and WO_3/metal samples is shown in Figure 3.8; the summary of the parameters at the maximum power point is also presented in Table 3.1.

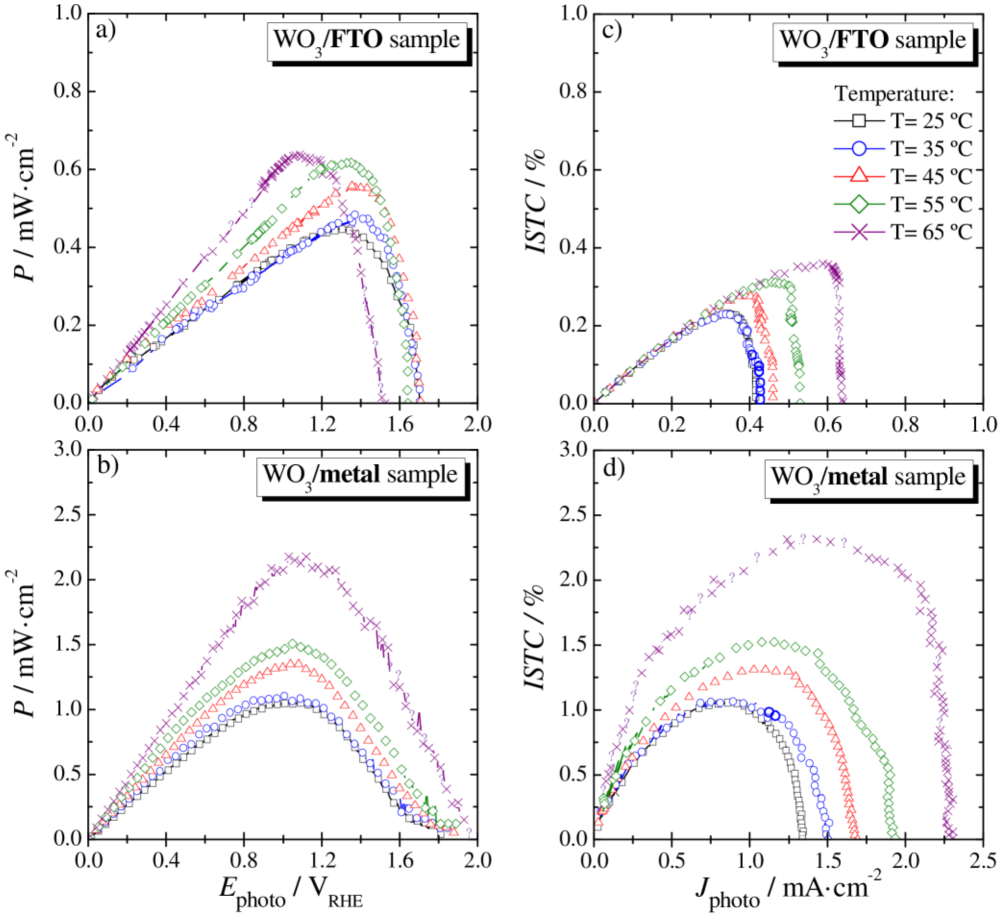

Figure 3.8: Temperature effect in the intrinsic power characteristics, *i.e.* the power (P) and intrinsic solar to chemical ($ISTC$) conversion efficiencies, of the WO_3 photoanodes: (a) and (c) WO_3/FTO sample; and (b) and (d) WO_3/metal sample. (□) T = 25 ºC, (○) T = 35 ºC, (△) T = 45 ºC, (◇) T = 55 ºC, (×) T = 65 ºC.

Figure 3.8 shows that maximum power and intrinsic solar to chemical conversion efficiencies increase with temperature for both types of WO_3 photoanodes, being the obtained values higher for the WO_3/metal sample, as expected from the J-V characteristics. However, the fill factor parameter for the WO_3/FTO sample increases only until 45 ºC (see Table 3.1). This can be explained by the enhanced charge recombination loss for temperatures higher than 45 ºC, since a reduction of FF is normally reached when the recombination rate is significantly higher than the extraction rate [22]. Actually this was validated by EIS measurements (Figure 3.7), where the recombination rate constant of the bulk electrons with holes strongly increases for the two higher temperatures. The results indicated that the trend of each intrinsic power parameters depends on the recombination rate constant, which is also affected by the temperature and the semiconductor interfaces present in the solar cell [23]. Therefore, a PEC device equipped with the WO_3/FTO photoanode showed the optimal performance conditions when operating at 45 ºC, ensuring simultaneously the highest fill factor, *FF* = 72.69 %, a power conversion, *P*, value of *ca.* 0.57 $mW{\cdot}cm^{-2}$ and an intrinsic solar to chemical conversion, *ISTC*, efficiency value of *ca.* 0.28 %. Regarding the cell using the WO_3/metal sample, even if the best performance was observed at 65 ºC (*FF* = 50.84 %, *P* = 2.20 $mW{\cdot}cm^{-2}$ and *ISTC* = 2.38 %) the improvement in terms of *FF* is only *ca.* 0.55 % due to a noticeable increase of the k_r value – see Figure 3.7f. Balancing this behavior with an increased dark current at 65 ºC (Figure 3.2), the best operating temperature should be considered at 55 ºC.

Table 3.1: Intrinsic power characteristics of the WO_3/FTO and WO_3/metal samples; J_{photo}, V_{photo}, *P*, *FF* and *ISTC* efficiency obtained at MPP.

Samples	***T* / ºC**	**J_{photo} / $mA{\cdot}cm^{-2}$**	**E_{photo} / V_{RHE}**	***P* / $mW{\cdot}cm^{-2}$**	***FF* / %**	***ISTC* / %**
WO_3/FTO	25	0.34	1.30	0.44	63.54	0.23
	35	0.35	1.37	0.48	66.24	0.23
	45	0.42	1.36	0.57	72.69	0.28
	55	0.46	1.35	0.62	70.88	0.31
	65	0.59	1.09	0.64	65.24	0.36
WO_3/metal	25	1.05	0.99	1.04	46.98	1.06
	35	1.09	1.11	1.21	48.08	1.11
	45	1.28	1.12	1.43	49.57	1.31
	55	1.51	1.14	1.52	50.56	1.54
	65	1.95	1.13	2.20	50.84	2.38

3.3.2 Stability Behavior of the PEC cell at High Temperatures

The performance histories of the WO_3/FTO and WO_3/metal samples were evaluated at the best operating temperature abovementioned, 45 ºC for WO_3/FTO and 55 ºC for WO_3/metal samples. A reference stability test was also performed at room temperature (25 ºC) with a fresh WO_3/FTO sample. Figure 3.9 plots the photocurrent histories over 72 hours under continuous 1-sun AM 1.5 G illumination for both samples.

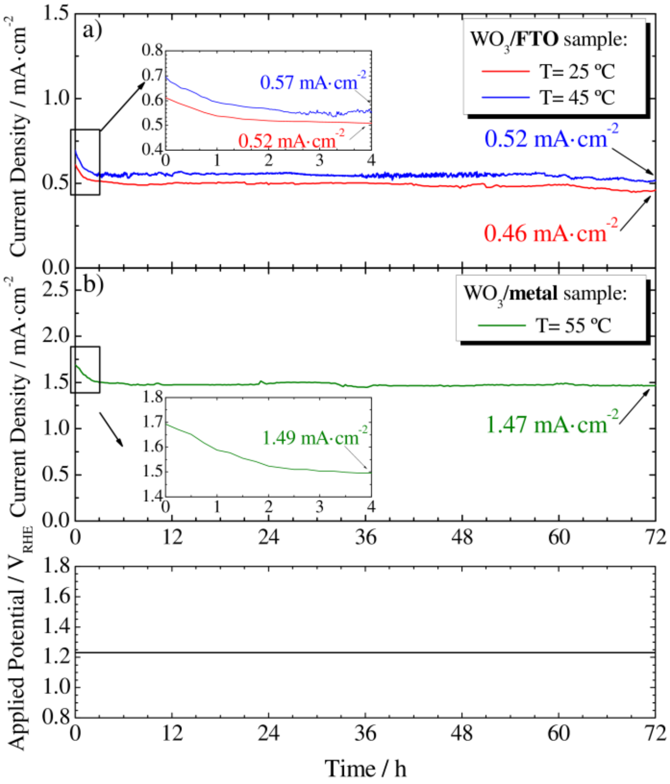

Figure 3.9: Photocurrent histories of the WO_3 photoanodes tested over 72 h at a constant potential of *ca.* 1.23 V_{RHE}, under continuous 1-sun AM 1.5 G illumination and at different temperatures: (a) WO_3/FTO samples aged at 25 ºC (red line) and 45 ºC (blue line); and (b) WO_3/metal sample aged at 55 ºC (green line). Inset plot for the first 4 h of stability tests.

From Figure 3.9 significant photocurrent density decrease is observed during the initial period of 4 h for both samples, which is typical for the WO_3 photoanodes, as reported elsewhere [10, 11]. Photocurrent density of the WO_3/FTO photoanode remains mostly stable over 60 h (after the initial period) with an average value of 0.51 mA·cm^{-2}

and 0.57 mA·cm^{-2} for samples aged at 25 ºC and 45 ºC, respectively. The test was stopped after 72 h, when the photocurrent of both samples lost *ca.* 10 %. Since the reference stability test at 25 ºC and the test at 45 ºC showed similar behaviors, it can be concluded that temperature increase up to 45 ºC allows to improve the efficiency of the PEC cell with no significant influence on the stability performance. The *J*-*V* characteristics of both samples before and after running the stability tests at 25 ºC and 45 ºC are shown in Figure 3.10.

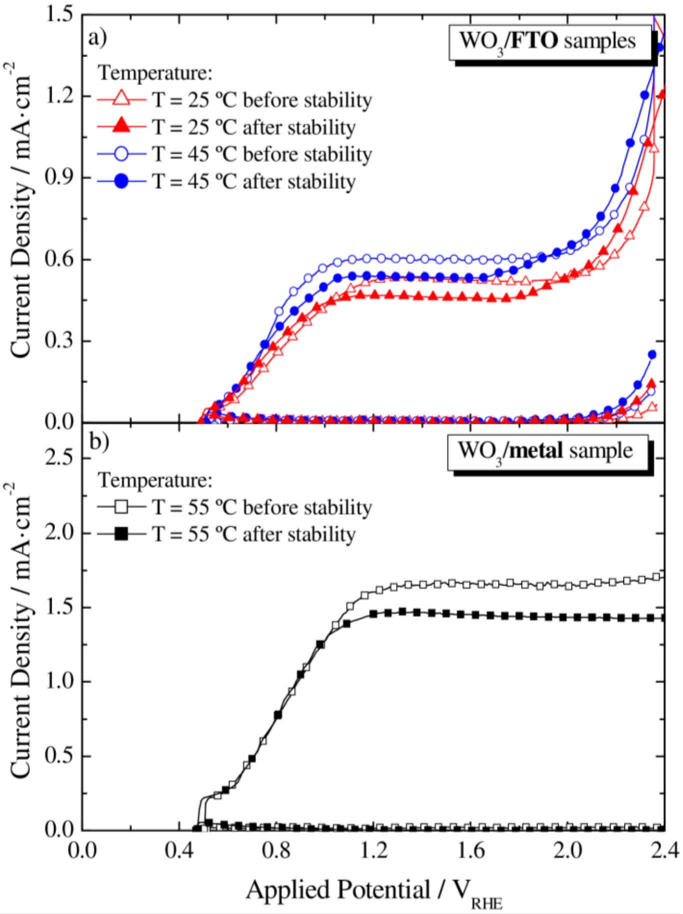

Figure 3.10: Photocurrent density-voltage (*J*-*V*) characteristics of the WO$_3$ photoanodes tested in the dark (dashed lines) and under 1-sun AM 1.5 G illumination (solid lines) before and after stability test: (a) WO$_3$/FTO samples: fresh cell at *T* = 25 ºC (△) and at *T* = 45 ºC (○), aged cell after 72 h of stability at *T* = 25 ºC (▲) and at T = 45 ºC (●); (b) WO$_3$/metal sample: fresh cell at *T* = 25 ºC (□) and at *T* = 55 ºC (○), aged cell after 72 h of stability at *T* = 25 ºC (■) and at *T* = 55 ºC (●).

Under simulated sunlight conditions and at 25 ºC, the photocurrent of the WO_3/FTO sample at 1.23 V_{RHE} decreased after the stability test from *ca.* 0.56 $mA·cm^{-2}$ to 0.47 $mA·cm^{-2}$; likewise, at 45 ºC it decreased from *ca.* 0.66 $mA·cm^{-2}$ to 0.53 $mA·cm^{-2}$. In dark conditions, the onset potential for both samples tends to appear at lower potentials after aging, *i.e.* moved from 2.1 V_{RHE} to 2.0 V_{RHE}. The dark current onset at lower potentials may be related to semiconductor detachment from the substrate, allowing FTO areas to contact directly with the electrolyte.

The morphology of the WO_3/FTO film was then investigated by SEM and EDS before and after performing the stability tests to assess the surface integrity of the samples – Figure 3.11. Before the aging test, SEM images of the WO_3/FTO sample show a network of plate-like particles with diameters of a few tens of nanometers (ranging from 20 to 50 nm) partly fused together, forming a WO_3 nanocrystalline film of *ca.* 1.1 µm thick – *cf.* Figure 3.11a [12]. The EDS analysis of area Z1 in Figure 3.11a (3) displays just the presence of tungsten (W) and oxygen (O) elements. Figure 3.11b (4) and Figure 3.11c (7) show similar film morphology for WO_3/FTO samples after performing the stability tests at 25 ºC and 45 ºC, respectively. The aged WO_3 surfaces seem to present higher porosity assigned to material detachment from the FTO glass substrate. Figure 3.11b (5) shows two distinct areas in the sample aged at 25 ºC: area Z1 that apparently was unaffected by corrosion and area Z2 affected by film degradation. In the sample aged at 45 ºC it can be detected three different areas: an intact area (Z1) and two degraded areas (Z2 and Z3) – *cf.* Figure 3.11c (8). For both aged samples, the EDS analysis confirmed the presence of tin (Sn) in the areas potentially affected by corrosion; these results are in agreement with other studies [5, 19]. Since the samples aged at 25 ºC and 45 ºC show similar morphologic degradation, it can be concluded that the photocurrent loss should not be ascribed to the temperature effect.

a) Before Testing

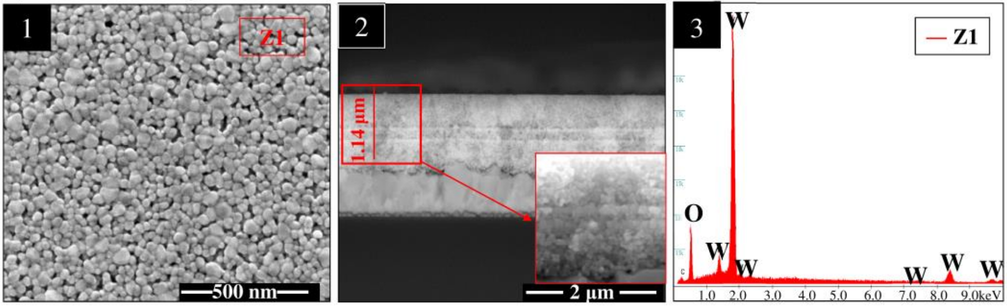

b) After Aging Tests at 25 ºC

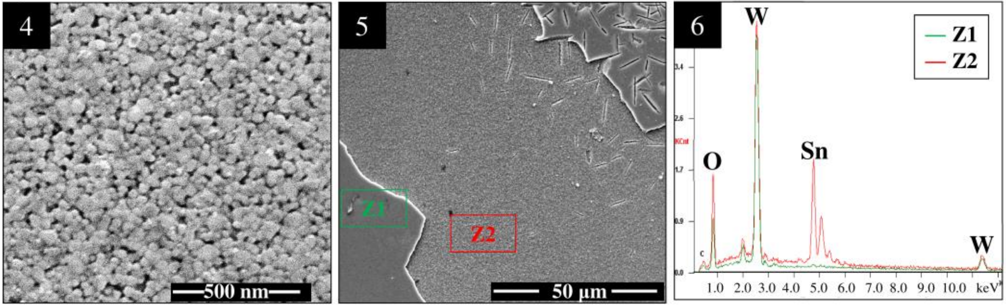

c) After Aging Tests at 45 ºC

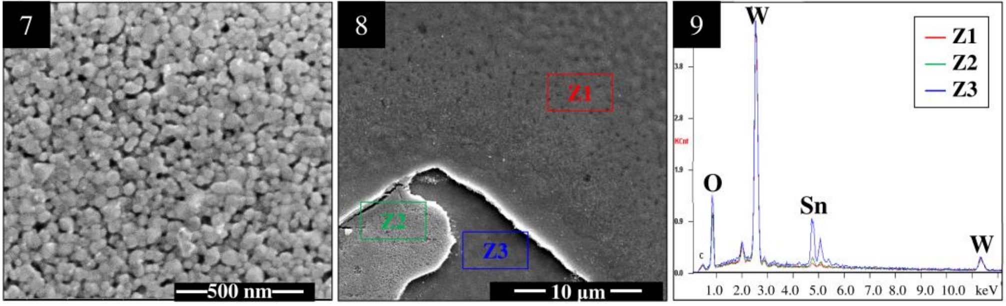

Figure 3.11: SEM images of the WO_3/FTO photoanodes. (a) Before testing: (1) surface top view; (2) cross sectional view; (3) EDS analysis of the surface with the identification of the tungsten and oxygen peaks. (b) After aging tests at 25 °C: (4) surface view; (5) surface with an intact area (*Z1*) and an area affected by film degradation (*Z2*); (6) EDS analysis on the two delimited areas with the identification of the tungsten, oxygen and tin peaks. (c) After aging tests at 45 °C: (7) surface view; (8) surface with an intact area (*Z1*) and areas affected by film degradation (*Z2* and *Z3*); (9) EDS analysis on the three delimited zones with the identification of the tungsten, oxygen and tin peaks.

Concerning the stability performance of the WO_3/metal sample evaluated at 55 °C, after a photocurrent decrease of *ca.* 9 % during the initial 4 h, the generated photocurrent density remained almost stable for whole period of 72 h – see Figure

3.9b. Thus, a photocurrent value of *ca.* 1.47 mA·cm^{-2} was reached at the end, corresponding to *ca.* 2 % decrease after the initial period. From the *J-V* characteristics, no significant differences in the dark current were observed before and after running the aged tests, as shown in Figure 3.10.

Figure 3.12 shows SEM images of the fresh and aged WO_3/metal sample. The fresh sample presents the typical “crispy” surface composed of nanoparticles (*ca.* 50 - 100 nm) interconnected by a nanoscopic structure with an average layer thickness of *ca.* 3.5 µm [17]. This consists of a two-layers nanostructure: a compact oxide layer of *ca.* 1.3 µm originated by the first anodization of the starting tungsten foil, followed by a porous nanoparticle oxide layer of *ca.* 2.2 µm – *cf.* Figure 3.12a (2). No morphologic changes were observed on the aged sample. Moreover, EDS analysis of both samples only detected W and O elements – *cf.* Figure 3.12 (3) and (6).

a) Before Testing

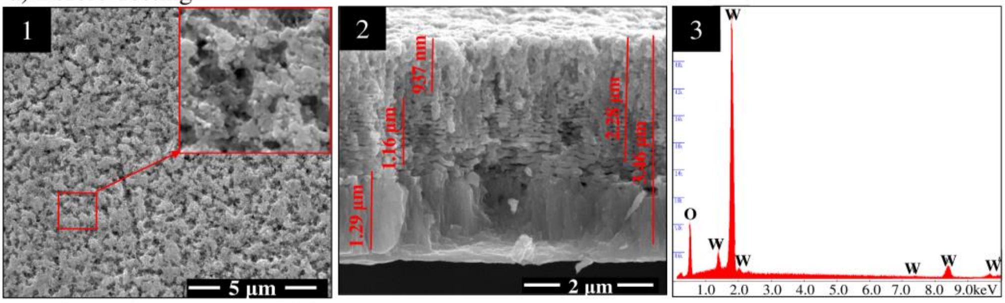

b) After Aging Tests at 55 ºC

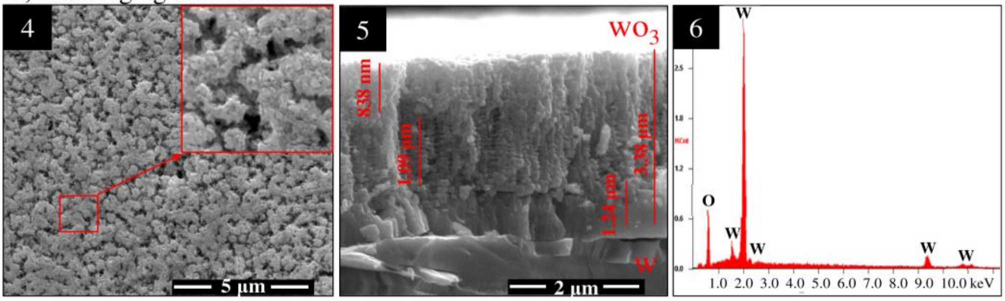

Figure 3.12: SEM images of the WO_3/metal photoanodes (a) before testing and (b) after aging tests at 55 ºC, respectively: (1) and (4) surface top view; (2) and (5) cross sectional view; (3) and (6) EDS analysis with the identification of the tungsten and oxygen peaks.

The crystallinity of the WO_3 films also influences the efficiency and stability of the PEC water splitting cells, since the number of grain boundaries and recombination centers associated with the degree of photoelectrode crystallinity control the photoelectrochemical properties of the films [12, 24]. In this regard, XRD patterns of the WO_3 films before and after aging tests were obtained and are presented in Figure 3.13.

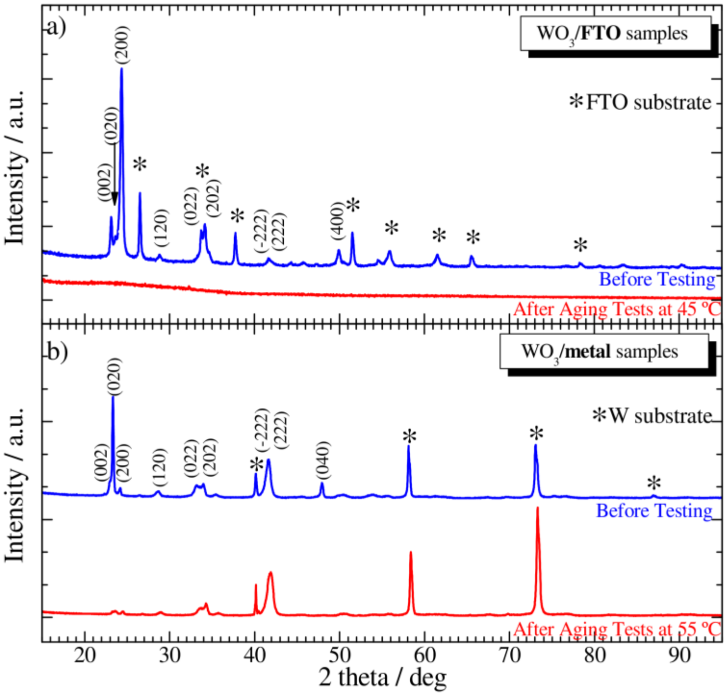

Figure 3.13: XRD spectra of the WO_3 photoanodes: (a) WO_3/FTO sample aged at 45 ºC and (b) WO_3/metal sample aged at 55 ºC. Blue and red lines correspond to signs of the WO_3 samples before testing and after aging tests, respectively. Main peaks from the FTO-glass and tungsten substrates are also labeled with "*".

For WO_3/FTO samples the reflection peaks of the fresh sample (blue line) completely matches with WO_3 monoclinic phase (JCPDS 01-083-0950) - Figure 3.13a; a series of peaks (labeled with asterisk "*") originated from the dense $F:SnO_2$ layer (FTO) (cassiterite), underneath the semiconductor layer, are also detected. The XRD spectrum of a preferentially orientated monoclinic WO_3 film exhibits the characteristic triplet for peaks at 23.1º, 23.6º and 24.4º, corresponding to (002), (020) and (200) planes; peaks at range 33º – 35º and 41º – 42º are also presented but with less intensity. This sample shows a high intensity peak at 24.4º, indicating a (200) preferential orientation of the WO_3 crystallites parallel to the FTO glass substrate. However, the aged WO_3/FTO sample (red line) showed an amorphous structure. This should contribute to the photocurrent decrease after 60 h, since it is known that improved crystallinity is advantageous to the photoelectrode performance, ascribed to the decreased number of recombination sites [24].

On the other hand, for fresh and aged WO_3/metal sample, the diffraction patterns indicate the presence of a crystalline monoclinic phase – *cf.* Figure 3.13b. Again, the WO_3 patterns are superimposed on the metallic tungsten substrate pattern. Before testing (blue line), the WO_3/metal film presented a (020) preferential orientation, although the double peak around 41.6º, representing the (-222) and (222) planes, is also strong. Despite the WO_3 films for WO_3/FTO and WO_3/metal samples were both monoclinic phase, they had different preferential orientation of crystal faces. This can be related to different fabrication methods as well as different film adhesion to the substrate that should be accounted for the photocurrent and stability performance of the semiconductor materials. After aging tests (red line), the double peak at 41.6º was the mainly detected, indicating the preferential orientation of the aged WO_3 crystal faces to the (-222) and (222) planes. Interestingly, the presence of this double peak with an intensity order similar to the fresh sample can justify the high stability performance of the WO_3 photoanodes anodized on tungsten foil substrates. Hence, the relatively good crystallinity of this sample and the preservation of morphology contributed to its highest PEC performance for oxygen evolution reaction. The optimal operation temperature for WO_3/metal photoanode is then 55 ºC, since it ensures simultaneously the highest photocurrent density and stable performance.

3.4 CONCLUSIONS

The temperature influence on the PEC cell performance using WO_3 photoanodes for water splitting was studied. The WO_3 photoanodes were prepared on different substrates by using two techniques: deposition by blade spreading method on a FTO glass substrate and anodization of a tungsten foil substrate. Herein, the main goal was the assessment of the substrate type role on the photoelectrode performance as a function of the temperature. *J-V* characteristic curves, EIS measurements and aging tests were used, as well as SEM and XRD analysis, to assess the morphology and crystallography of the prepared WO_3 samples.

The PEC device was characterized from 25 ºC to 65 ºC, with steps of 10 ºC. At 25 ºC, the highest photocurrent density was reached for the WO_3/metal photoanode, *ca.* 0.94 $mA \cdot cm^{-2}$ at 1.23 V_{RHE}, whereas a photocurrent of *ca.* 0.36 $mA \cdot cm^{-2}$ was obtained for the WO_3/FTO sample. These differences are not only due to the semiconductor preparation method but also to the much higher charge transport resistance imposed by the FTO substrate. When the temperature is further increased to 45 ºC, the generated photocurrent increased *ca.* 20 % in the case of the WO_3/FTO sample and *ca.* 29 % for the WO_3/metal sample, both at 1.23 $V_{RHE.}$ At the maximum tested temperature (65 ºC) both samples generated higher photocurrents at 1.23 V_{RHE}, *i.e.* 2.02 $mA \cdot cm^{-2}$ and 0.62 $mA \cdot cm^{-2}$ for the WO_3 photoanodes on FTO and metal substrates, respectively. However, the WO_3/metal showed a small current under dark conditions, while the WO_3/FTO exhibited already a quite high dark current onset potential at *ca.* 1.80 V_{RHE}. The negative shift on the dark current onset potential of the WO_3/FTO was mainly attributed to temperature effect on FTO glass substrate and not to the photoanode material.

The *J-V* and impedance measurements allowed concluding about the optimal operating temperature for each type of tungsten trioxide photoelectrodes under study: 45 ºC for the WO_3/FTO sample and 55 ºC and the WO_3/metal sample. For higher temperatures, an increased recombination rate of the bulk electrons with holes was observed, which is in direct kinetic competition with water oxidation and, consequently, should affect the overall performance of the photoanodes. The aging tests performed at these temperatures showed that WO_3/metal has simultaneously the best stability and performance for the oxygen evolution reaction. No degradation was observed for aged WO_3/metal film; this behavior might be related to the preferential orientation of the crystal faces – *cf.* (-222) and (222) planes. WO_3/FTO photoanode exhibited a slight photocurrent decrease after aging for both temperatures tested (25 ºC and 45 ºC). The performance loss was attributed to changes in the monoclinic crystalline structure of the WO_3/FTO film, *i.e.* the semiconductor layer became amorphous. Therefore, the substrate and application method have a significant role on the photoelectrode energy performance and stability.

ACKNOWLEDGMENTS

P. Dias and T. Lopes are grateful to the Portuguese Foundation for Science and Technology (FCT) for their PhD fellows (references: SFRH/BD/81016/2011 and SFRH/BD/62201/2009, respectively). L. Andrade acknowledges European Research Council (ERC) for funding within project BI-DSC – Building Integrated Dye sensitized Solar Cells (contract number: 321315). This work was financially supported by Project UID/EQU/00511/2013-LEPABE (Laboratory for Process Engineering, Environment, Biotechnology and Energy – EQU/00511) by FEDER funds through Programa Operacional Competitividade e Internacionalização – COMPETE2020 and by national funds through FCT (Project H2Solar; reference PTDC/EQU-EQU/107990/2008). Financial support by FP7 within Project NanoPEC - Nanostructured Photoelectrodes for Energy Conversion (contract number: 227179) is also acknowledged. The authors would like to acknowledge the fruitful discussions with Dr. C. Mateos-Pedrero and Dr. P. Tavares concerning the XRD analysis. The authors are also thankful to CEMUP for the SEM/EDS analysis.

REFERENCES

1. Grätzel, M., *Photoelectrochemical cells.* Nature, **2001**. 414(6861): p. 338-344.
2. Lopes, T., Dias, P., Andrade, L. and Mendes, A., *An innovative photoelectrochemical lab device for solar water splitting.* Solar Energy Materials and Solar Cells, **2014**. 128: p. 399-410.
3. Haussener, S., Hu, S., Xiang, C., Weber, A.Z. and Lewis, N.S., *Simulations of the irradiation and temperature dependence of the efficiency of tandem photoelectrochemical water-splitting systems.* Energy & Environmental Science, **2013**. 6(12): p. 3605-3618.
4. Andrade, L., Lopes, T. and Mendes, A., *Dynamic Phenomenological Modeling of Pec Cells for Water Splitting Under Outdoor Conditions.* Energy Procedia, **2012**. 22: p. 23-34.
5. Dias, P., Lopes, T., Andrade, L. and Mendes, A., *Temperature effect on water splitting using a Si-doped hematite photoanode.* Journal of Power Sources, **2014**. 272: p. 567-580.
6. Guillén, C. and Herrero, J., *TCO/metal/TCO structures for energy and flexible electronics.* Thin Solid Films, **2011**. 520(1): p. 1-17.
7. Granqvist, C.G., *Transparent conductors as solar energy materials: A panoramic review.* Solar Energy Materials and Solar Cells, **2007**. 91(17): p. 1529-1598.
8. Stefik, M., Cornuz, M., Mathews, N., Hisatomi, T., Mhaisalkar, S. and Grätzel, M., *Transparent, Conducting* Nb:SnO_2 *for Host–Guest Photoelectrochemistry.* Nano Letters, **2012**. 12(10): p. 5431-5435.
9. Kumar, V. and Wang, H., *Selection of metal substrates for completely solution-processed inverted organic photovoltaic devices.* Solar Energy Materials and Solar Cells, **2013**. 113: p. 179-185.
10. Solarska, R., Jurczakowski, R. and Augustynski, J., *A highly stable, efficient visible-light driven water photoelectrolysis system using a nanocrystalline* WO_3 *photoanode and a methane sulfonic acid electrolyte.* Nanoscale, **2012**. 4(5): p. 1553-1556.
11. Qi, H., Wolfe, J., Wang, D., Fan, H.J., Fichou, D. and Chen, Z., *Triple-layered nanostructured* WO_3 *photoanodes with enhanced photocurrent generation and*

superior stability for photoelectrochemical solar energy conversion. Nanoscale, **2014**. 6(22): p. 13457-13462.

12. Santato, C., Odziemkowski, M., Ulmann, M. and Augustynski, J., *Crystallographically Oriented Mesoporous* WO_3 *Films: Synthesis, Characterization, and Applications.* Journal of the American Chemical Society, **2001**. 123(43): p. 10639-10649.
13. Liu, X., Wang, F. and Wang, Q., *Nanostructure-based* WO_3 *photoanodes for photoelectrochemical water splitting.* Physical Chemistry Chemical Physics, **2012**. 14(22): p. 7894-7911.
14. Zhu, T., Chong, M.N. and Chan, E.S., *Nanostructured Tungsten Trioxide Thin Films Synthesized for Photoelectrocatalytic Water Oxidation: A review.* ChemSusChem, **2014**. 7(11): p. 2974-2997.
15. Meda, L., Tozzola, G., Tacca, A., Marra, G., Caramori, S., Cristino, V. and Alberto Bignozzi, C., *Photo-electrochemical properties of nanostructured* WO_3 *prepared with different organic dispersing agents.* Solar Energy Materials and Solar Cells, **2010**. 94(5): p. 788-796.
16. Meda, L., Tacca, A., Bignozzi, C.A., Caramori, S. and Cristino, V., *Modified tungsten oxide and process for its preparation*. **2012**, Google Patents.
17. Tacca, A., Meda, L., Marra, G., Savoini, A., Caramori, S., Cristino, V., Bignozzi, C.A., Pedro, V.G., Boix, P.P., Gimenez, S. and Bisquert, J., *Photoanodes Based on Nanostructured* WO_3 *for Water Splitting.* ChemPhysChem, **2012**. 13(12): p. 3025-3034.
18. T. Lopes, L.A., A. Mendes, *Photoelectrochemical Cells for Hydrogen Production from Solar Energy*, in *Solar Energy Sciences and Engineering Applications*, N.E.A. Akbarzadeh, Editor. **2013**, CRC Press. p. 293–341.
19. Lopes, T., Andrade, L., Le Formal, F., Gratzel, M., Sivula, K. and Mendes, A., *Hematite photoelectrodes for water splitting: evaluation of the role of film thickness by impedance spectroscopy.* Physical Chemistry Chemical Physics, **2014**. 16(31): p. 16515-16523.
20. Bignozzi, C.A., Caramori, S., Cristino, V., Argazzi, R., Meda, L. and Tacca, A., *Nanostructured photoelectrodes based on* WO_3*: applications to photooxidation of aqueous electrolytes.* Chemical Society Reviews, **2013**. 43(6): p. 2228-2246.

21. Dotan, H., Mathews, N., Hisatomi, T., Grätzel, M. and Rothschild, A., *On the Solar to Hydrogen Conversion Efficiency of Photoelectrodes for Water Splitting.* The Journal of Physical Chemistry Letters, **2014**. 5(19): p. 3330-3334.
22. Bartesaghi, D., Perez, I.d.C., Kniepert, J., Roland, S., Turbiez, M., Neher, D. and Koster, L.J.A., *Competition between recombination and extraction of free charges determines the fill factor of organic solar cells.* Nat Commun, **2015**. 6: p. 7083.
23. Macaira, J., Mesquita, I., Andrade, L. and Mendes, A., *Role of temperature in the recombination reaction on dye-sensitized solar cells.* Physical Chemistry Chemical Physics, **2015**. 17(35): p. 22699-22710.
24. Ng, C., Ng, Y.H., Iwase, A. and Amal, R., *Influence of Annealing Temperature of* WO_3 *in Photoelectrochemical Conversion and Energy Storage for Water Splitting.* ACS Applied Materials & Interfaces, **2013**. 5(11): p. 5269-5275.

CHAPTER 4

EXTREMELY STABLE BARE HEMATITE PHOTOANODE FOR SOLAR WATER SPLITTING

4

EXTREMELY STABLE BARE HEMATITE PHOTOANODE FOR SOLAR WATER SPLITTING

Paula Dias, António Vilanova, Tânia Lopes, Luísa Andrade and Adélio Mendes

Adapted from Nano Energy, 2016, 23

ABSTRACT

Photoelectrodes that are efficient, highly stable, made from low cost materials and easily prepared using inexpensive techniques are required for commercially viable photoelectrochemical (PEC) water splitting technology. Hematite is one of few materials that is being considered for this application. In this work, bare hematite thin films prepared by spray pyrolysis were systematically optimized following a design of experiments approach. A response surface methodology was applied to factors: i) sprayed volume of solution; ii) temperature of the glass substrate during the deposition; and iii) time gap between sprays and the optimized operating conditions obtained were v = 42 mL, T = 425 ºC and t = 35 s. The optimized hematite photoelectrode showed a photocurrent density of *ca.* 0.94 $mA \cdot cm^{-2}$ at 1.45 V_{RHE}, without dopants or co-catalysts, which is remarkable for a thin film of *ca.* 19 nm. The stability of this photoelectrode was assessed over 1000 h of PEC operation under 1-sun of simulated sunlight. A record-breaking result was obtained with no evidences of hematite film degradation neither of current density loss. These results open the door to turn PEC cells into a competitive technology in the solar fuel economy.

Keywords: Hematite Photoanodes, Photoelectrochemical Water Splitting, Spray Pyrolysis, Design of Experiments, Thin Films, Long-term Stability.

4.1 INTRODUCTION

Numerous metal oxide semiconductors have been tested for photoelectrochemical (PEC) water splitting and hematite (α-Fe_2O_3) photoanode is emerging as one of the most promising materials [1, 2]. Hematite offers a favorable combination of good visible light absorption (up to 590 nm), excellent chemical stability, non-toxicity, abundance and low price [3, 4]. Additionally, with a bandgap of 2.1 eV, α-Fe_2O_3 has a potential to convert *ca.* 16.8 % of the solar energy into hydrogen (STH), corresponding to a maximum thermodynamic STH efficiency of 12.6 $mA \cdot cm^{-2}$ [1, 5]. Recent works reviewing the progress of hematite photoanode identified many challenges to be overcome for an efficient performance in a PEC water splitting system [6, 7]:

i. Band edges not being properly aligned to the redox levels, *i.e.* flatband potential too low in energy for water reduction;
ii. Large overpotential for water oxidation, which can be addressed through the combination of two or more semiconductors in a tandem arrangement, *e.g.* a photocathode [8] or a photovoltaic (PV) cell [9, 10];
iii. Low absorption coefficient, requiring a long photon penetration depth with thicker films of 400 – 500 nm for complete light absorption [6];
iv. Poor majority carrier conductivity, demanding for high doping levels that will increase the ionized donor concentration and thus electrical conduction;
v. Short holes diffusion length (L_D = 2 – 4 nm), due to the ultrafast recombination of photogenerated minority carriers [11].

Research efforts along these drawbacks and further fundamental studies of PEC properties of hematite have shown: i) improvement of generated photocurrent density by morphology optimization (*e.g.* using different deposition methods [6]) and doping (*e.g.* with Si [12], Ti [13], Sn [14], Pt [15]); ii) improvement of generated photopotential minimizing the electron-hole recombination, especially at the photoelectrode surface [16]; and iii) reduction of the electrochemical activation overpotential using co-catalysts (*e.g.* IrO_2 [17], Co-Pi [15], $NiFeO_x$ [18]). Figure 4.1 shows the performance of an ideal hematite photoanode [6].

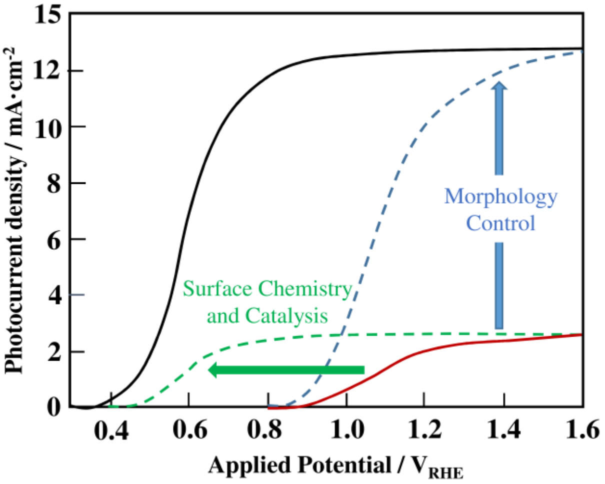

Figure 4.1: Ideal hematite performance (black line) compared to the typical performance (red line) under 1-sun AM 1.5 G illumination (adapted from ref. [6]).

The performance of hematite photoanodes is, therefore, very sensitive to the deposition method, either in terms of efficiency and stability. Innovative ways to control the morphology should be developed to optimize the hematite feature size/film thickness and crystals structure at nanometer length scale [19]. There are many deposition methods reported to deposit hematite: i) solution-based colloidal [15]; ii) electrochemical iron oxide nanostructuring; iii) spray pyrolysis (SP) and ultrasonic spray pyrolysis (USP) [20]; iv) atmospheric pressure chemical vapor deposition (APCVD) [17]; v) physical vapor deposition (PVD) [21]; and vi) atomic layer deposition (ALD) [11]. Table 4.1 reviews the hematite photoanodes literature, indicating the preparation techniques and the obtained photoresponse and stability.

Recently, Guo *et al.* [22] achieved a new record-breaking of *ca.* 5.70 mA·cm^{-2} at 1.23 V$_{RHE}$ with Ru-doped α-Fe_2O_3 nanorods films. This highly photoactive material was prepared by doctor blading process and followed by an annealing treatment at 700 ºC in air, showing a film thickness of 500 nm. However, the preparation of hematite thin films is desirable considering their charge transport limitation, *i.e.* thin films should minimize the recombination losses while light absorption is adaptable by the nanostructure thickness. Indeed, spray pyrolysis and ALD are the techniques that allow to deposit thinner films with good uniformity and photocurrent performance.

In the present study, hematite thin films were prepared by spray pyrolysis exhibiting high performance and great reproducibility, which is crucial for future industrial applications. The prepared hematite thin films revealed to be highly stable producing *ca.* 0.94 mA·cm^{-2} at 1.45 V_{RHE} over 1000 h of sunlight exposure (AM 1.5 G, 100 mW·cm^{-2}) in a 1 M NaOH electrolyte solution.

Table 4.1: Overview of the reported results for hematite photoanodes performance; grouped by technique and ordered by photoresponse, J_{photo}.

Technique	**Feature size/ Thickness**	**Dopant/ Treatment**	**PEC conditions**	**J_{photo} (1.23 V_{RHE})**	**Stability**	**Ref./ Date**
SP	50 – 100 nm	None/ None	1 M NaOH; 130 mW·cm^{-2}	0.2 mA·cm^{-2}		[23]/ 2005
SP	200 nm thick	Si/ SnO_2 underlayer	1 M NaOH; 80 mW·cm^{-2}	0.4 mA·cm^{-2}		[24]/ 2008
SP	23.3 nm thick	None/ TEOS underlayer	1 M NaOH; 100 mW·cm^{-2} (AM 1.5 G)	0.4 mA·cm^{-2}		[25]/ 2010
SP	30 nm thick	None/ Ga_2O_3 overlayer + Co^{2+} co-catalyst	1 M NaOH; 100 mW·cm^{-2}	0.4 mA·cm^{-2}	Stable over 4 h	[26]/ 2011
SP	30 nm thick	None/ Ga_2O_3 underlayer	1 M NaOH; 100 mW·cm^{-2}	0.4 mA·cm^{-2}		[27]/ 2011
SP	30 nm thick	None/ None	0.2 M Na_2SO_4; 100 mW·cm^{-2}	0.4 mA·cm^{-2}		[28]/ 2015
SP	800 nm thick	Al + Ti/ None	0.1 M NaOH; 150 W Xe lamp	1.1 mA·cm^{-2}		[29]/ 2005
SP	20 nm thick	Ti/ None	1 M NaOH; 150 mW·cm^{-2}	1.2 mA·cm^{-2}		[30]/ 2010
USP	50 nm thick	Si/ TEOS	1 M NaOH; 100 mW·cm^{-2}	0.3 mA·cm^{-2}	10 % decay after 144 h	[31] / 2014
USP	30 nm thick	Nb/ Ga_2O_3 overlayer + Co-Pi co-catalyst	1 M NaOH; 100 mW·cm^{-2}	0.5 mA·cm^{-2}		[11]/ 2014

USP	145 nm thick	Si (TEOS)/ None	1 M NaOH; 100 mW·cm^{-2}	0.9 mA·cm^{-2} and IPCE 16 % at 375 nm		[32]/ 2006
USP	100 nm	None/ None	1 M NaOH; 130 mW·cm^{-2}	1.1 mA·cm^{-2} and IPCE 16 % at 375 nm		[23]/ 2005
ALD	25 nm thick	None/ None	1 M NaOH; 100 mW·cm^{-2}	0.3 mA·cm^{-2}		[33]/ 2010
ALD	12 nm thick	TiO_2 underlayer + $Ni(OH)_2$ co-catalyst	1 M NaOH; 100 mW·cm^{-2}	0.3 mA·cm^{-2}		[34]/ 2015
ALD	22 nm thick	None/ Ga_2O_3 underlayer + Co-Pi co-catalyst	1 M NaOH; 100 mW·cm^{-2}	0.7 mA·cm^{-2}	Stable over 1 h	[35]/ 2014
ALD	32 nm thick	None/ Ga_2O_3 underlayer + $Ni(OH)_2$ co-catalyst	1 M NaOH; 100 mW·cm^{-2}	0.7 mA·cm^{-2}	Stable over 100 s	[36]/ 2014
APCVD	100 – 150 nm	None/ CoFPc co-catalyst	0.1 M NaOH; 100 mW·cm^{-2}	0.9 mA·cm^{-2} (bare: 0.3 mA·cm^{-2})	Stable over 1 h	[37]/ 2015
APCVD	500 nm thick	Si (TEOS)/ TEOS underlayer + $Co(NO_3)_2$ co-catalyst	1 M NaOH; 100 mW·cm^{-2}	2.7 mA·cm^{-2} and IPCE 36 % at 400 nm		[38]/ 2006
APCVD	700 nm thick	Si (TEOS)/ Al_2O_3 overlayer and Co^{2+} co-catalyst	1 M NaOH; 100 mW·cm^{-2}	2.7 mA·cm^{-2}	Unstable over 1 h	[39]/ 2011
APCVD	700 nm thick	Si (TEOS)/ IrO_2 co-catalyst	1 M NaOH; 100 mW·cm^{-2}	3.0 mA·cm^{-2} and IPCE 50 % at 320 nm	Slight decay over 200 s	[17]/ 2010
ED[a]	23 nm/ 920 nm thick	Zr/ None	1 M NaOH, 150 mW·cm^{-2}	0.1 mA·cm^{-2}	Stable over 1 h	[40]/ 2010
ED	70 – 100 nm/ 1.3 – 1.8 µm thick	Cd/ None	1 M NaOH, 410 mW·cm^{-2}	1.4 mA·cm^{-2}		[41]/ 2011

ED	20 – 50 nm	Mo/ None	1 M NaOH, 410 $mW\cdot cm^{-2}$	1.5 $mA\cdot cm^{-2}$ and IPCE 8 % at 400 nm		[42]/ 2008
ED	100 – 200 nm/ 200 – 300 nm thick	Ti + Zn/ None	1 M NaOH; 100 $mW\cdot cm^{-2}$	1.5 $mA\cdot cm^{-2}$		[43]/ 2014
PVD (PLD[b])	70 nm thick	None/ TEOS underlayer	1 M NaOH; 100 $mW\cdot cm^{-2}$	0.3 $mA\cdot cm^{-2}$		[44]/ 2010
PVD (HiPMS[c])	45 nm thick	None/ None	1 M NaOH; 100 $mW\cdot cm^{-2}$	0.3 $mA\cdot cm^{-2}$ and IPCE 11 % at 350 nm	Stable over 3 h	[45]/ 2015
PVD (PLD)	70 nm thick	None/ FeOOH co-catalyst	1 M NaOH; 100 $mW\cdot cm^{-2}$	0.9 $mA\cdot cm^{-2}$ IPCE 20 % at 400 nm (bare: 0.2 $mA\cdot cm^{-2}$)	4.4 % decay over 70 h	[21]/ 2015
Single crystal	µm	Nb/ None	1 M NaOH; 100 W/Hg lamp (20 $mW\cdot cm^{-2}$)	135 $\mu A\cdot cm^{-2}$ and IPCE 37 % at 370 nm		[46]/ 1988
Sintered p-crystalline disk	µm	Si/ None	1 M NaOH; 100 $mW\cdot cm^{-2}$	125 $\mu A\cdot cm^{-2}$ and IPCE 34 % at 400 nm		[47]/ 1982
Solution-based colloidal	30 – 40 nm/ 300 nm thick	Ti/ SiO2	1 M NaOH, 100 $mW\cdot cm^{-2}$	0.8 $mA\cdot cm^{-2}$ IPCE 47 % at 350 nm		[48]/ 2010
Solution-based colloidal	500 nm thick	None/ Pi coating	0.1 M K-Pi; 100 $mW\cdot cm^{-2}$	1.3 $mA\cdot cm^{-2}$ (bare: 0.3 $mA\cdot cm^{-2}$)	Stable over 3 h (bare: 75 % decay)	[49]/ 2014
Solution-based colloidal	40 nm/ 100 nm thick	Sn/ None	1 M NaOH, AM 1.5 G 100 $mW\cdot cm^{-2}$	1.9 $mA\cdot cm^{-2}$ and IPCE 19.2 % at 400 nm		[14]/ 2011
Solution-based colloidal	500 nm thick	P/ Co-Pi co-catalyst	1 M NaOH; 100 $mW\cdot cm^{-2}$	3.1 $mA\cdot cm^{-2}$ (bare: 0.8 $mA\cdot cm^{-2}$)	12 % decay after 1 h (bare: stable over 40 h)	[49]/ 2015
Solution-based colloidal	50 nm/ 500 nm thick	Pt/ Co-Pi co-catalyst	1 M NaOH; 100 $mW\cdot cm^{-2}$	4.3 $mA\cdot cm^{-2}$ and IPCE 60 % at 375 nm (bare: 1.3 $mA\cdot cm^{-2}$)	Stable over 3 h	[15]/ 2013

Solution-based colloidal	500 nm thick	Ru	1 M NaOH; 100 mW·cm^{-2}	5.7 mA·cm^{-2} and IPCE 82 % at 320 nm (bare: 0.31 mA·cm^{-2})	[22]/ 2015

[a] **ED:** electrodeposition

b **PLD:** pulsed layer deposition

c **HiPIMS:** high impulse power magnetron sputtering

4.2 EXPERIMENTAL

4.2.1 HEMATITE PHOTOANODES PREPARATION

The synthesized materials were prepared by spray pyrolysis in an in-house assembled setup consisting of: i) spray pyrolysis chamber; ii) automatic syringe pump; iii) liquid and air feeding system; and iv) spray nozzle and its control system; v) heating plate and its control system – Figure 4.2. The spray nozzle (Spraying Systems Co. model SU J4B-SS) was fed with an ethanolic solution of iron (iron (III) acetylacetonate - $Fe(AcAc)_3$) and mixed with compressed air, directing the spray to the substrates at *ca.* 2 bar. An automatic syringe pump (Cronus programmable Sigma 2000 C, SMI-Labhut Ldt, UK) was used to deliver 1 mL of 10 mM of $Fe(AcAc)_3$ (99.9 %, Aldrich) in EtOH (99.5 %, Aga) to the spray head, at a flowrate of 12 mL·min^{-1} (spray length of 5 s). The heated plate, 18 × 18 cm^2, displayed a uniform surface temperature regulated up to 550 ºC. The substrates were placed on the heated plate at constant temperature; a range of 400 ºC to 500 ºC was tested. After the spray deposition, the hematite samples were air-annealed for 30 min at 550 ºC, before being cooled down to the room temperature. This setup allows depositing homogeneous films up to 10 × 10 cm^2. For each set of parameters tested, three samples were prepared to assess the reproducibility.

The photoanodes were prepared on 2.2 mm thick, 7 Ω·square^{-1} fluorine-doped tin oxide (FTO) coated glass substrates (Solaronix, Switzerland). The glasses were adequately cleaned as described elsewhere [50]. A TEOS (tetraethyl orthosilicate) pre-treatment was also performed to allow better α-Fe_2O_3 film organization, reducing the interfacial strain between the FTO layer and the hematite crystals and, consequently, a photoactivity response improvement [25]. The FTO-glass substrates were heated at 450 ºC and *ca.* 1.5 mL of a diluted TEOS solution (10 % volume in ethanol) were hand-sprayed with a glass atomizer onto the heated substrates. These samples were cooled down before heating again to deposit the hematite film.

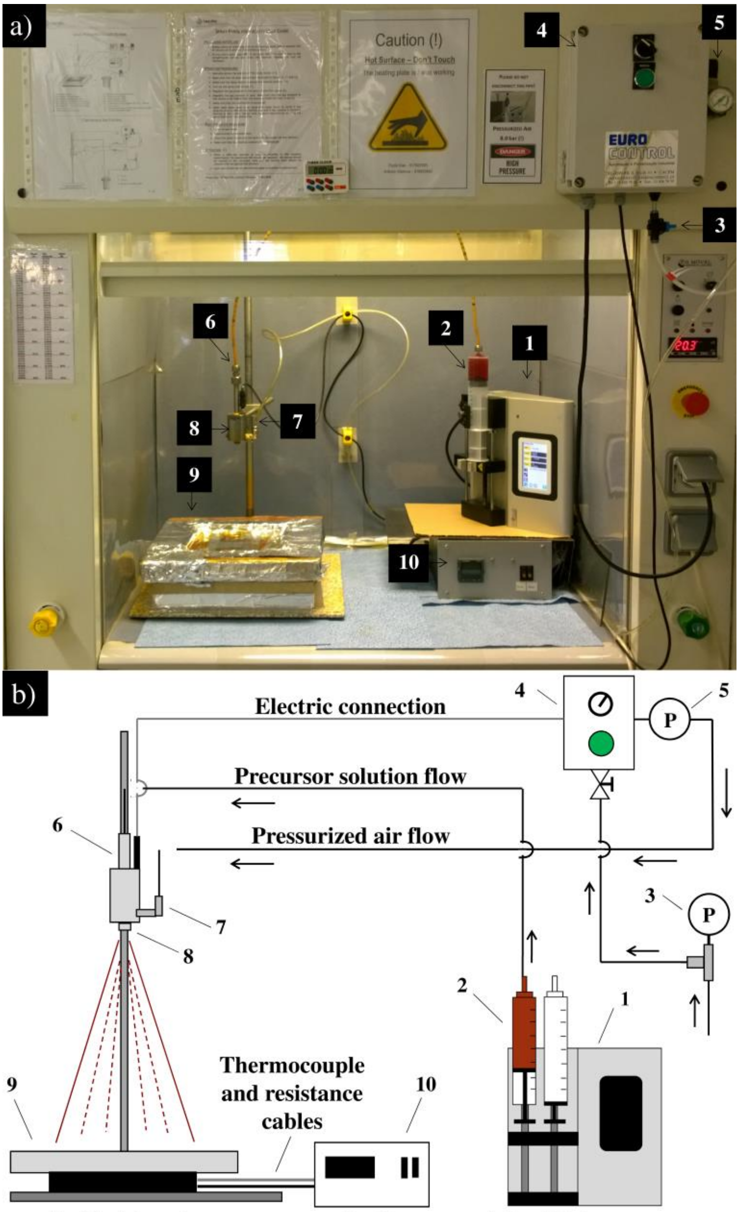

1 – Double syringe pump
2 – Plastic syringes
3 – Pressurized air
4 – Spray control box
5 – Pressurized air outlet
6 – Precursor solution inlet
7 – Pressurized air inlet
8 – Spray nozzle
9 – Heating plate with ceramic insulation
10 – Temperature control box

Figure 4.2: Spray pyrolysis setup assembled for the deposition of hematite films: (a) photograph; and (b) schematic representation.

4.2.2 RESPONSE SURFACE METHODOLOGY

According to literature [12, 23], the deposition of hematite films by spray pyrolysis technique strongly depends on several operating parameters. An optimization procedure is necessary to obtain the best operating conditions and, therefore, to develop an efficient and stable photoanode. This optimization was done using a response surface methodology implemented in a commercial software (JMP 8.0.2, SAS software). This method combines mathematical and statistic tools for studying effective way processes where responses are dependent on several operating variables [51]. In this work the central composite design method was considered for fitting the obtained second order models. The selected response variable was the photocurrent density (J_{photo}, in mA·cm^{-2}) generated by the prepared material at a bias potential of 1.45 V_{RHE}.

Several preliminary tests were performed to assess the influence of different operating conditions on the performance of the bare hematite photoanodes. The deposition parameters selected for optimization were: i) sprayed solution volume (v); ii) temperature of the glass substrate during the deposition (T); and iii) time gap between sprays (t) – Table 4.2. The following parameters were set constant: i) concentration of the iron solution was 10 mM; ii) distance of the spray head to the sample was 20 cm and; iii) annealing temperature was 550 ºC.

Table 4.2: Central composite design factors and their respective levels.

Factor	**Symbol**	**Level**		
		-1	**0**	**1**
***v* / mL**	x_1	30	45	60
***T* / ºC**	x_2	400	450	500
***t* / s**	x_3	30	45	60

For generating the design matrices, dimensionless (coded) factors (X_i), ranging from –1 to +1 were used. These factors are computed from their actual values (x_i), middle value and the semi-variation interval according to [52]:

$$X_1 = \frac{x_1 - 45}{15}; \qquad X_2 = \frac{x_2 - 450}{50}; \qquad X_3 = \frac{x_3 - 45}{15} \tag{4.1}$$

4.2.3 ELECTROCHEMICAL CHARACTERIZATION

A PEC cell device known as “cappuccino” [53] was chosen to perform the electrochemical characterization of the prepared hematite photoanodes - Figure 4.3. This cell was filled with a 1 M NaOH (25 ºC, pH 13.6) electrolyte solution in which the photoelectrode was immersed. The surface area illuminated was *ca.* 0.5 cm^2 defined by an external mask. A standard three-electrode configuration was used: Ag/AgCl/Sat. KCl (Metrohm, Switzerland) as a reference electrode (RE), 99.9 % pure platinum wire (Alfa Aesar®, Germany) as counter electrode (CE) and hematite photoanodes as working electrodes (WE).

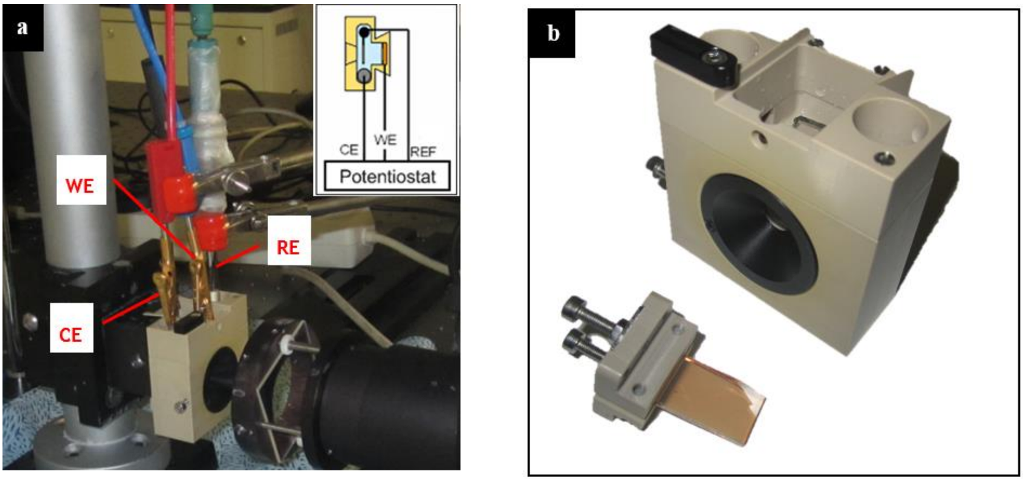

Figure 4.3: Details of the test bench: (a) the cappuccino PEC cell in a three-electrode configuration; and (b) the cappuccino PEC cell with a hematite photoelectrode placed on the sample holder.

J-V MEASUREMENTS

J-V characteristic curves were obtained applying an external potential bias to the cell and measuring the generated photocurrent using a ZENNIUM workstation (Zahner Elektrik, Germany) controlled by Thales software package (Thales Z 2.0). The applied potential bias was reported as a function of the reversible hydrogen electrode (RHE). The measurements were performed at room temperature in dark and under 1-sun simulated sunlight, at a scan rate of 10 mV·s^{-1} between 0.80 and 1.80 V$_{RHE}$. A class B solar simulator equipped with a 150 W Xe lamp (Oriel, Newport, USA) and an

AM 1.5 G filter (100 mW·cm^{-2}; Newport, USA) was used; the light beam was calibrated with a c-Si photodiode (Newport, USA).

EIS MEASUREMENTS

EIS analyses were performed applying a small potential sinusoidal perturbation to the system. The amplitude and the phase shift of the resulting current response was recorded using also the ZENNIUM workstation. The frequency range was 0.1 Hz – 100 kHz and the amplitude 10 mV. The measurements were carried out in dark conditions and the range of the applied potential was equal to that of the photocurrent measurements (0.80 – 1.80 V_{RHE}) with a step of 50 mV. An appropriate electrical analog was then fitted to the EIS spectra using the ZView software (Scribner Associates Inc., USA).

STABILITY TESTS

During stability tests the hematite photoanodes were continuously submitted to 1-sun simulated solar illumination (100 mW·cm^{-2}) at 1.45 V_{RHE}. The photocurrent density response was monitored as a function of time using an AUTOLAB electrochemical station (Metrohm Autolab B.V., Netherlands). The lamp power used was a Plasma-I AS1300 light engine (Plasma International, Germany) equipped with a standard sulphur lamp (SS0); a c-Si photodiode was used for light calibration. The photocurrent history of the prepared hematite photoanodes was assessed over 1000 h.

DETERMINATION OF INTRINSIC SOLAR TO CHEMICAL CONVERSION EFFICIENCY

Dotan *et al.* [54] proposed the intrinsic solar to chemical (*ISTC*) conversion efficiency model, obtained from the photocurrent density-voltage (*J-V*) characteristic curves in the dark and under illumination. Briefly, this parameter indicates the efficiency of the photoanode in converting photonic energy into chemical energy used for oxidizing water. Thus, the *ISTC* efficiency of the photoanode is given by [54]:

$$ISTC = \eta_{\mathrm{el}} \left. \frac{J_{\mathrm{photo}} \times E_{\mathrm{photo}}}{P_{\mathrm{light}}} \right|_{\mathrm{AM\ 1.5\ G}} \cong \frac{1.23(V_{\mathrm{RHE}})}{U_{\mathrm{dark}}(V_{\mathrm{RHE}})} \left[\frac{J_{\mathrm{photo}}\left(\mathrm{mA \cdot cm^{-2}}\right) \times E_{\mathrm{photo}}(\mathrm{V})}{100(\mathrm{mW \cdot cm^{-2}})} \right] \quad (4.2)$$

where η_{el} is the electrolysis efficiency, J_{photo} is the generated photocurrent, E_{photo} is the correspondent photopotential and U_{dark} is the potential that must be applied to the photoanode in order to reach the respective current in the dark. After computing the photocurrent (J_{photo}) and photopotential (E_{photo}) from *J*-*V* curves, the photocurrent as a function of the photopotential was drawn to obtain the intrinsic photovoltaic characteristics of the photoanode, *i.e.* the photocurrent density measured under short-circuit conditions (J_{sc}) and open-circuit photopotential (V_{oc}). The intrinsic photovoltaic power (*P*) of the photoanode is the product of photocurrent to the photopotential; by plotting it *vs.* photopotential, the maximum power point (MPP) can be obtained and also the respective potential (E_{MPP}) and current (J_{MPP}).

4.2.4 STRUCTURAL CHARACTERIZATION

FILM THICKNESS DETERMINATION

UV-visible absorption data were used to estimate the hematite samples thickness. Since there is a similarity in the shape of the spectra for all samples, their thicknesses can be estimated assuming a Lambertian absorption behavior:

$$\ln(1 - abs) = -\alpha \cdot \ell \qquad (4.3)$$

where *abs* is the absorbance, α is the hematite absorbance coefficient (44 nm)$^{-1}$ at 400 nm [55] and ℓ is the thickness of the hematite film in nanometers. An UV-vis-NIR spectrophotometer (Shimadzu Scientific Instruments Inc., model UV-3600, Kyoto) was used to obtain the absorbance of the prepared hematite samples. It was decided to measure the reflectance and transmittance of all samples and then to calculate the absorbance by subtracting both to the incident radiation. Finally, the absorbance was corrected by subtracting the FTO glass absorbance (control).

SCANNING ELECTRON MICROSCOPY (SEM) ANALYSIS

SEM was used to obtain information on the morphology and surface topography of the prepared materials. The morphology of the hematite films was characterized using a high-resolution scanning electron microscope (Quanta 400 FEG, FEI Company, USA); the analyses were made at CEMUP (Centro de Materiais da Universidade do Porto). The acceleration voltage was 15 keV while an in-lens detector was employed with a working distance of about 10 mm. The surface of fresh and aged samples was examined in order to identify and analyze modifications in their surface morphology.

X-RAY DIFFRACTION (XRD) ANALYSIS

XRD analysis was carried out in a PANalytical X’Pert MPD (Spectris plc, England) equipped with an X’Celerator detector and secondary monochromator (Cu $K\alpha\,\lambda$ = 0.154 nm, 40 kV, 30 mA; data recorded at a 0.017 step size, 100 $\text{s}\cdot\text{step}^{-1}$). Rietveld refinement with Powder-Cell software was used to identify the crystallographic phases from the XRD diffraction patterns.

4.2.5 ELECTROLYTE CHARACTERIZATION

INDUCTIVELY COUPLED PLASMA (ICP) TECHNIQUE

ICP-AES (atomic emission spectroscopy) technique was used to determine the concentration of iron in the NaOH electrolyte solution used in the stability test. Electrolyte samples of *ca.* 50 cm^3 were tested.

4.3 RESULTS AND DISCUSSION

4.3.1 RESPONSE SURFACE METHODOLOGY

A design of experiments (DoE) approach was used to optimize the bare hematite deposition. Table 4.3 shows the experiments plan generated by the DoE software; a second order polynomial equation was fitted to the obtained results:

$$y = f_0 + \sum_{i=1}^{3} f_\text{i} X_\text{i} + \sum_{i=1}^{3}\sum_{j=1}^{3}\left(f_\text{ij} X_\text{i} X_\text{j} + f_\text{ii} X_\text{i}^2 \right) \tag{4.4}$$

where y is the process response, X_i are the dimensionless process factors, a_0 is the interception coefficient, a_i are the coefficients related to the dimensionless factors X_i, a_ij correspond to the cross interaction between different factors and a_ii are the coefficients related to the quadratic effects (curvature).

Table 4.3: Actual and coded values for the central composite design run conditions.

Runs	Actual values			Coded values		
	x_1 / mL	x_2 / ºC	x_3 / s	X_1	X_2	X_3
1	30	500	60	-1	1	1
2	60	400	30	1	-1	-1
3	30	400	60	-1	-1	1
4	60	450	45	1	0	0
5	45	500	45	0	1	0
6	45	450	45	0	0	0
7	45	450	60	0	0	1
8	60	400	60	1	-1	1
9	60	500	60	1	1	1
10	30	450	45	-1	0	0
11	45	400	45	0	-1	0
12	60	500	30	1	1	-1
13	30	500	30	-1	1	-1
14	30	400	30	-1	-1	-1
15	45	450	45	0	0	0
16	45	450	30	0	0	-1

A standard least squares analysis was performed and the *p*-values (*Prob* > *F*) were used to assess the relevance of each factor to the process response. Smaller *p*-values correspond to the higher significance factors, *i.e.* *p*-values < 0.05 indicate that the parameter has a relevant effect on the response with a confidence level of more than 95 %. A factor has a marginal effect on the model response when 0.05 < *p*-value < 0.15 and should be neglected if *p*-values > 0.15 [51]. Following these criteria, the final model is:

$$\begin{aligned} J = 0.852 + 0.003X_1 - 0.058X_2 - 0.019X_3 + 0.016X_1X_2 + \\ 0.053X_1X_3 - 0.066X_1^2 - 0.068X_2^2 - 0.036X_3^2 \end{aligned} \tag{4.5}$$

The fitting model was used to predict the photocurrent density obtained at 1.45 V_{RHE}. Figure 4.4 shows the corresponding parity plot.

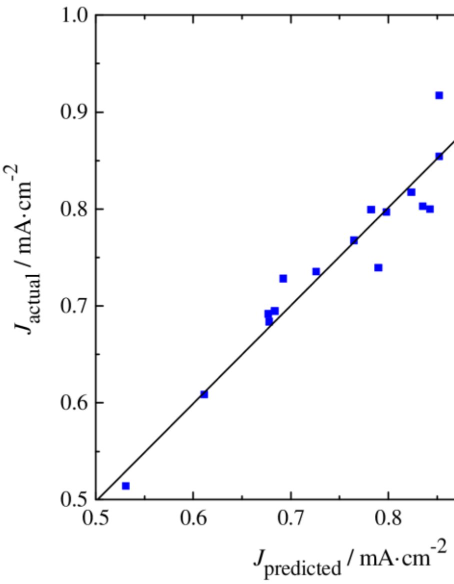

Figure 4.4: Parity plot of experimental *vs.* predicted photocurrent values for the prepared hematite samples.

The parity plot indicates a quite good agreement of the empirical model to the experimental values, which is also confirmed by the high correlation coefficient of the fitting model ($R^2 = 0.92$). The empirical model was then used to study the influence of each operating parameter on the photocurrent density - Figure 4.5.

Based on the interpolating model, the operating conditions that give the highest photocurrent density at 1.45 V_{RHE}, $J_{photo} = (0.90 \pm 0.06)$ mA·cm^{-2}, are the following: $v = 42$ mL, $T = 425$ ºC and $t = 35$ s. A new deposition was then performed using these optimal conditions and the prepared hematite samples showed an average photocurrent density of (0.94 ± 0.04) mA·cm^{-2}, in line with the empirical model. The film thickness of the optimized sample, estimated from Equation (4.3), was *ca.* (18.8 ± 0.1) nm; the literature refers that a film thickness of *ca.* (20.0 ± 2.2) nm maximizes the internal quantum yield [56].

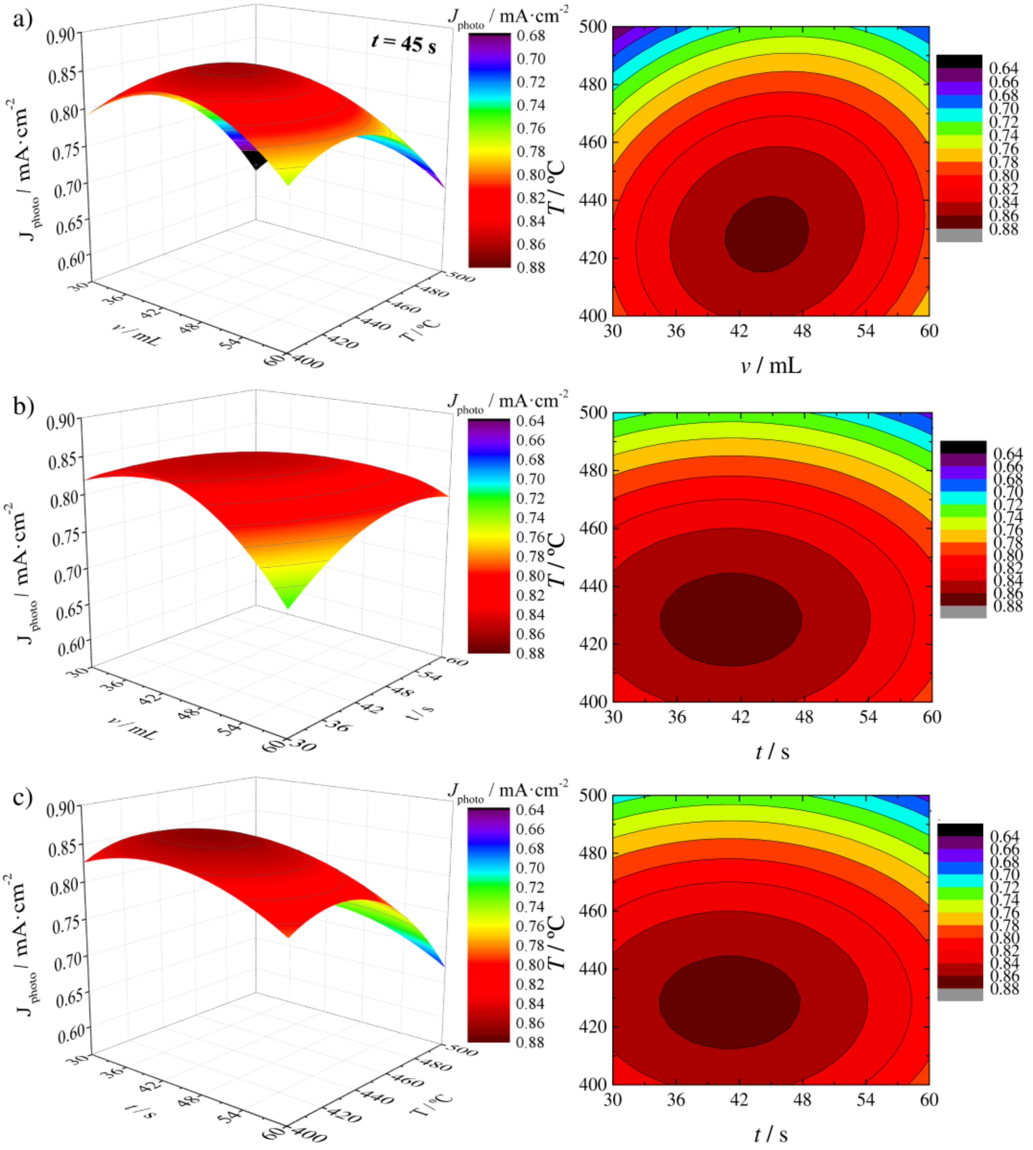

Figure 4.5: Predicted photocurrent density (J_{photo}) as a function of: (a) sprayed solution volume (v) and temperature of the glass substrate during the deposition (T) for a time gap between sprays of 45 s (t); (b) v and t for T = 450 ºC; and (c) t and T for v = 45 mL.

4.3.2 *J-V* CHARACTERISTIC CURVES

The performance of the bare hematite photoanodes was assessed based on the photocurrent-voltage (*J-V*) curves in dark and under 1-sun AM 1.5 G illumination (100 mW·cm^{-2}) conditions. The characteristic curves of each photoanode sample are summarized in Table 4.4. The replicated curves differ less than 10 % from each other.

Table 4.4: Experimental conditions of the DoE (sprayed solution volume – v, temperature of substrate during the deposition – T and time gap between sprays – t), correspondent photocurrent density values at 1.45 V$_{RHE}$ (experimentally – J_{actual} and predicted by DoE – $J_{predicted}$) and thickness of the prepared hematite photoanodes – ℓ.

v / mL	T / ºC	t / s	J_{actual} / mA·cm^{-2}	$J_{predicted}$ / mA·cm^{-2}	ℓ / nm
30	500	60	0.51	0.53	16.73
60	400	30	0.73	0.69	22.12
30	400	60	0.70	0.68	17.28
60	450	45	0.74	0.79	23.60
45	500	45	0.74	0.73	18.48
45	450	45	0.92	0.85	19.86
45	450	60	0.80	0.80	19.77
60	400	60	0.77	0.77	21.33
60	500	60	0.69	0.68	24.47
30	450	45	0.80	0.78	22.70
45	400	45	0.80	0.84	23.39
60	500	30	0.61	0.61	24.43
30	500	30	0.68	0.68	18.73
30	400	30	0.82	0.82	12.89
45	450	45	0.85	0.85	22.65
45	450	30	0.80	0.84	20.88
42	425	35	0.94	0.90	18.84

The *J-V* characteristic curve for the best performing hematite sample prepared at the optimized conditions is shown in Figure 4.6a. Under dark conditions the current steeply increased for a potential higher than 1.66 V$_{RHE}$, indicating the electrochemical water oxidation onset potential. Under sunlight conditions the sample showed an onset potential at *ca.* 0.95 V$_{RHE}$ and photocurrent densities of *ca.* 0.67 mA·cm^{-2} at the potential of reversible oxygen electrode (1.23 V_{RHE}) and *ca.* 0.94 mA·cm^{-2} at 1.45 V_{RHE}. These performance values represent one of the highest photocurrents ever reported for bare hematite photoanodes. To date, the best performing hematite photoanode was reported by Guo *et al.* [22] for Ru-doped α-Fe_2O_3 nanorod films; however, the bare hematite sample (prepared by doctor blading method and then annealed at 750 ºC) showed a low photocurrent of *ca.* 0.31 mA·cm^{-2} at 1.23 V_{RHE}. Among hematite samples prepared by spray pyrolysis, the present result is *ca.* 65 % greater [25].

From the *J-V* plots, the intrinsic power characteristics of the photoelectrode were then obtained as reported elsewhere [54]. First, the photocurrent (J_{photo}) and photopotential (E_{photo}) were determined from the difference between the light and dark currents and potentials, respectively. After computed these parameters, the J_{photo} was plotted as a function of the E_{photo} to obtain the photocurrent density measured under short-circuit conditions (J_{sc}) and the open-circuit photopotential (V_{oc}) - Figure 4.6b. Consequently, the intrinsic photovoltaic power (P) of the photoanode, which is given by the product of J_{photo} by E_{photo}, was plotted *vs.* E_{photo} (Figure 4.6c). The potential applied to the photoanode under light, U_{light}, is also shown in secondary *y* axis of these figures *vs.* E_{photo}. Thus, the optimized hematite photoelectrode reached a maximum power of 0.43 %, showing that this sample generated an electric power of 0.43 mW·cm^{-2} from the solar-simulated light power of 100 mW·cm^{-2}. At this point, the photoanode delivers the highest power with $E_{MPP} = 0.54$ V by applying a potential, U_{light}, of *ca.* 1.30 V_{RHE}. A fill factor of 50.55 % at the maximum power point was obtained; fill factor values of less than 40 % are generally observed with hematite photoelectrodes [54, 56].

The intrinsic solar to chemical (*ISTC*) conversion efficiency of the photoanode was computed from Equation (4.2) and it was plotted in Figure 4.6d as a function of the generated photocurrent density, J_{photo}. The *ISTC* efficiency reached a maximum of *ca.* 0.29 % at $J_{MPP} = 0.80$ mA·cm^{-2}; this defines the optimal conditions for operating the PEC cell. This photocurrent could only be obtained in the dark at a potential of 1.85 V_{RHE} (see Figure 4.6a) meaning that the simulated solar light power saved 0.54 V from the external power source, *i.e.* a power of 0.43 mW·cm^{-2} ($0.54 \times J_{MPP}$). Therefore, the conversion efficiency of the electrolysis reaction ($\eta_{el} \approx 1.23/U_{dark} = 66.40$ %) reduced the electric power saved, which is the light-induced contribution to the chemical power produced by the photoanode of *ca.* 0.29 mW·cm^{-2} (66.40 % × 0.43 mW·cm^{-2}).

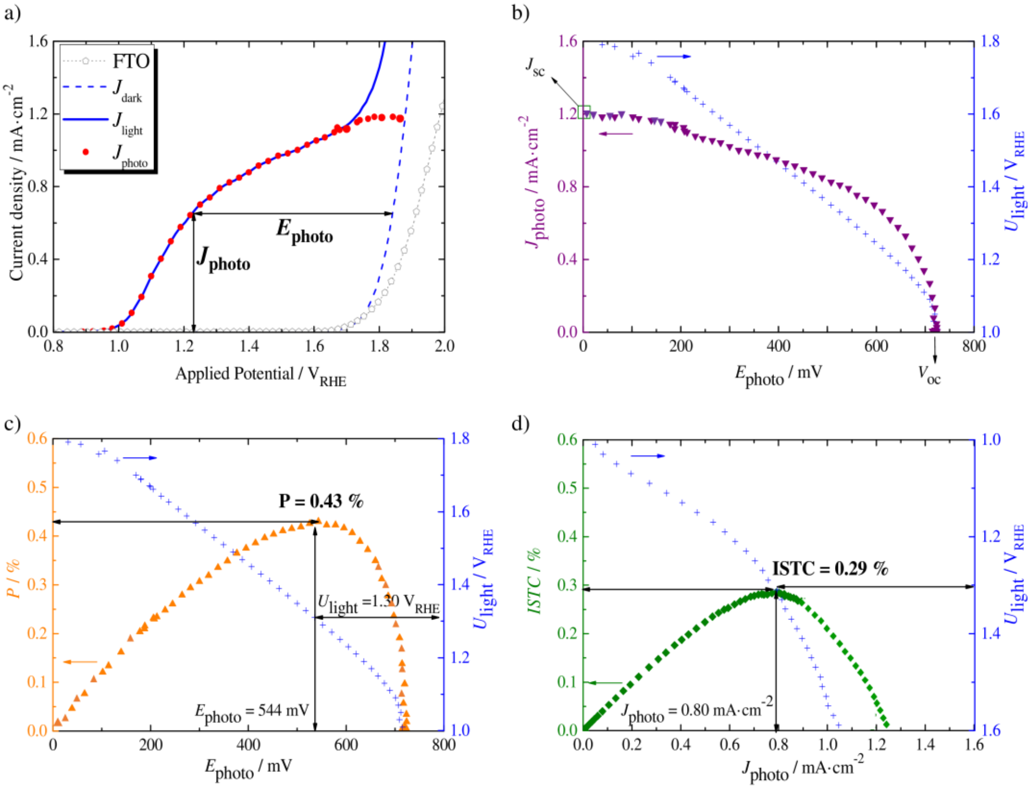

Figure 4.6: (a) *J*-*V* characteristic curves obtained in the dark (dashed blue line) and under 1-sun AM 1.5 G illumination (100 mW·cm^{-2}, solid blue line) and the generated photocurrent, J_{photo} (●). (b) Photocurrent (▼) as a function of the photopotential. (c) Intrinsic photovoltaic power (▲) as a function of the photopotential. (d) *ISTC* efficiency (♦) as a function of the photocurrent density. The secondary *y* axis on the right of the plots (b), (c) and (d) shows the potential (U_{light}) that was applied to the photoanode by the potentiostat under light conditions.

4.3.3 ELECTROCHEMICAL IMPEDANCE SPECTROSCOPY

The electrochemical impedance measurements were performed in the dark and using a three-electrode configuration. In this configuration the potential is measured with respect to a fixed reference potential, short-circuited with the Pt counter electrode. This enables the detailed study of the electrochemical phenomena occurring at the interface between photoelectrode and electrolyte. Herein, the EIS data were analyzed based on the Randles electrical analogue circuit [11]. This electrical analogue comprises a series resistance (R_{Series}) and a simple resistor-capacitor (RC) element assigned to the semiconductor/electrolyte charge transfer resistance, R_{CT}, together with bulk capacitance, C_{Bulk} - Figure 4.7a.

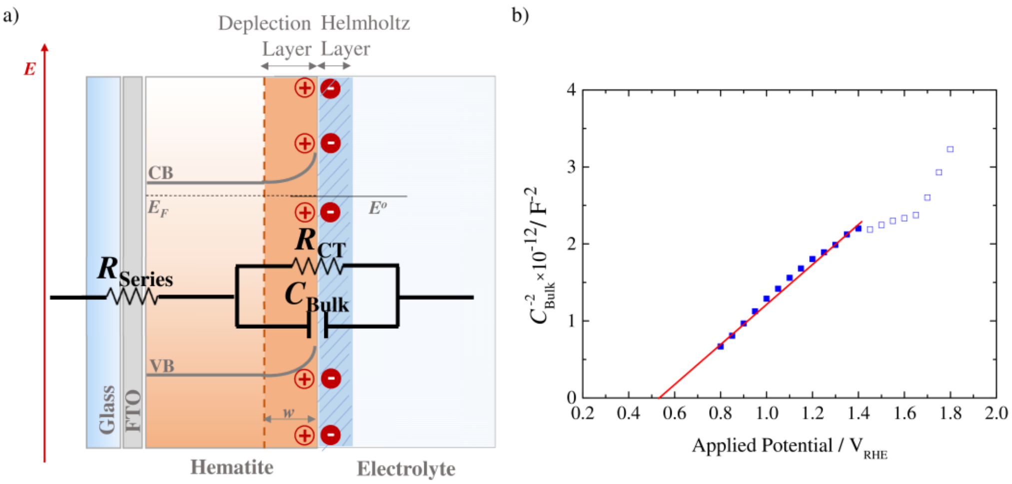

Figure 4.7: (a) Energy diagram of the semiconductor/electrolyte interface and the electrical circuit analogue used to fit the impedance measurements in the dark of the optimized hematite sample. (b) Mott-Schottky analysis: the inverse of the square bulk capacitance (C_{Bulk}) is plotted *vs.* the potential bias applied.

For using the Mott-Schottky model two main assumptions must be guaranteed: i) the space charge (C_{SC}) and Helmholtz (C_{H}) capacitances can only be fitted as a single capacitance, the so-called C_{Bulk}, since the contribution of the double layer capacitance to the total capacitance would be negligible (2 – 3 orders of magnitude higher); and ii) the fitting should be made at the high frequency range of the impedance spectra, in the order of kHz [55]. Then, the flat band potential, E_{fb}, and the donor density, N_{D}, were obtained from Equation (4.6):

$$\frac{1}{C_{\mathrm{Bulk}}^{2}}=\frac{2}{\varepsilon_0\varepsilon_{\mathrm{r}}qN_{\mathrm{D}}A^{2}}\left(\left(E_{\mathrm{bias}}-E_{\mathrm{fb}}\right)-\frac{kT}{q}\right) \tag{4.6}$$

where ε_0 is the vacuum permittivity (8.85×10^{-12} C·V^{-1}·m^{-1}), ε_{r} is the dielectric constant of the semiconductor (assumed to be 80 for undoped hematite photoanodes [12]), q is the elementary charge, A is the active area, k is the Boltzmann constant, T is the absolute temperature, and E_{bias} is the applied bias potential. Plotting C_{Bulk}^{-2} as a function of the applied bias potential, a straight line was obtained in the linear region of the plot, from 0.80 to 1.40 $\mathrm{V_{RHE}}$, as shown in Figure 4.7b. N_{D} value was determined from the slope of this line, while the E_{fb} value was obtained extrapolating the interception of the straight line with the axis of the applied potential. From Equation (4.6), E_{fb} = 0.54 $\mathrm{V_{RHE}}$ and $N_{\mathrm{D}} = 2.42 \times 10^{18}$ cm^{-3}. These values are in good agreement with the ones found in the literature; consistent values of E_{fb} from 0.40 – 0.60 $\mathrm{V_{RHE}}$ and N_{D} on the order of 10^{17} to 10^{21} cm^{-3} have been reported for undoped and heavily doped hematite samples, respectively [6]. Thus, the obtained value for the donor density confirmed that the pre-treatment with TEOS before spraying the ultra-thin Fe_2O_3 layer is not acting as a doping agent.

4.3.4 LONG-TERM STABILITY

Recent studies have increasingly mentioned the importance of obtaining highly stable photoelectrodes as a critical objective to achieve commercial viability of photoelectrochemical hydrogen production devices [57]. Therefore, the stability of the optimised hematite sample was evaluated during a period of time of 1000 h under a bias potential of 1.45 $\mathrm{V_{RHE}}$ and 1-sun AM 1.5 G illumination (100 mW·cm^{-2}). The photocurrent history is plotted in Figure 4.8. The photocurrent density values, obtained every 48 h, are presented in Table 4.5.

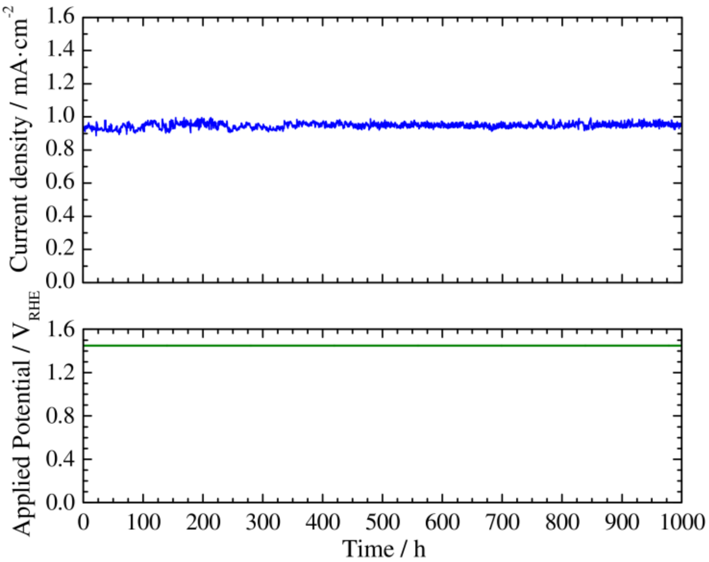

Figure 4.8: Polarization curve of the optimized hematite samples prepared by spray pyrolysis (solid blue line) obtained under a constant bias of 1.45 V_{RHE} and simulated solar illumination (100 $mW \cdot cm^{-2}$).

Table 4.5: Photocurrent density (*J*) values obtained from the *J-V* curves at 1.45 V_{RHE} for different times (*t*) under continuous exposure to simulated sunlight radiation.

***t* /h**	**0**	**48**	**96**	**144**	**192**	**240**	**288**	**336**	**384**	**432**	**500**
***J* /mA·cm^{-2}**	0.94	0.92	0.92	0.91	0.98	0.94	0.95	0.97	0.97	0.94	0.95
***t* /h**	**528**	**576**	**624**	**672**	**720**	**768**	**816**	**864**	**912**	**960**	**1000**
***J* /mA·cm^{-2}**	0.95	0.94	0.95	0.96	0.95	0.95	0.95	0.95	0.95	0.94	0.95

From Figure 4.8 it can be concluded that the optimized hematite sample is stable over 1000 h (approximately 42 days) with an average photocurrent density of *ca.* 0.95 $mA \cdot cm^{-2}$. To the best knowledge of the authors there are no published results for stability of hematite photoanodes for such long period. Figure 4.9 shows the *J-V* characteristic curves obtained before performing the stability test and after 500 and 1000 h of simulated sunlight exposure; no significant differences were observed for the response under light conditions. On the other hand, the dark current onset potential shifted slightly to lower potentials, which may be related to increased FTO areas exposed to electrolyte [31, 55, 58]. Figure 4.10 shows SEM images and EDS analyses of the fresh and aged hematite photoelectrode.

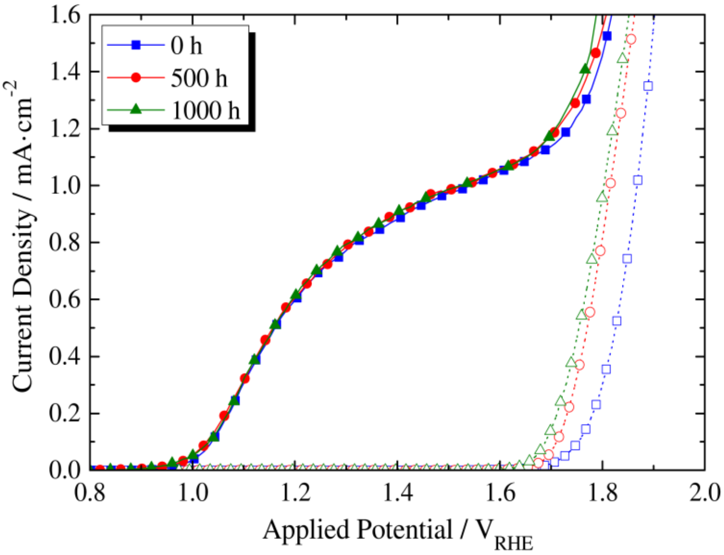

Figure 4.9: *J-V* characteristics of the optimised hematite sample prepared by spray pyrolysis, before starting the stability test, 0 h (■), and after 500 h (●) and 1000 h (▲), in the dark (dashed lines) and under 1-sun AM 1.5 G illumination (100 mW·cm^{-2}, solid lines) conditions.

Figure 4.10 confirms that the optimized hematite photoanode displays a very uniform surface fully covering the underneath FTO layer. The film growth follows a layer-plus-island growth, known as a Stranski–Krastanov mode [25, 59]. The morphology is in straight agreement with previous hematite structures deposited by spray pyrolysis [39]. No significant differences are observed between the fresh and aged sample (see Figure 4.10c and Figure 4.10d, respectively). Moreover, the global EDS analyses are also similar, as shown in Figure 4.10e and f. This behavior was not observed for hematite samples prepared using non-optimized preparation conditions. For example, a sample prepared with parameters v = 70 mL, T = 450 ºC and t = 45 s showed a photocurrent density of *ca.* 0.62 mA·cm^{-2} at 1.45 V$_{RHE}$. After a stability test of 168 h the dark current onset potential increased 150 mV and the SEM images of the photoelectrode showed hematite free areas – whiter regions at Figure 4.11.

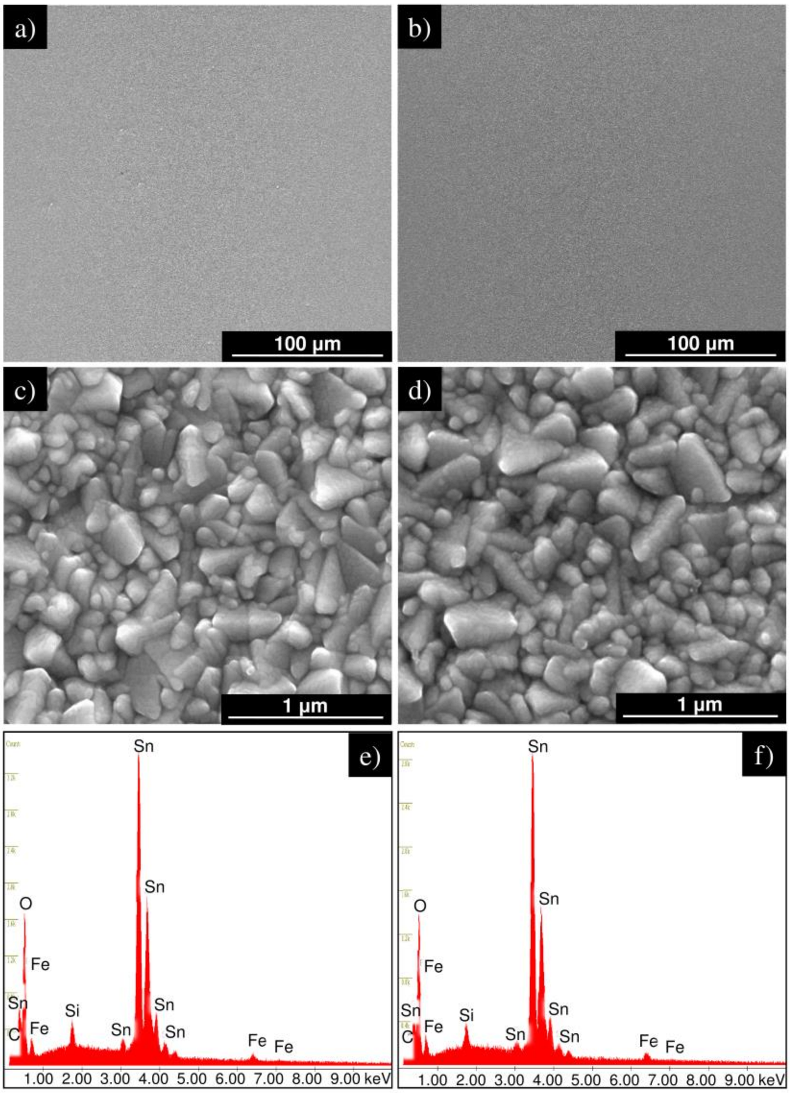

Figure 4.10: Top view SEM images and EDS analyses of the optimised hematite film before [left-side] and after [right-side] the stability test over 1000 h.

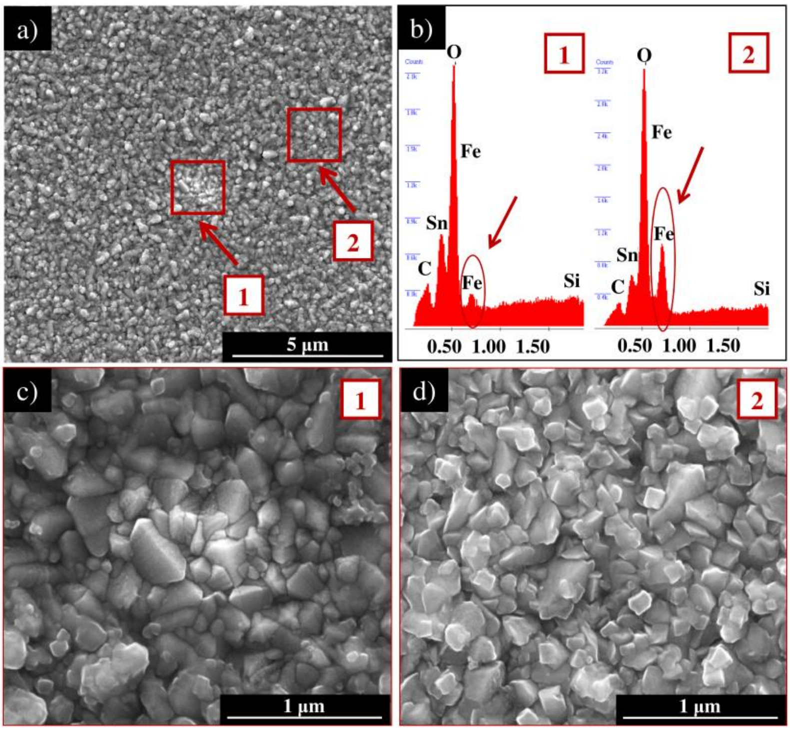

Figure 4.11: Top view SEM images of the aged hematite film produced under the following conditions: v = 70 mL, T = 450 ºC and t = 45 s; the stability test was performed for 168 h. (a) global view of the sample surface with the delimitation of an area affected by corrosion (1) and an unaffected area (2); (b) EDS analysis on the two delimited zones with the identification of the iron peaks; (c) closer view on the area affected by corrosion; and (d) closer view on the intact area.

X-ray diffraction (XRD) analyses (Figure 4.12) of the optimized photoelectrode sample showed a very broad peak along the (110) plane found at 35.5° (reference pattern number: 01-085-0599) [15]. Since the hematite film is very thin, *ca.* 19 nm, the XRD diffraction pattern should superimpose the FTO background. However, above 550 ºC β-FeOOH phase originates α-Fe$_2$O$_3$ [60] and according to Kment *et al.* [45] highly oriented films along the (110) direction should be obtained, which facilitate electron transport in the hematite photoanodes. After the 1000 h stability period no significant changes in the film crystallinity were observed.

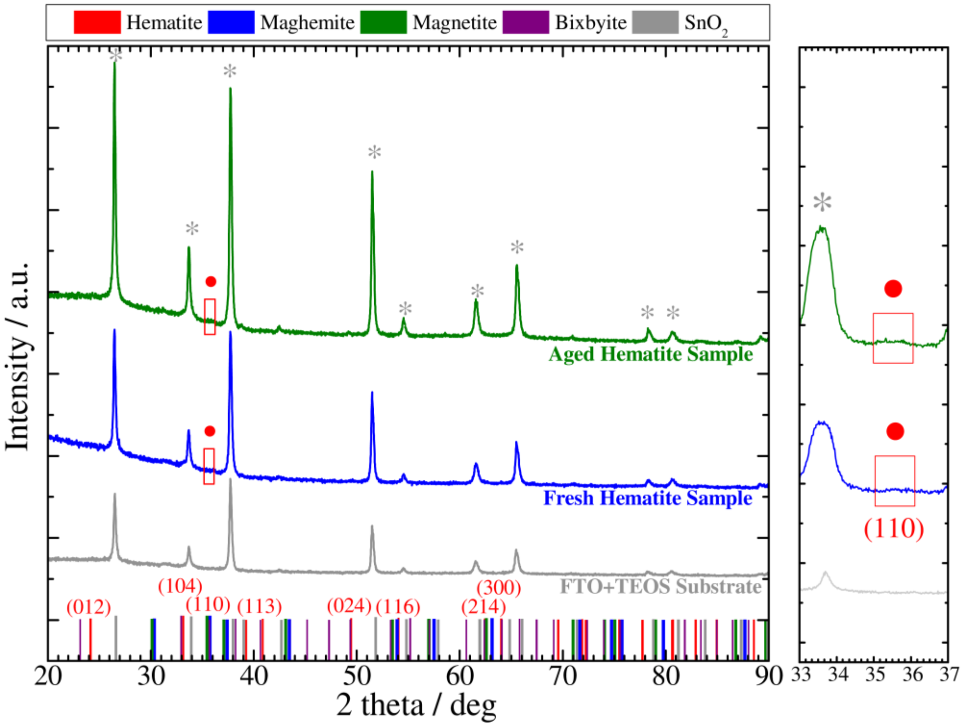

Figure 4.12: XRD spectra of iron oxide film on F:SnO_2 conducting glass prepared by spray pyrolysis before (the so-called fresh sample – blue spectra) and after (the so-called aged sample – green spectra) performing the stability test for 1000 h. The FTO glass substrate (the so-called FTO + TEOS Substrate – grey spectra) corresponds to the SnO_2 signals. The signals of Fe_2O_3 phases of hematite, maghemite, magnetite and bixbyite correspond to red, blue, green and purple lines, respectively, from the International Centre for Diffraction Data (ICDD) database. Main peaks from the substrate are also labeled with "*" and from the hematite phase with "●". On the right-side is a zoom-out of the left-side from 33° to 37°.

The electrolyte solution used in the stability test was also analyzed by inductively coupled plasma (ICP) spectroscopy; a fresh electrolyte sample was also analyzed as control. Since an iron concentration of *ca.* 88 $\mu g \cdot L^{-1}$ was detected in the control, the results were merely supportive of the film corrosion hypothesis. The electrolyte used in the aging test showed an iron concentration of *ca.* 143 $\mu g \cdot L^{-1}$ suggesting minimal material detachment from the film surface, probably resulting from the mechanical erosion by the oxygen evolution. Literature reports tremulously high iron concentration increase during the aging tests; for example, Mendes *et al.* [31] reported an increase of 1 $mg \cdot L^{-1}$ only after 72 h of aging.

4.4 CONCLUSIONS

The present work focused on improving the performance (photocurrent density and stability) of hematite photoanodes using a DoE approach. The optimized preparation parameters were: i) amount of volume solution sprayed (v); ii) temperature of the glass substrate during the deposition (T); and iii) time gap between sprays (t). The set of preparation conditions found to maximize the photocurrent density were: v = 42 mL, T = 425 ºC and t = 35 s. The optimized hematite film showed a photocurrent density of *ca.* 0.94 mA·cm^{-2} at 1.45 V$_{RHE}$, a fill factor of 50.55 % and an intrinsic solar to chemical conversion efficiency of *ca.* 0.29 %. SEM analysis confirmed the full surface coverage with well-organized and uniform hematite film. The deposited hematite film by spray pyrolysis showed a thickness of *ca.* 18.8 nm. X-ray diffraction detected only pure α-Fe_2O_3 phase, with the (110) preferential orientation.

One of the most important contributions of this work is the long-term stability study. The prepared hematite photoanode generated a constant photoresponse over 1000 h under simulated sunlight exposure. SEM, EDS, XRD and ICP analyses confirmed the stability of the prepared hematite sample.

ACKNOWLEDGMENTS

P. Dias and T. Lopes are grateful to FCT for their PhD and Postdoc grants (references: SFRH/BD/62201/2009 and SFRH/BPD/102408/2014, respectively). A. Vilanova acknowledge the European Commission through the Seventh Framework Programme under Grant Agreement No. 621252 (PECDEMO). L. Andrade acknowledge the European Commission through the Seventh Framework Programme, the Specific Programme "Ideas" of the European Research Council for research and technological development as part of an Advanced Grant under Grant Agreement No. 321315 (BI-DSC). This work was financially supported by Project UID/EQU/00511/2013-LEPABE (EQU/00511) by FEDER funds through Programa Operacional Competitividade e Internacionalização – COMPETE2020 and by national funds through FCT - Fundação para a Ciência e a Tecnologia. The authors are very thankful to P. Tavares from UME-UTAD and C. Mateos-Pedrero for assisting in the interpretation of the XRD spectra and to CEMUP for the SEM and EDS analyses.

REFERENCES

1. Warren, S.C., Voïtchovsky, K., Dotan, H., Leroy, C.M., Cornuz, M., Stellacci, F., Hébert, C., Rothschild, A. and Grätzel, M., *Identifying champion nanostructures for solar water-splitting.* Nat Mater, **2013**. 12(9): p. 842-849.
2. Liu, J., Cai, Y.Y., Tian, Z.F., Ruan, G.S., Ye, Y.X., Liang, C.H. and Shao, G.S., *Highly oriented Ge-doped hematite nanosheet arrays for photoelectrochemical water oxidation.* Nano Energy, **2014**. 9: p. 282-290.
3. Bora, D.K., Braun, A. and Constable, E.C., *"In rust we trust". Hematite - the prospective inorganic backbone for artificial photosynthesis.* Energy & Environmental Science, **2013**. 6(2): p. 407-425.
4. Young, K.M.H., Klahr, B.M., Zandi, O. and Hamann, T.W., *Photocatalytic water oxidation with hematite electrodes.* Catalysis Science & Technology, **2013**. 3(7): p. 1660-1671.
5. Marusak, L.A., Messier, R. and White, W.B., *Optical absorption spectrum of hematite, α-*Fe_2O_3 *near IR to UV.* J. Phys. Chem. Solids, **1980**. 41(9): p. 981-984.
6. Sivula, K., Le Formal, F. and Grätzel, M., *Solar Water Splitting: Progress Using Hematite (α-*Fe_2O_3*) Photoelectrodes.* ChemSusChem, **2011**. 4(4): p. 432-449.
7. Lindgren, T., Wang, H., Beermann, N., Vayssieres, L., Hagfeldt, A. and Lindquist, S.-E., *Aqueous photoelectrochemistry of hematite nanorod array.* Solar Energy Materials and Solar Cells, **2002**. 71(2): p. 231-243.
8. Jang, J.-W., Du, C., Ye, Y., Lin, Y., Yao, X., Thorne, J., Liu, E., McMahon, G., Zhu, J., Javey, A., Guo, J. and Wang, D., *Enabling unassisted solar water splitting by iron oxide and silicon.* Nat Commun, **2015**. 6: p. 7447.
9. Brillet, J., Yum, J.-H., Cornuz, M., Hisatomi, T., Solarska, R., Augustynski, J., Graetzel, M. and Sivula, K., *Highly efficient water splitting by a dual-absorber tandem cell.* Nat Photon, **2012**. 6(12): p. 824-828.
10. Gurudayal, Sabba, D., Mulmudi, H.K., Wong, L.H., Barber, J., Grätzel, M. and Mathews, N., *Perovskite- Hematite Tandem Cells for Efficient Overall Solar Driven Water Splitting.* Nano Letters, **2015**. 15(6): p. 3833-3839.
11. Steier, L., Herraiz-Cardona, I., Gimenez, S., Fabregat-Santiago, F., Bisquert, J., Tilley, S.D. and Grätzel, M., *Understanding the Role of Underlayers and*

Overlayers in Thin Film Hematite Photoanodes. Advanced Functional Materials, **2014**. 24(48): p. 7681-7688.

12. Cesar, I., Sivula, K., Kay, A., Zboril, R. and Grätzel, M., *Influence of Feature Size, Film Thickness, and Silicon Doping on the Performance of Nanostructured Hematite Photoanodes for Solar Water Splitting.* The Journal of Physical Chemistry C, **2008**. 113(2): p. 772-782.
13. Hu, Y.-S., Kleiman-Shwarsctein, A., Stucky, G.D. and McFarland, E.W., *Improved photoelectrochemical performance of Ti-doped* α-Fe_2O_3 *thin films by surface modification with fluoride.* Chemical Communications, **2009**(19): p. 2652-2654.
14. Ling, Y., Wang, G., Wheeler, D.A., Zhang, J.Z. and Li, Y., *Sn-Doped Hematite Nanostructures for Photoelectrochemical Water Splitting.* Nano Letters, **2011**. 11(5): p. 2119-2125.
15. Kim, J.Y., Magesh, G., Youn, D.H., Jang, J.-W., Kubota, J., Domen, K. and Lee, J.S., *Single-crystalline, wormlike hematite photoanodes for efficient solar water splitting.* Sci. Rep., **2013**. 3: p. 2681.
16. Le Formal, F., Pendlebury, S.R., Cornuz, M., Tilley, S.D., Grätzel, M. and Durrant, J.R., *Back Electron–Hole Recombination in Hematite Photoanodes for Water Splitting.* Journal of the American Chemical Society, **2014**. 136(6): p. 2564-2574.
17. Tilley, S.D., Cornuz, M., Sivula, K. and Grätzel, M., *Light-Induced Water Splitting with Hematite: Improved Nanostructure and Iridium Oxide Catalysis.* Angew. Chem., Int. Ed., **2010**. 49(36): p. 1521-3773.
18. Morales-Guio, C.G., Mayer, M.T., Yella, A., Tilley, S.D., Grätzel, M. and Hu, X., *An Optically Transparent Iron Nickel Oxide Catalyst for Solar Water Splitting.* Journal of the American Chemical Society, **2015**. 137(31): p. 9927-9936.
19. Li, Z., Luo, W., Zhang, M., Feng, J. and Zou, Z., *Photoelectrochemical cells for solar hydrogen production: current state of promising photoelectrodes, methods to improve their properties, and outlook.* Energy & Environmental Science, **2013**. 6(2): p. 347-370.
20. Hisatomi, T., Dotan, H., Stefik, M., Sivula, K., Rothschild, A., Grätzel, M. and Mathews, N., *Enhancement in the Performance of Ultrathin Hematite Photoanode*

for Water Splitting by an Oxide Underlayer. Advanced Materials, **2012**. 24(20): p. 2699-2702.

21. Yu, Q., Meng, X., Wang, T., Li, P. and Ye, J., *Hematite Films Decorated with Nanostructured Ferric Oxyhydroxide as Photoanodes for Efficient and Stable Photoelectrochemical Water Splitting.* Advanced Functional Materials, **2015**. 25(18): p. 2686-2692.
22. Guo, X., Wang, L. and Tan, Y., *Hematite nanorods Co-doped with Ru cations with different valence states as high performance photoanodes for water splitting.* Nano Energy, **2015**. 16: p. 320-328.
23. Duret, A. and Gratzel, M., *Visible Light-Induced Water Oxidation on Mesoscopic α-Fe_2O_3 Films Made by Ultrasonic Spray Pyrolysis.* The Journal of Physical Chemistry B, **2005**. 109(36): p. 17184-17191.
24. Liang, Y., Cristina, S.E. and van de Krol, R., *Photoelectrochemical Characterization of Sprayed α-Fe_2O_3 Thin Films: Influence of Si Doping and SnO2 Interfacial Layer.* International Journal of Photoenergy, **2008**: p. 739864.
25. Formal, F.L., Grätzel, M. and Sivula, K., *Controlling Photoactivity in Ultrathin Hematite Films for Solar Water-Splitting.* Advanced Functional Materials, **2010**. 20(7): p. 1099-1107.
26. Hisatomi, T., Le Formal, F., Cornuz, M., Brillet, J., Tetreault, N., Sivula, K. and Gratzel, M., *Cathodic shift in onset potential of solar oxygen evolution on hematite by 13-group oxide overlayers.* Energy & Environmental Science, **2011**. 4(7): p. 2512-2515.
27. Hisatomi, T., Brillet, J., Cornuz, M., Le Formal, F., Tetreault, N., Sivula, K. and Gratzel, M., *A Ga_2O_3 underlayer as an isomorphic template for ultrathin hematite films toward efficient photoelectrochemical water splitting.* Faraday Discussions, **2012**. 155: p. 223-232.
28. Mariño-Otero, T., Oliver-Tolentino, M.A., Aguilar-Frutis, M.A., Contreras-Martínez, G., Pérez-Cappe, E. and Reguera, E., *Effect of thickness in hematite films produced by spray pyrolysis towards water photo-oxidation in neutral media.* International Journal of Hydrogen Energy, **2015**. 40(17): p. 5831-5836.
29. Jorand Sartoretti, C., Alexander, B.D., Solarska, R., Rutkowska, I.A., Augustynski, J. and Cerny, R., *Photoelectrochemical Oxidation of Water at*

Transparent Ferric Oxide Film Electrodes. The Journal of Physical Chemistry B, **2005**. 109(28): p. 13685-13692.

30. Kumari, S., Singh, A.P., Sonal, Deva, D., Shrivastav, R., Dass, S. and Satsangi, V.R., *Spray pyrolytically deposited nanoporous* Ti^{4+} *doped hematite thin films for efficient photoelectrochemical splitting of water.* International Journal of Hydrogen Energy, **2010**. 35(9): p. 3985-3990.
31. Dias, P., Lopes, T., Andrade, L. and Mendes, A., *Temperature effect on water splitting using a Si-doped hematite photoanode.* Journal of Power Sources, **2014**. 272: p. 567-580.
32. Cesar, I., Kay, A., Gonzalez Martinez, J.A. and Gratzel, M., *Translucent Thin Film* Fe_2O_3 *Photoanodes for Efficient Water Splitting by Sunlight: Nanostructure-Directing Effect of Si-Doping.* Journal of the American Chemical Society, **2006**. 128(14): p. 4582-4583.
33. Klahr, B.M., Martinson, A.B.F. and Hamann, T.W., *Photoelectrochemical Investigation of Ultrathin Film Iron Oxide Solar Cells Prepared by Atomic Layer Deposition.* Langmuir, **2011**. 27(1): p. 461-468.
34. Steier, L., Luo, J., Schreier, M., Mayer, M.T., Sajavaara, T. and Grätzel, M., *Low-Temperature Atomic Layer Deposition of Crystalline and Photoactive Ultrathin Hematite Films for Solar Water Splitting.* ACS Nano, **2015**. 9(12): p. 11775–11783.
35. Zandi, O. and Hamann, T.W., *Enhanced Water Splitting Efficiency Through Selective Surface State Removal.* The Journal of Physical Chemistry Letters, **2014**. 5(9): p. 1522-1526.
36. Young, K.M.H. and Hamann, T.W., *Enhanced photocatalytic water oxidation efficiency with* $Ni(OH)_2$ *catalysts deposited on [small alpha]-*Fe_2O_3 *via ALD.* Chemical Communications, **2014**. 50(63): p. 8727-8730.
37. Joya, K.S., Morlanes, N., Maloney, E., Rodionov, V. and Takanabe, K., *Immobilization of a molecular cobalt electrocatalyst by hydrophobic interaction with a hematite photoanode for highly stable oxygen evolution.* Chemical Communications, **2015**. 51(70): p. 13481-13484.
38. Kay, A., Cesar, I. and Gratzel, M., *New Benchmark for Water Photooxidation by Nanostructured* α-Fe_2O_3 *Films.* Journal of the American Chemical Society, **2006**. 128(49): p. 15714-15721.

39. Le Formal, F., Tetreault, N., Cornuz, M., Moehl, T., Gratzel, M. and Sivula, K., *Passivating surface states on water splitting hematite photoanodes with alumina overlayers.* Chemical Science, **2011**. 2(4): p. 737-743.
40. Kumar, P., Sharma, P., Shrivastav, R., Dass, S. and Satsangi, V.R., *Electrodeposited zirconium-doped α-*Fe_2O_3 *thin film for photoelectrochemical water splitting.* International Journal of Hydrogen Energy, **2011**. 36(4): p. 2777-2784.
41. Bak, A., Choi, W. and Park, H., *Enhancing the photoelectrochemical performance of hematite (α-*Fe_2O_3*) electrodes by cadmium incorporation.* Applied Catalysis B: Environmental, **2011**. 110: p. 207-215.
42. Kleiman-Shwarsctein, A., Hu, Y.-S., Forman, A.J., Stucky, G.D. and McFarland, E.W., *Electrodeposition of α-*Fe_2O_3 *Doped with Mo or Cr as Photoanodes for Photocatalytic Water Splitting.* The Journal of Physical Chemistry C, **2008**. 112(40): p. 15900-15907.
43. Mirbagheri, N., Wang, D., Peng, C., Wang, J., Huang, Q., Fan, C. and Ferapontova, E.E., *Visible Light Driven Photoelectrochemical Water Oxidation by Zn- and Ti-Doped Hematite Nanostructures.* ACS Catalysis, **2014**. 4(6): p. 2006-2015.
44. Junyu, C., Tetsuya, K., Naoki, K. and Jinhua, Y., *Photoanodic properties of pulsed-laser-deposited α-*Fe_2O_3 *electrode.* Journal of Physics D: Applied Physics, **2010**. 43(32): p. 325101.
45. Kment, S., Schmuki, P., Hubicka, Z., Machala, L., Kirchgeorg, R., Liu, N., Wang, L., Lee, K., Olejnicek, J., Cada, M., Gregora, I. and Zboril, R., *Photoanodes with Fully Controllable Texture: The Enhanced Water Splitting Efficiency of Thin Hematite Films Exhibiting Solely (110) Crystal Orientation.* ACS Nano, **2015**. 9(7): p. 7113-7123.
46. Sanchez, C., Sieber, K.D. and Somorjai, G.A., *The photoelectrochemistry of niobium doped α-*Fe_2O_3*.* Journal of Electroanalytical Chemistry and Interfacial Electrochemistry, **1988**. 252(2): p. 269-290.
47. Shinar, R. and Kennedy, J.H., *Photoactivity of doped α-*Fe_2O_3 *electrodes.* Solar Energy Materials, **1982**. 6(3): p. 323-335.

48. Brillet, J., Grätzel, M. and Sivula, K., *Decoupling Feature Size and Functionality in Solution-Processed, Porous Hematite Electrodes for Solar Water Splitting.* Nano Letters, **2010**. 10(10): p. 4155-4160.
49. Kim, J.Y., Jang, J.-W., Youn, D.H., Magesh, G. and Lee, J.S., *A Stable and Efficient Hematite Photoanode in a Neutral Electrolyte for Solar Water Splitting: Towards Stability Engineering.* Advanced Energy Materials, **2014**. 4(13): p. 1614-6840.
50. Dias, P., Schreier, M., Tilley, S.D., Luo, J., Azevedo, J., Andrade, L., Bi, D., Hagfeldt, A., Mendes, A., Grätzel, M. and Mayer, M.T., *Transparent Cuprous Oxide Photocathode Enabling a Stacked Tandem Cell for Unbiased Water Splitting.* Advanced Energy Materials, **2015**. 5(24): p. 1614-6840.
51. Montgomery, D.C., *Design and Analysis of Experiments*. 8th ed. **2012**: Wiley.
52. Myers, R.H., Montgomery, D.C. and Anderson-Cook, C.M., *Response Surface Methodology: Process and Product Optimization Using Designed Experiments*. 3rd ed. **2011**: Wiley.
53. Lopes, T., Andrade, L., Ribeiro, H.A. and Mendes, A., *Characterization of photoelectrochemical cells for water splitting by electrochemical impedance spectroscopy.* International Journal of Hydrogen Energy, **2010**. 35(20): p. 11601-11608.
54. Dotan, H., Mathews, N., Hisatomi, T., Grätzel, M. and Rothschild, A., *On the Solar to Hydrogen Conversion Efficiency of Photoelectrodes for Water Splitting.* The Journal of Physical Chemistry Letters, **2014**. 5(19): p. 3330-3334.
55. Lopes, T., Andrade, L., Le Formal, F., Gratzel, M., Sivula, K. and Mendes, A., *Hematite photoelectrodes for water splitting: evaluation of the role of film thickness by impedance spectroscopy.* Physical Chemistry Chemical Physics, **2014**. 16(31): p. 16515-16523.
56. Klahr, B.M. and Hamann, T.W., *Current and Voltage Limiting Processes in Thin Film Hematite Electrodes.* The Journal of Physical Chemistry C, **2011**. 115(16): p. 8393-8399.
57. Jacobsson, T.J., Fjallstrom, V., Edoff, M. and Edvinsson, T., *Sustainable solar hydrogen production: from photoelectrochemical cells to PV-electrolyzers and back again.* Energy & Environmental Science, **2014**. 7(7): p. 2056-2070.

58. Dias, P., Lopes, T., Meda, L., Andrade, L. and Mendes, A., *Photoelectrochemical water splitting using WO3 photoanodes: the substrate and temperature roles.* Physical Chemistry Chemical Physics, **2016**. 18(7): p. 5232-5243.
59. Eaglesham, D.J. and Cerullo, M., *Dislocation-free Stranski-Krastanow growth of Ge on Si(100).* Physical Review Letters, **1990**. 64(16): p. 1943-1946.
60. Annamalai, A., Subramanian, A., Kang, U., Park, H., Choi, S.H. and Jang, J.S., *Activation of Hematite Photoanodes for Solar Water Splitting: Effect of FTO Deformation.* The Journal of Physical Chemistry C, **2015**. 119(7): p. 3810-3817.

CHAPTER 5

PHOTOELECTROCHEMICAL WATER OXIDATION USING HEMATITE PHOTOANODES COATED WITH RUTHENIUM DIOXIDE

5

PHOTOELECTROCHEMICAL WATER OXIDATION USING HEMATITE PHOTOANODES COATED WITH RUTHENIUM DIOXIDE

Paula Dias, Luísa Andrade and Adélio Mendes

Under Submission

ABSTRACT

The surface defects originate the low photopotentials observed on hematite photoanodes, limiting their performance for photoelectrochemical water oxidation. This work focuses on the surface modification of hematite thin films combining two strategies: annealing at high temperatures (800 ºC) and coating with RuO_2 co-catalyst. The annealing at 800 ºC improved both the morphology and the electronic structure due to the diffusion of tin ions from the FTO layer into the hematite lattice. RuO_2 is a highly active co-catalyst for the water oxidation on hematite photoanodes and when sintered at 200 ºC originated a cathodic shift of the onset potential of *ca.* 360 mV. This synergetic effect resulted in a turn-on potential of 0.52 V_{RHE} and a final photopotential of *ca.* 0.95 V. A photocurrent density of *ca.* 0.98 $mA\cdot cm^{-2}$ was obtained at 1.23 V_{RHE}, corresponding to around 50 % increase compared with bare hematite. The study allowed obtaining an improved understanding of the water oxidation reaction at the hematite photoelectrode surface.

Keywords: Hematite Photoanodes, Photoelectrochemical Water Splitting, Photopotential, Surface Modification, Annealing Treatment, RuO_2 co-catalyst.

5.1 INTRODUCTION

Hematite presents several favorable characteristics that turn this material very attractive for solar-driven water splitting, namely, a 2.1 eV bandgap, appropriate valence band (VB) position towards water oxidation, chemical stability, abundance and low-cost [1, 2]. However, the hematite conduction band (CB) is more positive than hydrogen evolution reaction and so its integration in a tandem PEC device with a photocathode or a photovoltaic cell can solve this mismatch [3]. Despite these encouraging characteristics, the highest solar-to-hydrogen (STH) efficiency achieved so far is 3.1 % [4], though STH efficiencies lower than 1 % are more typically reported using hematite photoanodes [3, 5].

The overall STH efficiency is mainly controlled by the efficiency of three general processes: i) light harvesting/charge separation – η_{light}; ii) charge transport/ recombination within the semiconductor – η_{ct}, *i.e.* fraction of VB holes that reach the semiconductor/electrolyte interface and CB electrons reaching the back contact; and iii) hole collection at electrode surface – η_{hc}, *i.e.* fraction of surface holes that oxidize water subtracted from the ones that recombine at the surface [6] - Figure 5.1a.

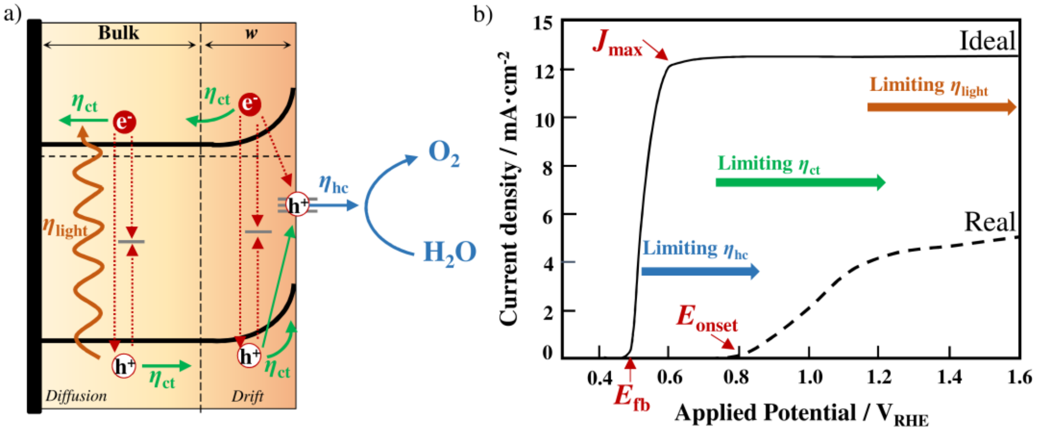

Figure 5.1: (a) Schematic energetics and charge transfer processes under PEC water oxidation using hematite photoanodes. The water oxidation photocurrent is controlled by the efficiency of light harvesting (η_{light}), charge transport (η_{ct}), and holes collection (η_{hc}). Red arrows indicate recombination pathways (adapted from ref. [6]). (b) PEC performance comparison between a state-of-the-art (real) photoanode and an ideal photoanode. The arrows indicate the main performance limiting factors for increasing anodic potential: first, η_{hc} at the hematite/electrolyte interface, then η_{ct} within hematite, and finally η_{light} in the semiconductor (adapted from ref. [5]).

Figure 5.1b compares the behavior of an ideal hematite photoanode, where the plateau photocurrent is the maximum photocurrent in the optical limit (J_{max} = 12 mA·cm^{-2}) and the onset potential (E_{onset}) equals the flatband potential (E_{fb} is normally between 0.4 and 0.6 V_{RHE}) [7]; the photocurrent should reach J_{max} within 0.1 V from E_{onset} [5]. State-of-the-art nanostructured hematite photoanodes show J_{max} = 5.7 mA·cm^{-2} at 1.23 V_{RHE} and E_{onset} of *ca.* 0.7 V_{RHE} [8]; however, the potential for reaching the maximum photocurrent density is very high for practical PEC devices.

The photoelectrochemical activity of hematite is limited by its relatively long visible light absorption depth (hundred nanometers) and a very short minority carrier lifetime and mobility; both combined hinder efficient carrier separation and transport (decrease of η_{light} and η_{ct}) [3, 9]. Bulk modifications, *e.g.* by doping [8, 10], nanostructuring [11, 12] or surface modification [13, 14], have shown to be effective in alleviating this problem. In addition, the oxygen evolution reaction (OER) kinetics is reported to be sluggish, increasing the recombination of the surface holes with conduction band electrons competes with the forward water oxidation efficiency (low η_{hc}) [15]. The water oxidation mechanism on hematite surfaces is currently subject of intense investigation; Young *et al.* [1] proposed the following reaction scheme:

$$h^+(VB) + Fe\text{-}OH \rightarrow Fe\text{-}O + H^+ \tag{5.1}$$

$$h^+(VB) + Fe\text{-}O + H_2O \rightarrow Fe\text{-}OOH + H^+ \tag{5.2}$$

$$h^+(VB) + Fe\text{-}OOH \rightarrow O_2 + Fe + H^+ \tag{5.3}$$

$$h^+(VB) + Fe + H_2O \rightarrow Fe\text{-}OH + H^+ \tag{5.4}$$

The OER involves four holes for each O_2 molecule produced and the formation of reaction intermediates, such as Fe-O and Fe-OOH. This is consistent with the hypothesis that the OER occurs via the holes trapping at Fe species on the electrode surface and then the transport of these holes to the electrolyte (rate limiting step) [1, 5]. These states are often referred as surface states; the recombination at surface states of hematite is the process mostly contributing to the large potential necessary to oxidize water [6]. When a high anodic potential is applied to hematite, the holes are transferred to electrolyte with an efficiency, η_{hc}, close to unity [5]. Understanding the loss mechanisms at the hematite surface is critical to solve the highly anodic electrochemical potential required to initiate the OER and then the energy efficiency improvement.

The recent advances using hematite photoanodes for PEC water splitting are then focused on lowering the high onset potential for the OER by hematite surface treatment, since the semiconductor/electrolyte interface has proven to strongly influence the charge separation/recombination, the catalytic activity and also the stability of the photoelectrode [5, 16]. Several strategies have been investigated in the field, such as: introducing overlayers on top of hematite [9, 17], reducing the surface defects by coating oxide layers between hematite and the electron collector/substrate [18, 19], using co-catalysts [20-22], optimizing the post-fabrication annealing conditions [14, 23], *etc.*

In the present study, a synergetic combination of surface modification by high temperature annealing at 800 ºC and by coating ruthenium dioxide (RuO_2) co-catalyst was used to cathodically shift the onset potential, aiming at to minimize the surface state recombination. The shift in the water oxidation potential upon surface modification has been attributed to the mitigation of Fermi level pinning at the hematite/electrolyte interface and, thus, enhanced band bending [24]. The annealing of hematite thin films at 800 ºC was found to passivate the surface states, minimizing the recombination, but it also promotes the diffusion of Sn atoms from the FTO (fluorine-doped tin oxide) layer into the hematite lattice, enhancing the PEC properties of the hematite [25]. On the other hand, RuO_2 was used as a co-catalyst to accelerate the OER kinetics, since it is considered as the material showing the highest catalytic activity among the single-transition metal oxides [26, 27]. While RuO_2 has already been tested as an OER co-catalyst for overall water splitting on $Ga_{1-x}Z_xN_{1-x}O_x$ [28] and for the HER on Cu_2O [29, 30], its performance as co-catalyst for the OER was not yet fully investigated. However, organometallic Ru-containing complexes of Ru(tpy)(pba)Cl Ru (II) were tested on hematite by Chen *et al.* [31], showing an onset potential shift of *ca.* 300 mV.

The optimization of hematite surface is made using ultrathin films (*ca.* 19 nm) prepared by spray pyrolysis; this photoanode material was recently reported exhibiting high stability performance over 1000 h of sunlight exposure in a 1 M NaOH electrolyte solution [32]. The RuO_2 electrodeposition conditions were varied for the improvement of onset potential and photocurrent density, as well as the temperature and time of annealing treatment. The optimized hematite thin film coated with RuO_2 co-catalyst allows obtaining a low turn-on potential of *ca.* 0.52 V_{RHE} and a high photopotential of *ca.* 0.95 V.

5.2 EXPERIMENTAL

5.1.1 HEMATITE PHOTOANODES PREPARATION

Ultrathin films of hematite were deposited on 1 mm thick, 10 $\Omega\cdot square^{-1}$ conducting fluorine doped tin oxide ($F:SnO_2$) coated glass substrates (Solaronix, Switzerland) by spray pyrolysis using the in-house assembled setup [32]. The FTO-glasses were adequately cleaned as described elsewhere [30]. The substrates were first pretreated with tetraethyl orthosilicate (TEOS) to allow better Fe_2O_3 film organization, reducing the interfacial strain between the FTO layer and the hematite crystals and, consequently, a photoactivity response improvement [33]. The FTO-glass substrates were heated at 450 ºC and *ca.* 1.5 mL of a diluted TEOS solution (10 % volume in ethanol) were hand-sprayed with a glass atomizer onto the heated substrates. These samples were cooled down before heating again to deposit the hematite film. To prepare the hematite films, a solution containing 10 mM iron(III) acetylacetonate ($Fe(acac)_3$) in EtOH was sprayed onto a temperature controlled substrate surface heated at 425 ºC with a spray nozzle from a distance of *ca.* 20 cm. A solution volume of 42 mL was sprayed with a time gap between sprays of 35 s, corresponding to a final film thickness of *ca.* 19 nm. After the spray deposition, the hematite samples were air-annealed for 30 min at 550 ºC, before being cooled down to the room temperature. These conditions were previously optimized through a design of experiments approach [32].

The hematite thin films were then subjected to a high-temperature annealing at 800 ºC in air for various periods of time (5 min, 10 min and 20 min).

5.1.2 DEPOSITION OF RuO_2 CO-CATALYST

RuO_2 co-catalyst was electrodeposited under galvanostatic conditions using an aqueous solution of 1.3 mM $KRuO_4$; the deposition was made at room temperature. Since the initial pH of the deposition bath strongly influences the rate of RuO_2 electrodeposition [34], a fresh $KRuO_4$ solution was made before each deposition. A platinum wire was used as counter-electrode. A constant current density (among 5 - 30 $\mu A\cdot cm^{-2}$) was applied for different periods of time (5 min, 15 min, 30 min, 1 h, 2 h, 4 h and 8 h) to deposit RuO_2 films on hematite thin film photoelectrode surfaces. The electrodeposited films were then sintered at 200 ºC over 2 h.

5.1.3 ELECTROCHEMICAL CHARACTERIZATION

A PEC cell device known as "cappuccino" was chosen to perform the electrochemical characterization of the prepared hematite photoanodes [35]. The cell was filled with 1 M NaOH (pH 13.6) electrolyte aqueous solution and the surface area illuminated was 0.238 cm^2 defined by an internal mask. A standard three-electrode configuration was used: Ag/AgCl/Sat. KCl (Metrohm, Switzerland) as a reference electrode, 99.9 % pure platinum wire (Alfa Aesar®, Germany) as counter-electrode and hematite photoanodes as working electrodes.

J-V MEASUREMENTS

J-V characteristic curves were obtained applying an external potential bias to the cell and measuring the generated photocurrent using a ZENNIUM workstation (Zahner Elektrik, Germany) controlled by Thales software package (Thales Z 2.0). The applied potential bias was reported as a function of the reversible hydrogen electrode (RHE). The measurements were performed at room temperature in dark and under 1-sun simulated sunlight, at a scan rate of 10 $mV\cdot s^{-1}$ between 0.80 and 1.80 V_{RHE}. A class B solar simulator equipped with a 150 W Xe lamp (Oriel, Newport, USA) and an AM 1.5 G filter (100 $mW\cdot cm^{-2}$; Newport, USA) was used; the light beam was calibrated with a c-Si photodiode (Newport, USA).

During stability tests the hematite photoanodes were continuously submitted to simulated solar illumination (100 $mW\cdot cm^{-2}$, 1-sun AM 1.5 G) at an applied potential of *ca.* 1.00 V_{RHE}. The photocurrent density response was monitored as a function of time using the same electrochemical station.

EIS MEASUREMENTS

EIS analyses were performed applying a small potential sinusoidal perturbation to the system. The amplitude and the phase shift of the resulting current response was recorded using also the ZENNIUM workstation. The frequency range was 0.1 Hz – 100 kHz and the amplitude 10 mV. The measurements were carried out in the dark and under 1-sun AM 1.5 G illumination conditions and the range of the applied potential was equal to that of the photocurrent measurements (0.80 – 1.80 V_{RHE}) with a step of 50 mV. An appropriate electrical analog was then fitted to the EIS spectra using the ZView software (Scribner Associates Inc., USA).

5.1.4 STRUCTURAL CHARACTERIZATION

FILM THICKNESS DETERMINATION

UV-visible absorption data were used to estimate the hematite samples thickness. Since there is a similarity in the shape of the spectra for all samples, their thicknesses can be estimated assuming a Lambertian absorption behavior:

$$\ln(1-abs) = -\alpha \cdot \ell \tag{5.5}$$

where *abs* is the absorbance, α is the hematite absorbance coefficient $(44\ \text{nm})^{-1}$ at 400 nm [36] and ℓ is the thickness of the hematite film in nanometers. An UV-vis-NIR spectrophotometer (Shimadzu Scientific Instruments Inc., model UV-3600, Kyoto) was used to obtain the absorbance of the prepared hematite samples. It was decided to measure the reflectance and transmittance of all samples and then to calculate the absorbance by subtracting both to the incident radiation. Finally, the absorbance was corrected by subtracting the FTO glass absorbance (control).

SCANNING ELECTRON MICROSCOPY (SEM) ANALYSIS

SEM was used to obtain information on the morphology of the prepared materials. The morphology of the hematite films was characterized using a high-resolution scanning electron microscope (Quanta 400 FEG, FEI Company, USA); the analyses were made at CEMUP (Centro de Materiais da Universidade do Porto). The acceleration voltage was 15 keV while an in-lens detector was employed with a working distance of about 10 mm. The surface of fresh and aged hematite samples was examined in order to identify and analyze modifications in their surface morphology.

ATOMIC FORCE MICROSCOPY (AFM) ANALYSIS

AFM was used to obtain the surface topography and roughness of the prepared hematite photoanodes before and after surface modifications with RuO_2 co-catalyst and high-temperature annealing. The surface roughness, R_q, extracted from the topography of the studied surfaces was defined as the root-mean-square value of the image pixel height. A Nanoscope Multimode Atomic Force Microscope (Veeco Instruments Inc., USA) was used in non-contact mode; the analyses were made at CEMUP (Centro de Materiais da Universidade do Porto).

X-RAY DIFFRACTION (XRD) ANALYSIS

XRD analysis was carried out in a PANalytical X'Pert MPD (Spectris plc, England) equipped with an X'Celerator detector and secondary monochromator (Cu $K\alpha\,\lambda$ = 0.154 nm, 40 kV, 30 mA; data recorded at a 0.017 step size, 100 s·step^{-1}). Rietveld refinement with Powder-Cell software was used to identify the crystallographic phases from the XRD diffraction patterns.

X-RAY PHOTOELECTRON SPECTROSCOPY (XPS) ANALYSIS

XPS analysis was performed in a Kratos Axis Ultra HAS (Kratos Analytical, England) spectrometer using a monochromatic Al K α radiation (1486.6 eV) and operating at 15 kV (300 W). The XPS spectra were deconvoluted with the XPSPEAK 4.1 software, using non-linear least squares fitting routine after a Shirley-type background subtraction (or linear, taking in account the data). The surface atomic percentages were calculated from the corresponding peak areas and by using the sensitivity factors provided by the manufacturer. This technique was used to investigate the surface chemistry of bare hematite, of hematite annealed at 800 °C and of RuO_2-coated hematite photoelectrodes.

5.3 RESULTS AND DISCUSSION

Many strategies are being followed to lower the onset potential of hematite photoelectrodes; in particular, surface treatments are being extensively used to address the intrinsic defects expected to improve charge separation by minimizing charge recombination. Herein, the onset potential was reduced combining a surface coating with an efficient co-catalyst and high temperature annealing.

5.1.5 HEMATITE SURFACE COATING WITH RuO_2 CO-CATALYST

The surface modification of hematite photoanodes with a water oxidation co-catalyst should accelerate the kinetics of water oxidation and reduce the surface recombination rate. It must be emphasized that the preparation and morphology of hematite film highly influence its photoelectrochemical performance and stability. An ideal co-catalyst would minimize the unfavorable energetic relation between intermediate species of the water oxidation mechanism [26]. To date, many co-catalysts were studied to cathodically shift the photocurrent onset potential such as CoO_x [11], Co-Pi [37], IrO_2 [20], $NiFeO_x$ [22] and $Ni(OH)_2$ [38]. RuO_2 is recognized as one of the most active catalyst for oxygen evolution both in acidic and alkaline electrolytes [26, 39]; however, its use with a hematite photoelectrode has never been addressed [5].

In this work, RuO_2 co-catalyst was electrodeposited onto hematite surface using an aqueous solution of $KRuO_4$, avoiding the use of harmful reagents such as carbonyl derivatives and poison chlorides [40]. The film was formed via reduction of the perruthenate anions by conduction band electrons of hematite to form densely packed particles. Despite the cathodic electrodeposition potential depends upon nature of substrate, bath temperature and metal ion concentration, the parameters that influence the most the uniformity and thickness of the RuO_2 films are the applied current density and the time of deposition. The current densities applied for the catalyst electrodeposition took place at relatively low potentials, insufficient for water oxidation [41]. Though, larger overpotentials were observed at initial stage of deposition, attributed to the high energy barrier of Ru metal oxide nucleation onto the substrate [34].

The galvanostatic electrodeposition conditions were optimized playing with the following operating conditions: i) applied current density, in the range of 5 - 30 $\mu A\cdot cm^{-2}$ and ii) deposition time (5 min, 15 min, 30 min, 1 h, 2 h, 4 h and 8 h). The films deposited at low current densities proved to be quite uniform and so a constant current density of *ca.* 5 $\mu A\cdot cm^{-2}$ was considered for the subsequent optimization.

The film thickness of the co-catalyst coating can be estimated based on the amount of current passing during the deposition time, taking into consideration that three electrons are involved in the deposition of one Ru atom (Ru^{7+} in the $KRuO_4$ precursor goes to Ru^{4+} in RuO_2) and a Faradaic efficiency of *ca.* 20 % [41]. For instance, the thickness of the RuO_2 layer obtained from a constant current density of 5 $\mu A\cdot cm^{-2}$ over 2 h (charge of *ca.* 36 $mC\cdot cm^{-2}$) is *ca.* 4.5 nm, assuming a density of the crystalline RuO_2 of 6.93 $g\cdot cm^{-3}$ [41]. However, the deposited catalyst is a hydrous, amorphous layer and then an accurate measurement of RuO_2 film thickness becomes difficult [30]. To avoid ambiguity in the discussion of the RuO_2 films properties, thicknesses are expressed as to the amount of electrical charge density for the deposition.

The photoelectrochemical performances of a bare hematite (BH) photoanode and RuO_2-coated hematite (HRu) photoanodes with different thicknesses were then evaluated based on the photocurrent-voltage characteristics in dark and under 1-sun AM 1.5 G illumination - Figure 5.2. A three-electrode configuration in 1 M NaOH electrolyte was used.

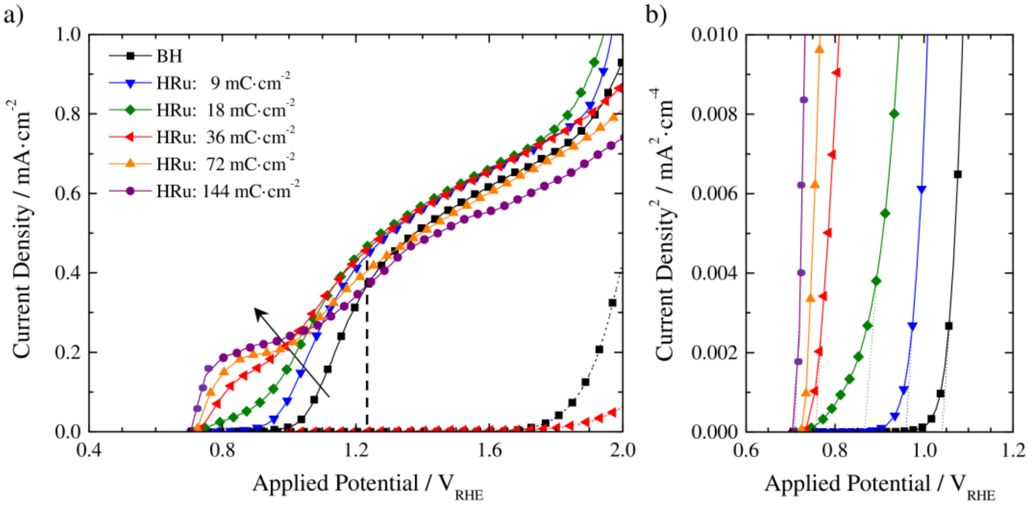

Figure 5.2: (a) *J-V* characteristic curves measured in the dark and under 1-sun AM 1.5 G illumination conditions for a bare hematite (BH) photoanode (■) and RuO_2-coated hematite (HRu) photoanodes prepared applying a charge density of *ca.* 9 (▼), 18 (◆), 36 (◀), 72 (▲) and 144 (●) mC·cm^{-2}; (b) Butler plots in which the turn-on potential is defined as the value at which the extrapolation of the linear relationship between $(J_{photo})^2$ and applied potential intercepts with $(J_{photo})^2 = 0$.

From Figure 5.2a is clear that the coating of hematite photoanodes with RuO_2 co-catalyst decreases the photocurrent onset potential, improving the water oxidation efficiency. For the bare hematite (BH) photoanode under dark conditions, the current density rises steeply for a potential higher than 1.70 V$_{RHE}$ - the so-called dark current. Under sunlight conditions, BH shows an onset potential of 1.04 V$_{RHE}$ and a photocurrent density of *ca.* 0.36 mA·cm^{-2} at the potential of reversible oxygen electrode (1.23 V$_{RHE}$), reaching a plateau of *ca.* 0.55 mA·cm^{-2} at 1.45 V$_{RHE}$. Considering HRu sample prepared with a charge density of 36 mC·cm^{-2}, the photocurrent onset potential was cathodically shifted to *ca.* 0.72 V$_{RHE}$, with a dark current onset potential similar to the bare sample. A photocurrent density of *ca.* 0.23 mA·cm^{-2} was obtained at 1.00 V$_{RHE}$, where BH shows mostly no photocurrent. Gains in photocurrent are less substantial at higher applied potentials, *i.e.* a current increase of *ca.* 28 % and 7 % were achieved at 1.23 V_{RHE} and 1.45 V_{RHE}, respectively. Increasing the RuO_2 film thickness (HRu sample with 144 $mC{\cdot}cm^{-2}$) yields better PEC performance at more negative potentials, *i.e.* until 1.10 V_{RHE}, but the current density values starts lower for higher potentials. Moreover, the hematite electrode surface was visibly darker after deposition of higher amount of catalyst, *e.g.* 144 $mC{\cdot}cm^{-2}$. This appearance is not desirable if a semi-transparent photoanode is desired for tandem applications.

The PEC data can alternatively be analyzed by the method proposed by Butler [42] – Figure 5.2b – that provides information about the light-to-charge energy-conversion performance of the electrode. Butler derived the following relation $\left(E - E_{\text{fb}}\right) \propto \left(J_{\text{photo}} / \alpha w q P_{\text{light}}\right)$, in which α is the optical absorption coefficient, q is the elementary charge, w is the space charge width and P_{light} is the light intensity. When the charge transfer across the semiconductor/electrolyte interface is slow, as for hematite, the Butler equation should carry information about the overpotentials, $\left(E - E_{\text{fb}}\right)$ [22]. From the Butler plot, the RuO_2 coating with 36 $mC{\cdot}cm^{-2}$ caused a photocurrent onset potential shift in the negative direction of *ca.* 300 mV compared with bare hematite. For BH photoanode, the onset potential of *ca.* 1.04 V_{RHE} results from a severe Fermi level pinning effect, which is the key reason for the low photopotentials observed.

Figure 5.3 shows the behavior of the onset cathodic shift (obtained from the Butler plots) and the photocurrent obtained at 1.23 V_{RHE} as a function of the catalyst amount deposited. The cathodic shift of the photocurrent onset potential increases with RuO_2 thickness, as expected for efficient co-catalysts, but it quickly levels out above at 300 - 350 mV for thicknesses greater than 36 $mC{\cdot}cm^{-2}$. Thick layers of RuO_2 may inhibit rapid charge transport up to the electrolyte, thus restricting current flow and favoring recombination between photogenerated conduction band electrons and accumulated holes at the RuO_2 surface. This may justify the observed photocurrent decrease for higher potentials in the *J*-*V* curves. Based on Figure 5.2a and Figure 5.3, the electrodeposition condition that maximizes both the cathodic onset shift as well as the photocurrent density corresponds to an applied charge density of 36 $mC{\cdot}cm^{-2}$; three samples were prepared for each RuO_2 thickness and the results showed high reproducibility. Hereafter, RuO_2-coated hematite photoanode prepared with 36 $mC{\cdot}cm^{-2}$ is called as HRu sample.

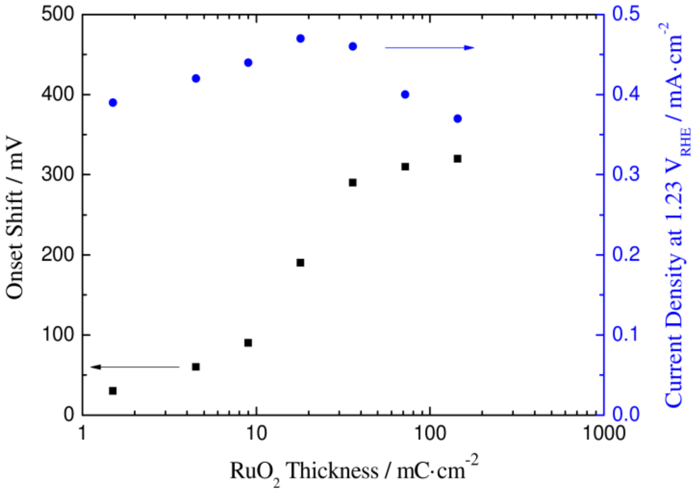

Figure 5.3: Potential shift of the photocurrent onset (■) and obtained photocurrent density at 1.23 V_{RHE} (●) as a function of the RuO_2 thickness deposited for the prepared hematite samples.

As abovementioned, bare hematite is a self-limiting photoanode in which positive surface charge accumulation inhibits band bending through quasi-Fermi level pinning, leading to rapid electron-hole recombination at low applied bias [43]. Thus, the primary role of the RuO_2 co-catalyst is to catalyze water oxidation at the lowest potentials that avoids positive charge accumulation at the hematite surface. However, the data shown in Figure 5.2a, and in particular for low potentials, leads to hypothesize about the overlap of two mechanisms for water oxidation in RuO_2-coated hematite photoanodes: one involving water oxidation catalyzed by RuO_2 and the other directly at the hematite surface. The contribution of each mechanism depends on the co-catalyst film thickness. Therefore, for thin RuO_2 layers, the majority of oxygen evolution seems to occur via RuO_2 at low bias potentials, but the hematite surface mechanism dominates at higher potentials. Hematite photoanodes with thicker catalyst layers oxidize water mostly via RuO_2 co-catalyst. Gamelin and his co-workers reported very recently a similar behavior for mesostructured α-Fe_2O_3 photoanodes decorated with Co-Pi [43], a co-catalyst extensively studied for hematite photoanodes [9, 37].

A slow decrease in the cathodic shift is observed upon successive *J*-*V* scans in alkaline media, although the shift can be fully restored with the application of more catalyst, as reported for IrO_2 co-catalyst [20]. This is not desirable for practical applications and so the stability of the RuO_2 layer should be improved. A post-annealing treatment was found to play an important role on the structure and electrochemical performance of ruthenium oxides, improving the structural organization and stability. Fang *et. al.* [44] reported that an annealing in air at 200 ºC for 2 h helps the amorphous-to-crystalline phase transformation, creating a suitable nanostructure that balances electronic and hole conduction with enhanced electrochemical performance. Figure 5.4 plots the *J-V* curves for the prepared photoanodes before and after annealing at temperatures up to 400 ºC.

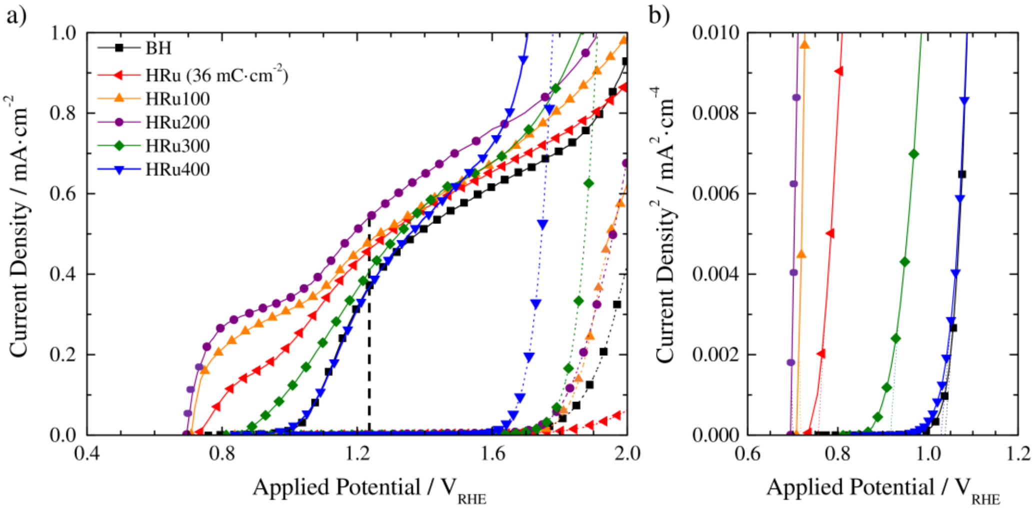

Figure 5.4: (a) *J-V* characteristic curves measured in the dark and under 1-sun AM 1.5 G illumination conditions for the bare hematite (BH) photoanode (■) and RuO$_2$-coated hematite photoanode without annealing (HRu sample with 36 mC·cm^{-2}, ◀). HRu photoanodes were further annealed in air at 100 ºC (HRu100, ▲), 200 ºC (HRu200, ●), 300 ºC (HRu300, ◆) and 400 ºC (HRu400, ▼); and (b) correspondent Butler plots.

The photoelectrochemical performance increased by post-annealing the RuO$_2$-coated hematite photoanodes at 100 ºC (HRu100) and 200 ºC (HRu200) over 2 h. For temperatures above 300 ºC, the as-deposited RuO$_2$ amorphous film should be converted to crystalline; however, amorphous RuO$_2$ favors less OER overpotentials than crystalline films [45]. Though, a significant decrease on the potential onset of the photocurrent was observed for samples annealed at 300 ºC and 400 ºC, the dark current onset also begun early. For samples annealed at 100 ºC and 200 ºC, no significant differences were observed for their dark currents. A turn-on photopotential of *ca.* 0.68 V$_{RHE}$ was observed with the HRu200 photoanode, followed by a huge photocurrent increase of more than 180 % at 0.80 V_{RHE}, 50 % at 1.00 V_{RHE} and 18 % at 1.23 V_{RHE}, compared with a bare hematite (BH) photoanode. An onset cathodic shift of *ca.* 360 mV was then obtained, which is one of the highest values reported for catalyst-based hematite water oxidation reaction without additional absorbers [22]. The morphology of bare hematite and RuO_2-coated hematite films with and without annealing treatment at 200 ºC was analyzed by scanning electron micrograms (SEM) - Figure 5.5.

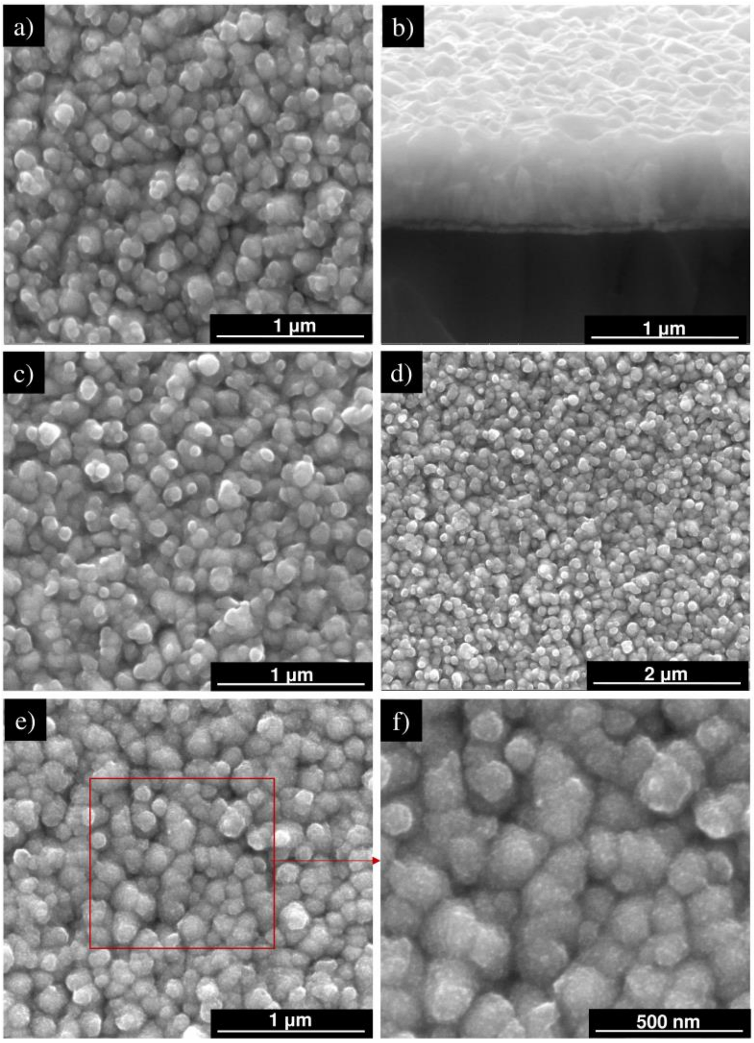

Figure 5.5: SEM images: (a) surface top-view and (b) cross-sectional view of the bare hematite film (BH); (c) and (d) surface view of the RuO_2-coated hematite film (HRu), with magnifications of 100000× and 50000×, respectively; (e) and (f) surface view of the HRu after annealing at 200 ºC (HRu200), with magnifications of 100000× and 200000×, respectively.

The top-view SEM images revealed that all of the prepared films were quite uniform. Figure 5.5a shows a thin and very dense film of hematite crystals over the FTO-glass substrate typical of a layer-plus-island growth, known as a Stranski–Krastanov mode [32, 33]. Figure 5.5b shows a cross-section SEM image of the bare hematite (BH) film (deposited on a FTO layer of *ca.* 500 nm); this figure does not allow to obtain the film thickness, which was estimated to be *ca.* 19 nm by UV-visible absorption. Figure 5.5c and d display a very thin and uniform layer of RuO_2 coated atop the hematite thin film (HRu sample with 36 $mC \cdot cm^{-2}$), presenting an average grain size of (133 ± 34) nm. The annealing treatment at 200 ºC smoothened the surface of the RuO_2 coating (HRu200 sample), allowing to increase the grain size to *ca.* (214 ± 48) nm - Figure 5.5e. Additionally, from Figure 5.5f the RuO_2 layer exhibits small grains with a spherical morphology that should limit the developed space charge layer, enabling better hole diffusion to the electrode surface; thus, reflecting the high current densities obtained in Figure 5.4.

Atomic force microscopy (AFM) scan images of bare hematite (BH) and RuO_2 coated-hematite films with and without annealing treatments at 200 ºC over 2 h also revealed differences in their surface topography. Figure 5.6 shows representative $1 \times 1\ \mu m^2$ images of the surfaces. BH thin film presents a significant surface roughness of *ca.* R_q = 27.4 nm (root-mean-square value of the image pixel height), slightly higher than the RuO_2-coated hematite film (HRu), *i.e.* R_q = 22.9 nm – Figure 5.6a. This suggests that RuO_2 film covers the hematite surface homogenously and fills some voids in the hematite film surface, which can actually be seen in Figure 5.5. Thereafter, annealing the RuO_2 film at 200 ºC (HRu200) mostly did not change the roughness of the film (R_q = 22.5 nm); the annealed RuO_2 film actually displays smoother surface at large with small grains on the surface as illustrate in Figure 5.7.

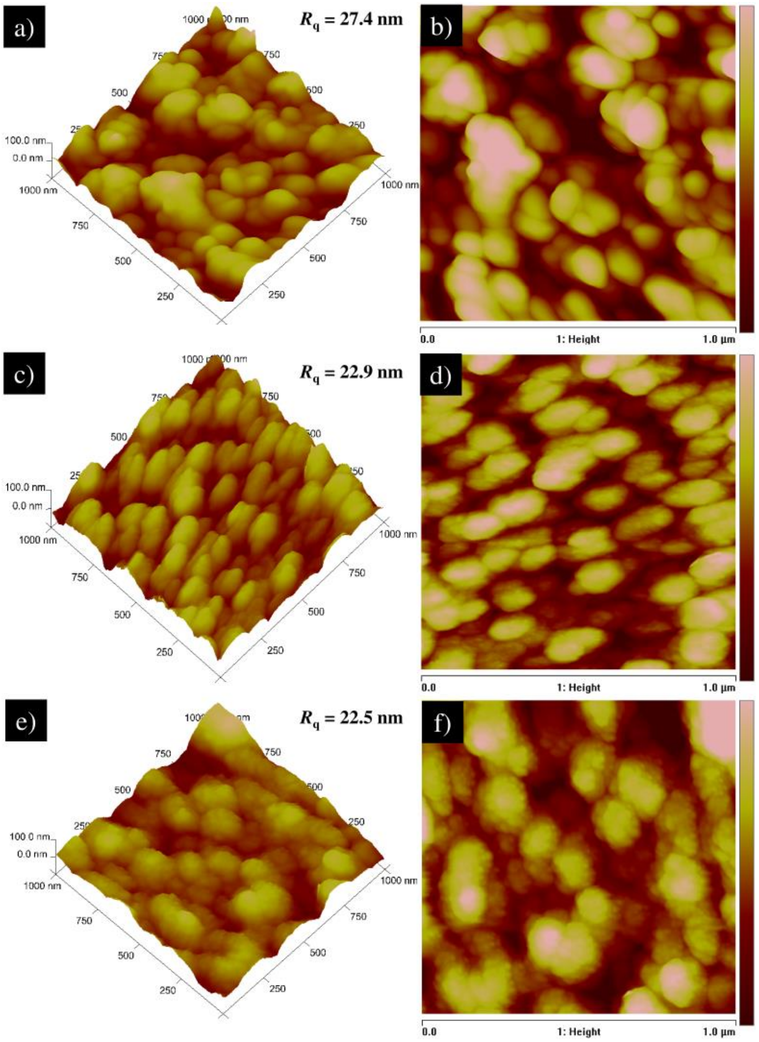

Figure 5.6: Surface topography obtained using 3D [left-side] and 2D [right-side] AFM scan images for: (a) and (b) bare hematite (BH) thin film; (c) and (d) RuO_2-coated hematite film (HRu); (e) and (f) RuO_2-coated hematite film after the annealing treatment at 200 ºC over 2 h (HRu200). The image scale is 1 × 1 µm^2 and R_q is the root mean square roughness of the surface.

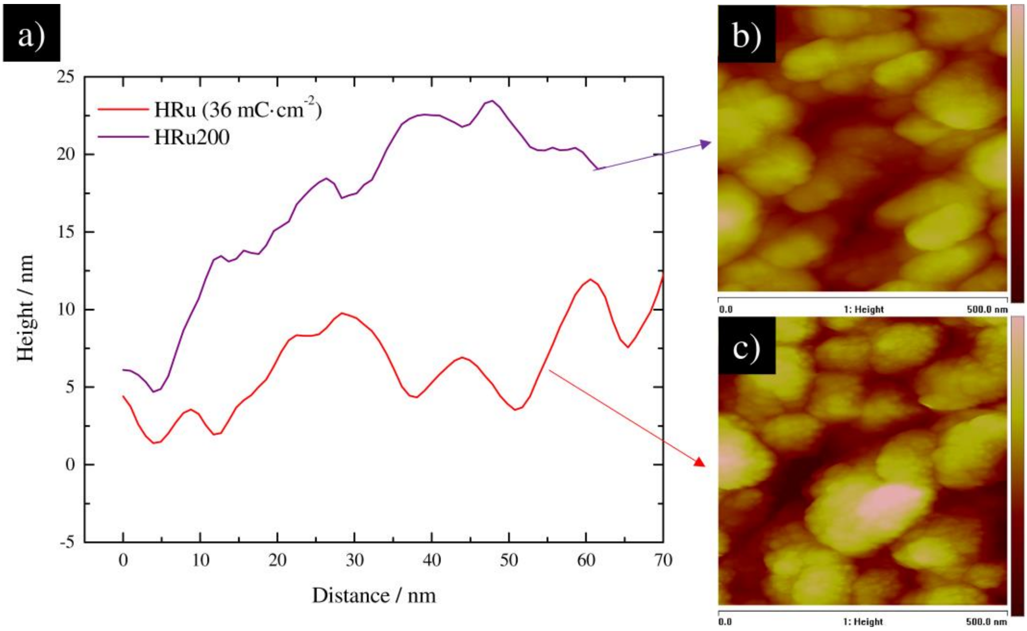

Figure 5.7: Surface topography obtained using AFM scan images for the RuO_2-coated hematite films: (a) profile height of both samples; 2D images of (b) as-prepared (HRu sample) and (c) after annealing treatment at 200 ºC (HRu200 sample). The AFM image scale is 500 × 500 μm^2.

X-ray diffraction (XRD) was used to obtain information about the crystalline nature of the prepared photoelectrodes – see Figure 5.8. The obtained X-ray diffractograms shows mainly peaks of the FTO (F:SnO_2) coating layer where Fe_2O_3 signal pattern is superimposed. Bare hematite (BH) photoanode shows two peaks due to pure α-Fe_2O_3 (hematite), namely the (104) plane found at 35.8º and the (110) plane found at 35.8º. The strong diffraction peak at 33.3º, corresponding to the (110) plane of a pseudo-cubic system, indicates the strong preferential crystal orientation for electron transport in hematite photoanodes. Much weaker peaks are observed for planes (012) at 24.2º, (024) at 49.6º and (116) at 54.2º. No other phases of Fe_2O_3 could be observed in the XRD patterns. When coated with RuO_2 co-catalyst (HRu sample), the Fe_2O_3 peaks are less intense compared with the BH sample and no RuO_2 characteristic peaks are observed in Figure 5.8; RuO_2 layer is amorphous as previously mentioned. After annealing the RuO_2-coated hematite film at 200 ºC (HRu200 sample), the RuO_2 diffuse scattering peak at 36º reported by Fang *et al.* [44] is not detected. Herein, the RuO_2-coated hematite film only displays two strong peaks at 33.3º and 35.8º, characteristic of hematite film.

The characteristic hematite peak at 35.8º may superimpose the expected signal of RuO_2, at 36º, which should be rather small due to the very thin RuO_2 film thickness, *ca.* 5 nm. Despite no evidences of amorphous-to-crystalline phase transformation, the morphology (Figure 5.5) and topography (Figure 5.6) of the HRu200 film indicate a better surface organization.

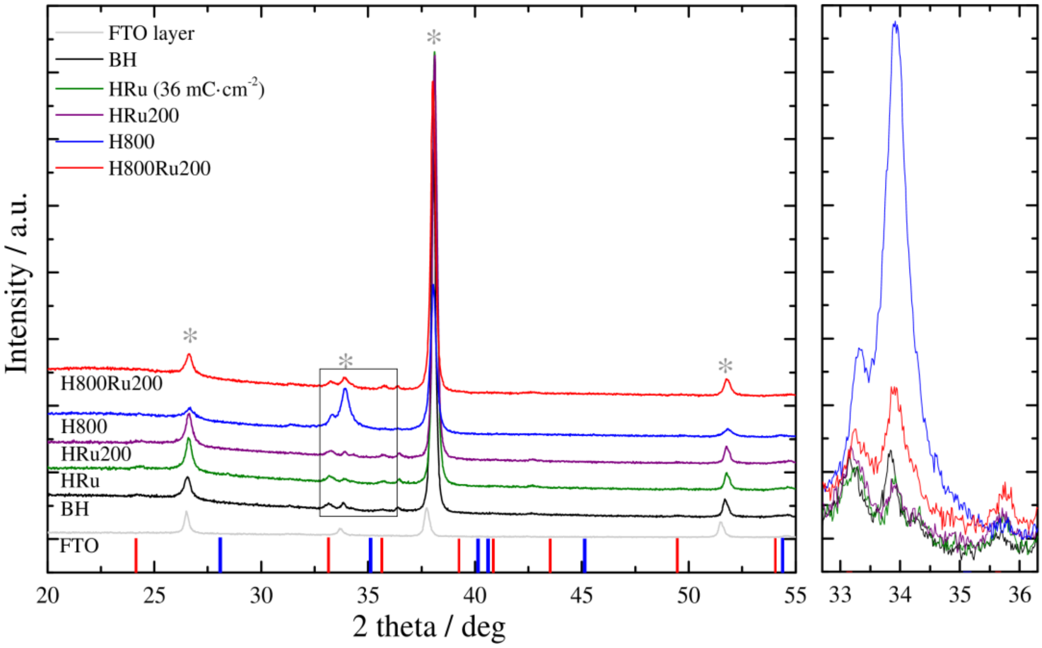

Figure 5.8: XRD spectra of the prepared photoanodes: bare hematite (BH, black line), RuO_2-coated hematite (HRu, green line), RuO_2-coated hematite sintered at 200 ºC (HRu200, purple line), hematite annealed at 800 ºC (H800, blue line), hematite annealed at 800 ºC and coated with RuO_2 further sintered at 200 ºC (H800Ru200, red line). The FTO glass substrate (grey line) corresponds to the SnO_2 signals (ICDD reference pattern number: 96-100-0063). The signals of hematite (ICDD reference pattern number: 96-101-1241) and RuO_2 (ICDD reference pattern number: 96-101-0059) phases correspond to red and blue column bars, respectively. Main peaks from the FTO substrate are labelled with "*". On the right-side is a zoom-out of the left-side from 33º to 37º.

5.1.6 HIGH-TEMPERATURE ANNEALING OF THE HEMATITE PHOTOANODES

Annealing at elevated temperatures (higher than 650 ºC) has been recently reported to cathodically shift the water oxidation onset potential; this shift was assigned to the decrease of hematite surface defects [6]. Also, the diffusion of Sn from the FTO layer into the hematite lattice, expected for temperatures above 650 ºC, contributes for photocurrent enhancement [46]. The prepared hematite photoelectrodes were sintered at 550 ºC for 30 min to induce the phase transition from β-FeOOH to pure α-Fe_2O_3; however, only temperatures above 800 ºC can fully remove the hydroxyl groups from the hematite [47]. For that reason, hematite photoanodes were further annealed at 800 ºC for various periods of time (5, 10 and 20 min). Figure 5.9 shows the *J-V* curves for a typical bare hematite film (sintered at 550 ºC for 30 min) and after high-temperature annealing treatments.

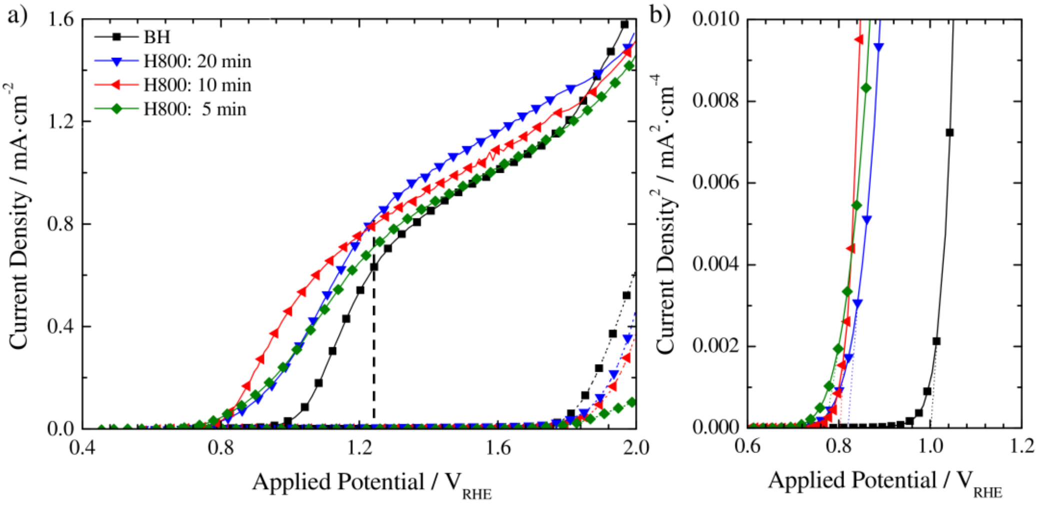

Figure 5.9: (a) *J-V* characteristic curves measured in the dark and under 1-sun AM 1.5 G illumination conditions for the bare hematite (BH) photoanode sintered at 550 ºC (■) and hematite photoanodes and after annealing treatment at 800 ºC (H800) for different periods: 20 min (◆), 10 min (◀) and 5 min (▼); and (b) correspondent Butler plots.

The bare hematite (BH) photoanode sintered at 550 ºC (control sample) exhibited a late photocurrent onset potential of *ca.* 1.00 V_{RHE} with a photocurrent response of 0.62 mA·cm^{-2} at 1.23 V_{RHE} and 0.90 mA·cm^{-2} at 1.45 V_{RHE} [32]. On the other hand, hematite heat-treated at 800 ºC (H800 samples) showed a dramatic improvement in their photocurrent onset potential, showing a cathodic shift of around 200 mV; similar cathodic shifts were reported by other research groups [14, 21, 48]. Despite an annealing time of 5 min being sufficient to cathodically shift the turn-on potential to *ca.* 0.78 V_{RHE}, the best overall performance (onset potential and photocurrents) was obtained for sample annealed at 800 ºC over 10 min. For this sample, the photocurrent onset potential starts at *ca.* 0.80 V_{RHE} and showed a noticeable photocurrent of *ca.* 0.48 $mA\cdot cm^{-2}$ at 1.00 V_{RHE} compared to the control BH sample (< 0.01 $mA\cdot cm^{-2}$). At 1.23 V_{RHE} a photocurrent of *ca.* 0.79 $mA\cdot cm^{-2}$ was obtained, which is one of the best reported performances for a thin-film of bare hematite photoanode; the state-of-the-art bare hematite film showed a current density of *ca.* 0.31 $mA\cdot cm^{-2}$ [8]. By further increasing the annealing time to 20 min, the performance increased at higher potentials (10 % increase at 1.45 V_{RHE}), but a slight decrease is observed for lower potentials, *i.e.* the current decreased to *ca.* 0.20 $mA\cdot cm^{-2}$ at 1.00 V_{RHE}. Hereafter, the hematite thin film annealed at 800 ºC for 10 min is called as H800 sample.

Figure 5.10 shows SEM and AFM images of the best performing hematite thin films (H800 - annealing temperature of 800 ºC during 10 min). The morphological structure did not change after the high-temperature treatment; however, the average grain size slightly increased possibly driven by grain aggregation occurred in the annealing process, *i.e.* the grain size increased from (97 ± 12) nm to (128 ± 17) nm for the bare hematite and hematite annealed films, respectively. This behavior effectively reduces the grain boundaries that can act as electron traps in the photoanodes [49]. AFM images also shows a smoother surface after annealing at 800 ºC, as a result of the significant roughness decrease to R_q = 18.1 nm. From Figure 5.8 the H800 sample displays similar X-ray patterns with a predominant (110) diffraction peak compared with BH sample. However, the peaks of the H800 sample are sharper, with a decrease in full width at half-maximum (fwhm), showing a significant increase in crystallite size.

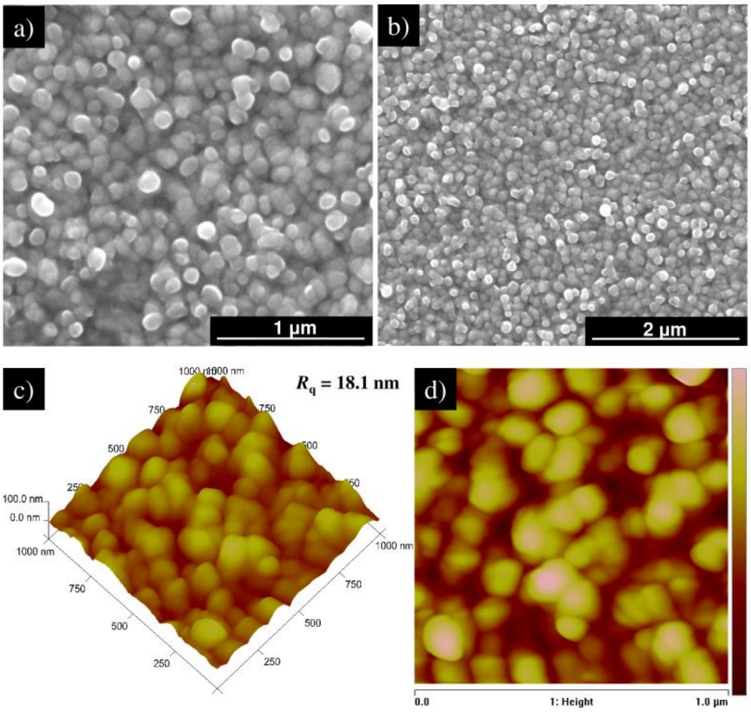

Figure 5.10: Surface top-view SEM images of the hematite photoanode annealed at 800 ºC over 10 min (H800 sample), with magnifications of (a) 100000× and (b) 50000×. Surface topography obtained using: (c) 3D AFM scan image (1 × 1 μm^2 image scale) and (d) 2D image.

X-ray photoelectron spectroscopy (XPS) was assessed to obtain information about the surface chemistry of the prepared photoanodes - Figure 5.11. For all hematite photoanodes, the C 1s photoelectron peak (Figure 5.11e) should be attributed to adventitious carbon contamination. Bare hematite (BH) film sintered at 550 ºC presents mainly iron and oxygen elements on XPS spectra shown in Figure 5.11a. Silicon is also detected, which is related to the TEOS pre-treatment performed before hematite thin film deposition. The O 1s signal position at 529.3 eV and the separation of Fe 2p peaks (Fe $2p_{3/2}$ at 711.0 eV from Fe $2p_{1/2}$ at 529.7 eV) are in good agreement with the presence of iron (III) oxide - Figure 5.11c and b, respectively. After annealing treatment at 800 ºC (H800 sample), a shift on the position of Fe 2p, O 1s and C 1s peaks to higher binding energies is observed, but their shape is similar to BH sample. As expected, Sn was detected on the surface XPS spectra of the H800 sample - Figure 5.11d. The H800 sample exhibits two peaks at 495.1 eV and 486.4 eV due to the presence of Sn(IV) species, corresponding to the Sn 3d$_{3/2}$ and Sn 3d$_{5/2}$ peaks, respectively [25]. The presence of Sn at the surface of H800 photoanode (overall amount of *ca.* 0.69 at%) suggests a thermally induced diffusion of Sn ions from the FTO layer [49], since no traces of Sn was detected for the BH sample.

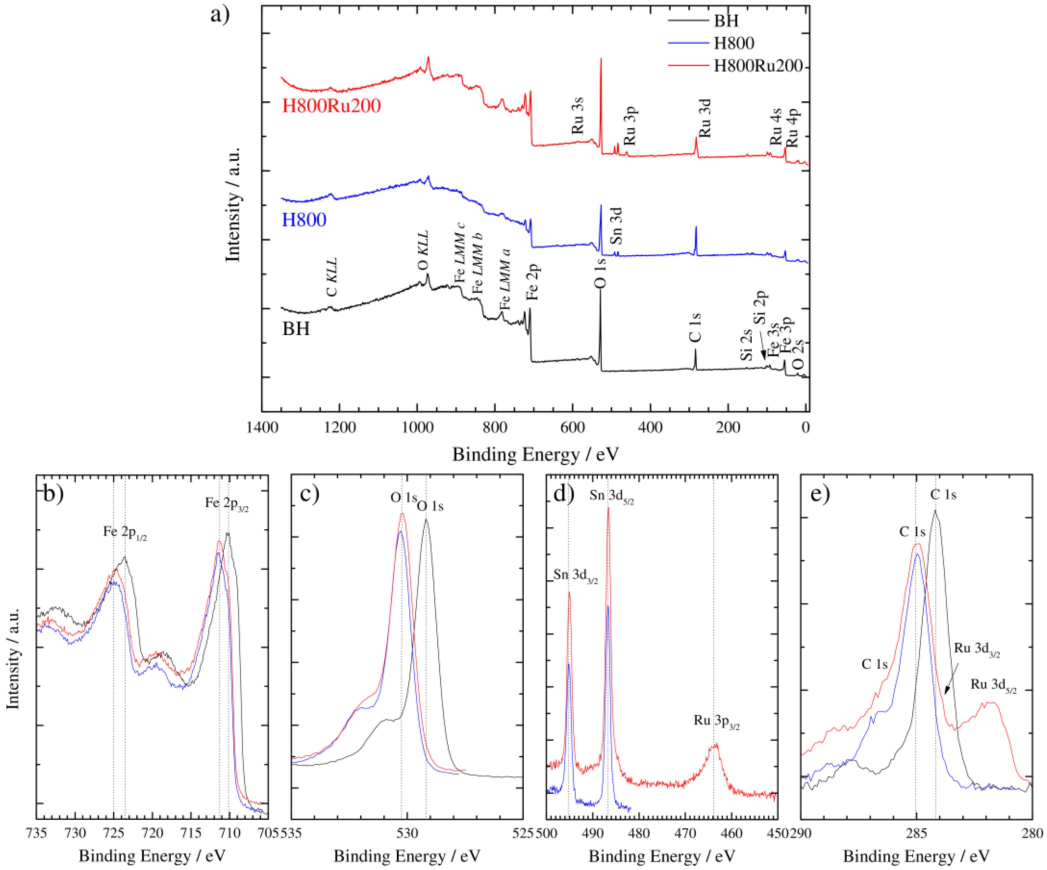

Figure 5.11: (a) Surface wide-scan XPS spectra for the bare hematite (BH), hematite annealed at 800 ºC (H800) and RuO$_2$-coated hematite sintered at 200 ºC (H800Ru200) photoanodes. Detailed regions for: (b) Fe 2p; (c) O 1s; d) Sn 3d and Ru 3p; and (e) C 1s and Ru 3d.

Summarizing, the high temperature annealing (800 ºC) improves the water oxidation efficiency through three mechanisms: i) the grain aggregation allows a compact hematite structure to be formed that decreases the amount of recombination centers on the surface; ii) better hematite crystallinity improves charge carrier extraction; and iii) Sn doping from the FTO layer to the hematite lattice enhances both the electron donor density and electrical conductivity.

5.1.7 SYNERGETIC COMBINATION OF HIGH-TEMPERATURE ANNEALING AND RuO_2 SURFACE COATING

For obtaining high-energy performing photoelectrodes, hematite photoelectrodes were annealed at 800 ºC and coated with RuO_2 (charge of 36 mC·cm^{-2}) and further sintered at 200 ºC (the so-called H800Ru200 sample) - Figure 5.12. A significant decrease on the turn-on potential of *ca.* 0.52 V_{RHE} was achieved with this optimized photoelectrode as illustrated in Figure 5.12a. Photocurrent densities of *ca.* 0.29 mA·cm^{-2} and 0.60 mA·cm^{-2} were obtained at 0.60 and 1.00 V_{RHE}, respectively; when compared with bare hematite, it shows an increase higher than 50 % at 1.23 V_{RHE}. Again, water oxidation seems to be catalyzed by RuO_2 co-catalyst at the onset potential range (lower applied bias) and directly at the hematite surface at greater applied potentials, as observed in Figure 5.2.

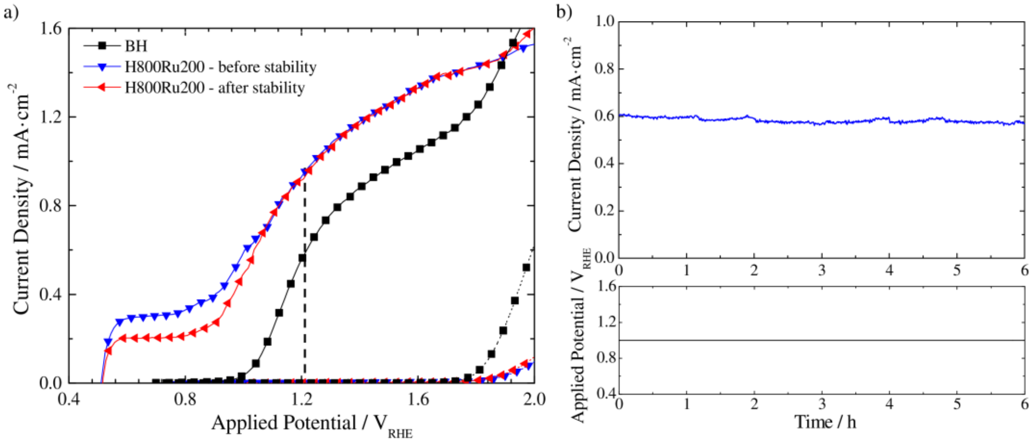

Figure 5.12: (a) *J-V* characteristics of the bare hematite (BH sample) photoanode (■) and the H800Ru200 sample, before starting the stability test (▼) and after 6 h of testing (◀), in the dark (dashed lines) and under 1-sun AM 1.5 G illumination (solid lines) conditions. (b) Polarization curve of the H800Ru200 photoanode obtained under a constant bias of 1.00 V_{RHE} and simulated solar illumination (AM 1.5 G, 100 mW·cm^{-2}).

The stability of the optimized sample was evaluated over 6 h of simulated sunlight exposure at a constant potential of 1.00 V_{RHE} – Figure 5.12b. The electrolyte solution was continuously bubbled with nitrogen during the measurements to facilitate the removal of evolved oxygen from the RuO_2 electrode surface. The oxygen removal decreases the water oxidation overpotential and benefits the electrode stability [27]. The photocurrent density decreased to 0.57 mA·cm^{-2} at 1.00 V_{RHE} after the stability period, corresponding to *ca.* 5 % decrease. The loss of current is not uniform over the *J-V* characteristic curve, Figure 5.12a, but shows a measurable decrease only for the low potential range, where RuO_2 is thought to control the water electrooxidation. This loss should be related to the loss/detachment of RuO_2, as illustrated in Figure 5.14d. This shift can be fully restored with the application of more catalyst, data not shown.

Figure 5.13 shows the open circuit potential (OCP) difference between dark and illumination (E_{photo}), which is directly related to the photopotential. A photopotential of *ca.* 350 mV was obtained for the bare hematite (BH) photoanode, in line with previous reports [22], while the RuO_2-coated hematite (HRu200) photoanode exhibited E_{photo} = 500 mV. Interestingly, after annealing at 800 ºC, the original photopotential increased even more, for E_{photo} = 750 mV. Lastly, a remarkable E_{photo} = 950 mV was obtained for the optimized RuO_2-coated hematite photoanode, *i.e.* H800Ru200 sample. A larger photopotential means that less potential bias is required to promote oxygen evolution [22]. To the best knowledge of the authors, the final photopotential of 0.95 V is the highest reported for hematite-based PEC water splitting [50].

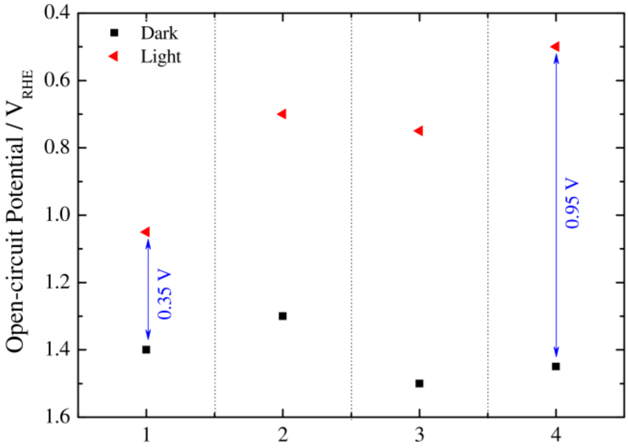

Figure 5.13: Open circuit potential difference between dark (■) and light (◀) conditions for the photoanodes under study: (1) bare hematite (BH sample), (2) RuO_2-coated hematite (HRu sample - 36 mC·cm^{-2}), (3) hematite annealed at 800 ºC over 10 min (H800 sample), and (4) optimized RuO_2-coated hematite sintered at 200 ºC (H800Ru200 sample).

Figure 5.14 shows SEM and AFM surface images of a fresh H800Ru200 sample; EDS analyses of fresh and aged photoelectrode are also displayed. Figure 5.14a and b confirm that the optimized hematite photoanode presents a very organized structure and the RuO_2 co-catalyst fully covered the hematite surface. The morphology is similar to the hematite film after annealing at 800 ºC (H800 sample shown in Figure 5.10), but the characteristic RuO_2 small grains after sintering at 200 ºC are not as clear as in Figure 5.5. This may justify the smaller photocurrents obtained at lower potentials compared to Figure 5.9. Therefore, further optimization of RuO_2 loading in the smoothened hematite surface is needed to obtain even higher photopotentials. No significant morphological differences were observed between the fresh and aged sample, though the observed photocurrent decrease during the stability test - Figure 5.14. Moreover, the EDS analyses of both fresh and aged H800Ru200 sample are similar, with the exception of Ru and O elements that tends to slightly decrease at aged sample, as presented in Figure 5.14d. The topography of the fresh H800Ru200 photoanode analyzed by AFM also reveals a smoother surface after coating with RuO_2, *i.e.* R_q decreased to *ca.* 15.1 nm (Figure 5.14e and f).

Figure 5.8 displays the XRD diffractogram obtained for the H800Ru200 sample; the preferential hematite crystal orientation along (110) plane is similar to BH and H800 photoanodes. The intensity of the strong peak of (104) plane found at 33.3º decreases and the peak the (110) plane found at 35.8º increases, which can be related to the RuO_2 coating; however, no RuO_2 signal were detected. XPS analysis displayed in Figure 5.11 reveals the presence of Fe, O, C, Si, Sn and Ru elements for the H800Ru200 photoanode. No appreciable variations in the position and shape of Fe 2p, O 1s and Sn 3d peaks were observed compared with H800 sample. The Ru $3p_{3/2}$ peak presented in Figure 5.11d is attributed to the RuO_2 component (463.6 eV). However, the Ru 3d core levels in the C 1s region (Figure 5.11c) is quite complex due to the overlapping between C 1s and Ru $3d_{3/2}$ XPS data; a total of eight components including peaks assigned to the Ru 3d photoelectrons was observed. Deconvolution analysis yielded two well-defined emission lines at 281.8 and 283.7 eV assigned to Ru $3d_{5/2}$ and Ru $3d_{3/2}$, respectively. These peaks are typical of the Ru^{4+} oxidation state of ruthenium, which confirmed the presence of a RuO_2 film [51]. Finally, intensity increase of the asymmetric O 1s emission line (Figure 5.11c) can be attributed to the lattice oxygen in the RuO_2 film. The surface of H800Ru200 sample presented very small amount of

RuO_2, confirming the expected small amount of RuO_2 co-catalyst deposited (*ca.* 4.5 nm thick).

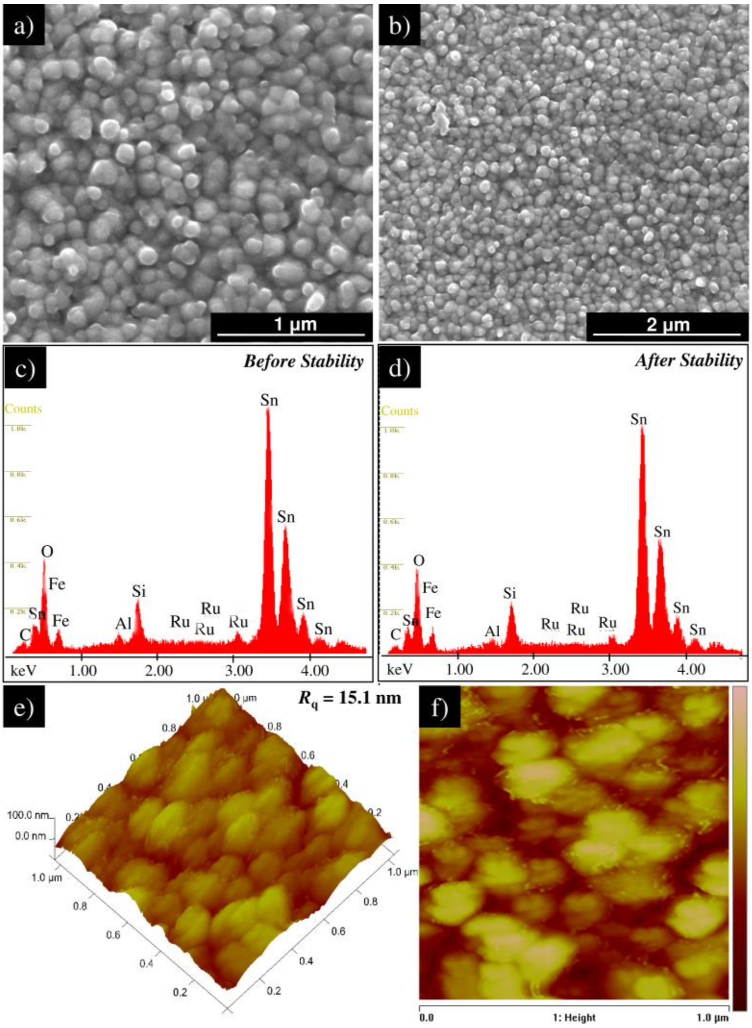

Figure 5.14: Surface top-view SEM images of fresh H800Ru200 photoanode with magnifications of (a) 100000× and (b) 50000×. EDS analyses for the H800Ru200 sample: (c) before and (d) after the stability test over 6 h. Surface topography of fresh H800Ru200 photoanode obtained using: (e) 3D AFM scan image (1 × 1 μm^2 image scale) and (f) 2D image.

Electrochemical impedance measurements were performed using a three-electrode configuration in dark and under 1-sun AM 1.5 G illumination conditions: of bare hematite (BH), hematite annealed at 800 ºC (H800) and optimized RuO_2-coated hematite (H800Ru200) photoanodes. Representative Nyquist plots obtained at 1.00 V_{RHE} under dark conditions are shown in Figure 5.15a.

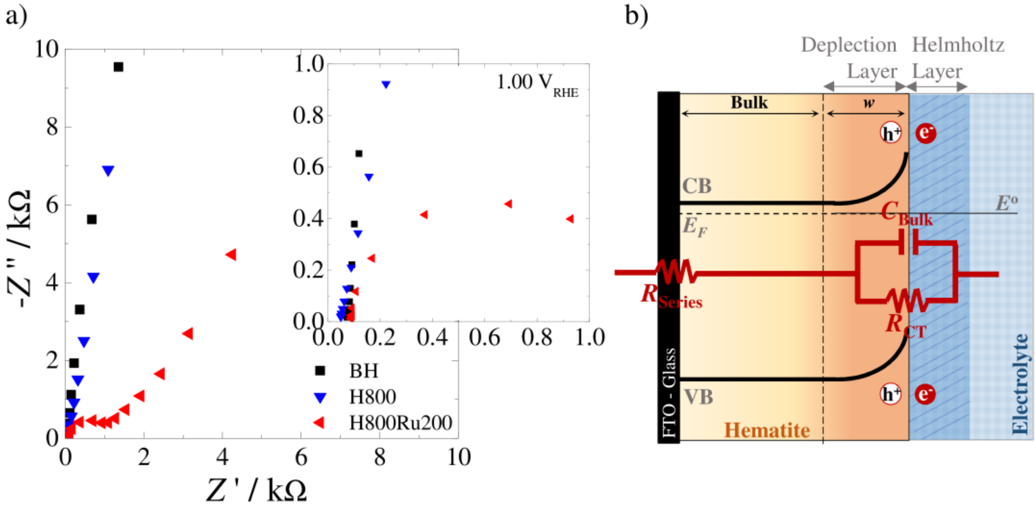

Figure 5.15: (a) Nyquist plots obtained in the dark at 1.00 V_{RHE} for bare hematite (BH, ■), hematite annealed at 800 ºC (H800, ▼) and optimized RuO_2-coated hematite (H800Ru200, ◀) photoanodes; and (b) electrical circuit analogue used to fit the impedance data under dark conditions.

The EIS measurements in dark of the bare hematite photoelectrode with and without annealing treatment at 800 ºC show only one semicircle, whereas for RuO_2-coated hematite photoelectrode shows two semicircles. However, for potentials higher than 1.25 V_{RHE} it is only observed one semicircle also for RuO_2-coated hematite photoelectrode. The low-frequency (high impedance) semicircle disappears since the contribution of the RuO_2 tends to decrease at higher potentials, *i.e.* the oxygen evolution seems to occur via the hematite surface at higher potentials, as previously observed (Figure 5.2). In this case, a Randles electrical analogue circuit was employed to fit the impedance data, which comprises a series resistance (R_{Series}) and a simple resistor-capacitor (RC) element assigned to the semiconductor/electrolyte charge transfer resistance, R_{CT}, together with bulk capacitance, C_{Bulk} – Figure 5.15b.

The Mott-Schottky analysis was performed in the dark at high frequency range of the impedance spectra, in the order of kHz [36]. The flat band potential, E_{fb}, and the donor density, N_{D}, were then estimated using the following equation:

$$\frac{1}{C_{\mathrm{Bulk}}^{2}} = \frac{2}{\varepsilon_0 \varepsilon_{\mathrm{r}} q N_{\mathrm{D}} A^{2}} \left(\left(E - E_{\mathrm{fb}} \right) - \frac{kT}{q} \right) \tag{5.6}$$

where ε_0 is the vacuum permittivity (8.85×10^{-12} C·V^{-1}·m^{-1}), ε_{r} is the dielectric constant of the semiconductor (assumed to be 80 for undoped hematite photoanodes [10]), q is the elementary charge, A is the active area, k is the Boltzmann constant, T is the absolute temperature, and E is the applied potential. Plotting C_{Bulk}^{-2} as a function of the applied bias potential, a straight line can be fitted to the linear region of the plot, from 0.80 to 1.40 $\mathrm{V_{RHE}}$, as shown in Figure 5.16. N_{D} value was determined from the slope of this line, while E_{fb} value was obtained extrapolating the interception of the straight line with the axis of the applied potential; Table 5.1 shows the obtained values.

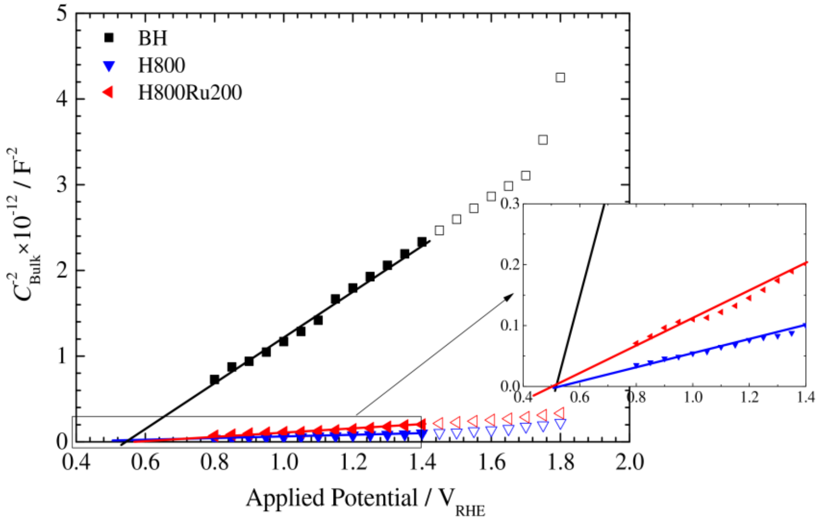

Figure 5.16: Mott-Schottky analysis of bare hematite (BH, ■), hematite annealed at 800 ºC (H800, ▼) and optimized RuO_2-coated hematite (H800Ru200, ◀) photoanodes.

Table 5.1: Flatband potential (E_{fb}) and donor density concentration (N_D) values obtained from Mott-Schottky measurements in the dark for the three photoelectrodes under study.

Samples	**E_{fb} / V_{RHE}**	**N_D / cm^{-3}**
BH	0.54	2.32×10^{18}
H800	0.57	5.38×10^{19}
H800Ru200	0.52	2.88×10^{19}

From the slope of the Mott-Schottky plots (Figure 5.16) it can be seen that hematite photoelectrodes annealed at 800 ºC (both H800 and H800Ru200) have an order of magnitude higher donor density (N_D) than bare hematite (BH). This great increase should be related to the migration of Sn from the FTO layer, as mentioned before. It should be emphasized that a photoelectrode with higher N_D shows higher electrical conductivity. RuO_2-coated hematite photoelectrode (H800Ru200) exhibits a E_{fb} = 0.52 V_{RHE}, which is the observed onset potential for this photoelectrode – Figure 5.12a. This result suggests the role of RuO_2 co-catalyst in increasing the band bending that further improves the PEC performance; similar observations were reported for Co-Pi co-catalyst as described elsewhere [52].The obtained values are consistent with the ones found in literature for hematite photoelectrodes: E_{fb} range from 0.40 – 0.60 V_{RHE} and N_D on the order of $10^{17} – 10^{21}$ cm^{-3} for undoped and heavily doped hematite samples, respectively [7].

Figure 5.17a displays the Nyquist plots under illumination conditions for the three photoelectrodes under study. Herein, two semicircles can be seen for all photoelectrodes: a small semicircle in the high frequency range ascribed to the charge-transfer process in the bulk of hematite photoelectrode; and the low-frequencies arc attributed to the electron transfer at hematite surface states or RuO_2 layer, respectively for hematite and RuO_2-coated hematite photoelectrodes. The low-frequency semicircle is smaller for H800Ru200 sample, indicating a faster surface water oxidation. However, at more positive potentials (> 1.25 V_{RHE}), the low-frequency semicircle tends to disappear for all samples, showing that the charge transfer from the surface states of hematite or the RuO_2 co-catalyst to electrolyte solution is not the rate-limiting step of water oxidation [9].

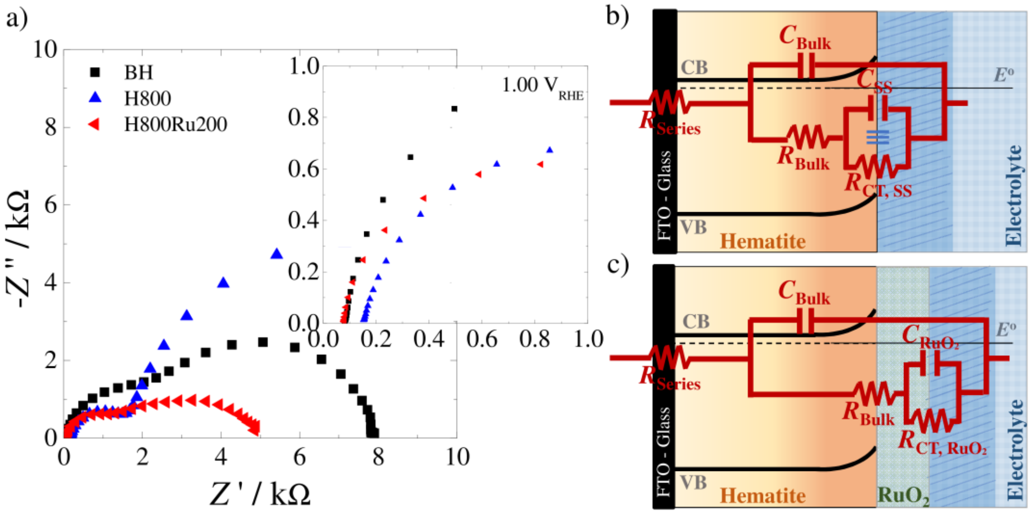

Figure 5.17: (a) Nyquist plots obtained under 1-sun AM 1.5 G illumination and at 1.00 V_{RHE} for bare hematite (BH, ■), hematite annealed at 800 ºC (H800, ▼) and optimized RuO_2-coated hematite (H800Ru200, ◀) photoanodes; electrical circuit analogue used to fit the impedance data under illumination for the photoelectrodes under study: (b) BH and H800 samples and (c) H800Ru200 sample.

For interpreting the EIS data under illumination conditions the equivalent circuit proposed by Klahr *et al.* [9] was considered. Figure 5.17b shows the equivalent circuit used for bare hematite and hematite annealed at 800 ºC photoelectrodes, consisting of a R_{Series}, then a C_{Bulk} in parallel with a resistance from the charge transport/recombination within the bulk semiconductor (R_{Bulk}) and a RC unit consisting of a charge transfer resistance from the surface states ($R_{CT,\ SS}$) to electrolyte in parallel with its correspondent capacitance (C_{SS}). This model highlights the central role of a surface states acting as recombination centres, either trapping electrons from the conduction band and holes from the valence band within the hematite bulk, or affecting the charge transfer from the semiconductor to redox species. For the RuO_2-coated hematite electrode, additional electrical components were added accounting to the co-catalyst layer: the charge transfer resistance from the RuO_2 surface layer ($R_{CT,\ RuO2}$) and its capacitance (C_{RuO2}). However, this equivalent circuit could not fit the impedance spectra and, thus, it was simplified to the equivalent circuit illustrated in Figure 5.17c; a similar observation was reported for hematite electrodes coated with Co-Pi [53]. Therefore, the obtained impedance parameters for bare hematite, hematite annealed at 800 ºC (C_{Bulk},

R_{Bulk}, C_{SS} and $R_{CT,\ SS}$) and RuO_2-coated hematite photoelectrodes (C_{Bulk}, R_{Bulk}, C_{RuO2} and $R_{CT,\ RuO2}$) are presented *vs.* applied potential – Figure 5.17. The series resistance, R_{Series}, was essentially constant and small for all the applied potentials, which is consistent with ohmic behavior at the FTO/hematite interface. R_{Series} values were higher for hematite photoanode annealed at 800 ºC possible due to loss of Sn from the FTO layer – inset plot of Figure 5.18a.

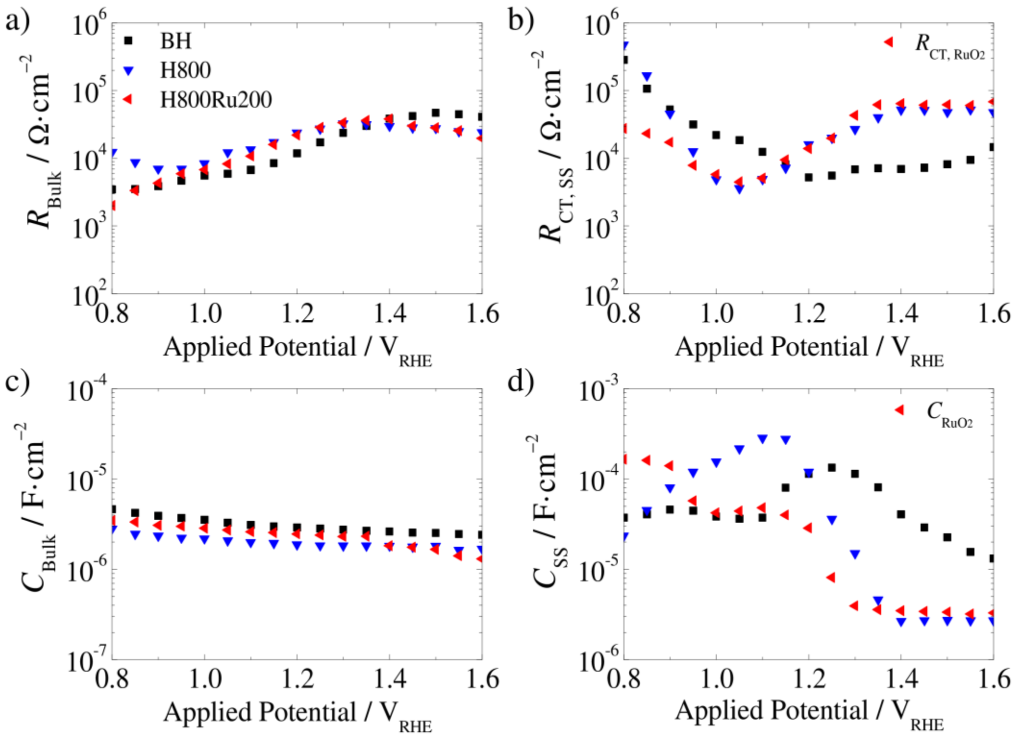

Figure 5.18: Impedance parameters obtained from fitting the EIS data under illumination for bare hematite (BH, ■), hematite annealed at 800 ºC (H800, ▼) and optimized RuO_2-coated hematite (H800Ru200, ◀) photoanodes.

From Figure 5.18a the charge transport resistance within the bulk semiconductor, R_{Bulk}, shows a similar trend for all photoelectrodes from 1.00 to 1.70 V_{RHE}; it increases after *ca.* 1.00 V_{RHE} to a maximum of *ca.* 3.85 $\Omega\cdot cm^{-2}$ at 1.50 V_{RHE}. However, at lower potentials (< 1.20 V_{RHE}) R_{Bulk} for the H800Ru200 photoanode is lower than for hematite photoanodes (BH and H800), suggesting that the RuO_2 co-catalyst influences the surface electron-hole recombination.

The charge transfer resistance, R_{CT}, drops until the onset potential for PEC water oxidation (*ca.* 1.23 V_{RHE}) and it drops exponentially for the RuO_2-coated hematite photoelectrode. After this potential, $R_{CT,\ RuO2}$ closely resembles $R_{CT,\ SS}$ for hematite photoelectrode annealed at 800 ºC; for bare hematite photoelectrode, the $R_{CT,\ SS}$ is smaller throughout the applied potential range. Thus, the charge transfer from RuO_2 to electrolyte is not the limiting rate to oxidize water when the applied potential is higher than 1.40 V_{RHE}, as observed in Figure 5.2. At these potentials the photocurrent density is controlled by the number of holes that reach hematite surface for both bare and RuO_2-coated hematite photoanodes [9]. Comparing Figure 5.18a and b, R_{Bulk} is lower than $R_{CT,\ RuO2}$ at potentials lower than 1.23 V_{RHE}, which evidences a faster charge transfer of holes from the valence band of hematite to the RuO_2.

The bulk capacitance, C_{Bulk}, is essentially constant for the applied potentials, as illustrated in Figure 5.18c. On the other hand, the capacitance of the surface states associated to hematite, C_{SS}, or of the RuO_2 surface, C_{RuO2}, varies with the applied potential - Figure 5.18d. C_{SS} peaks near the water oxidation onset potential, which correlates with the observed minimum of $R_{CT,\ SS}$; the potential at which these features happen, coincides with the photocurrent onset potential. This behavior is not observed for H800Ru200 photoelectrode. At cathodic potentials (< 1.00 V_{RHE}) C_{RuO2} is mainly constant and presents the highest values; in this region water oxidation seems to be catalyzed by RuO_2 co-catalyst, which captures efficiently the photogenerated holes.

The water oxidation kinetics and electron-hole recombination are the main processes controlling the performance of hematite photoanodes [54]. The sluggish kinetics of the multistep oxygen evolution reaction, with four holes being required to drive the oxidation of two molecules of water and one molecule of oxygen, increases the recombination probability. The bulk recombination (> 5 nm from the semiconductor liquid junction) is almost independent of the hematite surface modification [43]; its contribution may be regarded as part of the photoelectrode charge separation and was not considered here. On the other hand, the electron-hole recombination at hematite surface is expected to be a bispecies process, depending on the electron and hole densities. Actually, the yield of surface holes depends on both the applied bias and the excitation density; the recombination becomes slower as the steady state electron density in the film reduces under positive bias. Moreover, the electron density of the film should be independent of the light intensity and the recombination tends to behave linearly with the irradiance; this behavior suggests a pseudo first-order recombination rate with respect to hole concentration [15], and the rate constant is denoted as k_{rec}. The timescale of water oxidation is independent of the photogenerated holes concentration, indicating that the mechanism of water oxidation on hematite proceeds via a sequence of single-hole oxidation steps. Therefore, the charge transfer rate constant (k_{CT}), which corresponds to the reaction between surface trapped holes and water/surface-bound water is assumed to be first-order in hole density [43]. From the photoelectrodes EIS analysis under illumination conditions, the k_{CT} can be obtained directly at the maximum phase angle of the charge transfer semicircle in the Nyquist plots, *i.e.* the charge transfer time constant $\tau_{CT} = R_{CT} \cdot C_{CT}$. The rate constants k_{CT} and k_{rec} are related to the resistance parameters measured by EIS (R_{Bulk} and R_{CT}) by the following equation [55]:

$$\frac{R_{\mathrm{Bulk}}}{R_{\mathrm{CT}}} = \frac{k_{\mathrm{CT}}}{\left(nk_{\mathrm{Bulk}} + k_{\mathrm{rec}}\right)} = \gamma\left(E\right)\frac{k_{\mathrm{CT}}}{k_{\mathrm{rec}}} \tag{5.7}$$

where n is the electron density (taken to be constant at constant illumination intensity), k_{Bulk} is the bulk electron trapping rate constant and $\gamma(E)$ is the probability of electron-trap occupation at a given trap energy and E is the applied potential. $\gamma(E)$ is given by the potentials and the trap depth (taking values between 0 and 1) [55]:

$$\gamma\left(E\right) = \left[1 + \exp\left(\frac{E_{\mathrm{F}} - E_{\mathrm{T}}}{k_{\mathrm{B}}T}\right) \cdot \exp\left(-\frac{qE}{k_{\mathrm{B}}T}\right)\right]^{-1} \tag{5.8}$$

where E_F is the Fermi level at equilibrium and E_T is the energy of the electron trap. At zero potential bias, $\gamma(E)$ depends exclusively on the trap depth in the bandgap. However, it converges to the unity as the potential increases [43] allowing the simplification of equation (5.8): $R_{\mathrm{Bulk}}/R_{\mathrm{CT}} = k_{\mathrm{CT}}/k_{\mathrm{rec}}$.

The water oxidation quantum efficiency (φ) can then be calculated using these parameters:

$$\eta_{\mathrm{OER}} = \frac{k_{\mathrm{CT}}}{\left(k_{\mathrm{CT}} + k_{\mathrm{rec}}\right)} \tag{5.9}$$

Figure 5.19 summarizes the values of k_{CT}, k_{rec} and η_{OER} parameters *vs* the applied potential. The charge transfer rate constant (k_{CT}) for hematite photoanodes (BH and H800 samples) is in the range of 1 – 10 s^{-1} at potentials below 1.10 V_{RHE}, which is the typical range for efficient water oxidation, exhibiting lifetimes of holes in the order of

0.1 – 1 s [56]. From Figure 5.19a is also observed a k_{CT} increase for RuO_2-coated hematite photoanode, showing that RuO_2 is an efficient water oxidation electrocatalyst and that at low applied potentials the OER occurs mainly at the co-catalyst surface, as previously observed. However, k_{CT} should be independent of the applied potential for an ideal PEC system; this change should be related to the Fermi-level pinning [43]. Fermi-level pinning has been reported for hematite photoanodes in aqueous electrolyte, which is the main reason for late turn-on potential required for PEC water oxidation [43, 57]. Indeed, the RuO_2 layer has the ability to store holes at its surface, reducing the positive charge accumulation at hematite, which is expected to decrease the degree of the pinned Fermi level and then allow the band bending to increase at lower potentials [58].

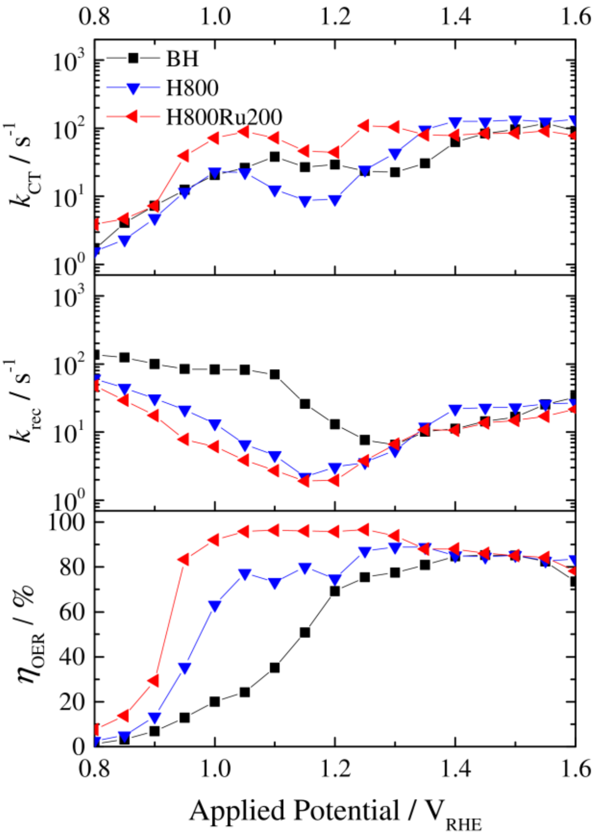

Figure 5.19: (a) Charge transfer rate constants, k_{CT}; (b) recombination rate constants, k_{rec}; and (c) water oxidation quantum efficiencies, η_{OER}, obtained from the EIS data under illumination for bare hematite (BH, ■), hematite annealed at 800 °C (H800, ▼) and optimized RuO_2-coated hematite (H800Ru200, ◀) photoanodes.

Electron-hole recombination rate constants, k_{rec}, between 100 and 1 s^{-1} for the applied potentials under study were obtained - Figure 5.19b. Bare hematite photoanode shows a k_{rec} one order of magnitude higher than k_{CT} for potentials below 1.20 V_{RHE}, as reported elsewhere.[59, 60] The much faster recombination compared to the charge transfer determines the overpotential and, consequently, the PEC performance of the hematite photoanodes. Moreover, at these potentials the recombination for BH photoanode is considerably higher than that for H800, which is still higher than that for H800Ru200. In the absence of RuO_2, the recombination phenomena would occur either within the bulk or at surface of hematite and it tends to decrease as the potential increases; whereas the k_{rec} is limited by the flux of holes to the hematite surface at the RuO_2/hematite interface. This justifies that the high temperature annealing treatment and the addition of RuO_2 co-catalyst indeed reduce the surface recombination.

Figure 5.19c plots the water oxidation quantum efficiency *vs* the applied potential; the shape of these curves are similar to the *J-V* plot shown in Figure 5.12. RuO_2-coated hematite photoanode shows greater quantum efficiencies, with values above 90 % for potentials higher than 1.00 V_{RHE}. The efficiency slightly decreases for high applied potentials (> 1.30 V_{RHE}), which should be due to deviations of charge transfer kinetics models under large degree of band bending [58]. Indeed, the H800Ru200 photoelectrode presented a lower flatband potential (Table 5.1), indicating that the new heterojunction increased the band bending in hematite by reduction of surface states on the RuO_2 layer. The improvement of interfacial hole transfer by catalysis and by suppressing the surface recombination influences the PEC efficiency and strongly increases the photopotential (shown in Figure 5.13).

5.4 CONCLUSIONS

Hematite thin films annealed at 800 ºC over 10 min showed an earlier onset potential at *ca.* 0.80 V_{RHE} and an increased photocurrent of 0.48 $mA\cdot cm^{-2}$ at 1.00 V_{RHE} compared with the hematite control sample (onset potential at *ca.* 1.00 V_{RHE} and photocurrent lower than 0.01 $mA\cdot cm^{-2}$). The hematite performance was further improved coupling it with a highly active RuO_2 co-catalyst. The co-catalyst thickness balances the electron-hole recombination and charge transfer kinetics; at the optimal RuO_2 thickness, the water oxidation catalysis was assigned to RuO_2 co-catalyst at the onset potential range and to hematite for greater applied potentials. Therefore, hematite thin films coated with electrodeposited RuO_2 (optimal load corresponding to a charge density of 36 mC·cm^{-2}) and sintered at 200 ºC demonstrated to be effective decreasing the onset potential to *ca.* 0.52 V_{RHE}, closer to its flatband potential. This corresponds to a cathodic shift of the onset potential higher than 400 mV and a final photopotential of *ca.* 0.95 V, which is the highest reported for hematite-based photoanodes. RuO_2 worked as a hole storage layer to enhance the charge transfer kinetics and minimize the surface recombination, resulting in improved quantum efficiency and PEC performance at low bias potentials. For potentials over 1.10 V_{RHE}, no significant photocurrent losses were observed over 6 h of stability test under continuous AM 1.5 G illumination. For the lower potential range, it was observed a 5 % decrease assigned to the loss of RuO_2 catalyst. The use of favorable electrolytes should allow to significantly extending the RuO_2 co-catalyst stability, while the introduction of a non-noble metal, such as Co and Ni, on the top of RuO_2 structure should improve the stability and reduce co-catalyst cost without affecting the catalytic activity. Future research efforts should focus both on retarding the surface electron-hole recombination and on improving intrinsic electronic structure of hematite to achieve longer photoexcited charge carrier lifetime.

ACKNOWLEDGMENTS

P. Dias is grateful to FCT for her PhD fellow (reference: SFRH/BD/62201/2009). L. Andrade acknowledges ERC for funding within project BI-DSC (contract number: 321315). This work was partially supported by the PECDEMO project co-funded by Europe’s Fuel Cell and Hydrogen Joint Undertaking (FCH JU) under Grant Agreement No. 621252) and Project UID/EQU/00511/2013 - LEPABE and by FEDER funds through COMPETE2020. The authors are very thankful to A. Apolinário for performing the SEM/EDS and AFM analyses and for the fruitful discussions. Prof Carlos Sá, from CEMUP, for the support on the analysis of XPS data and Prof. Pedro Tavares, from UME-UTAD, for assisting in the interpretation of the XRD spectra.

REFERENCES

1. Young, K.M.H., Klahr, B.M., Zandi, O. and Hamann, T.W., *Photocatalytic water oxidation with hematite electrodes.* Catalysis Science & Technology, **2013**. 3(7): p. 1660-1671.
2. Warren, S.C., Voïtchovsky, K., Dotan, H., Leroy, C.M., Cornuz, M., Stellacci, F., Hébert, C., Rothschild, A. and Grätzel, M., *Identifying champion nanostructures for solar water-splitting.* Nat Mater, **2013**. 12(9): p. 842-849.
3. Sivula, K., *Nanostructured Fe_2O_3 Photoanodes*, in *Photoelectrochemical Hydrogen Production*, R. van de Krol and M. Grätzel, Editors. **2012**, Springer US. p. 121-156.
4. Brillet, J., Yum, J.-H., Cornuz, M., Hisatomi, T., Solarska, R., Augustynski, J., Graetzel, M. and Sivula, K., *Highly efficient water splitting by a dual-absorber tandem cell.* Nat Photon, **2012**. 6(12): p. 824-828.
5. Iandolo, B., Wickman, B., Zoric, I. and Hellman, A., *The rise of hematite: origin and strategies to reduce the high onset potential for the oxygen evolution reaction.* Journal of Materials Chemistry A, **2015**. 3(33): p. 16896-16912.
6. Zandi, O. and Hamann, T.W., *The potential versus current state of water splitting with hematite.* Physical Chemistry Chemical Physics, **2015**. 17(35): p. 22485-22503.
7. Sivula, K., Le Formal, F. and Grätzel, M., *Solar Water Splitting: Progress Using Hematite (α-Fe_2O_3) Photoelectrodes.* ChemSusChem, **2011**. 4(4): p. 432-449.
8. Guo, X., Wang, L. and Tan, Y., *Hematite nanorods Co-doped with Ru cations with different valence states as high performance photoanodes for water splitting.* Nano Energy, **2015**. 16: p. 320-328.
9. Klahr, B., Gimenez, S., Fabregat-Santiago, F., Hamann, T. and Bisquert, J., *Water Oxidation at Hematite Photoelectrodes: The Role of Surface States.* Journal of the American Chemical Society, **2012**. 134(9): p. 4294-4302.
10. Cesar, I., Sivula, K., Kay, A., Zboril, R. and Grätzel, M., *Influence of Feature Size, Film Thickness, and Silicon Doping on the Performance of Nanostructured Hematite Photoanodes for Solar Water Splitting.* The Journal of Physical Chemistry C, **2008**. 113(2): p. 772-782.

11. Kay, A., Cesar, I. and Gratzel, M., *New Benchmark for Water Photooxidation by Nanostructured α-*Fe_2O_3 *Films.* Journal of the American Chemical Society, **2006**. 128(49): p. 15714-15721.
12. Mayer, M.T., Lin, Y., Yuan, G. and Wang, D., *Forming Heterojunctions at the Nanoscale for Improved Photoelectrochemical Water Splitting by Semiconductor Materials: Case Studies on Hematite.* Accounts of Chemical Research, **2013**. 46(7): p. 1558-1566.
13. Hisatomi, T., Dotan, H., Stefik, M., Sivula, K., Rothschild, A., Grätzel, M. and Mathews, N., *Enhancement in the Performance of Ultrathin Hematite Photoanode for Water Splitting by an Oxide Underlayer.* Advanced Materials, **2012**. 24(20): p. 2699-2702.
14. Zandi, O. and Hamann, T.W., *Enhanced Water Splitting Efficiency Through Selective Surface State Removal.* The Journal of Physical Chemistry Letters, **2014**. 5(9): p. 1522-1526.
15. Pendlebury, S.R., Cowan, A.J., Barroso, M., Sivula, K., Ye, J., Gratzel, M., Klug, D.R., Tang, J. and Durrant, J.R., *Correlating long-lived photogenerated hole populations with photocurrent densities in hematite water oxidation photoanodes.* Energy & Environmental Science, **2012**. 5(4): p. 6304-6312.
16. Thorne, J.E., Li, S., Du, C., Qin, G. and Wang, D., *Energetics at the Surface of Photoelectrodes and Its Influence on the Photoelectrochemical Properties.* The Journal of Physical Chemistry Letters, **2015**. 6(20): p. 4083-4088.
17. Badia-Bou, L., Mas-Marza, E., Rodenas, P., Barea, E.M., Fabregat-Santiago, F., Gimenez, S., Peris, E. and Bisquert, J., *Water Oxidation at Hematite Photoelectrodes with an Iridium-Based Catalyst.* The Journal of Physical Chemistry C, **2013**. 117(8): p. 3826-3833.
18. Steier, L., Herraiz-Cardona, I., Gimenez, S., Fabregat-Santiago, F., Bisquert, J., Tilley, S.D. and Grätzel, M., *Understanding the Role of Underlayers and Overlayers in Thin Film Hematite Photoanodes.* Advanced Functional Materials, **2014**. 24(48): p. 7681-7688.
19. Hisatomi, T., Le Formal, F., Cornuz, M., Brillet, J., Tetreault, N., Sivula, K. and Gratzel, M., *Cathodic shift in onset potential of solar oxygen evolution on hematite by 13-group oxide overlayers.* Energy & Environmental Science, **2011**. 4(7): p. 2512-2515.

20. Tilley, S.D., Cornuz, M., Sivula, K. and Grätzel, M., *Light-Induced Water Splitting with Hematite: Improved Nanostructure and Iridium Oxide Catalysis.* Angew. Chem., Int. Ed., **2010**. 49(36): p. 1521-3773.
21. Kim, J.Y., Magesh, G., Youn, D.H., Jang, J.-W., Kubota, J., Domen, K. and Lee, J.S., *Single-crystalline, wormlike hematite photoanodes for efficient solar water splitting.* Sci. Rep., **2013**. 3: p. 2681.
22. Du, C., Yang, X., Mayer, M.T., Hoyt, H., Xie, J., McMahon, G., Bischoping, G. and Wang, D., *Hematite-Based Water Splitting with Low Turn-On Voltages.* Angewandte Chemie International Edition, **2013**. 52(48): p. 12692-12695.
23. Hu, Y.-S., Kleiman-Shwarsctein, A., Stucky, G.D. and McFarland, E.W., *Improved photoelectrochemical performance of Ti-doped* α*-*Fe_2O_3 *thin films by surface modification with fluoride.* Chemical Communications, **2009**(19): p. 2652-2654.
24. Barroso, M., Mesa, C.A., Pendlebury, S.R., Cowan, A.J., Hisatomi, T., Sivula, K., Grätzel, M., Klug, D.R. and Durrant, J.R., *Dynamics of photogenerated holes in surface modified* α*-*Fe_2O_3 *photoanodes for solar water splitting.* Proceedings of the National Academy of Sciences of the United States of America, **2012**. 109(39): p. 15640-15645.
25. Annamalai, A., Subramanian, A., Kang, U., Park, H., Choi, S.H. and Jang, J.S., *Activation of Hematite Photoanodes for Solar Water Splitting: Effect of FTO Deformation.* The Journal of Physical Chemistry C, **2015**. 119(7): p. 3810-3817.
26. Fabbri, E., Habereder, A., Waltar, K., Kotz, R. and Schmidt, T.J., *Developments and perspectives of oxide-based catalysts for the oxygen evolution reaction.* Catalysis Science & Technology, **2014**. 4(11): p. 3800-3821.
27. Zeradjanin, A.R., Topalov, A.A., Van Overmeere, Q., Cherevko, S., Chen, X., Ventosa, E., Schuhmann, W. and Mayrhofer, K.J.J., *Rational design of the electrode morphology for oxygen evolution - enhancing the performance for catalytic water oxidation.* RSC Advances, **2014**. 4(19): p. 9579-9587.
28. Teramura, K., Maeda, K., Saito, T., Takata, T., Saito, N., Inoue, Y. and Domen, K., *Characterization of Ruthenium Oxide Nanocluster as a Cocatalyst with* $(Ga_{1-x}Zn_x)(N_{1-x}O_x)$ *for Photocatalytic Overall Water Splitting.* The Journal of Physical Chemistry B, **2005**. 109(46): p. 21915-21921.
29. Azevedo, J., Steier, L., Dias, P., Stefik, M., Sousa, C.T., Araujo, J.P., Mendes, A., Graetzel, M. and Tilley, S.D., *On the stability enhancement of cuprous oxide water*

splitting photocathodes by low temperature steam annealing. Energy & Environmental Science, **2014**. 7(12): p. 4044-4052.

30. Dias, P., Schreier, M., Tilley, S.D., Luo, J., Azevedo, J., Andrade, L., Bi, D., Hagfeldt, A., Mendes, A., Grätzel, M. and Mayer, M.T., *Transparent Cuprous Oxide Photocathode Enabling a Stacked Tandem Cell for Unbiased Water Splitting.* Advanced Energy Materials, **2015**. 5(24): p. 1614-6840.
31. Chen, X., Ren, X., Liu, Z., Zhuang, L. and Lu, J., *Promoting the photoanode efficiency for water splitting by combining hematite and molecular Ru catalysts.* Electrochemistry Communications, **2013**. 27: p. 148-151.
32. Dias, P., Vilanova, A., Lopes, T., Andrade, L. and Mendes, A., *Extremely stable bare hematite photoanode for solar water splitting.* Nano Energy, **2016**. 23: p. 70-79.
33. Formal, F.L., Grätzel, M. and Sivula, K., *Controlling Photoactivity in Ultrathin Hematite Films for Solar Water-Splitting.* Advanced Functional Materials, **2010**. 20(7): p. 1099-1107.
34. Park, B.-O., Lokhande, C.D., Park, H.-S., Jung, K.-D. and Joo, O.-S., *Cathodic electrodeposition of* RuO_2 *thin films from* $Ru(III)Cl_3$ *solution.* Materials Chemistry and Physics, **2004**. 87(1): p. 59-66.
35. Lopes, T., Andrade, L., Ribeiro, H.A. and Mendes, A., *Characterization of photoelectrochemical cells for water splitting by electrochemical impedance spectroscopy.* International Journal of Hydrogen Energy, **2010**. 35(20): p. 11601-11608.
36. Lopes, T., Andrade, L., Le Formal, F., Gratzel, M., Sivula, K. and Mendes, A., *Hematite photoelectrodes for water splitting: evaluation of the role of film thickness by impedance spectroscopy.* Physical Chemistry Chemical Physics, **2014**. 16(31): p. 16515-16523.
37. Zhong, D.K. and Gamelin, D.R., *Photoelectrochemical Water Oxidation by Cobalt Catalyst (“Co−Pi”)/*α*-*Fe_2O_3 *Composite Photoanodes: Oxygen Evolution and Resolution of a Kinetic Bottleneck.* Journal of the American Chemical Society, **2010**. 132(12): p. 4202-4207.
38. Steier, L., Luo, J., Schreier, M., Mayer, M.T., Sajavaara, T. and Grätzel, M., *Low-Temperature Atomic Layer Deposition of Crystalline and Photoactive Ultrathin*

Hematite Films for Solar Water Splitting. ACS Nano, **2015**. 9(12): p. 11775–11783.

39. Over, H., *Surface Chemistry of Ruthenium Dioxide in Heterogeneous Catalysis and Electrocatalysis: From Fundamental to Applied Research.* Chemical Reviews, **2012**. 112(6): p. 3356-3426.
40. Rossetti, I. and Forni, L., *Effect of Ru loading and of Ru precursor in Ru/C catalysts for ammonia synthesis.* Applied Catalysis A: General, **2005**. 282(1–2): p. 315-320.
41. Tilley, S.D., Schreier, M., Azevedo, J., Stefik, M. and Graetzel, M., *Ruthenium Oxide Hydrogen Evolution Catalysis on Composite Cuprous Oxide Water-Splitting Photocathodes.* Advanced Functional Materials, **2013**. 24(3): p. 1616-3028.
42. Butler, M.A., *Photoelectrolysis and physical properties of the semiconducting electrode WO2* Journal of Applied Physics, **1977**. 48(5): p. 1914-1920.
43. Carroll, G.M., Zhong, D.K. and Gamelin, D.R., *Mechanistic insights into solar water oxidation by cobalt-phosphate-modified [small alpha]-*Fe_2O_3 *photoanodes.* Energy & Environmental Science, **2015**. 8(2): p. 577-584.
44. Fang, W.-C., Huang, J.-H., Chen, L.-C., Su, Y.-L.O. and Chen, K.-H., *Effect of temperature annealing on capacitive and structural properties of hydrous ruthenium oxides.* Journal of Power Sources, **2006**. 160(2): p. 1506-1510.
45. Kang, D., Kim, T.W., Kubota, S.R., Cardiel, A.C., Cha, H.G. and Choi, K.-S., *Electrochemical Synthesis of Photoelectrodes and Catalysts for Use in Solar Water Splitting.* Chemical Reviews, **2015**. 115(23): p. 12839-12887.
46. Warwick, M.E.A., Carraro, G., Gasparotto, A., Maccato, C., Barreca, D., Sada, C., Bontempi, E., Gönüllü, Y. and Mathur, S., *Interplay of thickness and photoelectrochemical properties in nanostructured* α-Fe_2O_3 *thin films.* physica status solidi (a), **2015**. 212(7): p. 1501-1507.
47. Sivula, K., Zboril, R., Le Formal, F., Robert, R., Weidenkaff, A., Tucek, J., Frydrych, J. and Grätzel, M., *Photoelectrochemical Water Splitting with Mesoporous Hematite Prepared by a Solution-Based Colloidal Approach.* Journal of the American Chemical Society, **2010**. 132(21): p. 7436-7444.
48. Ling, Y., Wang, G., Wheeler, D.A., Zhang, J.Z. and Li, Y., *Sn-Doped Hematite Nanostructures for Photoelectrochemical Water Splitting.* Nano Letters, **2011**. 11(5): p. 2119-2125.

49. Mettenbörger, A., Gönüllü, Y., Fischer, T., Heisig, T., Sasinska, A., Maccato, C., Carraro, G., Sada, C., Barreca, D., Mayrhofer, L., Moseler, M., Held, A. and Mathur, S., *Interfacial insight in multi-junction metal oxide photoanodes for water-splitting applications.* Nano Energy, **2016**. 19: p. 415-427.
50. Jang, J.-W., Du, C., Ye, Y., Lin, Y., Yao, X., Thorne, J., Liu, E., McMahon, G., Zhu, J., Javey, A., Guo, J. and Wang, D., *Enabling unassisted solar water splitting by iron oxide and silicon.* Nat Commun, **2015**. 6: p. 7447.
51. Uddin, M.T., Nicolas, Y., Olivier, C., Servant, L., Toupance, T., Li, S., Klein, A. and Jaegermann, W., *Improved photocatalytic activity in* RuO_2*-ZnO nanoparticulate heterostructures due to inhomogeneous space charge effects.* Physical Chemistry Chemical Physics, **2015**. 17(7): p. 5090-5102.
52. Barroso, M., Cowan, A.J., Pendlebury, S.R., Grätzel, M., Klug, D.R. and Durrant, J.R., *The Role of Cobalt Phosphate in Enhancing the Photocatalytic Activity of* α-Fe_2O_3 *toward Water Oxidation.* Journal of the American Chemical Society, **2011**. 133(38): p. 14868-14871.
53. Klahr, B., Gimenez, S., Fabregat-Santiago, F., Bisquert, J. and Hamann, T.W., *Photoelectrochemical and Impedance Spectroscopic Investigation of Water Oxidation with "Co–Pi"-Coated Hematite Electrodes.* Journal of the American Chemical Society, **2012**. 134(40): p. 16693-16700.
54. Thorne, J.E., Jang, J.-W., Liu, E.Y. and Wang, D., *Understanding the origin of photoelectrode performance enhancement by probing surface kinetics.* Chemical Science, **2016**.
55. Bertoluzzi, L. and Bisquert, J., *Equivalent Circuit of Electrons and Holes in Thin Semiconductor Films for Photoelectrochemical Water Splitting Applications.* The Journal of Physical Chemistry Letters, **2012**. 3(17): p. 2517-2522.
56. Le Formal, F., Pendlebury, S.R., Cornuz, M., Tilley, S.D., Grätzel, M. and Durrant, J.R., *Back Electron–Hole Recombination in Hematite Photoanodes for Water Splitting*. Journal of the American Chemical Society, **2014**. 136(6): p. 2564-2574.
57. Lefrou, C., Fabry, P. and Poignet, J.-C., *Thermodynamic features,* in *Electrochemistry*. **2012**, Springer Berlin Heidelberg. p. 119-168.
58. Li, W., He, D., Sheehan, S.W., He, Y., Thorne, J.E., Yao, X., Brudvig, G.W. and Wang, D., *Comparison of heterogenized molecular and heterogeneous oxide*

catalysts for photoelectrochemical water oxidation. Energy & Environmental Science, **2016**.

59. Klahr, B., Gimenez, S., Fabregat-Santiago, F., Bisquert, J. and Hamann, T.W., *Electrochemical and photoelectrochemical investigation of water oxidation with hematite electrodes.* Energy & Environmental Science, **2012**. 5(6): p. 7626-7636.
60. Le Formal, F., Sivula, K. and Grätzel, M., *The Transient Photocurrent and Photovoltage Behavior of a Hematite Photoanode under Working Conditions and the Influence of Surface Treatments.* The Journal of Physical Chemistry C, **2012**. 116(51): p. 26707-26720.

CHAPTER 6

TRANSPARENT CUPROUS OXIDE PHOTOCATHODE ENABLING A STACKED TANDEM CELL FOR UNBIASED WATER SPLITTING

6

TRANSPARENT CUPROUS OXIDE PHOTOCATHODE ENABLING A STACKED TANDEM CELL FOR UNBIASED WATER SPLITTING

Paula Dias, Marcel Schreier, S. David Tilley, Jingshan Luo, João Azevedo, Luísa Andrade, Dongqin Bi, Anders Hagfeldt, Adélio Mendes, Michael Grätzel and Matthew T. Mayer

Adapted from Advanced Energy Materials, 2015, 24(5)

ABSTRACT

Photoelectrochemical (PEC) water splitting represents an attractive method of capturing and storing the immense energy of sunlight in the form of hydrogen, a clean chemical fuel. Given the large energetic demand of water electrolysis, and the defined spectrum of photons available from incident sunlight, a two absorber tandem device is required to achieve high efficiencies. The two absorbers should be of different and complementary bandgaps, connected in series to achieve the necessary potential, and arranged in an optical stack configuration to maximize the utilization of sunlight. This latter requirement demands a top device that is responsive to high-energy photons but also transparent to lower-energy photons which pass through to illuminate the bottom absorber. Here, cuprous oxide (Cu_2O) is employed as a top absorber component, and the factors influencing the balance between transparency and efficiency toward operation in a tandem configuration are studied. Photocathodes based on Cu_2O electrodeposited onto conducting glass substrates treated with thin, discontinuous layers of gold achieve reasonable sub-bandgap transmittance while retaining performances comparable to their opaque counterparts. This new high performance transparent photocathode is demonstrated in tandem with a hybrid perovskite photovoltaic cell, resulting in a full device capable of standalone sunlight-driven water splitting.

Keywords: Cu_2O Photocathodes, Photoelectrochemical Water Splitting, Optical Tandems, Solar Fuels, Metal Oxides, Perovskite Photovoltaics.

6.1 INTRODUCTION

No ideal single material has been discovered that can drive stand-alone photoelectrochemical (PEC) water splitting with reasonable efficiency, although high-throughput searches are underway [1, 2]. A more promising approach is to employ a two-absorber tandem comprising a wider bandgap transparent top absorber stacked above a smaller bandgap device [3]. By detailed balance calculations, the ideal pair of bandgaps would be approximately 1.7 eV (absorbing wavelengths up to 730 nm) and 1.1 eV (up to 1127 nm) [4]. The theoretical maximum water splitting efficiency for such a system exceeds that of a single-absorber system, a result of the more complete solar spectral utilization and the ability to produce additive photopotential toward the electrolysis demand.

Dual-absorber tandem devices can be accomplished with photoanode–photocathode systems (PA/PC PEC tandem) [5, 6] or photoelectrode–photovoltaic coupled devices (PEC/PV tandem) [7] to generate the sufficient driving force for standalone solar water splitting while simultaneously maximizing the fraction of solar energy collected. Among the various studied tandem configurations [8], the benchmark performances were achieved by devices using efficient III–V materials [9, 10]. Since the balance between materials availability, fabrication cost, and device performance must be optimized to realize a competitive device, most recent attention has targeted the discovery and development of Earth-abundant materials for using toward these goals. A tandem cell combining an Earth-abundant solar cell with an oxide-based photoelectrode could be an ideal solution to obtain cost-effective unassisted water splitting [3].

Studies employing the PEC/PV configuration have mostly focused around the use of n-type semiconductors for water oxidation as the PEC component, largely due to the number of promising candidate materials in this class, their suitable bandgaps, and their Earth-abundant nature. Among them, Fe_2O_3 [7, 11], $BiVO_4$ [12-15], and WO_3 [7, 16, 17] photoanodes have been employed most commonly in approaches succeeding at unassisted water splitting. Comparatively fewer Earth-abundant candidates exist for photocathode PEC devices, with even fewer demonstrated toward complete water splitting in tandem systems [5, 6, 18]. While photocathode stability can prove to be a challenge, Seger *et al.* [19] have recently suggested that when effective surface passivation strategies are used, tandems based on photocathodes as the larger bandgap component may offer several advantages over photoanode-based approaches [19].

To this end, p-type photocathode materials for water reduction are a topic of ongoing research [20-23]. Copper oxide-based materials, such as cuprous oxide (Cu_2O), have gained significant interest due to their elemental abundance, scalable synthesis techniques, and natural p-type character [24]. Moreover, the Cu_2O bandgap energy around 2.1 eV exhibits great potential for solar hydrogen production, although its poor stability in aqueous solutions is a limiting factor for its use. Paracchino *et al.* [25] developed a highly active and stable multilayer composite photocathode that consists of a p–n junction between electrodeposited p-type Cu_2O and n-type overlayers of Al-doped zinc oxide (AZO) and TiO_2, activated with Pt co-catalyst. This material achieved a high photocurrent of 7.60 $mA{\cdot}cm^{-2}$ at 0 V_{RHE} and remained active for 1 h of testing [25]. The photoactivity of Cu_2O was then optimized through controlling the electrodeposition conditions (pH, temperature and deposition current density) [26], the atomic layer deposition (ALD) temperature [27] and the electrolyte pH and composition; a stability of 62 % over 10 h of testing under AM 1.5 G chopping illumination (biased at 0 V_{RHE} in pH 5 electrolyte) was reported [27]. Furthermore, RuO_x top layer was investigated as a co-catalyst [28] and, together with a steam treatment of the multilayer structures, showed a stable photocurrent of *ca.* 5 $mA{\cdot}cm^{-2}$ during 50 h (photocurrent loss < 10 %) under 1-sun of light chopping [29]. This photocathode material was recently demonstrated as part of a PA/PC PEC tandem capable of complete water splitting at modest efficiency [5].

Despite the recent success with this device architecture, the photopotential produced by this photocathode alone is insufficient to drive complete water splitting, so it should ideally be incorporated as the top, wide-bandgap component of a tandem system. However, the fact that the Cu_2O thin films are typically electrodeposited onto an opaque Au layer precludes their use as a top absorber. Therefore, the development of an efficient and stable transparent Cu_2O thin film device is an important goal, wherein the portion of solar radiation not absorbed by the photocathode can be transmitted and utilized by a second photoabsorber. In this work, an innovative tandem device was enabled by the development of a transparent and stable Cu_2O photocathode, which when connected in series with a hybrid perovskite photovoltaic was demonstrated to perform unassisted sunlight-driven water splitting.

6.2 EXPERIMENTAL

6.2.1 CUPROUS OXIDE PHOTOCATHODES PREPARATION

The films of cuprous oxide were electrodeposited onto fluorine-doped tin oxide (FTO, TEC-15, NSG glass) substrates with or without Au treatments. The FTO-glass substrates were cleaned by sequential ultrasonic treatments in soapy water (15 min), acetone (15 min), ethanol (15 min), and deionized water (15 min). The substrates were then coated with various treatments of Au by direct current (DC) sputtering. The standard opaque films of *ca.* 150 nm were deposited at a calibrated rate of 1.1 $nm \cdot s^{-1}$ (after depositing a 10 nm Cr adhesion layer). The transparent Au treatments (without Cr layers) were performed at a calibrated rate of 0.2 $nm \cdot s^{-1}$ for durations 5, 15 and 25 s to yield the substrates labeled herein by their nominal thicknesses of 1, 3 and 5 nm Au, respectively.

The electrodeposition of Cu_2O from a basic solution of lactate-stabilized copper sulphate was performed as described previously [30]. The electrodeposition was performed in galvanostatic mode (constant current density of -0.10 $mA \cdot cm^{-2}$) by using a two-electrode configuration with a platinum mesh as the counter electrode. The time of deposition was varied during the experiments among 105 minutes, 50 min and 25 min to study the effect of Cu_2O thickness on the transparency of the film. Cu_2O thicknesses of roughly 500 nm, 260 nm and 100 nm were achieved, respectively for 105 min, 50 min and 25 min of deposition time; the film thickness was confirmed by cross-sectional SEM (Figure 6.7).

ATOMIC LAYER DEPOSITION

To protect the Cu_2O films against photocathodic decomposition in water, ultrathin n-type oxides overlayers were deposited by atomic layer deposition (ALD) using a thermal ALD system (Savannah 100, Cambridge Nanotech), as described previously [31]. Before ALD deposition, the samples were rinsed with distillate water and dried with argon. The ALD protective structure consisted of 20 nm of Al:ZnO (AZO; deposited at 120 °C using precursors of diethyl zinc, trimethylaluminum, and water vapor) followed by 100 nm of TiO_2 (deposited at 150 °C using precursors of tetrakis(dimethylamino)titanium at 75 °C and H_2O_2 50 % in water at 25 °C).

CO-CATALYST DEPOSITION

After ALD, the electrode areas were defined by encapsulation using hot glue or opaque epoxy. Onto the exposed active area, RuO_2 co-catalyst was galvanostatically deposited under illumination using an aqueous solution of 1.3 mM $KRuO_4$. The deposition was carried out at a current density of $-28.3\ \mu A\cdot cm^{-2}$ for 15 – 20 min under simulated 1-sun illumination, following the procedure described previously [31]. A schematic representation of the electrode structure is presented in Figure 6.1.

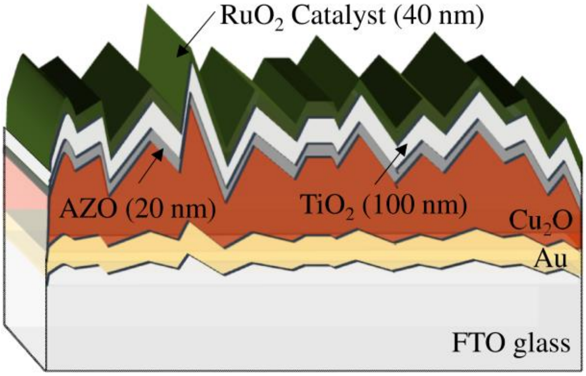

Figure 6.1: Schematic representation of the prepared Cu_2O photocathode structure.

6.2.2 PHOTOVOLTAIC PREPARATION

A 50 nm compact TiO_2 blocking layer was first deposited onto the surface of a pre-cleaned FTO substrate by spray pyrolysis on a hotplate at 450 ºC using Ti-isopropoxide and acetylacetone in ethanol. Then a nanostructured layer of TiO_2 was deposited by spin-coating diluted Dyesol paste (18 NR-T), and sintering at 500 ºC for 20 min. The desired perovskite solutions of $(FAPbI)_{3-x}(MAPbI_3)_x$, were prepared by dissolution of CH_3NH_3Br, $NH_2CH{=}NH_2I$, with PbI_2 and $PbBr_2$ in the mixed solvent of dimethyl sulfoxide (DMSO) and dimethylformamide (DMF). The mixed perovskite film was obtained by spin-coating the precursor solution, followed by anti-solvent treatment. The coated films were then placed on a hot plate set at 100 ºC to evaporate the solvent. The composition of hole transport material was 2,2′, 7,7′-tetrakis-(N,N-di-p-methoxyphenyl-amine)-9,99-spirobifluorene (spiro-OMeTAD, 0.06 M, Lumtec.), bis(trifluoromethane)sulfonimide lithium salt (LiTFSI, 0.03 M, 99.95 %, Aldrich), FK209 ($Co[t\text{-}BuPyPz]_3[PF_6]_3$, 0.0024 M), and 4-tert-butylpyridine (0.2 M, 99 %, Aldrich) in anhydrous chlorobenzene (99.8 %, Aldrich). The perovskite sensitized TiO_2 films were coated with hole transporter medium (HTM) solution using spin-coating, followed by deposition of Au (80 nm) as electrode by thermal evaporation.

6.2.3 IrO_2 ANODE PREPARATION

A 1.8 cm^2 square piece of titanium foil (99.7 %, 0.25 mm, Sigma Aldrich) was etched for 60 min in boiling oxalic acid (1 M, ≥ 97 %, anhydrous, Fluka). Subsequently, H_2IrCl_6 (30 µL, 0.2 M, 99.9 %, hydrate, ABCR) in isopropanol (ACS Reagent, Merck) were drop cast on the foil. This was followed by drying at 70 ºC for 10 min and calcination at 500 ºC for 10 min in air. The step was repeated 3 times on each side of the Ti foil, resulting in the deposition of 6.3 mg of IrO_2 onto each side.

6.2.4 TANDEM ASSEMBLY AND TESTING

After defining the active area of the transparent photocathode using opaque epoxy (Loctite Hysol 9461), the device was fixed into a custom gas-tight test cell with front and back windows of quartz, gas inlet (submerged) and outlet (headspace) tubes, and feedthroughs for the anode, cathode, and reference electrodes. The IrO_2 anode was positioned to the side, *ca.* 1 cm away from the photocathode surface. The pH 5 electrolyte solution (15 mL) was filled into the cell, rapid stirring was applied, and a 20 mL·min^{-1} flow of He was continuously bubbled through the cell. Behind the electrochemical cell, against the rear quartz window, was placed the perovskite photovoltaic cell which was illuminated by light passing through the photocathode aperture. The photovoltaic FTO contact (electron collector) was connected to the photocathode by a short wire, while its gold contact (hole collector) was connected to the IrO_2 anode (through a potentiostat in two-electrode configuration with zero applied bias to measure the short circuit current). The cell was illuminated from the front window by simulated sunlight from a 450 W Xe lamp (Osram, ozone-free) equipped with an AM 1.5 G filter (LOT-QD), calibrated with a silicon diode to 1-sun intensity. For in-line characterization of evolved hydrogen and oxygen gases, the outflow was periodically injected into a gas chromatograph (TRACE Ultra with PDD detector, Thermo Scientific; ValcoPLOT Molesieve 5 Å fused silica column).

6.2.5 ELECTROCHEMICAL CHARACTERIZATION

The photoelectrochemical cell performance was evaluated in a standard three-electrode configuration using the Cu_2O device as photocathode, a Pt wire as counter electrode, and a reference electrode of Ag/AgCl/Sat. KCl. The electrolyte solution was 0.5 M Na_2SO_4 buffered with 0.1 M phosphate to obtain pH 5.

J-V MEASUREMENTS AND STABILITY TESTS

An Ivium Potentiostat/Galvanostat was used to acquire the photoresponse under chopped irradiation from a 450 W Xenon lamp (Osram, ozone-free) equipped with an IR/UV filter (KG3 filter, 3 mm, Schott). The photoelectrochemical cell was positioned for illumination at 1-sun intensity, the position determined by measuring the short circuit current on a calibrated silicon diode fitted with a KG3 filter to obtain low spectral mismatch with the AM 1.5 G spectrum across the relevant wavelength range of 300 – 800 nm. The scan rate for all photocurrent density-potential (*J*–*V*) studies was 10 $mV\cdot s^{-1}$ in the cathodic direction. The potential was reported against the reversible hydrogen electrode (RHE) when a three-electrode configuration is used. The electrolyte was continuously bubbled with nitrogen during the *J*–*V* measurements and stability tests to remove oxygen and thus eliminate signals of oxygen reduction.

EIS MEASUREMENTS

EIS analyses were performed applying a small potential sinusoidal perturbation to the system. The amplitude and the phase shift of the resulting current response was recorded using also an Ivium Potentiostat/Galvanostat workstation. The frequency range used was 0.1 Hz – 1 MHz under an AC amplitude of 5 mV. The measurements were carried out in dark conditions by applying a bias of 0.5 V_{RHE} in pH 5 solution.

IPCE MEASUREMENTS

IPCE measurements were performed under light from a 300 W Xenon lamp (Cermax PE 300 BUV) passing through a monochromator (Bausch & Lomb). In three-electrode configuration the photocathode current response was measured while holding the potential constant. This photoresponse was compared against that of a calibrated Si photodiode to determine the IPCE at each wavelength.

6.2.6 SPECTROSCOPIC AND MICROSCOPIC CHARACTERIZATION:

The morphology of the substrates and photoelectrodes was characterized using a high-resolution scanning electron microscope (Zeiss Merlin) with an in-lens secondary electron detector. Cross-sectional images were acquired from freshly cleaved surfaces. Total transmittance spectra were measured with a spectrophotometer (Shimadzu UV-3600) equipped with an integrating sphere. The partial devices were tested directly in air, whereas the full devices were wetted with water and sandwiched between quartz slides in order to approximate the optical behavior of the device within the photoelectrochemical cell. The absence of sample was used as a transmittance blank in order to account for the contribution of every layer in the device.

6.3 RESULTS AND DISCUSSION

6.3.1 TRANSPARENT GOLD SUBSTRATES FOR CU_2O PHOTOCATHODES

The photocathode device structure employed herein is depicted in Figure 6.2. Electrodeposited p-type Cu_2O serves as the light absorbing component, producing photogenerated electrons for water reduction. As previously demonstrated, atomic layer deposition (ALD) overlayers of Al:ZnO (AZO) and TiO_2 enable heterojunction formation and corrosion protection [27], respectively, and electrodeposited RuO_2 represents a highly active and stable co-catalyst for the hydrogen evolution reaction [28]. In this study, these three overlayers remained unchanged while the substrate and absorber characteristics were varied.

In the majority of previous works employing Cu_2O as photoabsorber in PV and PEC devices, a thick and opaque gold film was used as the hole-collecting contact to Cu_2O [20, 24, 32, 33]. This arrangement prevents implementation of such devices in an optical tandem, since the long-wavelength portion of the solar spectrum cannot pass through to the second absorber. Herein, the first task was to adapt the substrate for enabling light transmittance. Films of the transparent conducting oxide $F:SnO_2$ (FTO) on glass are routinely used as substrate for transparent electronic devices, so the photocathode synthesis was attempted using Au-free, pristine FTO-glass as substrate.

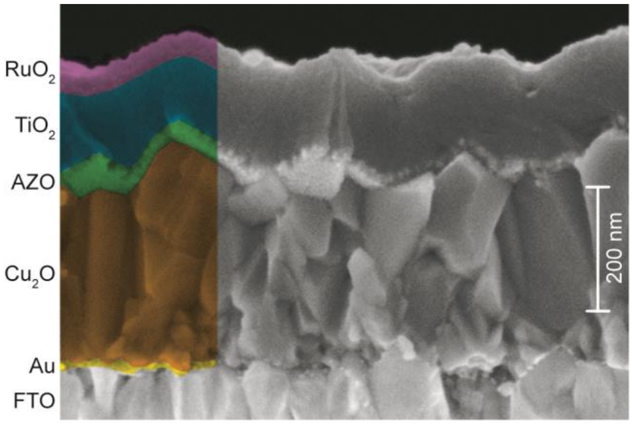

Figure 6.2: Cross-section scanning electron microscopy image of a Cu_2O photocathode device based on a FTO substrate treated with a 3 nm dose of Au. False-color was added to aid visualization of the layers.

The photocurrent density–potential (*J–V*) response of the device formed on bare FTO was considerably poorer than that of a typical device grown on a continuous 150 nm thick Au film, as shown in Figure 6.3. For a photocathode driving water reduction, the goal is to achieve large photocurrents at potentials well positive of the reversible potential of hydrogen evolution, *i.e.* at 0 V_{RHE}. The typical device based on thick Au exhibits a photocurrent (J_{photo}) onset potential of *ca.* 0.5 V_{RHE}, and reaches cathodic J_{photo} approaching −6 mA·cm^{-2} at 0 V_{RHE}, a performance that is among the best for photoelectrodes based on metal oxide semiconductors. However, the PEC response suffered significantly in the absence of Au, with a very gradual onset and a J_{photo} reaching only −2 mA·cm^{-2} at 0 V_{RHE} – Figure 6.3. This transparent, Au-free device ultimately reached significant photocurrents, but only at large overpotential for water reduction; J_{photo} of *ca.* −4.50 mA·cm^{-2} at −0.50 V_{RHE}. This behavior suggests that a significant resistive element is present in this device configuration. A key role of the substrate contact to Cu_2O is to form an ohmic junction for photogenerated hole collection [24, 34]. Due to the relatively large work function of p-type Cu_2O, this constrains the contact material to one with a comparable or larger work function. It is likely that the Cu_2O contact with FTO is not an ideal ohmic junction, but rather forms a slight Schottky barrier opposing the collection of holes, and therefore contributes to the worsening of the *J–V* response. Indeed, electrochemical impedance spectroscopy analysis revealed a resistive element for this bare FTO device, a feature that was non-existent in devices with Au at the interface with Cu_2O – see Figure 6.4.

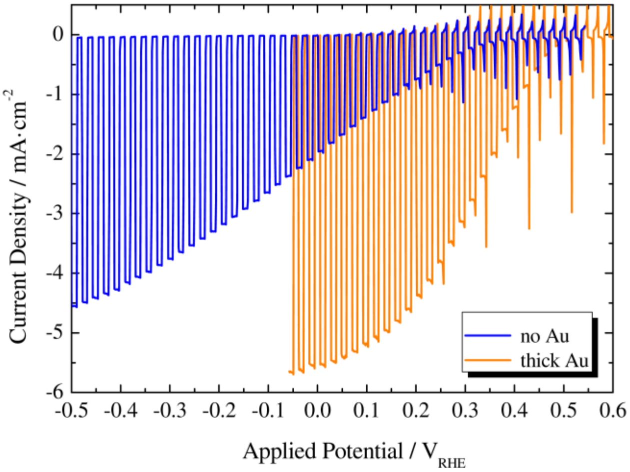

Figure 6.3: *J–V* characteristics under 1-sun intensity chopped illumination for Cu_2O photocathodes synthesized both with and without the presence of a 150 nm thick Au substrate layer.

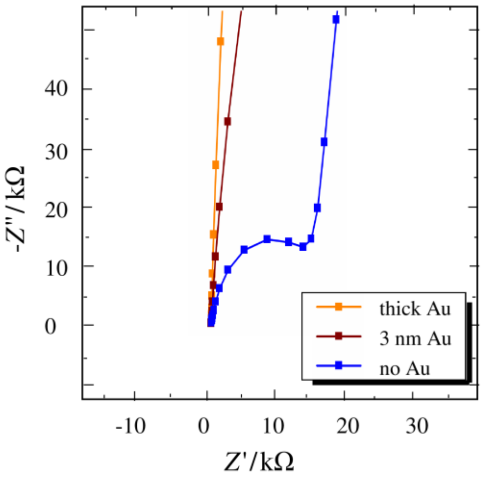

Figure 6.4: Nyquist plots of the Cu_2O photocathodes in dark, biased at 0.5 V$_{RHE}$ in pH 5 solution, measured at frequencies from 1 MHz to 0.1 Hz under an AC amplitude of 5 mV. The high-frequency regime is shown, in which an obvious resistive element appears for the device without Au; this element does not appear when Au is present at the interface.

Additionally, the electrodeposited Cu_2O exhibited quite different morphology when grown on bare FTO, proceeding by the nucleation and growth of large and dispersed Cu_2O crystals, in contrast to the dense, uniform and continuous growth of Cu_2O films when using a gold-coated substrate. This behavior is shown in Figure 6.5 via scanning electron microscopy (SEM) images of the different substrates before and after device fabrication, correlating with previous reports on the substrate dependence of Cu_2O electrodeposition [35]. Therefore, the Au substrate seems to affect both the electronics of the junction and the quality of the electrodeposited films, making its presence important for the device performance, but a challenge given the present goal of transparent devices.

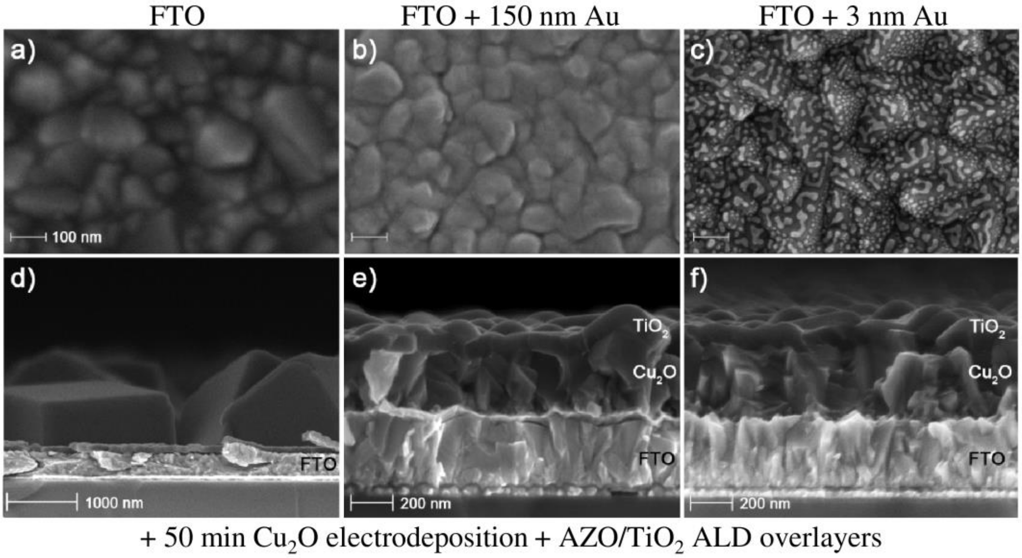

Figure 6.5: Scanning electron micrographs of different substrates before (top row) and after (bottom row) device fabrication following identical treatments (50 min Cu_2O electrodeposition followed by atomic layer deposition of AZO and TiO_2 overlayers). The substrates examined were: (a) bare FTO-glass, (b) FTO with a 150 nm thick Au film, and (c) FTO with a 3 nm dose of Au (scale bars: 100 nm). On bare FTO, the Cu_2O nucleates and grows into large, distinct crystalline particles (d), whereas on both 150 nm (e) and 3 nm (f) Au-treated substrates the Cu_2O growth is uniform, dense and continuous.

To overcome these limitations while also allowing a high degree of transparency, very thin layers of Au were used, therefore, exploring the effect of using substrates of FTO treated by brief sputter depositions of Au. As shown in Figure 6.5c, sputtering Au for an equivalent dose (based on calibrated film deposition rates) of 3 nm led to the formation of a discontinuous island coating on the FTO surface. Note that the Au substrates are herein labeled by their nominal thickness based on calibrated sputter deposition rates, although this does not accurately define the discontinuous morphology. Interestingly, Cu_2O electrodeposition onto these Au island substrates resulted in dense, uniform and crystalline films (Figure 6.5f), similar to those deposited onto thick Au and in contrast to the large Cu_2O particles that form on bare FTO substrates. Examination of the transmittance of Au-coated FTO-glass (Figure 6.6a) revealed that these substrates exhibit reasonable transparency across the spectrum, but the transparency drops with increasing amounts of gold.

Indeed, employing these as substrates for the fabrication of Cu_2O photocathodes, the PEC devices showed efficient performances. Figure 6.6b presents the PEC response for devices based on the three different Au-treated substrates, revealing that even a small amount of gold can enable photocathodes with onset potentials and photocurrent density values comparable to that obtained on thick Au. The performance is dependent on the amount of Au used, as the shape of the *J–V* curve improves with increased Au. For the smallest dose of 1 nm Au, the slow, rather linear photocurrent increase is likely due to a series resistance effect resulting from the limited interfacial area between Au and Cu_2O. With increased Au, the apparent fill factor of the curves improves, but the transparency begins to suffer as a result of the coalescence of Au particles and the formation of continuous films. Note that the photocurrent transient behavior near the photocurrent onset, similar across all devices studied here, seems to result from the capacitive charging of the TiO_2 overlayer or the RuO_2 co-catalyst; these observations are presently under study. Therefore, FTO-glass substrates with slight Au treatments were established as suitable substrates for enabling transparent Cu_2O-based devices, while identifying that the balance between transmittance and performance will be important in optimizing the tandem device. In this regard, the 3 nm dose of sputtered Au was selected as substrate for the studies continued below.

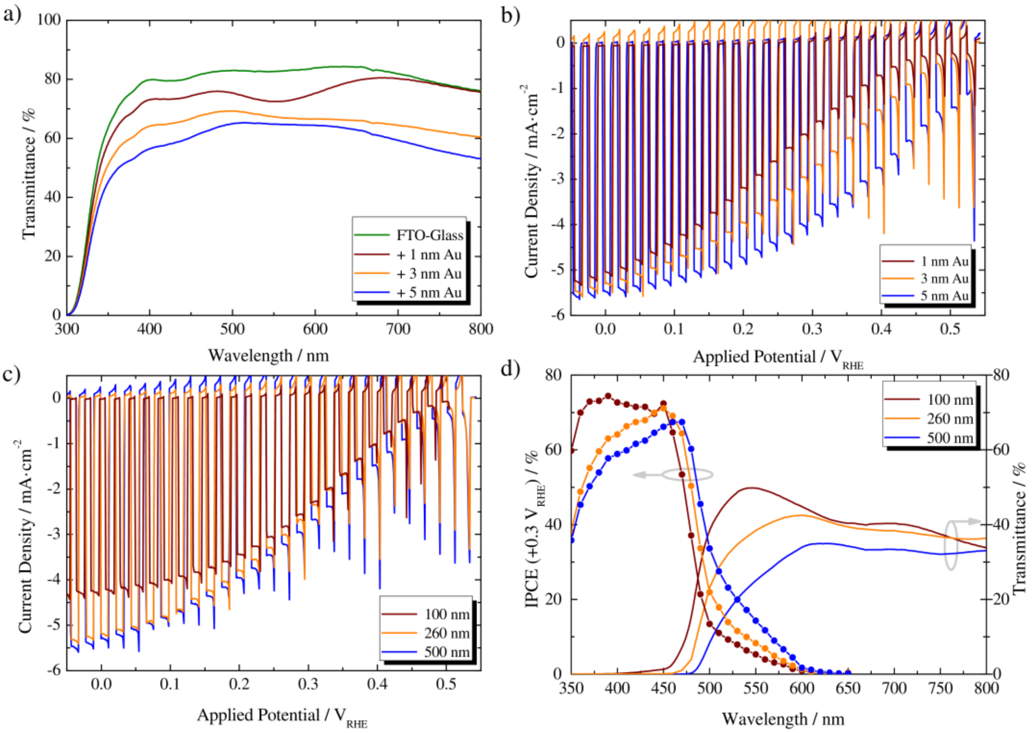

Figure 6.6: Optical and photoelectrochemical effects of Au and Cu_2O thickness variation: (a) transmittance spectra of FTO-glass substrates with the addition of various doses of sputtered Au; (b) *J*–*V* characteristics of photocathodes based on 105 min Cu_2O electrodepositions onto substrates of various Au treatments, under 1-sun intensity chopped illumination; (c) *J*–*V* characteristics; and (d) IPCE and transmittance spectra for devices of varied Cu_2O thickness formed onto 3 nm Au treated substrates. The devices are labeled by approximate Cu_2O thickness. The transmittance spectra were obtained on samples in air. The IPCE responses were measured while biased at +0.3 V_{RHE}. All photocathodes in (b–d) were tested following 15 min of RuO_2 catalyst deposition on their surfaces.

6.3.2 EFFECTS OF Cu_2O ABSORBER THICKNESS

The next parameter to consider is the Cu_2O absorber layer thickness. Previous reports employed Cu_2O films of 500 nm or greater, while other groups have used thicknesses of several µm for photovoltaics based on electrodeposited Cu_2O [32, 33]. Meanwhile, the device transparency and the application of Cu_2O in dual-absorber tandems have been little explored [36, 37]. In this work, transparency was an important factor and, therefore, a series of Cu_2O thicknesses was also examined by varying the duration of electrodeposition onto substrates of FTO treated with 3 nm doses of Au. Three durations were explored, with 105, 50 and 25 min electrodepositions producing film thicknesses of *ca.* 500, 260 and 100 nm, respectively (see Figure 6.7 for electron micrographs and photographs of the films).

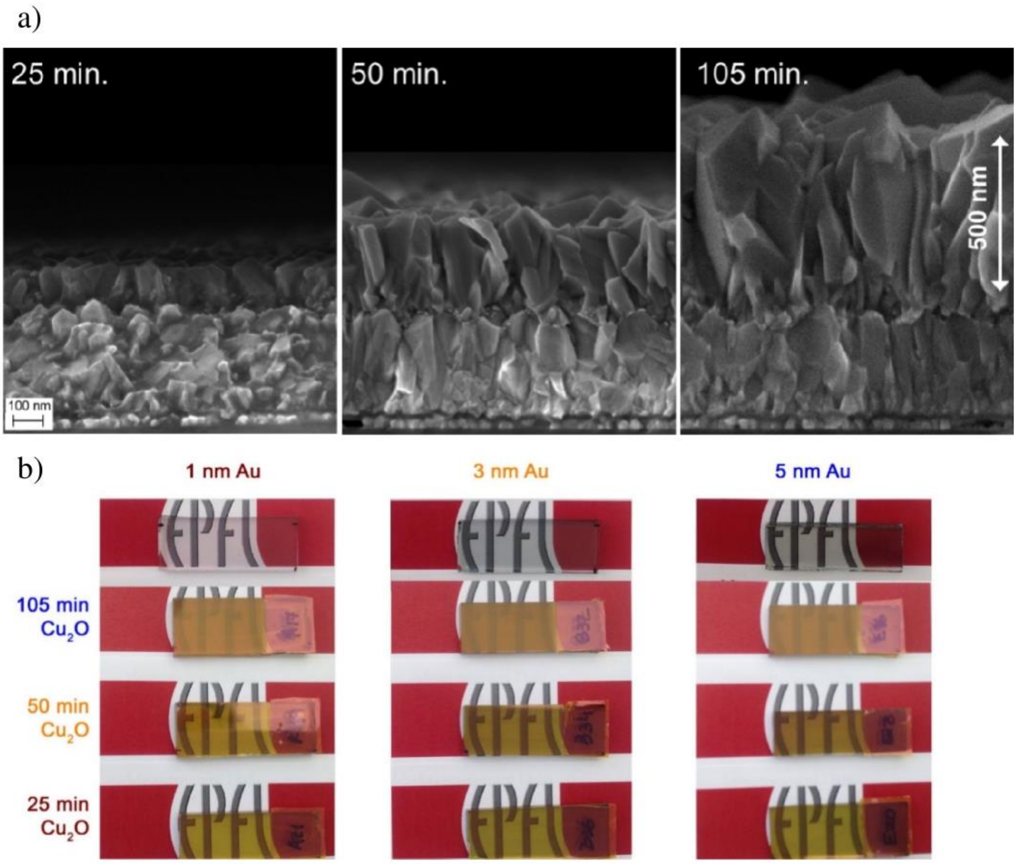

Figure 6.7: (a) Cross-section micrographs of Cu_2O films electrodeposited for different durations onto 3 nm Au-treated FTO-glass substrates. (b) Photographs of Cu_2O films of different deposition durations onto different Au-treated substrates.

As shown in Figure 6.6c the devices exhibited varying photocathode performances. The device with the thinnest absorber layer (100 nm) showed diminished plateau photocurrents, whereas the 260 nm and 500 nm films exhibited nearly identical *J–V* responses, both being comparable to the performance on a typical thick Au substrate. Variation in the absorber thickness modifies the light absorption profile and the resulting quantum efficiency spectra. In Figure 6.6d, the incident photon-to-current conversion efficiencies (IPCE) of the devices under monochromatic illumination reveal the changes in spectral response. Although the bandgap of Cu_2O is often stated as being *ca.* 2.1 eV, the nature of this transition is direct but forbidden, whereas the first allowed transition occurs at around 2.5 eV [24, 38]. This effect is clearly seen as an inflection in the IPCE spectra, where photons of lower energy (wavelengths longer than 500 nm) are poorly utilized by these thin Cu_2O films. Film thicknesses of several µm are required for significant absorption in this range [36], but for a stacked tandem device the transmittance of long-wavelength photons is an important factor, and it can be seen that even a 500 nm Cu_2O film contributes to a significantly decreased transmittance as compared to a 260 nm Cu_2O device (Figure 6.6d). This loss is possibly due to an increase in scattering or reflection due to the visibly larger degree of surface roughness for the thick Cu_2O films (Figure 6.7a). Furthermore, the response to short wavelengths decreases with thicker absorber layers, a result of the poor majority carrier (hole) collection in thick films. The 50 min electrodeposition photocathode was then selected as a relatively optimized candidate for balancing photoelectrochemical performance with optical transparency in the complete water splitting device.

6.3.3 TANDEM DEVICE FOR COMPLETE WATER SPLITTING

A schematic of the assembled tandem device is shown in Figure 6.8, where the two absorbers are placed back-to-back, the photovoltaic electron collector is wired to the photocathode, and its hole collector is wired to a water oxidation anode. In a dual-absorber PEC/PV tandem, the photoelectrode and the photovoltaic utilize photons of different regions of the solar spectrum to enable broad sunlight harvesting. Furthermore, since they will be connected in series and operated at the same current density, it is desirable for their individual photocurrent responses to be well matched. In Figure 6.9a, the IPCE responses of the photocathode and the perovskite photovoltaic (behind the photocathode) are multiplied by the 1-sun AM 1.5 G photon flux to reveal the expected photogenerated electron flux from each device, which when integrated yields their expected photocurrent densities.

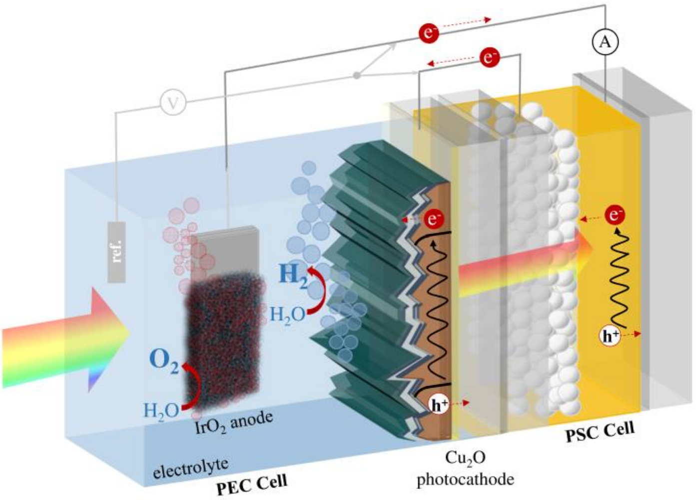

Figure 6.8: Schematic of the Cu_2O–perovskite–IrO_2 tandem cell during operation. An ammeter (*A*) is employed to monitor the short circuit current flowing through the unbiased tandem device, while a voltmeter (*V*) is used to periodically measure the potentials of the anode and cathode contacts against a reference electrode in the solution.

In constructing a PEC/PV tandem for complete water splitting, three components are required: a suitably transparent photocathode driving hydrogen evolution, a photovoltaic cell responsive to the transmitted photons and an anode for oxygen evolution. Among water oxidation catalysts, IrO_2 is known to be a top performer [39], and was, therefore, the anode choice for this proof-of-concept device. Even so, the water oxidation reaction imparts a large energetic demand on the overall water splitting processes, especially in near-neutral solutions, and significant overpotentials beyond the reversible potential for oxygen evolution (1.23 V_{RHE}) are required to achieve meaningful current densities. In the tandem configuration employed here, the flat anode electrode is positioned parallel to the path of light, an approach that allows scaling its active area beyond that of the illuminated area as a tactic toward reducing the overpotential required for supporting the tandem photocurrent. In previous reports of PEC/PV tandems for unbiased water splitting, it has been common to either make no mention of the counter electrode dimensions or to employ counter electrode areas that are several times larger than the photoelectrode illuminated area [40-43]. This non-trivial parameter plays an important role in the tandem construction and performance, and here a catalyst with an active area of *ca.* 30 times that of the photocathode illuminated area was used. While the anode overpotential is a key challenge producing an efficient tandem device, this mismatch of electrode areas can actually highlight an advantage of a photocathode-based tandem. Since the oxygen evolution reaction, which exhibits significantly larger overpotentials than the hydrogen evolution reaction, occurs on a non-photoactive component, its relative area may be increased as long as the cell design allows its placement out of the path of illumination, an approach that is even more desirable when abundant catalyst materials are employed.

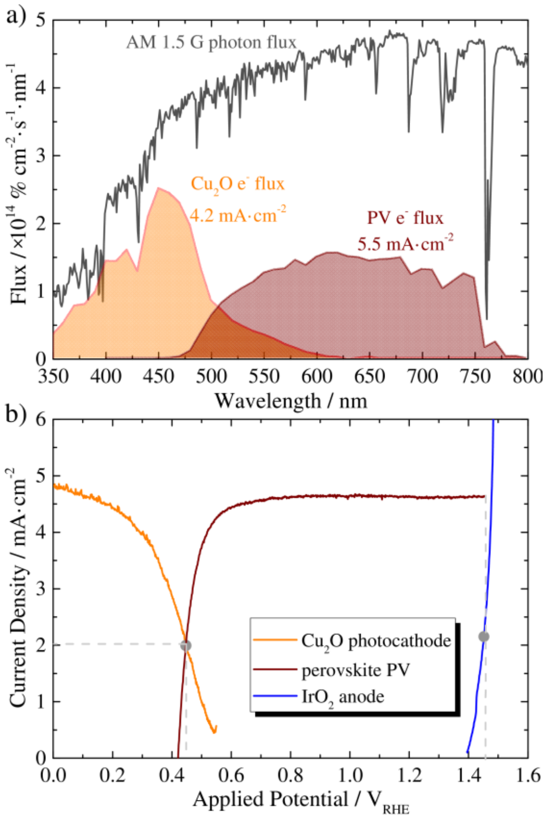

Figure 6.9: PEC/PV tandem assembly and operation. (a) Plot of the spectral flux of photons in the AM 1.5 G spectrum and the expected electron current flux of photocathode and PV obtained from multiplication of their respective IPCE responses by the photon flux (for IPCE acquisition, the photocathode was biased at +0.3 V_{RHE} and the PV was measured at short circuit). Integration yields the expected current densities labeled for each component. (b) *J*–*V* plots of the photocathode and anode components with overlaid *J*–*V* response of the PV cell. The photocathode configuration was 3 nm Au + 260 nm Cu_2O + ALD overlayers + 20 min RuO_2 surface catalyst. The position of the PV curve was defined by actual potential measurements at the PV electrode contacts after 60 min of tandem operation, as indicated by grey markers.

Figure 6.9b presents the *J–V* behavior of all three components tested individually, where the raw current of each was normalized by the photocathode illuminated area. Comparison of the photocathode and anode curves reveals the current-dependent additional potential needed to enable complete electrolysis. For instance, *ca.* 1 V is needed in order to drive a current density of *ca.* 2 mA·cm^{-2} between these electrodes. Few single-absorber photovoltaics are capable of photopotentials this large, but the emergent high-V_{oc} hybrid perovskite photovoltaics represent promising candidates for this application [44]. Herein, a perovskite solar cell (PV cell) based on the mixed-cation formulation formamidinium methylammonium lead iodide ($(MA)_x(FA)_{1-x}PbI_3$) was employed [45], which exhibits a V_{oc} under 1-sun illumination of 1.13 V (see Figure 6.10 for the photovoltaic cell *J–V* curves and IPCE analysis).

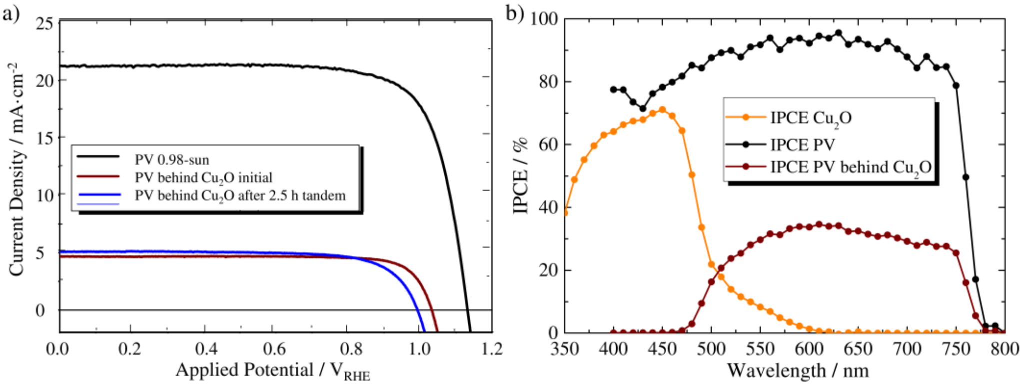

Figure 6.10: Photovoltaic cell characterization; (a) *J–V* curves of the $(MA)_x(FA)_{1-x}PbI_3$ PV under various illumination conditions (0.98-sun and behind Cu_2O in tandem configuration) scanned at 10 mV·s^{-1}; (b) IPCE response of the PV cell as well as the product of the IPCE and the measured Cu_2O transmittance to yield the expected IPCE of the PV when placed behind the photocathode. The photocathode IPCE is shown as well for reference.

The PV cell was placed against the back window of the sealed PEC cell and connected by wires to the electrodes. Since the PV is electrically in series between the anode and photocathode, its *J–V* response can be plotted between the electrode *J–V* curves in order to predict the tandem operation current. Under operation, the currents through each component are equal, and the potentials of each contact spontaneously adjust to reach this equilibrium. From Figure 6.9b, this treatment predicts an operating current density of *ca.* 2 mA·cm^{-2} for this tandem configuration. All components were then connected in series and the cell was illuminated with 1-sun intensity simulated sunlight, using a potentiostat to monitor the current flowing between the PV and anode (applying zero bias) while simultaneously performing in-line gas chromatography measurement of the evolved gases. Figure 6.11a shows the resulting measured current density, where it can be seen that the actual tandem performance corresponded well with that predicted by the separate component analysis. Measurement of both hydrogen and oxygen, important for proving complete water splitting [46], led to calculate Faradaic efficiencies around 100 % for each gas - Figure 6.11b.

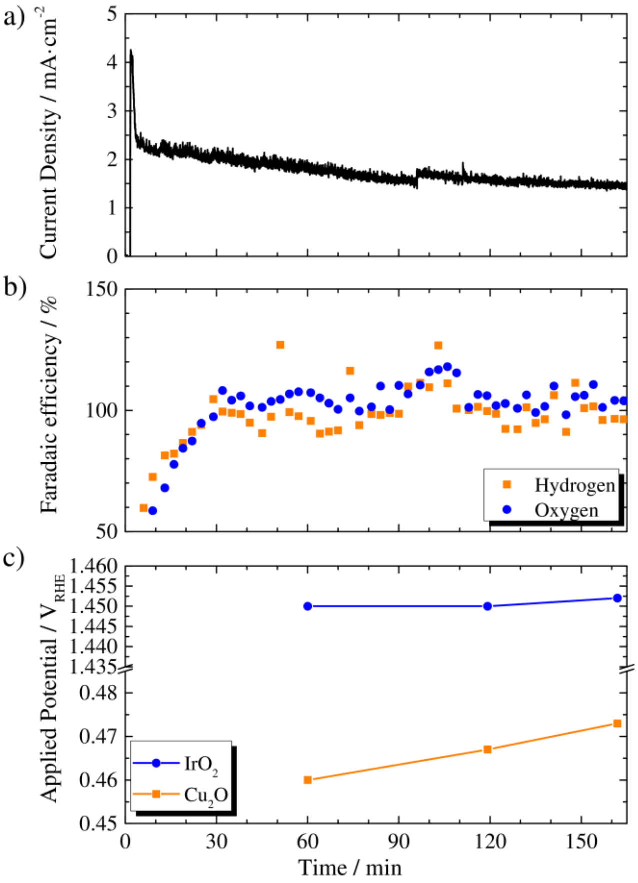

Figure 6.11: PEC/PV tandem assembly and operation: (a) photocurrent density history over time in the AM 1.5 G spectrum; (b) Faradaic efficiency from in-line gas measurements; and (c) potential measurements during operation of the complete assembled tandem in a sealed, stirred cell under continuous flow of He carrier gas, with a photocathode and photovoltaic illuminated area of *ca.* 0.057 cm^2. Approximately 30 min were required for the produced gases to reach equilibrium in the cell.

Variations in the gas measurements are a result of the build-up and release of bubbles on the electrode surfaces. A photocurrent-density of *ca.* 2 mA·cm^{-2} combined with the near-unity yield of evolved gases corresponds to a solar-to-hydrogen (STH) efficiency of *ca.* 2.5 % by Equation (6.1):

$$\mathrm{STH} = \left.\frac{J_{\mathrm{photo}} E_{\mathrm{photo}} \eta_{\mathrm{F}}}{P_{\mathrm{light}}}\right|_{\mathrm{AM\,1.5\,G}} = \frac{J_{\mathrm{photo}}\left(\mathrm{mA\cdot cm^{-2}}\right)\times 1.23\,\mathrm{V}\times \eta_{\mathrm{F}}}{100\left(\mathrm{mW\cdot cm^{-2}}\right)} \tag{6.1}$$

where J_{photo} is the photocurrent density during unbiased operation, 1.23 V is the standard-state potential for water electrolysis, η_{F} is the Faradaic efficiency of evolved hydrogen and P_{light} is the power of the incident illumination, taken here as 100 mW·cm^{-2} for the AM 1.5 G spectrum at 1-sun intensity. This efficiency, while modest in comparison to more sophisticated systems [8-10], represents an important advance among photocathode-based tandem devices employing Earth-abundant absorbers.

The tandem device was tested under continuous illumination for over two hours, during which time the photocurrent density slowly decreased to stabilize at *ca.* 1.5 mA·cm^{-2}. In addition to measurements of J_{photo} and η_{F}, monitoring the device potentials during operation revealed insight into the tandem operation. By periodically measuring the electrode potentials against a reference electrode in the cell as illustrated in Figure 6.8 and shown in Figure 6.11c, the anode potential revealed to be quite stable whereas the photocathode potential was shifted to more positive values over time. These changes were concurrent with the gradual decrease of device J_{photo}, and the behavior can be interpreted by referring to the analysis in Figure 6.9b. The measured potentials represent the potentials at the contacts between the PV cell and each electrode, equivalent to the labeled crossover points. Since the anode curve is steep, changes in current are accommodated with relatively little change in potential. For the photocathode, on the other hand, the observed positive shift in potential, combined with the decreasing measured J_{photo}, reveals that the performance decline is likely a result of a decrease in the PV photopotential. Indeed, when its *J–V* response was re-tested after tandem operation, V_{oc} and fill-factor of the PV cell exhibited a slight decrease (Figure 6.10). Despite this observation, it was noted that several recent works have demonstrated extended stability for hybrid perovskite photovoltaics [47, 48], and this is a topic of ongoing study for the device type employed here. Meanwhile, the photocathode was found to be robust. In an extended test, a representative Cu_2O photocathode of this same transparent configuration was found to be highly stable when tested for 24 hours under continuous operation, as shown in Figure 6.12.

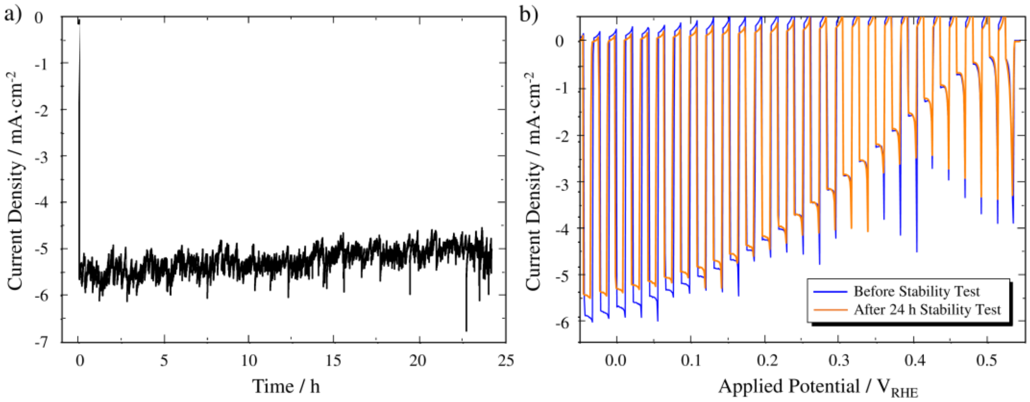

Figure 6.12: Representative photocathode stability study for a device based on 3 nm Au + 50 min Cu_2O: (a) chronoamperometry under continuous illumination while biased at 0 V_{RHE} for 24 h; and (b) *J*–*V* response before and after the stability test.

There are several clear paths toward improving upon this tandem efficiency, mostly based on the enhancement of the Cu_2O photocathode performance. As shown above, the photocurrent density is highly dependent on the operating potential. An increase in the photopotential of the device, manifesting as a positive shift in the *J*–*V* curve, would allow tandem operation at higher current density. For instance, a photopotential increase of *ca.* 0.2 V could enable a near-doubling of the operating current density to *ca.* 4 mA·cm^{-2}. Recently it has been shown that improving the nature of the Cu_2O–overlayer junction by using Ga_2O_3 interlayers can lead to significantly enhanced photopotentials [33, 49], an approach that may prove useful toward tandem applications. Improvement in the photocathode photocurrent is also needed, although the forbidden electronic transitions for photon energies below 2.5 eV require much thicker Cu_2O films for improved absorption in that range [38], posing a challenge when targeting high device transparency.

The tandem performance may also be improved by operating in a highly alkaline or acidic electrolyte more suitable for efficient electrolysis. Although rapid stirring was used here to prevent mass transport limitations and pH gradient build-up, it has been shown that devices in near-neutral solutions can be fundamentally limited in efficiency when operated for extended periods [50]. Furthermore, catalysts for water oxidation are generally more efficient in alkaline solutions, for which there are several desirable Earth-abundant candidates [39]. At present, TiO_2 overlayer approach was found to be insufficiently stable in alkaline conditions to allow a demonstration extended operation, but further study in this direction is ongoing [51], since a stable and efficient photocathode in alkaline solution would be highly desirable.

6.4 CONCLUSIONS

In this work, a PEC/PV water splitting tandem was constructed using a Cu_2O photocathode and a hybrid perovskite photovoltaic. In developing a transparent photocathode, it is discovered the important role of gold as substrate and explored how different aspects of the device architecture influence the balance between performance and transparency. This transparent Cu_2O photoelectrode enabled the construction of an optically-stacked two absorbers tandem device capable of performing standalone sunlight-driven water splitting at up to 2.5 % solar-to-hydrogen efficiency, a performance that may be significantly enhanced by further development of the Cu_2O photocathode.

ACKNOWLEDGMENTS

P. Dias and J. Azevedo are grateful to the Portuguese Foundation for Science and Technology (FCT) for their PhD Grants (References: SFRH/BD/81016/2011 and SFRH/BD/79207/2011, respectively). L. Andrade acknowledges European Research Council (Contract no: 321315) for financial support. Additionally, M. Schreier thanks Siemens AG, J. Luo thanks Nano-Tera (TANDEM project), M. Grätzel thanks the Swiss Federal Office for Energy (PECHouse project), and A. Hagfeldt thanks the Swiss National Science Foundation NRP70 programme (154002) for financial support. Special thanks to Jeong-Hyeok Im and F. Javier Ramos for their efforts in photovoltaic fabrication, and to Prof. K. Sivula for the use of the UV-vis spectrometer. The authors thank the European Commission for supporting this work through the following Seventh Framework Programme collaborative projects: PECDEMO (ref. n° 621252), BI-DSC (321315), PHOCS (309223), and MESOLIGHT (247404). Financial support by Project UID/EQU/00511/2013 - LEPABE and by FEDER funds through COMPETE2020 is also acknowledged.

REFERENCES

1. Castelli, I.E., Hüser, F., Pandey, M., Li, H., Thygesen, K.S., Seger, B., Jain, A., Persson, K.A., Ceder, G. and Jacobsen, K.W., *New Light-Harvesting Materials Using Accurate and Efficient Bandgap Calculations.* Adv. Energy Mater., **2015**. 5(2): p. 1400915.
2. Sliozberg, K., Schäfer, D., Erichsen, T., Meyer, R., Khare, C., Ludwig, A. and Schuhmann, W., *High-Throughput Screening of Thin-Film Semiconductor Material Libraries I: System Development and Case Study for Ti-W-O.* ChemSusChem, **2015**. 8(7): p. 1270-1278.
3. Prévot, M.S. and Sivula, K., *Photoelectrochemical Tandem Cells for Solar Water Splitting.* Journal of Physical Chemistry C, **2013**. 117(35): p. 17879-17893.
4. Hu, S., Xiang, C., Haussener, S., Berger, A.D. and Lewis, N.S., *An analysis of the optimal band gaps of light absorbers in integrated tandem photoelectrochemical water-splitting systems.* Energy & Environmental Science, **2013**. 6(10): p. 2984-2993.
5. Bornoz, P., Abdi, F.F., Tilley, S.D., Dam, B., van de Krol, R., Grätzel, M. and Sivula, K., *A Bismuth Vanadate-Cuprous Oxide Tandem Cell for Overall Solar Water Splitting.* Journal of Physical Chemistry C, **2014**. 118(30): p. 16959-16966.
6. Liu, C., Tang, J., Chen, H.M., Liu, B. and Yang, P., *A Fully Integrated Nanosystem of Semiconductor Nanowires for Direct Solar Water Splitting.* Nano Letters, **2013**. 13(6): p. 2989-2992.
7. Brillet, J., Yum, J.H., Cornuz, M., Hisatomi, T., Solarska, R., Augustynski, J., Grätzel, M. and Sivula, K., *Highly efficient water splitting by a dual-absorber tandem cell.* Nature Photonics, **2012**. 6(12): p. 823-827.
8. Ager Iii, J.W., Shaner, M., Walczak, K., Sharp, I.D. and Ardo, S., *Experimental Demonstrations of Spontaneous, Solar-Driven Photoelectrochemical Water Splitting.* Energy & Environmental Science, **2015**. 8(10): p. 2811-2824.
9. Licht, S., Wang, B., Mukerji, S., Soga, T., Umeno, M. and Tributsch, H., *Efficient Solar Water Splitting, Exemplified by RuO_2-Catalyzed AlGaAs/Si*

Photoelectrolysis. The Journal of Physical Chemistry B, **2000**. 104(38): p. 8920-8924.

10. Khaselev, O., Bansal, A. and Turner, J.A., *High-efficiency integrated multijunction photovoltaic/electrolysis systems for hydrogen production.* International Journal of Hydrogen Energy, **2001**. 26(2): p. 127-132.
11. Gurudayal, Sabba, D., Mulmudi, H.K., Wong, L.H., Barber, J., Grätzel, M. and Mathews, N., *Perovskite- Hematite Tandem Cells for Efficient Overall Solar Driven Water Splitting.* Nano Letters, **2015**. 15(6): p. 3833-3839.
12. Shi, X., Zhang, K., Shin, K., Ma, M., Kwon, J., Choi, I.T., Kim, J.K., Kim, H.K., Wang, D.H. and Park, J.H., *Unassisted photoelectrochemical water splitting beyond 5.7 % solar-to-hydrogen conversion efficiency by a wireless monolithic photoanode/dye-sensitised solar cell tandem device.* Nano Energy, **2015**. 13(0): p. 182-191.
13. Chen, Y.-S., Manser, J.S. and Kamat, P.V., *All Solution-Processed Lead Halide Perovskite-$BiVO_4$ Tandem Assembly for Photolytic Solar Fuels Production.* Journal of the American Chemical Society, **2015**. 137(2): p. 974-981.
14. Ding, C., Qin, W., Wang, N., Liu, G., Wang, Z., Yan, P., Shi, J. and Li, C., *Solar-to-hydrogen efficiency exceeding 2.5 % achieved for overall water splitting with an all earth-abundant dual-photoelectrode.* Physical Chemistry Chemical Physics, **2014**. 16(29): p. 15608-15614.
15. Han, L., Abdi, F.F., van de Krol, R., Liu, R., Huang, Z., Lewerenz, H.-J., Dam, B., Zeman, M. and Smets, A.H.M., *Efficient Water-Splitting Device Based on a Bismuth Vanadate Photoanode and Thin-Film Silicon Solar Cells.* ChemSusChem, **2014**. 7(10): p. 2832-2838.
16. Shaner, M.R., Fountaine, K.T., Ardo, S., Coridan, R.H., Atwater, H.A. and Lewis, N.S., *Photoelectrochemistry of core-shell tandem junction n-p^+-Si/n-WO_3 microwire array photoelectrodes.* Energy & Environmental Science, **2014**. 7(2): p. 779-790.
17. Walczak, K., Chen, Y., Karp, C., Beeman, J.W., Shaner, M., Spurgeon, J., Sharp, I.D., Amashukeli, X., West, W., Jin, J., Lewis, N.S. and Xiang, C., *Modeling, Simulation, and Fabrication of a Fully Integrated, Acid-stable, Scalable Solar-Driven Water-Splitting System.* ChemSusChem, **2015**. 8(3): p. 544-551.

18. Lin, C.-Y., Lai, Y.-H., Mersch, D. and Reisner, E., *$Cu_2O|NiO_x$ nanocomposite as an inexpensive photocathode in photoelectrochemical water splitting.* Chemical Science, **2012**. 3(12): p. 3482-3487.
19. Seger, B., Castelli, I.E., Vesborg, P.C.K., Jacobsen, K.W., Hansen, O. and Chorkendorff, I., *2-Photon tandem device for water splitting: comparing photocathode first versus photoanode first designs.* Energy & Environmental Science, **2014**. 7(8): p. 2397-2413.
20. Rowley, J.G., Do, T.D., Cleary, D.A. and Parkinson, B.A., *Combinatorial Discovery Through a Distributed Outreach Program: Investigation of the Photoelectrolysis Activity of p-Type Fe, Cr, Al Oxides.* ACS Applied Materials & Interfaces, **2014**. 6(12): p. 9046-9052.
21. Read, C.G., Park, Y. and Choi, K.-S., *Electrochemical Synthesis of p-Type CuFeO2 Electrodes for Use in a Photoelectrochemical Cell.* The Journal of Physical Chemistry Letters, **2012**. 3(14): p. 1872-1876.
22. Gu, J., Yan, Y., Krizan, J.W., Gibson, Q.D., Detweiler, Z.M., Cava, R.J. and Bocarsly, A.B., *p-Type $CuRhO_2$ as a Self-Healing Photoelectrode for Water Reduction under Visible Light.* Journal of the American Chemical Society, **2014**. 136(3): p. 830-833.
23. Dai, P., Li, W., Xie, J., He, Y., Thorne, J., McMahon, G., Zhan, J. and Wang, D., *Forming Buried Junctions to Enhance the Photovoltage Generated by Cuprous Oxide in Aqueous Solutions.* Angewandte Chemie International Edition, **2014**. 53(49): p. 13493-13497.
24. Meyer, B.K., Polity, A., Reppin, D., Becker, M., Hering, P., Klar, P.J., Sander, T., Reindl, C., Benz, J., Eickhoff, M., Heiliger, C., Heinemann, M., Bläsing, J., Krost, A., Shokovets, S., Müller, C. and Ronning, C., *Binary copper oxide semiconductors: From materials towards devices.* physica status solidi (b), **2012**. 249(8): p. 1487-1509.
25. Paracchino, A., Laporte, V., Sivula, K., Grätzel, M. and Thimsen, E., *Highly active oxide photocathode for photoelectrochemical water reduction.* Nat Mater, **2011**. 10(6): p. 456-461.
26. Paracchino, A., Brauer, J.C., Moser, J.-E., Thimsen, E. and Graetzel, M., *Synthesis and Characterization of High-Photoactivity Electrodeposited Cu_2O*

Solar Absorber by Photoelectrochemistry and Ultrafast Spectroscopy. The Journal of Physical Chemistry C, **2012**. 116(13): p. 7341-7350.

27. Paracchino, A., Mathews, N., Hisatomi, T., Stefik, M., Tilley, S.D. and Gratzel, M., *Ultrathin films on copper(i) oxide water splitting photocathodes: a study on performance and stability.* Energy & Environmental Science, **2012**. 5(9): p. 8673-8681.
28. Tilley, S.D., Schreier, M., Azevedo, J., Stefik, M. and Graetzel, M., *Ruthenium Oxide Hydrogen Evolution Catalysis on Composite Cuprous Oxide Water-Splitting Photocathodes.* Advanced Functional Materials, **2013**. 24(3): p. 1616-3028.
29. Azevedo, J., Steier, L., Dias, P., Stefik, M., Sousa, C.T., Araujo, J.P., Mendes, A., Graetzel, M. and Tilley, S.D., *On the stability enhancement of cuprous oxide water splitting photocathodes by low temperature steam annealing.* Energy & Environmental Science, **2014**. 7(12): p. 4044-4052.
30. Paracchino, A., Brauer, J.C., Moser, J.E., Thimsen, E. and Grätzel, M., *Synthesis and Characterization of High-Photoactivity Electrodeposited Cu_2O Solar Absorber by Photoelectrochemistry and Ultrafast Spectroscopy.* Journal of Physical Chemistry C, **2012**. 116(13): p. 7341-7350.
31. Tilley, S.D., Schreier, M., Azevedo, J., Stefik, M. and Grätzel, M., *Ruthenium Oxide Hydrogen Evolution Catalysis on Composite Cuprous Oxide Water-Splitting Photocathodes.* Advanced Functional Materials, **2014**. 24(3): p. 303-311.
32. McShane, C.M. and Choi, K.-S., *Junction studies on electrochemically fabricated p-n Cu_2O homojunction solar cells for efficiency enhancement.* Physical Chemistry Chemical Physics, **2012**. 14(17): p. 6112-6118.
33. Lee, Y.S., Chua, D., Brandt, R.E., Siah, S.C., Li, J.V., Mailoa, J.P., Lee, S.W., Gordon, R.G. and Buonassisi, T., *Atomic Layer Deposited Gallium Oxide Buffer Layer Enables 1.2 V Open-Circuit Voltage in Cuprous Oxide Solar Cells.* Advanced Materials, **2014**. 26(27): p. 4704-4710.
34. Rakhshani, A.E., *Preparation, characteristics and photovoltaic properties of cuprous oxide — a review.* Solid-State Electronics, **1986**. 29(1): p. 7-17.
35. Liu, Y.L., Liu, Y.C., Mu, R., Yang, H., Shao, C.L., Zhang, J.Y., Lu, Y.M., Shen, D.Z. and Fan, X.W., *The structural and optical properties of Cu_2O films*

electrodeposited on different substrates. Semiconductor Science and Technology, **2005**. 20(1): p. 44.

36. Pavan, M., Rühle, S., Ginsburg, A., Keller, D.A., Barad, H.-N., Sberna, P.M., Nunes, D., Martins, R., Anderson, A.Y., Zaban, A. and Fortunato, E., *TiO_2/Cu_2O all-oxide heterojunction solar cells produced by spray pyrolysis.* Solar Energy Materials and Solar Cells, **2015**. 132: p. 549-556.
37. Brown, K.E.R. and Choi, K.-S., *Electrochemical synthesis and characterization of transparent nanocrystalline Cu_2O films and their conversion to CuO films.* Chemical Communications, **2006** (31): p. 3311-3313.
38. Malerba, C., Biccari, F., Leonor Azanza Ricardo, C., D'Incau, M., Scardi, P. and Mittiga, A., *Absorption coefficient of bulk and thin film Cu_2O.* Solar Energy Materials and Solar Cells, **2011**. 95(10): p. 2848-2854.
39. McCrory, C.C.L., Jung, S., Peters, J.C. and Jaramillo, T.F., *Benchmarking Heterogeneous Electrocatalysts for the Oxygen Evolution Reaction.* Journal of the American Chemical Society, **2013**. 135(45): p. 16977-16987.
40. Brillet, J., Yum, J.-H., Cornuz, M., Hisatomi, T., Solarska, R., Augustynski, J., Graetzel, M. and Sivula, K., *Highly efficient water splitting by a dual-absorber tandem cell.* Nat Photon, **2012**. 6(12): p. 824-828.
41. Chen, Y.-S., Manser, J.S. and Kamat, P.V., *All Solution-Processed Lead Halide Perovskite-$BiVO_4$ Tandem Assembly for Photolytic Solar Fuels Production.* Journal of the American Chemical Society, **2014**. 137(2): p. 974-981.
42. Abdi, F.F., Han, L., Smets, A.H.M., Zeman, M., Dam, B. and van de Krol, R., *Efficient solar water splitting by enhanced charge separation in a bismuth vanadate-silicon tandem photoelectrode.* Nat Commun, **2013**. 4: p. 2195.
43. Khaselev, O. and Turner, J.A., *A Monolithic Photovoltaic-Photoelectrochemical Device for Hydrogen Production via Water Splitting.* Science, **1998**. 280(5362): p. 425-427.
44. Luo, J., Im, J.-H., Mayer, M.T., Schreier, M., Nazeeruddin, M.K., Park, N.-G., Tilley, S.D., Fan, H.J. and Grätzel, M., *Water photolysis at 12.3 % efficiency via perovskite photovoltaics and Earth-abundant catalysts.* Science, **2014**. 345(6204): p. 1593-1596.
45. Pellet, N., Gao, P., Gregori, G., Yang, T.-Y., Nazeeruddin, M.K., Maier, J. and Grätzel, M., *Mixed-Organic-Cation Perovskite Photovoltaics for Enhanced Solar-*

Light Harvesting. Angewandte Chemie International Edition, **2014**. 53(12): p. 3151-3157.

46. Chen, Z., Jaramillo, T.F., Deutsch, T.G., Kleiman-Shwarsctein, A., Forman, A.J., Gaillard, N., Garland, R., Takanabe, K., Heske, C., Sunkara, M., McFarland, E.W., Domen, K., Miller, E.L., Turner, J.A. and Dinh, H.N., *Accelerating materials development for photoelectrochemical hydrogen production: Standards for methods, definitions, and reporting protocols.* J. Mater. Res., **2010**. 25(01): p. 3-16.
47. Schreier, M., Curvat, L., Giordano, F., Steier, L., Abate, A., Zakeeruddin, S.M., Luo, J., Mayer, M.T. and Gratzel, M., *Efficient photosynthesis of carbon monoxide from* CO_2 *using perovskite photovoltaics.* Nat Commun, **2015**. 6: p. 7326.
48. Mei, A., Li, X., Liu, L., Ku, Z., Liu, T., Rong, Y., Xu, M., Hu, M., Chen, J., Yang, Y., Grätzel, M. and Han, H., *A hole-conductor–free, fully printable mesoscopic perovskite solar cell with high stability.* Science, **2014**. 345(6194): p. 295-298.
49. Li, C., Hisatomi, T., Watanabe, O., Nakabayashi, M., Shibata, N., Domen, K. and Delaunay, J.-J., *Positive onset potential and stability of* Cu_2O*-based photocathodes in water splitting by atomic layer deposition of a* Ga_2O_3 *buffer layer.* Energy & Environmental Science, **2015**. 8(5): p. 1493-1500.
50. Jin, J., Walczak, K., Singh, M.R., Karp, C., Lewis, N.S. and Xiang, C., *An experimental and modeling/simulation-based evaluation of the efficiency and operational performance characteristics of an integrated, membrane-free, neutral pH solar-driven water-splitting system.* Energy & Environmental Science, **2014**. 7(10): p. 3371-3380.
51. Morales-Guio, C.G., Liardet, L., Mayer, M.T., Tilley, S.D., Grätzel, M. and Hu, X., *Photoelectrochemical Hydrogen Production in Alkaline Solutions Using* Cu_2O *Coated with Earth-Abundant Hydrogen Evolution Catalysts.* Angewandte Chemie International Edition, **2015**. 54(2): p. 664-667.

CHAPTER 7

GENERAL CONCLUSIONS AND OUTLOOK

7

GENERAL CONCLUSIONS AND OUTLOOK

The present work studies the photoelectrochemical (PEC) water splitting using promising metal oxide semiconductors, such as hematite and tungsten trioxide photoanodes and cuprous oxide photocathodes, aiming efficient and stable devices. To accomplish the proposed goals, complete structural, morphological and electrochemical characterization, namely photocurrent density-voltage (*J*-*V*) characteristics, aging tests and electrochemical impedance spectroscopy (EIS), were performed for assessing PEC cells performance.

PEC cells for water splitting, as other solar devices, are very sensitive to temperature. Understanding the behavior of these devices as a function of temperature is particularly important for practical applications since under real outdoor conditions the temperature should range between subzero to *ca.* 70 ºC. An experimental test bench was built and a PEC cell setup designed with a temperature controlling system. The performance of Si-doped hematite photoanodes was assessed as a function of temperature. Within the temperature range considered, 25 ºC to 65 ºC, a global improvement of the energy performance with temperature was observed. The best operating conditions were obtained for *ca.* 45 ºC, which balances the energy efficiency and the photoanode stability (72 h). Moreover, a cathodic shift of the dark current onset potential was observed for higher temperatures. This effect was assigned to the role of the transparent conducting oxide applied to the substrate, FTO (fluorine doped tin oxide), on the water splitting. This role was further studied using two types of substrates; it was chosen tungsten trioxide photoanodes deposited on a FTO glass (WO_3/FTO) and anodized on a tungsten foil (WO_3/metal). An improvement in the photocurrent density with temperature was observed together with the cathodic shift of the onset potential for both samples. However, the WO_3/FTO exhibited already a quite high dark current onset potential at *ca.* 1.80 V_{RHE}, while the WO_3/metal showed almost negligible dark current. Thus, the earlier dark current onset observed for WO_3/FTO was assigned to the FTO layer and not to the effect of temperature on the photoanode material. The *J*-*V* and EIS measurements allowed concluding about the optimal operating temperature, 45 ºC for the WO_3/FTO sample and 55 ºC for the WO_3/metal sample, which balances the energy efficiency and the photoelectrode stability. For higher temperatures, the bulk electron-hole recombination phenomenon, which is in direct competition with water oxidation, greatly affects the overall performance of WO_3 photoanodes. The aging tests performed at these temperatures over 72 h showed that WO_3/metal has the best stability performance for the oxygen evolution reaction, maintaining its morphology and good crystallinity with minimal energy conversion efficiency losses after 4 h (< 2 %). For WO_3/FTO, a crystalline-to-amorphous phase transformation occurred during the stability test, which may justify the current decrease observed after the aging period. These findings provide crucial information about the role of substrate and preparation method on the photoelectrode energy performance and stability.

Furthermore, stability is one of the main concerns when future commercial applications are envisaged but hematite was reported as a highly stable semiconductor material. Herein, photoanodes of bare hematite prepared by spray pyrolysis were systematically optimized following a design of experiments approach. A response surface methodology was applied considering the following factors: i) sprayed volume of solution; ii) temperature of the glass substrate during the deposition; and iii) time gap between sprays. The optimized operating conditions obtained were $v = 42$ mL, $T = 425$ ºC and $t = 35$ s. The optimized hematite photoelectrode showed a photocurrent density of *ca.* 0.94 $mA \cdot cm^{-2}$ at 1.45 V_{RHE}, which is a remarkable value for an ultrathin film of *ca.* 18.8 nm. One of the most important contributions of the present work was the long-term stability study; the prepared hematite photoanode was extremely stable over 1000 h of PEC operation under 1-sun AM 1.5 G illumination. A record-breaking result, with no evidences of hematite film degradation neither of current density loss. This result opens the door to turn PEC cells into a competitive technology in the solar fuel economy.

Hematite is one of the most promising photoelectrodes for solar water splitting. Nevertheless, its performance as a photoanode is considerably lower than what is thermodynamically expected, mainly due to the high electrochemical potential usually needed to initiate water splitting and its low photopotential. This low photopotential is essentially related to surface defects, while decreasing the water oxidation overpotentials harnesses the available photopotential. A synergetic combination of surface passivation, obtained by annealing the hematite photoanode at 800 ºC and by coating with RuO_2 co-catalyst, was the strategy used to cathodically shift the photocurrent onset potential. The annealing at 800 ºC improved both the morphology and the electronic structure due to the diffusion of tin ions from the FTO layer into the hematite lattice, whereas the coating of RuO_2 co-catalyst (optimal load of 36 $mC \cdot cm^{-2}$) improved water oxidation kinetics and band bending. Therefore, RuO_2-coated hematite thin films further sintered at 200 ºC showed an onset potential of *ca.* 0.52 V_{RHE} (cathodic onset shift > 400 mV) and a noticeable photocurrent density of *ca.* 0.60 $mA \cdot cm^{-2}$ at 1.00 V_{RHE} was reached, compared to < 0.01 $mA \cdot cm^{-2}$ of the bare hematite. A final photopotential of *ca.* 0.95 V was obtained, which is the highest reported for hematite-based photoanodes. Future work should focus on improving the co-catalyst activity and stability to delivery at lower potentials high current densities; binary and complex co-catalysts are foreseen to this end.

A major drawback in PEC cells is therefore the lack of suitable photoelectrode materials available to promote the overall water splitting reaction without an external bias source. Dual-absorber tandem devices can be accomplished with photoanode–photocathode systems or photoelectrode-photovoltaic coupled devices to generate the sufficient driving force for standalone solar water splitting. However, a prerequisite of the photoelectrode is displaying high photopotential compatible with a single tandem arrangement of a PEC/PV cell. Literature studies employing PEC/PV tandem configuration have mostly focused around the use of n-type semiconductors for water oxidation since there are fewer Earth-abundant and stable candidates for photocathode PEC devices. Cu_2O photocathodes have been reported for the hydrogen evolution reaction due to their recent stability enhancement using protective overlayers of AZO/TiO_2 and RuO_2 co-catalyst. However, these films are typically electrodeposited on an opaque Au layer, which precludes their use in a tandem configuration. Here, the treatment of FTO glass substrates with thin layers of gold (*ca.* 3 nm Au) had a crucial role for the development of a highly performing semi-transparent Cu_2O photocathode as a top absorber. This material generated a photocurrent-density of *ca.* 5.50 $mA \cdot cm^{-2}$ that remained almost constant over 24 h. Therefore, the new transparent photoelectrode enabled the construction of an optically-stacked two absorbers tandem device with a hybrid perovskite photovoltaic cell. The innovative PEC/PV system performed standalone sunlight-driven water splitting at *ca.* 2.50 % solar-to-hydrogen efficiency, a performance that may be significantly enhanced by further improvements of the Cu_2O photocathode.

PEC hydrogen generation is not yet commercial and, in fact, to turn this technology cost-effective, solar-to-hydrogen energy conversion efficiency of 10 % and lifetimes of more than 1000 h have to be demonstrated up to 2017 to meet the FCH-JU's (Fuel Cells and Hydrogen Joint Undertaking) cost target of 5 € per kg H_2. Future directions are mainly focused on four crucial topics: i) development of stable and efficient metal oxide photoelectrodes, ii) optimization of tandem cell designs, iii) technology scale-up, and iv) techno-economic and life-cycle assessments.

The scientific challenges of PEC cell devices comprise the design of new, Earth-abundant light absorbing materials, such as heteronanostructures, with appropriate bandgap and band edge positions. Moreover, the development of transparent and high-performance electrocatalysts and ameliorated interfaces should facilitate oxygen and hydrogen evolution reactions, reducing recombination rates. Hematite photoanodes are very promising for oxygen evolution reaction, with a maximum thermodynamic STH efficiency of 16.8 %. The present study proved high stability in an alkaline medium (1000 h PEC operation) using an ultrathin hematite film; the films were prepared by spray pyrolysis, exhibiting great reproducibility for future industrial applications. Continued efforts to control the surface-related processes are strongly required for further enhancing the performance of photoelectrodes and PEC devices. Surface modifications can address the fundamental photoelectrode defects, *e.g.* stability, surface states, poor band bending, catalytic activity, *etc.* The use of RuO_2 as a highly active co-catalyst was effective on improving the hematite photopotential; however, the introduction of non-noble metals on the catalyst structure, such as Co and Ni, should enhance the photoelectrode performance, reducing also the final cost. Other water oxidation co-catalysts should be tested, *e.g.* $NiFeO_x$, in order to reach the maximum photocurrent near the onset potential, which would allow the tandem arrangement with a Si photocathode or a PV cell enabling unassisted water splitting. For harnessing better hematite performances, the recent advances are focused on using a host-guest approach, where the light absorption and water oxidation roles are decoupled from the electron conduction. For instance, depositing an extremely thin layer of hematite onto a WO_3 mesoporous host, its short carrier diffusion lengths limitation together with a photocurrent increase can be overcome. On the other hand, Cu_2O appears as an attractive photocathode material, since almost half of its thermodynamic STH conversion efficiency (maximum current density value of *ca.* 14.7 $mA{\cdot}cm^{-2}$) was already achieved. The weak point is the lack of chemical stability of the top protective layer at the pH values where the hydrogen evolution co-catalyst shows peak-performance. Additional efforts on finding solutions to deposit a crystalline and stable protective overlayer that minimizes deleterious electron trapping in the film are very important.

Despite many progresses, no single semiconductor material has been found that fulfills all the requirements needed to generate standalone water splitting devices. Dual light-absorber tandem devices enabling unbiased water splitting, mainly hybrid PEC/PV tandem systems, are considered the new generation for PEC hydrogen production. Recent breakthroughs have brought metal oxide photoelectrodes close to efficiency levels required for practical applications, but they also need to target high transparency when combined as top absorber materials; the later requirement sacrifices the light absorption and then the photoelectrode current. Thus, there are several clear paths toward improving upon tandem efficiencies, mostly based on the enhancement of the photoelectrode performance and the stability of the tandem device. For the proposed PEC/PV device, an increase in the photopotential of Cu_2O photoelectrode would allow tandem operation at higher currents, *e.g.* a photopotential increase of *ca.* 0.20 V could enable a near-doubling current density to *ca.* 4 $mA{\cdot}cm^{-2}$, the half-target to be attractive to industry.

Future improvements on the performance of photoelectrode and/or photovoltaic materials and the control device fabrication techniques, as well as the phenomenological understandings of PEC tandem systems should continue as long as the viable targets are not reached. Moreover, engineering of a practical design for large-area tandem devices allowing the recovery of hydrogen and oxygen gases remains a challenge. The use of inexpensive materials to convert the most renewable source of energy that is the sun will ultimately lead to a sustainable energy economy. Quoting Thomas Edison, we should continue to put money on the sun and solar energy: "*What a source of power!*"